Ilmenau University of Technology
Faculty of Computer Science and Automation

A System of Autonomously Flying Helicopters for Load Transportation

Markus Bernard

Submitted: 30.04.2013
Day of defense: 04.09.2013

Doctoral Adviser: Prof. Dr.-Ing. Armin Zimmermann
A dissertation submitted for the degree of Doktor-Ingenieur (Dr.-Ing.)

urn:nbn:de:gbv:ilm1-2013000484

Contents

Abstract

This work covers the design, realization and validation of an autonomous load transportation system, utilizing several small size helicopters. The number of participating helicopters is configurable for the described system, depending on the requirements of the transported load. The presented models and controllers have been validated in computer simulation and flight experiments.

Two non-linear models are presented: One model covers single-lift and one model covers dual- and multi-lift configurations. Simplified models are introduced beside the complex models, which are utilized for the translation controller design. These simplified models, in combination with a force generator model, which is described as well, are very good approximations of the presented non-linear models.

A generic orientation controller is presented, which is applicable for the control of all presented slung load configurations. The utilization of this controller significantly simplifies the design of the translation controllers. The independence from the actual slung load configuration is achieved through measurement of the rope force vector in the rope attachment point, which is located on the helicopter fuselage. This force vector summarizes the influence of the whole coupled system and allows the compensation of the orientation disturbances, caused by the coupling. Three translation controllers are described: A controller for single-lift configurations, which allows the active compensation of load oscillations and a distributed controller for multi-lift configurations. Additionally a dual-lift translation controller is presented, which resembles a combination of single- and multi-lift translation controller. The presented controllers for dual- or multi-lift configurations do not utilize auxiliary constructs, like spreader-bars.

The position of the load is estimated from the measured orientation of the rope, close to the helicopter fuselage. External disturbances, like wind gusts, are able to stimulate internal oscillations of the rope, which disturb the estimated load position. The internal motion of the rope as well as the influence of the used measurement device are analyzed and a flexible rope model is presented. This model is utilized for the further examination of the problem. Based on the results a load motion observer is developed and validated in several experiments. These experiments have demonstrated, that the load motion observer is essential for the safe operation of the slung load system, especially during bad weather conditions.

The derived non-linear models of the system as well as the proposed controllers for single- and multi-lift configurations have been validated in flight experiments. The system has been proven to be operable even in presence of adverse weather conditions.

1 Introduction

The airborne transportation of goods is a very important field of application for airplanes and helicopters. Beside the long range load transportation, which is usually performed by airplanes, there is a high demand for short range load transportation, which is usually performed by helicopters.

Examples of short range load transportation are the transportation of construction material to isolated places, of chopped trees to trucks, of water from a local lake to a fire. These examples already illustrate a key issue of the helicopter based load transportation: There are many goods that do not fit inside a helicopter fuselage. A solution is the so called "slung load transportation", where the load is suspended from the fuselage, using one or multiple cables. Another limitation is the low payload capacity of standard sized helicopters: A small Huges MD500E lifts only payloads up to 938 kg. The relatively large Eurocopter AS 332L2 lifts payloads up to 4500 kg, which is is still not much for industrial transportation purposes. This problem is alleviated through the use special transport helicopters, so called skycranes, like the S-64F, which supports slung loads of up to 11340 kg. The Mil Mi-26 helicopter has to be mentioned in this context, since it is the largest helicopter ever mass produced and it supports the slung load transportation for payloads up to 20000 kg.

However, many goods, which would benefit from airborne transportation, are still too heavy for a single helicopter. For example, the smallest (6x2.4x2.6 m) standard shipping container has an empty weight of 2200 kg and a net load of 28200 kg. Another example is the transportation and placement of a pre-build garage, with a weight of up to 25 tons. The transportation could be performed by trucks as well, but only if the placement area is accessible by wide roads. The payload limitation motivates the coupling of multiple helicopters, to allow the airborne load transportation, beyond the lifting capacity of a single helicopter. Operation costs do not scale linear with the payload capacity of helicopters, like shown in Table 1.1, which also motivates a coupling. Depending on the actual task, the coupled operation of multiple smaller helicopters can be more cost-effective than the operation of one larger helicopter with equal payload capacity.

Helicopter	Payload	Operation cost per hour	Operation cost per kg and hour
MD500E	938 kg	350 US$	0.373 US$
AS 332L2	4500 kg	958 US$	0.213 US$
S-64F	11340 kg	7500 US$	0.661 US$
Mi-26	20000 kg	11000 US$	0.550 US$

Table 1.1: Operation costs for different helicopter types

The manual piloting of slung loads is very difficult: The pilot needs intensive training and years of experience, before he can transport slung loads close to the payload limitation of the helicopter. Despite the need of very skillful pilots, the commercial single helicopter slung load transportation is very successful and many companies provide slung load transportation services. The slung load transportation, using two coupled helicopters, has been successfully demonstrated by military pilots. However, the experiment required careful coordination and was very stressful for the pilots. To the author's knowledge there has never been an attempt to use two or more coupled helicopters for commercial purposes, or to demonstrate a manual piloted load transportation, with three or more helicopters. The benefits of the coupled slung load transportation and the difficulties of the manual piloting, create the demand for an autonomous slung load transportation system. The development of such a system and its verification in flight experiments are the main aspects of this thesis. Small size helicopters, with a take of weight below 25 kg, have been used for the conduction of the flight experiments. The utilization of small size helicopters allowed the verification of the described models and control approaches with moderate efforts. The developed system can be transferred to full size helicopters with some minor modifications. Additionally, several practical applications exist for a system based on small size helicopters. For example the management and handling of natural disasters: First, the terrain of the disaster area is explored, using several uncoupled small size helicopters. Second, emergency supplies are transported to discovered victims, using the coupled system to increase the payload capacity.

1.1 Slung Load Systems

For this work the airborne slung load transportation is defined to be a method for the transportation of loads outside the fuselage of an airplane or helicopter, where the load is suspended from the fuselage using flexible ropes. The airborne slung load transportation is divided into high speed load transportation using airplanes, which is also called load towing, and low speed load transportation using helicopters, which includes the load lifting, transport and deployment.

For an airplane the fast forward flight is the normal flight condition. Therefore, the load is normally towed over a long distance and at the highest achievable speed. During high speed towing a towed body can exhibit strong longitudinal and lateral oscillations, depending on the shape of the body, length of the towing rope and the air-speed. There has been a lot of research on the towing of bodies at high speed, compare Sec. 1.4, therefore this work focuses on slung load operations at low speeds $\leq 50\,\mathrm{km/h}$ or during hovering. It should be noticed that most works cover towing operations using airplanes, where speeds of $200\,\mathrm{km/h}$ or less are considered to be low. The normal traveling speed of a full size helicopter is approximately $175\,\mathrm{km/h}$ and of a small size helicopter, between 15 kg and 25 kg, it is about $50\,\mathrm{km/h}$. Therefore, even with a limitation to speeds of $50\,\mathrm{km/h}$ or less, this work covers almost the full operating range of small size helicopters.

Forward flight and hovering are considered to be the most important operation modes of a helicopter. The higher maneuverability and lower maximum speed of helicopters,

Figure 1.1: Slung load configurations of a CH-54a skycrane (© United States Army - Redstone Arsenal, AL)

compared to most airplanes, characterize the differences between low speed and high speed load transportation tasks: The load is usually transported over a shorter distance, e.g. from a local lake to a forest fire, and the task usually includes not only the towing, but also the accurate pickup and placement of the load, e.g. for construction work in mountains. The low speed load transportation can be further subdivided, depending on the number of involved helicopters:

- Single-lift: A single helicopter is used for the slung load transportation.
- Dual-lift: Describes the slung load transportation using two helicopters. This is sometimes called "twin-lift" or "tandem configuration" in literature.
- Multi-lift: Describes the slung load transportation using three or more helicopters.

This work considers all configurations described above.

For each slung load configuration, single-, dual- and multi-lift, many load attachment configurations exist. Therefore, a short review of possible configurations is presented here. The single-lift, slung load transportation is the only configuration, which is used in real world applications, using manual piloted full size helicopters. A section of Wagtendonk's textbook [Wag06] for helicopter pilots covers possible load attachment configurations. According to his work, the number of used ropes depends mainly on the shape of the load, e.g. one rope for barrels, two ropes for the vertical transportation of logs or poles and four ropes for the transportation of bulky construction material. It is quite common that only a single short, max 25% of the main-rotor size, main rope is connected to the helicopter fuselage. The load is normally connected to the main rope, using one or more support ropes, see the left side of Fig. 1.1. On the contrary, it is possible to transport a load very close to the helicopter fuselage, using multiple short ropes, which are attached to several points of the fuselage, compare the right side of Fig. 1.1. In this case the ropes stabilize the load almost completely. In [DM85] an example for such a

Figure 1.2: Basic slung load configurations

mounting system is presented. However, these configurations usually require difficult load attachment maneuvers and are uncommon. This work covers only configurations, which have a single rope attachment point on the helicopter fuselage and multiple ropes can be connected to this single point.

Fig. 1.2 shows two basic slung load configurations, single- and multi-lift, which are closely examined in this work. The dual-lift configuration is considered to be an intermediate of these two configurations. The reason is, that in one horizontal axis the load is able to oscillate freely, like the load of a single-lift configuration, and in the other horizontal axis the load's motion is governed by the helicopters, like the load of a multi-lift configuration.

Most of the more complex slung load configurations are representable using these three configurations. For example, Ciolani and Kanning identify in their work 12 typical slung load configurations, see [CK92]: Three single-lift configurations, four single-lift configurations using a twin-rotor-helicopter, three dual-lift configurations and two multi-lift configurations. The theoretical results of this work are directly applicable to all configurations, but the twin rotor helicopter configurations, which would require an adaption of the helicopter models.

The three single-lift configurations, presented by Ciolani and Kanning, constitute different forms of a single, general configuration: Four support ropes are connected to four corners of a load. These support ropes are connected to a single main rope, which is

attached to the helicopter fuselage. The configurations differ only through length variation of main and support ropes. Two configurations represent extremes: a configuration without a main rope, with the direct attachment of the support ropes to single point on the helicopter fuselage, and a configuration without[1] support ropes, with the direct attachment of the main rope to the load. Support ropes normally increase the stability of the load orientation, depending on the dimensions of the load, the distance between the rope attachment points and the length of the support ropes. However, the support ropes do not prohibit a pendulum motion of the load, since they are either attached to the main rope, or to a single point on the fuselage. For all models presented in this work the load has been simplified as a mass point, which is justified by the limitation to low flight speeds and the small surface size of the transported loads. Therefore, the orientation of the load is neglected and all three single-lift configurations presented by Ciolani and Kanning become equivalent in terms of load motion. As a result, all three configurations are describable by one model and this model is presented in Sec. 5.1.1.

Ciolani and Kanning present two general types of dual- and multi-lift configurations: With and without spreader-bar[2]. A spreader-bar enforces the required separation distance between the helicopters during the dual- and multi-lift load transportation. During hovering without spreader-bar, the helicopter's main-rotor force is divided into lifting force, required to lift helicopter and load, and the force required to maintain the separation distance of the helicopters.

The spreader-bar configurations, unlike the other configurations presented by Ciolani and Kanning, are not covered by the basic configurations shown in Fig. 1.2. Spreader-bar configurations exhibit several drawbacks: First, an additional rigid body is introduced into the system, which influences the load's pendulum motion. The spreader-bar needs therefore to be considered in the models and during the controller design. Second, the spreader-bar provides an additional surface to external disturbances like wind gusts. These disturbances are propagated along the ropes to the helicopters and the load. Third, the additional weight of the spreader-bar needs to be compensated by the helicopters.

As a result, the use of spreader-bars increases the system complexity and the efficiency of spreader-bars is low for small size helicopter systems. Therefore, spreader-bar configurations are not considered in this work.

1.2 Scope of this Work

This work covers the design, development and validation of a load transportation system composed of multiple small size helicopters. Each helicopter is connected to the load through a single flexible rope. The number of participating helicopters is freely configurable and depends on the requirements of the transported load. This work consists of two major parts: "Modeling and Control of a Single Helicopter" and "Modeling and Control of Slung Load Systems".

[1] Very short support ropes are drawn, but they are not counted in a table, which is presented on the same page of Ciolani's and Kanning's publication.

[2] Additionally, they show a dual-lift configuration, where the load is utilized as spreader-bar.

Modeling and Control of a Single Helicopter The modeling and control of a single small size helicopter is a prerequisite for the modeling and control of slung load systems based on small size helicopters. Therefore, this section provides the basis for the further work.

The model of a single uncoupled small size helicopter is described in Ch. 3. The motion of a single small size helicopter is governed by its rigid body dynamics. Therefore, most of the chapter covers the rigid body model. The remaining dynamic properties of the helicopter, the dynamics of actuators and sensors as well as aerodynamics, are cumulatively modeled as a first-order delay, see Sec. 3.2-3.3 for details. The resulting non-linear model covers the most important properties of a single small size helicopter, and still exhibits a very clear structure and is well analyzable. These aspects are very important, since the model serves as a starting point for the derivation of the different slung load transportation models in Ch. 5.

In Ch. 4 a control approach for a single uncoupled helicopter is presented. Within this chapter four independent sub-controllers are identified. The heading controller, the orientation controller (excluding heading), the altitude controller and the translation controller (excluding altitude). Heading and altitude controller are directly utilizable for the control of the different slung load configurations, without any modification, like described in Ch. 4. An extended version of the presented orientation controller is utilized for the control of all slung load configurations in Ch. 6. The translation controller of an uncoupled helicopter is used as basis for the distributed controller of the multi-lift configuration.

The model and the controllers for an uncoupled small size helicopter are based on the work of the former[3] PDV-Robotics-Group of the Technische Universität Berlin. Model and controller have been described in [KDH+04, KBHK05, KBLH06]. The proposed control approach is very flexible, because of the decomposition into outer (translation) and inner loop (attitude) and the utilization of the system's inverse dynamics in the inner loop. This allows the non-linear helicopter controller to be used as a generic non-linear V-TOL controller, see [KBMH07, BKM+07].

Model and controller have been validated through many flight experiments. This provided the required confidence for the utilization as a development basis of the slung load system.

Modeling and Control of Slung Load Systems In this part the single-, dual- and multi-lift configuration models for simulation and controller design, as well as suitable control approaches are presented. The presented work extends the publications about the modeling and control of slung loads systems, which have been published by the author over the last years, see [BKH08b, BKH08a, BK09] and [BK10].

In Ch. 5 the models of different slung load configurations are presented. Two non-linear models are derived, discussed and verified in real flight experiments. These models are mainly derived for simulation purposes, including the testing of new control approaches. The verification against flight data shows, that these complex non-linear models are

[3] See the old homepage: *'http://pdv.cs.tu-berlin.de/lfafr/index.html'*.

very good approximations of the real systems. The first model is described Sec. 5.1.1 and covers single-lift configurations. The second model covers the dual- and multi-lift configurations, depending on the model parametrization, see Sec. 5.1.3 for details.

Additionally, two simplified models of the single- and multi-lift configuration are presented in Sec. 5.2.2 and Sec. 5.2.3. These models are used for the design of the translational controllers of the different slung load systems. Together with the linear force generator model developed in Sec. 5.2.1, the simplified models have been validated against the complex models. The simulation results of simplified and complex models match closely. Therefore, considering the validation of the complex models, the simplified models are considered to be good approximations of the real system.

A flexible rope model, including a Load Transportation Device (= LTD), is used to estimate the behavior of the rope and its impact on the estimated load motion. The development and verification of the model in laboratory experiments are described in Sec. 5.1.2.

Control approaches for single-, dual- and multi-lift configurations, as well as the treatment of control related problems, like the observation of the load motion, are described in Ch. 6. In Sec. 6.2 the design of a generic orientation controller, which is independent of the actual slung load configuration, is presented. The controller is based on the orientation controller of a single uncoupled helicopter, which is extended by a feed forward torque compensation. The utilization of the orientation controller significantly simplifies the design of the translation controllers, since only the translational influence of the coupled system, caused by the rope force, needs to be considered.

In Sec. 6.3-6.5 the translation controllers for the different slung load configurations are presented. All translation controllers utilize the same generic orientation controller.

The translation controller for single-lift configurations requires knowledge of the helicopter's acceleration. Therefore, based on the generation process of arbitrary forces, using the helicopter main-rotor, an acceleration estimation is presented. The estimation is described in Sec. 6.3. The estimated acceleration exhibits less noise than the acceleration derived from the GPS velocity or the acceleration directly measured by the IMU (= Inertial Measurement Unit).

In Sec. 6.4 two different translation controllers for multi-lift configurations are introduced: A centralized controller based on inverse dynamics and a decentralized controller. The decentralized controller is based on the translation controller of the single uncoupled helicopter. In this controller only the static influence of the load mass is included, and the influence of the coupled system is considered to be a disturbance. Despite this simplistic approach, the presented controller performs almost as well as the centralized controller.

The dual-lift configuration is considered to be a combination of single- and multi-lift configuration. Consequently the dual-lift translation controller combines single- and multi-lift controller, see Sec. 6.5. The single- and multi-lift controllers have been validated successfully in real flight experiments. The dual-lift controller has been tested in simulation.

The remainder of the Ch. 6 covers the estimation of the load motion. The rope is able to oscillate internally, which causes deviations between the estimated and real load motion.

An observer has been designed to improve the estimation of the true load motion. The observer has been validated in laboratory experiments and through real flight data. A significant improvement of the load motion estimation has been confirmed.

1.3 Main Results

This section covers the main results achieved during the development of the slung load transportation system for single-, dual- and multi-lift configurations. The author considers the experimental validation of the developed system to be the most important result of this work.

Experimental Validation of the Slung Load Transportation System The work for this thesis continuously alternated between theoretic research and experimental validation. Based on the results, a high confidence in the validity of the proposed modeling and control approaches has been created. Within the scope of this thesis two important milestones for the autonomous slung load transportation were achieved:

- The successful autonomous single-lift load transportation conducted on 28.11.2007[4]
- The world-wide first successful autonomous multi-lift load transportation conducted on 20.12.2007[5]

In the following the other results are described briefly:

Non-linear Models for Single- Dual- and Multi-Lift Configurations In Sec. 5.1 two non-linear models are presented. One model covers single-lift configurations and one model covers dual- and multi-lift configurations, depending on its parametrization. Both models have been validated using real-flight data and show good correspondence to the real system.

Linear Force Generator Model A linear force generator model is derived and validated in Sec. 5.2.1. The model is used to integrate the dynamics, of the generation of arbitrary forces, using a helicopter main-rotor, into simpler translational models.

Translational Models for Single- Dual- and Multi-Lift Configurations The translational models described in Sec. 5.2.2-5.2.3 utilize the linear force generator model. The complexity of these models is low compared to the non-linear models described in Sec. 5.1. However, the validation shows good correspondence between simple and complex models. The translational models are utilized for the controller design, because of their simplicity.

Generic Orientation Controller The generic orientation controller is derived and validated in Sec. 6.2. The controller utilizes a measurement of the force vector, which

[4] A video of the experiment is available: 'http://de.youtube.com/watch?v=J3gmzn0bSa4'.
[5] A video of the experiment is available: 'http://de.youtube.com/watch?v=tl6DYWNe9ac'.

results from the coupled slung load or load transportation system. A feed-forward approach is used to compensate the resulting torques, which are acting on the helicopter fuselage. A reliable stabilization of the helicopter orientation, independent from the actual slung load configuration, is achieved using the generic orientation controller. The controller therefore simplifies the design of the translation controllers and is utilized by all translation controllers presented in this thesis.

Translation Controllers for Single- Dual- and Multi-Lift Configurations The translation controllers for single-, dual- and multi-lift configurations are presented in Sec. 6.3-6.5. The single- and multi-lift controllers have been validated in real-flight experiments, see Ch. 7. The performance of the presented controllers is good enough to allow complex maneuvers and the operation during adverse weather conditions. The dual-lift controller has been tested in simulation like described in Sec. 6.5.

Load Motion Observer A load motion observer is presented in Sec. 6.6. Real-flight experiments have demonstrated that oscillations of LTD or rope can occur any time during flight, especially in the presence of strong wind gusts. The observer has been designed to estimate the actual load motion in the presence of rope or LTD oscillations. Without the load motion observer, these oscillations cause strong controller reactions and the system becomes unstable. The observer has been validated in the laboratory, see Sec. 6.6, and in real-fight experiments, see Sec. 7.1. The application of the observer allows a reliable operation of the system independent[6] of the weather conditions.

1.4 Literature Review

In this section the current state of the scientific and technical development is described. For clearness this review is split into the modeling and control of helicopters, the load towing at high speeds and the load transportation at low speeds.

1.4.1 Modeling and Control of Helicopters

The modeling of full-size helicopters has been a research topic for a very long time and much literature is available. However, the literature review about the modeling and control full-size helicopters is kept intentionally short. There is a lot of literature available about the modeling and control of small-size helicopters as well, which is closer related to the slung load system, based on small size helicopters, described in this thesis. Therefore, only three selected publications, covering full size helicopters, are presented.

The author wants to mention two books, which can be considered standard works in this field: The first one is written by A. R. S. Bramwell [Bra76] and the second book is written by W. Johnson [Joh94]. Both books intensively cover the dynamic behavior of full size helicopters, including aerodynamics and rigid body dynamics.

[6] Within reasonable limits.

A very interesting work about the control of full-size helicopters has been published by C. R. Frost. In his work [FTBL00] he describes the development of an autonomous full-size UAV, based on a BURRO helicopter sold by Kaman Aerospace. The document covers the first phase of a project, which aims at the development of an autonomous single-lift slung load transportation configuration. The described phase includes only the hovering and slow flight without external load, but the author is aware of a recent (January 2010) successful slung load transportation using the UAV.

B. Mettler describes in [MKT00] the modeling of a Yamaha R50 small-size helicopter. He derives the model using the same model identification techniques utilized by Frost. The mayor difference is the explicit inclusion of the Bell-Hiller-Stabilizer in the model. Mettler concludes that the dynamic behavior of a small-size helicopter is governed by its main-rotor and the Bell-Hiller-Stabilizer, and considers the Bell-Hiller-Stabilizer to function as lagged rate feed-back.

Another model of a small size helicopter has been developed by R. Cunha. In [CS03a, CS03b] he describes the model, and stresses the importance of main-rotor and Bell-Hiller-Stabilizer for the dynamic behavior of a small-size helicopter. In [CSP03] he presents a LQ-State-Feedback controller for his model, but unfortunately the document includes only simulation results. S. K. Kim presents in [KT98, KT04] the modeling of a small-size helicopter and the identification of model parameters. Similar to Mettler the interaction of main-rotor and Bell-Hiller-Stabilizer constitute a huge part of the work. The identified model is validated in flight experiments, and a good match of model and simulation has been achieved. An elaborated model of a small size helicopter is described by C. Deeg in [Dee06]. The presented modeling approach is validated using flight data of various platforms, including a CB5000 helicopter, which has also been utilized for the experiments presented in this thesis.

In [LCPMK03, LCPM03] M. La Civita proposes a H_∞ loop shaping controller to achieve very good control performance. Since, the controller is based on a linearized model about 30 different controllers are needed to cover the full flight envelope of the helicopter. However, the presented flight results are good. In his work [GMBO04] A. Gonzalez separates the system dynamics into fast dynamics (rotation) and slow dynamics (translation). He proposes a non-linear controller for the translation of the helicopter, but he presents only simulation results.

A very good survey of different small-size UAVs and research groups is presented by M. Béjar in [BOC07]. Additionally, he covers some aspects of model parameter identification and proposes two helicopter controllers for vertical flight.

The work [GSCA07] of B. Guerreiro is based on the model presented by Cunha. Guerreiro derives a H_2 controller with good trajectory tracking capabilities and considers the application of the system for Chimney inspection. Unfortunately he presents only simulation results.

H. Dharmayanda designed a LQR Controller, based on the model of B. Mettler. In [DKL+07] he describes the control approach and presents simulation results. A Composite Non-Linear Feedback-Controller is described by K. Peng in [PDB+07]. The controller is split into inner and outer loop, where a flight scheduler is generating commands for the outer loop.

Finally, H. J. Kim presents in his work [KSS02] a non-linear predictive controller. However, the main contribution of the document is the description of a flight management system, which allows the aerial vehicles to execute pursuit and evasion games. A few results from experiments are presented in the document, but it is not clear whether flight or simulation results are presented.

1.4.2 Slung Load Transportation at High Speeds (Towing)

One of the earliest publication about high speed towing, the author is aware of, has been written by H. Glauert in 1930. In his work [Gla30] he estimates the dependence of towed body stability on system parameters like airplane speed, rope length, rope properties and the properties of the towed body itself. In [Gla34] he includes a heavy towing cable in his estimation, which has been neglected in the first publication. Glauert provides several tables and graphs in these two documents, which allow a behavior estimation for different parameters of the towed body and the towing cable. The main motivation for his and others more recent publications is the identification of critical parameters for the slung load transportation at high speeds.

Based on Glauerts work, W. H. Phillips describes in [Phi44] the development of a towing body, which is stabilized by fins. His idea is the development of a body, which should not exhibit unstable oscillations for all feasible cable lengths. Although he did not succeed completely and concludes that there will always be an unstable region close to the airplane, he was able to improve the stability of the towed body. In [Phi49] he investigates the towing of airspeed heads, which provide only very little air-drag and therefore create only low tension in the towing cable. He discovered that air speeds lower than the wave propagation speed in the cable cause an amplification of cable oscillations. Since the tension of the cable is low for the airspeed heads, the wave propagation speed is low as well and limits the lower speed bound of the plane.

In two publications [Sha63b, Sha63a] R.E. Shanks investigates the towing of a parawing glider. The first publication covers the stability of the glider itself, and several adjustments are made to improve the stability of the glider. The second publication treats the attachment of cargo to the glider and its influence on the stability of the glider. The results of his work are in general positive, proving that the cargo transportation based on a towed parawing glider is feasible. Additionally Shanks investigates the towing behavior of a reentry vehicle in [Sha65], where the yaw angle of the vehicle is autonomously stabilized. The author considers this work to be one of the early publications, which marks the transition from passive stability improvements, like described in [PC73], towards the active stabilization of the towed body.

E.C. Micale describes in [MP73] a method to improve the lateral stability of the towed body, utilizing a rotating wheel. A similar approach is discussed by L. Feaster in [FPK77][7], which includes a comparison of a box shaped body, a boxed shaped body including fins and a boxed shaped body including a rotating wheel. Both documents conclude that a stability improvement using a rotating wheel is feasible.

[7] Although the load is towed by a helicopter, the author considers this work to belong to the class of high speed towing.

The publication of W. J. G. Pinsker [Pin70] describes the towing of an aircraft, using a helicopter. Similar to the publication [FPK77] of L. Feaster, the author considers this work to belong to the class of high speed towing. The possibility of the helicopter to influence the motion of the load is neglected, which is typical for the high speed towing. Only the stability of the towed load is investigated instead.

R. Raz [RRR89] assumes a stabilized helicopter and utilizes two actuated fins, attached to the load, to stabilize the towed load. The heading of the load is stabilized even at high towing speeds. Naturally, the fins are useless without sufficient air inflow, e.g. during hovering.

1.4.3 Slung Load Transportation at Low Speeds

Approximately 1970 the research focus changed to the modeling and control of slung load systems during hovering, where the load motion is directly stabilized through the control of the helicopter. First the publications, which treat slung load configurations composed of full-size helicopters, are presented. To improve clearness, the publications are sorted by the described configuration class: Single-, dual- and multi-lift configurations, compare Sec. 1.1 for a description of the classifications.

Full Size Single-Lift Configurations One of the first publications regarding the slung load transportation during hovering was written by A. R. Mettam. In his work [Met70] he examines pendulum oscillations caused by the downwash of the main-rotor. His work has been motivated by an incident during the winching of a towed body, where an oscillation caused the towing cable to snap. In the work of E. M. Cliff [CB75] the dynamic stability of helicopter and slung load during hovering is discussed, but similar to Mettam's publication no controller is considered.

N. K. Gupta presents in [GB76] a simple controller design based on linear quadratic synthesis. He considers vertical motion, heading and longitudinal/lateral motion to be almost independent for the equilibrium condition of the helicopter (hovering, load at rest). The presented controller considers the longitudinal/lateral motion of the helicopter and the load angles relative to the helicopter fuselage. The controller has been validated in simulation and its robustness has been demonstrated through parameter variation.

The measurement of electrical lines using a measurement body is a typical single-lift slung load operation and the scenario presented by D. Faille in [FvdW95]. He derives two non-linear models: One including a free measurement body and one including a measurement body attached to the power line. Reduced, linearized models are presented and used for the design of H_2 and H_∞ controllers. The performance of the proposed control approach has been demonstrated using a simulation of the non-linear models.

A direct commercial exploitation of Faille's results is difficult, time consuming and expensive. The reasons are the strict legal requirements for the operation of a fully autonomous load transportation system. However, a validated model of a single-lift slung load configuration has direct commercial use. For example the model may be used to predict critical helicopter/load configurations, which need to be avoided for safe, manual piloted, load transportation. For that reason L.S. Ciolani developed a model of a UH-60A

helicopter including an attached slung load, which he describes in [CMS+01]. The model is based on the frequency domain analysis of real flight data and wind tunnel tests. Finally, the model has been validated in flight experiments, and good correspondence between simulation and reality has been demonstrated. Following a similar intention, R. A. Stuckey presents in his publication [Stu01] a model of a CH-53D helicopter. The model is based on Ciolani's research results presented in [CK92], which are reviewed in the multi-lift paragraph below. A detailed analysis of a UH-60 model is presented by D. Fusato [FG02]. The model is evaluated for different load masses and cable lengths. The influence on the system stability, trim and frequency response are discussed, based on the simulation results.

The complexity of slung load transportation systems and the unavoidable simplifications during modeling and system analysis elevate the importance of a flight validation for the developed control algorithms. Unfortunately this is a very difficult task. The author has only knowledge of two autonomous slung load systems using full size helicopters: A Kaman K-MAX helicopter has been modified for fully autonomous operation and has been used for slung load transportation in [TTC04], and a guidance system called "iSLD-IVC" (= iMAR Slung Load Damping based on inertial stabilized vision control) developed by iMAR GmbH and the German Aerospace Center DLR. The latter does not close the control loop directly. Instead, the output of the controller is presented to the pilot using an artificial horizon instrument.

Full Size Dual-Lift Configurations A lot of research work covering dual-lift configurations was presented in the past. The author believes that there are two reasons for this: First, the possibility to overcome the payload limitation of a single helicopter. Second, the dual-lift configuration is still simple enough to be manually piloted, although the demands on the pilots are very high, which simplifies experiments and allows the consideration of a semi-autonomous operation.

It is noteworthy, that already in 1973 a patent, for a semi-autonomous dual-lift system, was granted to Maciolek [Mac73a, Mac73b]. Maciolek proposes a typical master-slave system, where one helicopter acts as master and one helicopter acts as slave. The pilot of the master helicopter controls the translation of master and slave helicopter, but the orientation of both helicopters is stabilized autonomously. Additionally, the pilot of the slave helicopter has the possibility to override the external piloted and semi-autonomous control signals. However, the author has found no indication that this system has ever been built or tested in flight.

In [HCC87] H. C. Curtis examines the stability of a dual-lift configuration. A model with 16 DoF (= Degrees of Freedom), $2 \cdot 6$ DoF for two helicopters and 4 DoF for spreader-bar and load, is presented and used as basis for his discussion. Curtis work is a theoretic analysis and neither flight validation nor control approach are presented.

A similar analysis of a dual-lift configuration is presented by R. A. Hess [HT88], where only the vertical and lateral motion of the system are considered. The analysis is based on computer simulation. Hess describes the results for the uncontrolled system, the system with orientation loops closed and the system with all loops closed. He concludes

amongst others, that a high bandwidth orientation control is essential for the stability of the system.

In [CK90] L. S. Ciolani presents a model of a dual-lift configuration. He considers non bowing cables, but a possible elastic suspension of the cables. The proposed model considers only rigid body dynamics, but beside a "typical" four-body configuration[8] (two helicopters, one spreader bar, one load) two three-body configurations[9] (two helicopter, one large load functioning as a spreader bar and two helicopters and one small load) are discussed.

A controller based on non-linear feedback linearisation is presented by P. K. A. Menon in [MPS91a]. Similar to Hess lateral and vertical motion is considered. Helicopters and load are simplified to be mass points in the utilized model, the cables are considered to be rigid and massless and a spreader-bar is not included. Menon compares the traditional, role based master-slave control to a cooperative control scheme. He concludes that a cooperative control exhibits better disturbance rejection.

A series of publications has been written by Mittal [MPS91b, MPS92, MP93] regarding the modeling and control of dual-lift slung load systems. He presents a non-linear model of a traditional four-body dual-lift configuration including a spreader-bar. A controller based on feed-back linearisation is applied to the model and the functioning of the controller is validated in simulation.

A controller based on a H_∞ design is presented by Reynolds in [RR92], where he considers a dual-lift configuration with spreader bar. The proposed controller utilizes a typical master-slave concept and is validated in simulation. Reynolds applies the controller to configurations with equal and non equal cable length and concludes that the performance is similar for both cases. He considers an non equal rope length to be beneficial, since a better separation of the main-rotor discs is achieved.

Finally the work of C. Lim [LJR99] should be mentioned, who describes a modeling, simulation and control environment for dual-lift configurations. The environment includes a model, covering the longitudinal and vertical motion of helicopters and load, and a H_∞ controller.

Full Size Multi-Lift Configurations Compared to the single- and dual-lift cases, the literature about full-size multi-lift configurations is very sparse. To the author's knowledge there has never been an attempt to pilot a full size multi-lift configuration manually or autonomously. This absence of successfully manual piloted flights, in contrast to the single- and dual-lift configurations, where such flights have been conducted, might be the reason why this configuration has been neglected by the research community. However, Ciolani publishes in [CK92] several models of single-, dual- and multi-lift configurations. The publication extends his previous work [CK90], which treats only the dual-lift configuration. Ciolani describes several models, but presents no control approaches for the described configurations. The author has found no reference covering the autonomous control of multi-lift configurations, based on full-size helicopters.

[8] Configurations 6, described in [CK90] page 6.
[9] Configurations 5 and 7, described in [CK90] page 6.

Load Transportation using Small Size UAVs Only a few publications cover the modeling and control of single-, dual- and multi-lift configurations, based on small-size UAVs. Most of the available documents combine the treatment of single-, dual- and multi-lift configurations. The further review is therefore sorted by author and/or research group.

M. Bissgard published several documents about the modeling and control of slung load systems. In [BBCH06] he describes a generic modeling approach for slung load systems. Helicopter(s) and load are modeled as rigid bodies, and a method developed by Udwadia and Kalaba is used to derive the equations of the system dynamics. This method allows the utilization of motion constrains, which are formulated in terms of constrained accelerations, see [UK96a] for details. The final model is composed of the unconstrained motion of helicopters and load and the motion constraints imposed by the ropes. The proposed model is flexible enough to cover single-, dual- and multi-lift configurations. Three of his publications [BlCHB07, BBlCH07, BlCHJB07] cover the state estimation for a single-lift slung load system. The system state is estimated from IMU and GPS measurement and vision based tracking of the load. The presented estimation techniques are verified in flight experiments using a Yamaha GT Max helicopter. In his PhD thesis [Bis07] Bissgard summarizes his previous work and presents two control approaches: First, a classical state-feedback design, based on a linearized single-lift model. Second, a combination of a delayed feedback controller and input shaping, which is usually applied for the control of overhead cranes, see [SSK97, SSD07]. The single-lift configuration controllers are validated in flight experiments, using a Yamaha GT Max and a Bergen Industrial Twin helicopter. The dual- and multi-lift configurations are treated only in theory and simulation.

J. Fink [FMKK09] and N. Michael [MKFK09a, MKFK09b, MFK10] published several documents about the cooperative multi-robot manipulation and transportation, which includes the multi-lift slung load transportation. They consider the problem to be equivalent to the manipulation of a platform using several cables. Their publications mainly focus on the motion planing aspect and cover the forward and inverse kinematics of the multi-robot platform, to estimate stable poses and generate suitable trajectories. The modeling and control of the utilized AscTec Hummingbird quadrotors is only mentioned shortly. Nevertheless, they present results of successful flight experiments: Three coupled quadrotor transport an external slung load, which exceeds the transportation capacity of a single quadrotor.

2 UAV System

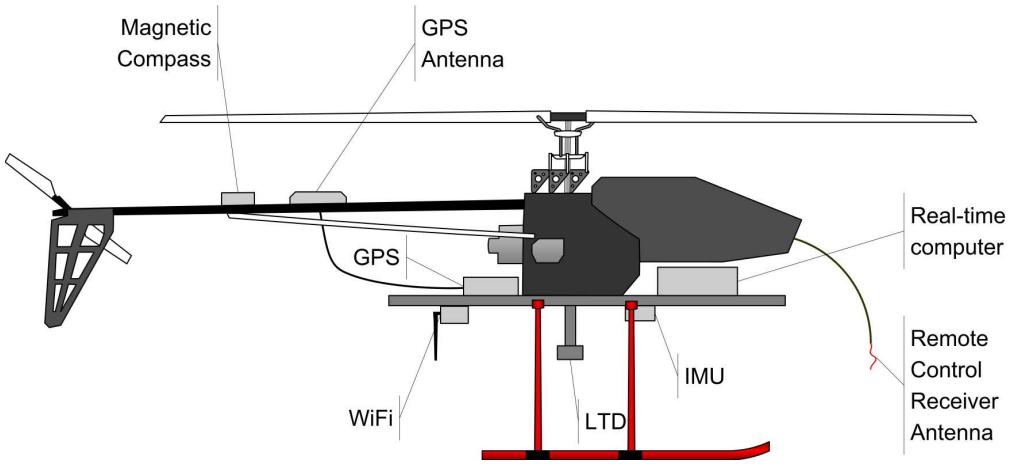

Figure 2.1: UAV used for flight experiments

The validation of the developed models and control approaches, using real-flight experiments, constitutes a very important part of this thesis. For that reason, a basis for the conduction of regular flight experiments is needed. The requirements for the system are the following:

- Reliable conduction of experiments with one or multiple helicopters
- Minimal risk for personal
- Minimal risk for equipment

The creation of the system required the development of special hard- and software, which is described in this chapter. In Sec. 2.1 the utilized UAVs are presented. Additional to the hardware required solely for autonomous operation, each UAV has one LTD (= Load Transportation Device), which is needed for single-, dual- and multi-lift operations. The LTD assembly is described in the same section as the UAVs.

In Sec. 2.2 the ground station is presented, which acts as real-time interface between the GUI (= Graphical User Interface) and the UAVs. In addition, the ground station manages the bidirectional distribution of real-time data and provides additional sensor information to the UAVs. The utilized software framework is discussed in Sec. 2.3. The framework provides a multi-process environment, which allows an efficient integration of Matlab/Simulink generated code and hand coded modules.

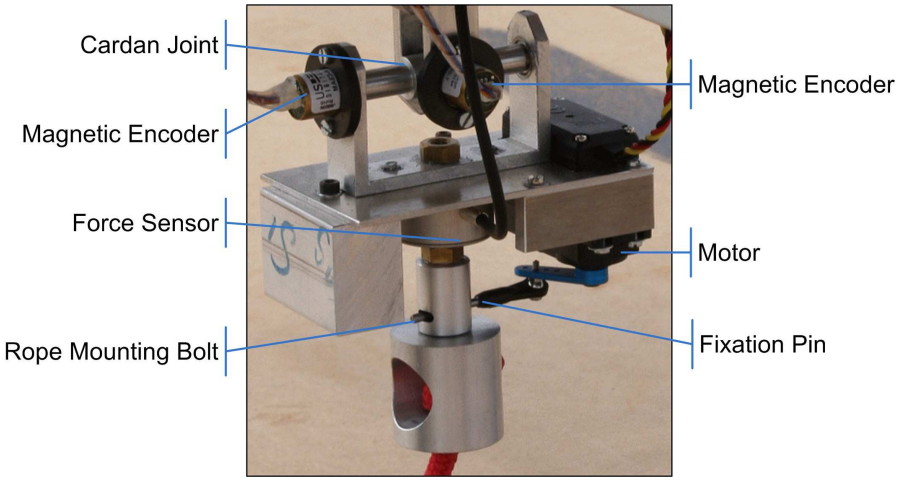

Figure 2.2: Load Transportation Device

2.1 Autonomous Helicopter

In Fig. 2.1 an UAV, as it has been used for flight experiments, is shown. The UAV is based on a CB5000 model helicopter, which is equipped with a 1.8 KW two stroke engine. The main-rotor has a diameter of 1.8 m and the rotation speed is about 1300 RPM. The weight of the UAV including all electronics is 13 kg and the UAV is capable of carrying 3 kg of additional payload.

The minimal system required for autonomous operation consists of a real-time computer, a GPS to estimate position and velocity of the fuselage, an IMU to determine the orientation and the angular velocity of the fuselage and a WiFi communication link for the data exchange with a ground station. A magnetic field sensor is mounted on the tail boom, in addition to the magnetic field sensor already integrated into the IMU. This is necessary, since the magneto ignition of the two-stroke engine creates too much disturbance near the fuselage and on the tail boom the vibrations are too strong for the IMU's gyroscopes and accelerometers.

Two aluminum strut profiles are mounted to the fuselage, building the main track, to which most components are attached to. Due to this architecture the components can be adjusted to move the CoM (= Center of Mass) of the UAV into the main-rotor axis. This significantly simplifies the modeling and control of the UAV, see Ch. 3 for more details. The manual placement of the CoM seems to be a big simplification, however for the manual piloting of small size helicopters it is a common practice to move CoM to a desirable position. For helicopters this is normally the main-rotor axis. Even for full size helicopters the correct position of the CoM has to be checked and adjusted before take off, see e.g. [Wag06].

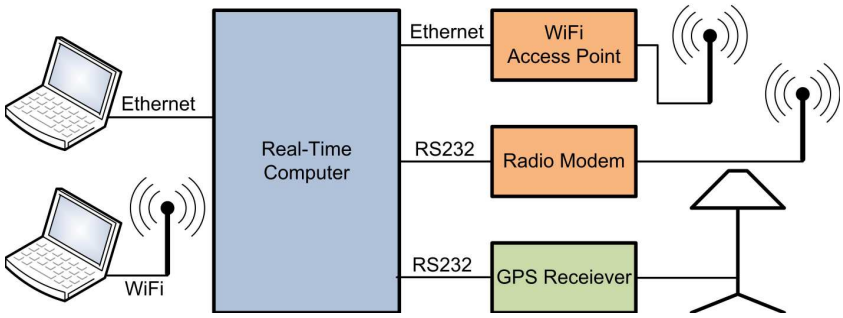

Figure 2.3: Ground Station

In Fig. 2.2 the LTD (= Load Transportation Device) used for the slung load transportation tasks is depicted. As shown in Fig. 2.1 the LTD is mounted directly underneath the main-rotor axis to reduce the influence of the coupled system on the CoM of the helicopter.

The LTD is composed of a two axis Cardan joint, with a magnetic angle sensor attached to each axis. A force sensor is mounted to the lower axis and a socket on the force sensor is used to attach the rope using a bolt. An actuated pin fixates the bolt, which allows to release the load after the deployment or to perform an emergency release during the flight. The measured angles as well as the measured force are utilized by the slung load controllers described in Ch. 6.

2.2 Ground Station

In Fig. 2.3 the schematic of the ground station is shown. The main component is the real-time computer, which utilizes the same multi-process framework as the real-time computers of the helicopters. GUI (= Graphical User Interface) clients, like the two laptops drawn on the left, connect to the ground station using either Ethernet or WiFi connections. The ground station allows an arbitrary[1] number of clients to connect simultaneously. Three primary services are provided by the ground station to the GUI clients:

Commanding The GUI clients are able to command the different UAVs, supplying valid desired positions or velocities.

Real-Time Data Distribution The ground station distributes the complete state of all connected UAVs to every GUI-client. All data is time-stamped and the correlation between the states of the different UAVs is preserved.

Logging The ground station provides a local logging mechanism and stores the log-data for offline-processing.

[1] Within technical limits.

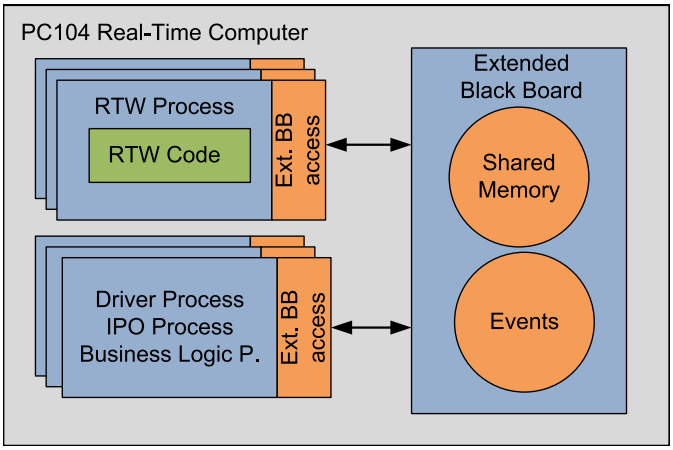

Figure 2.4: Real-Time Framework

Beside the services for the GUI clients, the ground station maintains the real-time connection links to the UAVs. Currently two connection types are supported: A high bandwidth, short range connection based on WiFi and a low bandwidth, long range connection using 2.4 GHz radio modems. The ground station distributes critical real-time data between the UAVs, like the state information of the complete system. In addition, the ground station provides external sensor information, like differential GPS correction data, which is acquired from a GPS receiver.

The utilization of a ground station, based on an additional real-time computer, seems redundant, since most functions could be realized within a GUI client as well. However, the proposed ground station setup has three mayor advantages:

- Non real-time GUI clients may connect or disconnect any time, without any impact on the functioning of the real-time system composed of ground station and UAVs. Even a crash of the GUI client or of the whole GUI computer is tolerated.
- The ground station real-time computer allows the real-time processing of UAV or external sensor data.
- The ground station provides the unified access to the UAVs, independent from the actual link between ground station and UAV.

The presented ground station has proven to be very useful during many experiments. The reliability gained from the additional real-time computer simplified the conduction of the experiments and improved the safety of the system.

2.3 Software

The autonomous system utilizes a multi process framework, based on an extended black board architecture, which features synchronized shared memory access and an event notification system. Additionally, it includes the possibility to embed C-code generated from

Matlab/Simulink models. Only a brief description of this framework is presented here, since this work mainly focuses on the modeling and control of slung load transportation systems.

In Fig. 2.4 the architecture of the real-time framework is depicted. The main component is the extended black board, which provides synchronized shared memory access, on change notification events and user defined events. An interface library provides unified access to the extended black board for the different processes. The library is drawn on the right side of the processes, using orange as background color.

There are two different sets of processes depicted in the figure. Processes based on code generated by Matlab/Simulink RTW (= Real-Time-Workshop) and hand coded processes. The framework provides a generic process stub, in which the RTW generated code is inserted. Only minimal changes are required to adapt the process stub to the code generated from a particular Matlab/Simulink model: The model input needs to be read from the shared memory and the model output needs to be written into the shared memory.

Processes based on Simulink models have been utilized for the implementation of controllers, observers and filters, since these tasks are easily implemented using Simulink models. The hand coded processes are utilized for tasks, which are difficult to implement using Simulink models. Examples for hand coded processes are: Driver processes, which need to implement a particular protocol, IPO (= Input-Processing-Output) processes and processes containing complex business logic. The combination of hand coded processes and processes based on Simulink models simplified the development of the load transportation system and decreased the required development time.

Finally, an important property of the RTW processes need to be mentioned: Matlab/Simulink allows to connect to a RTW process using the so called “external mode”. The external mode allows an online visualization of the model data and the modification of the model parameters. This method has been used, for example, to evaluate different parameter sets for the developed controllers during flight. This approach decreased the required development cycles drastically and simplified the creation of the load transportation system described in this thesis. The software system concept is described in more detail in [BKH06, Ber05].

3 Modeling of Small Size Helicopters

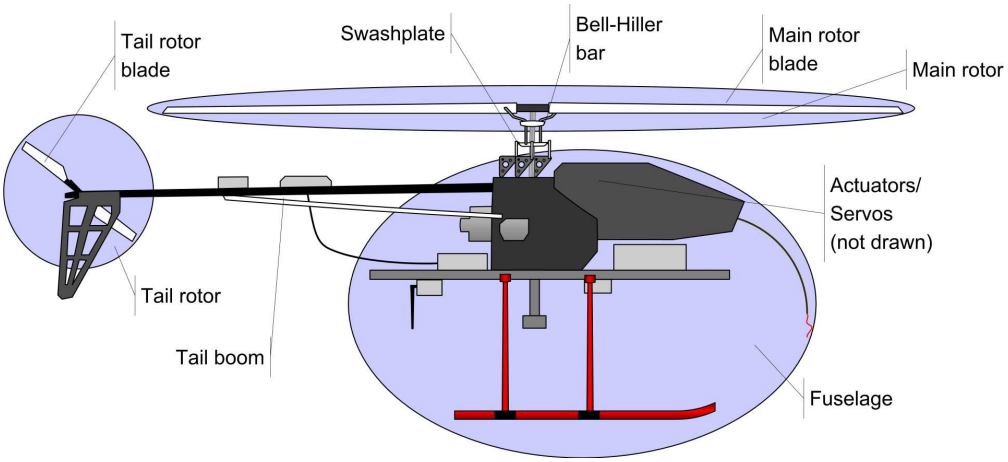

Figure 3.1: Mechanical components of a small size helicopter

This chapter describes the modeling of small size helicopters with a take off weight below 25 kg. The resulting non-linear model will be used in Ch. 5 as a basis for the development of the non-linear single-, dual- and multi-lift configuration models. A short summary of components, as shown in Fig. 3.1, relevant for the modeling of small size helicopters, as well as their most important properties, shall be given here. The main components of a small size helicopter are main-rotor, tail-rotor, fuselage, stabilizer-bar (Bell-Hiller-Bar), actuators (servos), sensors and the main-engine.

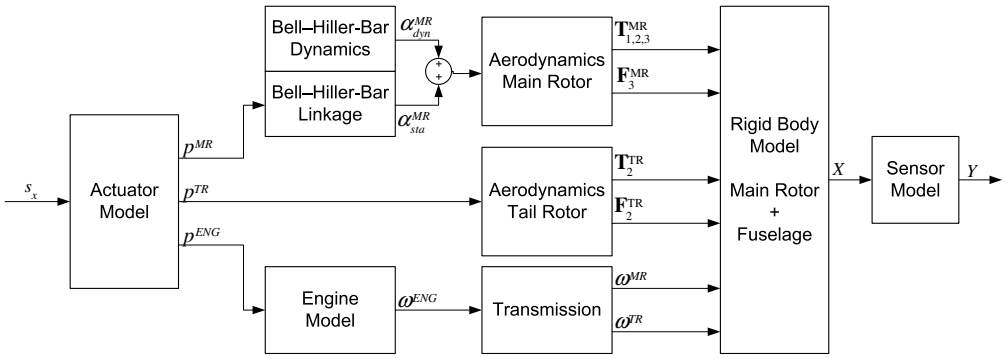

Figure 3.2: Structure of the small size helicopter model

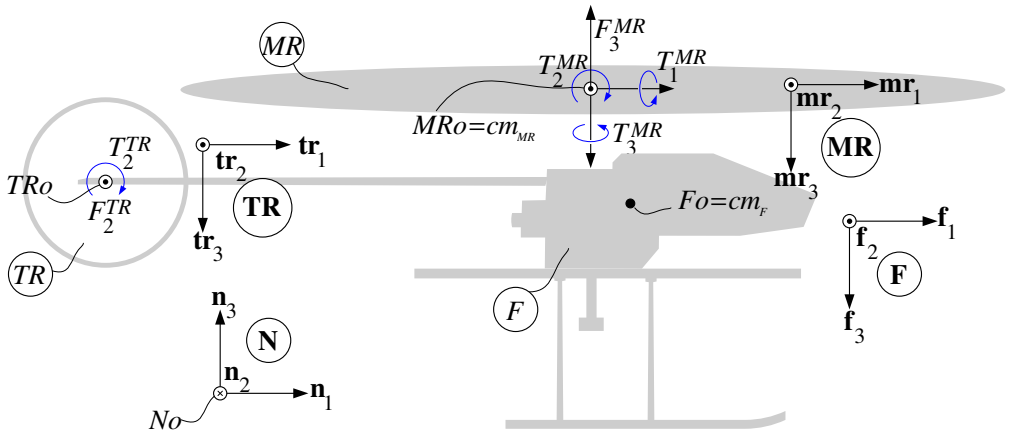

Figure 3.3: Rigid body model, definition of frames, forces and torques.

The general structure of the non-linear, small size helicopter model is depicted in Fig. 3.2. The model consists of aerodynamic models for main- and tail-rotor, rigid body models for main-rotor and fuselage and models for sensors and actuators. The aerodynamic influence of the helicopter fuselage consists mainly of air drag and swirl of the downwash. For a small size helicopter this influence is very small and therefore the aerodynamic behavior of the fuselage is neglected in the model. Detailed descriptions of the sub-models are presented in the following sections. The structure of each section is divided into three parts: A general description of the sub-system, the estimation of important properties and the modeling of these properties.

3.1 Rigid Body Model

The dynamic behavior of a small size helicopter is mainly governed by its rigid body dynamics. In Sec. 3.1.1 a contribution estimation is presented for main-rotor, tail-rotor and fuselage of the helicopter. Based on the results main-rotor and fuselage are modeled as rigid bodies and the tail-rotor is modeled as a massless force generator. The kinematic and dynamic equations of the model are presented in Sec. 3.1.2 and Sec. 3.1.3 respectively.

3.1.1 Estimation of Dynamic Contributions

In this section the dynamic contributions of fuselage, main- and tail-rotor are determined and compared. The models of the different bodies are chosen based on this estimation. Finally, the resulting mechanical model is described. In Fig. 3.3 the different rigid bodies of mechanical model are shown. The fuselage F, the main-rotor MR and the tail-rotor TR. The inertial frame is denoted **N** and the body frame of the helicopter is denoted **F**. The frames of main- and tail-rotor are indicated by **MR** and **TR** respectively.

Using the Euler equation Eq. 3.1 the resultant torques for the different rigid bodies are calculated.

$$\frac{d_N \mathbf{L}}{dt} = \mathbf{I}\alpha + \omega \times (\mathbf{I}\omega) = \mathbf{T} \tag{3.1}$$

Where $\mathbf{L}$ denotes the angular momentum and $\mathbf{T}$ denotes the resultant torque. To calculate the resultant torque, the moment of inertia $\mathbf{I}$ of the body, as well as approximations of the expected angular velocity ω and angular acceleration α need to be known. An expected average angular velocity of $|\omega| = \sqrt{3}\pi\,\mathrm{rad/s}$ and angular acceleration $|\alpha| = \sqrt{3}\pi\,\mathrm{rad/s^2}$ are assumed for the fuselage F. The angular velocity/acceleration of the fuselage, with respect to the inertial frame $\mathbf{N}$, are given by $\omega_{\mathbf{F-N}} = (\pm\pi,\, \pm\pi,\, \pm\pi)^T$, $\alpha_{\mathbf{F-N}} = (\pm\pi,\, \pm\pi,\, \pm\pi)^T$. The moment of inertia of the fuselage F, with respect to the fuselage's CoM cm_F, is given by Eq. 3.2. The parameters are mass of the fuselage $m_F = 12.5\,\mathrm{kg}$ and dimensions of the cuboid with $l_1 = 0.64\,\mathrm{m}$, $l_2 = 0.15\,\mathrm{m}$ and $l_3 = 0.25\,\mathrm{m}$.

$$\begin{aligned} \mathbf{I}^F &= I_{11}^F\,\mathbf{f}_1\mathbf{f}_1 + I_{22}^F\,\mathbf{f}_2\mathbf{f}_2 + I_{33}^F\,\mathbf{f}_3\mathbf{f}_3 \\ &= \frac{m_F\left(l_2^2 + l_3^2\right)}{12}\,\mathbf{f}_1\mathbf{f}_1 + \frac{m_F\left(l_1^2 + l_3^2\right)}{12}\,\mathbf{f}_2\mathbf{f}_2 + \frac{m_F\left(l_1^2 + l_2^2\right)}{12}\,\mathbf{f}_3\mathbf{f}_3 \end{aligned} \tag{3.2}$$

For main- and tail-rotor the moment of inertia is calculated with respect to $MRo = cm_{MR}$ and $TRo = cm_{TR}$. The used density function is given by $\rho(r) = \frac{m}{V} = m/(2\pi\,R\,h\,r)$, where R is the radius, h is the height and m is total mass of the rotor disc. The density function uniformly distributes the mass along the radius of the rotor disc. Therefore, every disc volume slice $V_s(r) = h\,\left(\pi(r+w)^2 - \pi(r-w)^2\right)$, of equal width w, has the same mass, independent from the selected radius r. Using the density function the moment of inertia for main- and tail-rotor are obtained, see Eq. 3.3 and Eq. 3.4. The parameters of the equations are mass and radius of the main-rotor ($m_{MR} = 0.5\,\mathrm{kg}$, $R_{MR} = 0.91\,\mathrm{m}$) and mass and radius of the tail-rotor ($m_{TR} = 0.1\,\mathrm{kg}$, $R_{TR} = 0.17\,\mathrm{m}$).

$$\begin{aligned} \mathbf{I}^{MR} &= I_{11}^{MR}\,\mathbf{mr}_1\mathbf{mr}_1 + I_{22}^{MR}\,\mathbf{mr}_2\mathbf{mr}_2 + I_{33}^{MR}\,\mathbf{mr}_3\mathbf{mr}_3 \\ &= \frac{m_{MR}\,R_{MR}^2}{6}\,\mathbf{mr}_1\mathbf{mr}_1 + \frac{m_{MR}\,R_{MR}^2}{6}\,\mathbf{mr}_2\mathbf{mr}_2 + \frac{m_{MR}\,R_{MR}^2}{3}\,\mathbf{mr}_3\mathbf{mr}_3 \end{aligned} \tag{3.3}$$

$$\begin{aligned} \mathbf{I}^{TR} &= I_{11}^{TR}\,\mathbf{tr}_1\mathbf{tr}_1 + I_{22}^{TR}\,\mathbf{tr}_2\mathbf{tr}_2 + I_{33}^{TR}\,\mathbf{tr}_3\mathbf{tr}_3 \\ &= \frac{m_{TR}\,R_{TR}^2}{6}\,\mathbf{tr}_1\mathbf{tr}_1 + \frac{m_{TR}\,R_{TR}^2}{3}\,\mathbf{tr}_2\mathbf{tr}_2 + \frac{m_{TR}\,R_{TR}^2}{6}\,\mathbf{tr}_3\mathbf{tr}_3 \end{aligned} \tag{3.4}$$

The angular speeds of main-rotor $\omega_{\mathbf{MR-N}}$ and tail-rotor $\omega_{\mathbf{TR-N}}$ are given by the angular velocity of the fuselage $\omega_{\mathbf{F-N}}$ and the angular speeds of the main- and tail-rotor discs relative to the fuselage: $\omega_{\mathbf{MR-F}} = (0,\, 0,\, 1300\,2\pi/60)^T$ and $\omega_{\mathbf{TR-F}} = (0,\, 0,\, 6000\,2\pi/60)^T$. The relationship is expressed by Eq. 3.5 and Eq. 3.6.

$$\omega_{\mathbf{MR-N}} = \omega_{\mathbf{MR-F}} + \omega_{\mathbf{F-N}} \approxeq (\pm\pi,\, \pm\pi,\, \pm\pi + 136)^T \tag{3.5}$$

$$\omega_{\mathbf{TR-N}} = \omega_{\mathbf{TR-F}} + \omega_{\mathbf{F-N}} \approxeq (\pm\pi,\, \pm\pi,\, \pm\pi + 628)^T \tag{3.6}$$

The angular accelerations $\alpha_{\mathbf{MR-N}}$ and $\alpha_{\mathbf{TR-N}}$ are calculated similar to the angular speeds. For normal flight conditions the angular speeds $\omega_{\mathbf{MR-F}}$ and $\omega_{\mathbf{TR-F}}$ are considered to be constant, with $\alpha_{\mathbf{MR-F}} = \alpha_{\mathbf{TR-F}} = (0,\, 0,\, 0)^T$. Based on the considerations

Eq. 3.7 and Eq. 3.8 are obtained.

$$\alpha_{\mathbf{MR-N}} = \alpha_{\mathbf{MR-F}} + \alpha_{\mathbf{F-N}} + \omega_{\mathbf{F-N}} \times \omega_{\mathbf{MR-F}} \quad (3.7)$$

$$\alpha_{\mathbf{TR-N}} = \alpha_{\mathbf{TR-F}} + \alpha_{\mathbf{F-N}} + \omega_{\mathbf{F-N}} \times \omega_{\mathbf{TR-F}} \quad (3.8)$$

Since all parameters, required by Eq. 3.1, are known and the dynamic contributions of the different rigid bodies is estimated. To maximize the resulting absolute torque $|\mathbf{T}|$ the actual values of $\omega_{\mathbf{F-N}}$ and $\alpha_{\mathbf{F-N}}$ are separately chosen for every body. The following table presents the results of the estimation:

Body	$\omega_{\mathbf{F-N}}$ ($^{\text{rad}}/_{\text{s}}$)	$\alpha_{\mathbf{F-N}}$ ($^{\text{rad}}/_{\text{s}^2}$)	$\mathbf{T}$ (Nm)	$\lvert\mathbf{T}\rvert$ (Nm)
F	$(-\pi, -\pi, \pi)$	(π, π, π)	$(0.69, 5.11, 5.39)^T$	7.46
MR	$(-\pi, \pi, \pi)$	(π, π, π)	$(59.93, 59.93, 0.43)^T$	84.75
TR	$(\pi, \pi, -\pi)$	(π, π, π)	$(0.95, 0.002, 0.95)^T$	1.35

The contribution of the main-rotor is approximately 11 times bigger than the contribution of the fuselage and 63 times bigger than the contribution of the tail-rotor. The conclusion is drawn, that, at least for the used CB5000 helicopter, the dynamic behavior is dominated by the main-rotor. The strong main-rotor influence, is explainable through the combination of high angular velocity of the main-rotor and the heavy and long main-rotor blades.

In the work [KBLH06] a similar estimation has been made for a LOGO 14 small size electric helicopter, with a weight of 3.3 kg. For the LOGO 14 the influence of the main-rotor is about 47 times bigger than the influence of the fuselage and about 39 times bigger than the influence of the tail-rotor. The results presented here are in general similar to the presented results in the publication. However, the presented values differ for two reasons: First, in this work $\omega_{\mathbf{F-N}}$ and $\alpha_{\mathbf{F-N}}$ have been chosen to maximize the influence of the respective body. Second, $\alpha_{\mathbf{MR-N}}$ and $\alpha_{\mathbf{MT-N}}$ have not been manually selected, but are calculated using Eq. 3.7-3.8.

The LOGO 14 and CB5000 helicopters represent the lower and the middle range of the considered weight class below 25 kg. In order to cover the full range of the weight class an additional estimation, for a custom design helicopter is created. The helicopter has a take off weight of 24.5 kg and a 2.2 m diameter rotor disc spinning at 1400 RPM. For that "huge" small size helicopter the influence of the main-rotor is about 6.6 times bigger than the influence of the fuselage and about 56 times bigger than the influence of the tail-rotor. The following table summarizes the results discussed above:

Helicopter	Mass	$\lvert\mathbf{T_F}\rvert$	$\lvert\mathbf{T_{MR}}\rvert$	$\lvert\mathbf{T_{TR}}\rvert$	Ratio $^1/_{\lvert\mathbf{T_{MR}}\rvert}$
LOGO 14	3.3 kg	0.39 Nm	18.24 Nm	0.47 Nm	($^1/_{47}$, 1, $^1/_{39}$)
CB5000	13.0 kg	7.46 Nm	84.75 Nm	1.35 Nm	($^1/_{11}$, 1, $^1/_{63}$)
Custom	24.5 kg	32.51 Nm	213.14 Nm	3.77 Nm	($^1/_{6.6}$, 1, $^1/_{56}$)

The contribution of the fuselage to the overall dynamics of the helicopter increases, with increasing size of the helicopter. This is caused by a major increase of the fuselage's

weight and volume compared to the weight increase of the main-rotor[1] blades. However, for a small size helicopter of the considered weight class the dynamic behavior is still dominated by the main-rotor.

3.1.2 Kinematics

Based on the results of the estimation above, the mechanical model of the helicopter is composed of two rigid bodies, the fuselage F and the main-rotor MR. The CoM cm of the helicopter is described relative to the inertial frame $\mathbf{N}$ by the following vector of generalized coordinates (x, y, z):

$$\mathbf{p}_{cm} = x\,\mathbf{n}_1 + y\,\mathbf{n}_2 + z\,\mathbf{n}_3 \tag{3.9}$$

The generalized speeds (u, v, w) are used to describe the velocity of the CoM cm of the helicopter:

$$\mathbf{v}_{cm} = \frac{d^{\mathbf{N}}\mathbf{p}}{dt} = \dot{x}\,\mathbf{n}_1 + \dot{y}\,\mathbf{n}_2 + \dot{z}\,\mathbf{n}_3 = u\,\mathbf{n}_1 + v\,\mathbf{n}_2 + w\,\mathbf{n}_3 \tag{3.10}$$

Using Eq. 3.9 and Eq. 3.10 the kinematic equations of the translation are derived:

$$\begin{aligned} \dot{x} &= u \\ \dot{y} &= v \\ \dot{z} &= w \end{aligned} \tag{3.11}$$

The orientation of the helicopter is described by the angles (ψ, θ, φ), which are the generalized coordinates of the orientation. They are equivalent to Euler-angles 3-2-1, which are defined as follows: The yaw angle ψ, describes the first rotation around the axis $\mathbf{n}_3 = \mathbf{f}_3$, the pitch angle θ describes the second rotation around the changed axis $\mathbf{f'}_2$ and φ describes the third rotation around the changed axis $\mathbf{f}''_1$.

The generalized speeds (p, q, r) describe the angular velocity of the fuselage relative to the inertial frame $\mathbf{N}$:

$$\omega_{\mathbf{F}-\mathbf{N}} = p\,\mathbf{f}_1 + q\,\mathbf{f}_2 + r\,\mathbf{f}_3 \tag{3.12}$$

Knowing that the angular velocity can be express as:

$$\omega_{\mathbf{F}-\mathbf{N}} = \left(\left(\frac{d^{\mathbf{N}}\mathbf{f}_2}{dt}\cdot\mathbf{f}_3\right)\mathbf{f}_1 + \left(\frac{d^{\mathbf{N}}\mathbf{f}_3}{dt}\cdot\mathbf{f}_1\right)\mathbf{f}_2 + \left(\frac{d^{\mathbf{N}}\mathbf{f}_1}{dt}\cdot\mathbf{f}_2\right)\mathbf{f}_3\right) \tag{3.13}$$

From Eq. 3.12 and Eq. 3.13 the kinematic equations of the rotation are derived:

$$\dot{\varphi} = p + \tan(\theta)(q\sin(\varphi) + r\cos(\varphi)) \tag{3.14}$$

$$\dot{\theta} = q\cos(\varphi) - r\sin(\varphi) \tag{3.15}$$

$$\dot{\psi} = (q\sin(\varphi) + r\cos(\varphi))/\cos(\theta) \tag{3.16}$$

To summarize the definitions above: The kinematic equations of the helicopter are given by Eqs. 3.11 and Eqs. 3.14-3.16. The state vector of the helicopter is defined as:

$$(x,\, y,\, z,\, \varphi,\, \theta,\, \psi,\, u,\, v,\, w,\, p,\, q,\, r)^T \tag{3.17}$$

[1] This is true for the tail rotor blades as well, but even near 25 kg the influence of the tail rotor is small.

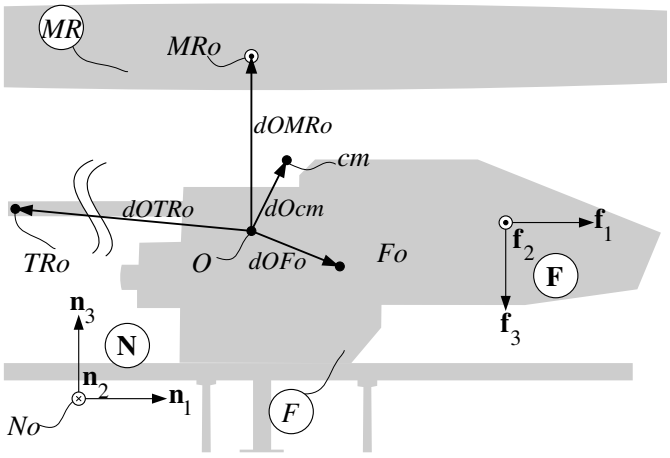

Figure 3.4: Body origins and distance vectors

3.1.3 Dynamics

The rigid bodies of the helicopter are modeled as follows: The fuselage becomes a rectangular cuboid, with a uniform mass distribution, and the main-rotor becomes a thin disc, where its mass distribution resembles a mass distribution equivalent to two rotating blades, compare Eq. 3.2 and Eq. 3.3. For simplicity the overall helicopter mass $m = m_F + m_{MR}$ is introduced, and only the masses of fuselage and main-rotor are considered. In Fig. 3.3 forces and torques, generated by main- and tail-rotor, are depicted: The main-rotor generates the force $\mathbf{F}^{MR} = F_3^{MR}\,\mathbf{f}_3$ acting on the point *MRo*, which is approximately perpendicular to the rotor disc, and the torques $\mathbf{T}^{MR} = T_1^{MR}\,\mathbf{f}_1 + T_2^{MR}\,\mathbf{f}_2 + T_3^{MR}\,\mathbf{f}_3$ around the axis $\mathbf{f}_{1,2,3}$. The tail-rotor *TR* is modeled to be a massless force and torque generator: The force $\mathbf{F}^{TR} = F_2^{TR}\,\mathbf{f}_2$ is acting on the massless point *TRo* and the torque $\mathbf{T}^{TR} = T_2^{TR}\,\mathbf{f}_2$ is acting around the axis $\mathbf{f}_2$.

In Fig. 3.4 the reference point O is drawn. The distance vectors **dOFo**, **dOMRo** and **dOTRo** connect the reference point O with the CoM of fuselage Fo, main-rotor *MRo* and tail-rotor *TRo* respectively. The distance vector **dOcm** connects the reference point O to the CoM of the whole helicopter. The dynamic equations were derived using the Kane-Method and the software tool Autolev. To improve simplicity the following convention is used for the remainder of this work: $s_x = \sin(x)$, $c_x = \cos(x)$, $t_x = \tan(x)$. The translation dynamics of the helicopter are described by the following equations:

$$\dot{u} = \left(F_3^{MR}(c_\varphi s_\theta c_\psi + s_\varphi s_\psi) + F_2^{TR}(s_\varphi s_\theta c_\psi - c_\varphi s_\psi)\right)/m \tag{3.18}$$

$$\dot{v} = \left(F_3^{MR}(c_\varphi s_\theta s_\psi - s_\varphi c_\psi) + F_2^{TR}(s_\varphi s_\theta s_\psi + c_\varphi c_\psi)\right)/m \tag{3.19}$$

$$\dot{w} = -G + \left(F_3^{MR} c_\varphi c_\theta + F_2^{TR} s_\varphi c_\theta\right)/m \tag{3.20}$$

Eqs. 3.18-3.20 create a direct relation between the acceleration of the helicopter's CoM and the forces F_3^{MR} and F_2^{TR} generated by the main- and tail-rotor. The accelerations $(\dot{u}, \dot{v}, \dot{w})$ are determined by the force of the main-rotor F_3^{MR}, tail-rotor F_2^{TR} and the

current orientation of the helicopter. Contrary to the equations of the translation dynamics, the equations of the rotation dynamics are quite complex. The non-simplified dynamic equations for a single helicopter are presented in the additional equations document, which is accompanying this thesis on CD, see [Ber13, page 5ff.]. To analyze these equations the following three simplifications are made:

1. **dOMRo** = $dOMRo_3\,\mathbf{f}_3$: The reference point O is located in the main-rotor axis. Until now the position of reference point O has been chosen freely, therefore this simplification is made without losing generality.

2. **dOTRo** = $dOTRo_1\,\mathbf{f}_1 + dOTRo_2\,\mathbf{f}_2$: The reference point O and the CoM of the tail rotor $\mathcal{T}Ro$ are located at the same height. This and the first simplification unambiguously determine the position of the reference point O. This simplification can be made without losing generality as well.

3. **dOFo** = $dOFo_3\,\mathbf{f}_3$: Together with the first simplification this implies that Fo is located within the main-rotor axis. This is the only simplification that imposes an actual constraint and reduces the class of helicopters representable by this model. However, for almost[2] all small size helicopters Fo can be placed in the main-rotor axis, moving components like batteries or payload. In fact, pilots of small size helicopters regularly check for the correct placement of the fuselage's CoM and adjust the position of Fo with additional weights or the relocation of components. Pilots of full-size helicopters are obligated to check for a correct placement of the CoM, see for example [Ser00, Bai08].

After these simplifications the rotation dynamics of the helicopter are described by Eqs. 3.21-3.23.

$$\dot{p} = \left(T_1^{MR}\,m - F_2^{TR}\,K_{TR} + q\,K_{p1} + q\,r\,K_{p2}\right)/K_{p3} \tag{3.21}$$

$$\dot{q} = \left(-(T_2^{MR} + T_2^{TR})\,m + p\,K_{q1} + p\,r\,K_{q2}\right)/K_{q3} \tag{3.22}$$

$$\dot{r} = \left(T_3^{MR} + F_2^{TR} dOTRo_1 + p\,q\,(I_{11}^F - I_{22}^F)\right)/(I_{33}^F + I_{33}^{MR}) \tag{3.23}$$

The equations include the constant coefficients K_m, K_{TR}, K_{px} and K_{qx} $(x = 1, 2, 3)$, which are defined by Eqs. 3.24. The coefficients depend only on constant parameters of the helicopter. It is important to recall, that ω_{MR} is considered to be constant.

$$\begin{aligned}
K_m &= (dOFo_3 - dOMRo_3)^2\; m_F\, m_{MR} \\
K_{TR} &= dOMRo_3\, m_{MR} + dOFo_3\, m_F \\
K_{p1} &= -I_{33}^{MR}\, m\, \omega_{MR} \\
K_{p2} &= K_m + (I_{22}^F - I_{33}^F - I_{11}^{MR})\, m \\
K_{p3} &= K_m + (I_{11}^F + I_{11}^{MR})\, m \\
K_{q1} &= I_{33}^{MR}\, m\, \omega_{MR} \\
K_{q2} &= -K_m - (I_{11}^F - I_{33}^F - I_{11}^{MR})\, m \\
K_{q3} &= K_m + (I_{22}^F + I_{11}^{MR})\, m
\end{aligned} \tag{3.24}$$

[2] The author is not aware of a helicopter with Fo outside the main-rotor axis.

Eq. 3.23 relates the change of the angular speed $\dot{r}$ and the force generated by the tail-rotor F_2^{TR}. The force F_2^{TR} and the torques $T_{1,2}^{MR}$ are considered control inputs. The torques T_3^{MR} and T_2^{TR} are mainly created by the airdrag of main- and tail-rotor and are therefore considered as disturbances. The equation is coupled to the angular rates p and q through the coupling term $p\,q\,(I_{11}^F - I_{22}^F)$. The remaining terms of the equation are constant.

For normal flight conditions, e.g. forward flight or hovering, the rates (p, q) are almost zero and the term $p\,q\,(I_{11}^F - I_{22}^F)$ becomes negligible small. Therefore, for the further analysis of Eq. 3.23 the coupling term $p\,q\,(I_{11}^F - I_{22}^F)$ is assumed to be a disturbance. The equation is rewritten to become $\dot{r} = K\,F_2^{TR} + Z\left(T_3^{MR},\, p,\, q\right)$, with K being a constant term and Z being a disturbance function. Based on these considerations the angular speed r behaves like a simple integrator of the force F_2^{TR}. This knowledge is used in Sec. 4 for the design of a decoupled tail-controller.

There is a high structural similarity between Eq. 3.21 and Eq. 3.22. Both equations are cross coupled: Eq. 3.21 is coupled to the angular speed q through the terms $q\,K_{p1}$, $q\,r\,K_{p2}$ and Eq. 3.22 is coupled to the angular speed p through the terms $p\,K_{q1}$, $p\,r\,K_{q2}$. Additionally, both equations are coupled to the angular speed r, through the term $q\,r\,K_{p2}$ or $p\,r\,K_{q2}$.

During the analysis of the rotation dynamics the disturbances F_2^{TR} and T_2^{TR} are considered constant. Assuming the angular speed r to be constant as well, Eq. 3.21 and Eq. 3.22 become linear with respect to $T_{1,2}^{MR}$. Two facts validate the assumption (r = const.): First, the angular speed r is normally controlled independently from the rates p and q. Usually a separate controller is utilized, which keeps r close to the desired angular speed r_{des}. This controller has at least twice the bandwidth of the controller for p and q. And second, for most maneuvers the desired angular speed r_{des} is zero, e.g. forward, backward or sideward flight, or constant, e.g. during a circle flight.

A closed form solution of Eq. 3.21 and Eq. 3.22 can be calculated under these assumptions and for constant control torques $T_{1,2}^{MR}$:

$$p\,(t) = \frac{m\,\left(T_2^{MR} + T_2^{TR}\right)}{K_{q1} + K_{q2}\,r} + C_1 \cosh(\alpha t) + C_2 \beta \sinh(\alpha t) \tag{3.25}$$

$$q\,(t) = -\frac{-F_2^{TR}\,K_{TR} + m\,T_1^{MR}}{K_{p1} + K_{p2}\,r} + C_2 \cosh(\alpha t) + C_1/\beta \sinh(\alpha t) \tag{3.26}$$

Where C_1 and C_2 are integration constants and α, β are given by the following equations:

$$\alpha = \sqrt{\frac{K_{p1} + K_{p2} r}{K_{p3}}}\sqrt{\frac{K_{q1} + K_{q2} r}{K_{q3}}} \tag{3.27}$$

$$\beta = \sqrt{\frac{K_{p1} + K_{p2} r}{K_{p3}}}\Big/\sqrt{\frac{K_{q1} + K_{q2} r}{K_{q3}}} \tag{3.28}$$

A gyroscopic phase shift of the main-rotor about 90° is identifiable in Eq. 3.25 and Eq. 3.26. The torque T_2^{MR} changes $p\,(t)$ and therefore acts around $\mathbf{f}_1$, and the torque T_1^{MR} changes $q\,(t)$ and therefore acts around $\mathbf{f}_2$. This is an important property of the main-rotor, which is reflected even by these simplified equations.

Eqs. 3.25-3.26 are simplified even further: The assumption $r = \text{const.}$ is extended to $r = 0$, which is still valid for many flight maneuvers, and the shape of the fuselage changes from a rectangular cuboid to a cube[3]. This results in the following equations:

$$p(t) = \frac{T_2^{MR} + T_2^{TR}}{I_{33}^{MR}\,\omega_{MR}} + C_1 \cos(\tilde{\alpha} t) - C_2 \sin(\tilde{\alpha} t) \tag{3.29}$$

$$q(t) = -\frac{T_1^{MR}}{I_{33}^{MR}\,\omega_{MR}} + C_2 \cos(\tilde{\alpha} t) + C_1 \sin(\tilde{\alpha} t) - F_2^{TR}\,K_{TR} / \left(I_{33}^{MR}\,m\,\omega_{MR}\right) \tag{3.30}$$

With $\tilde{\alpha}$ being defined by the following equation:

$$\tilde{\alpha} = \frac{I_{33}^{MR}\,m\,\omega_{MR}}{(dOFo_3 - dOMRo_3)^2\; m_F\,m_{MR} + I_{11}^{MR}\,m + I^F\,m} \tag{3.31}$$

The trigonometric terms of Eqs. 3.29-3.30 describe symmetric oscillations with frequency $\tilde{\alpha}$ in ($^{\text{rad}}/_{\text{s}}$). To analyze the influence of these oscillations on the helicopter dynamics, a frequency estimation has been made for a LOGO 14 helicopter in [KBLH06]. In the publication the following has been concluded: The frequency of the oscillations is too high for the helicopter to respond. Therefore, the trigonometric terms of Eqs. 3.29-3.30 are negligible and the equations[4] can be simplified to:

$$p = \frac{T_2^{MR}}{I_{33}^{MR}\omega_{MR}} \tag{3.32}$$

$$q = -\frac{T_1^{MR}}{I_{33}^{MR}\omega_{MR}} \tag{3.33}$$

Eqs. 3.32-3.33 show, that for helicopters with small fuselage the rotation dynamics of the angular rates p and q simplify to algebraic equations. This is an important conclusion and has mayor influence on the orientation controller design presented in Sec. 4.

A similar estimation has been made by the author for the CB5000 and the 24.5 kg custom design helicopter. Different from the publication [KBLH06] the fuselage is not simplified as a point mass for the estimation, but approximated by a cube with the volume of the cuboid. The oscillation frequency has been recalculated for the LOGO 14 to make the estimation comparable to the publication. The results are summarized in the following table[5]:

Helicopter	$\tilde{\alpha}$ ($^{\text{rad}}/_{\text{s}}$)	Freq. ($^{1}/_{\text{s}}$)	Period. (ms)	$\hat{\alpha}$ ($^{\text{rad}}/_{\text{s}}$)
LOGO 14 (from [KBLH06])	268	42.7	23	419
LOGO 14	107	17.0	59	419
CB5000	68	10.8	93	272
Custom (24.5 kg)	29	4.6	217	293

[3] With the inertia number $I^F = \sqrt[3]{I_{11}^F\,I_{22}^F\,I_{33}^F}$.

[4] Under the condition $F_2^{TR} = 0$ and $T_2^{TR} = 0$.

[5] For convenience the oscillation frequency and the oscillation period are presented in the table.

The column titled $\hat{\alpha}$ is explained later. The oscillation frequency of the LOGO 14 is much lower than estimated in [KBLH06]. The increased volume of the fuselage reduced $\tilde{\alpha}$ about 2.5 times, from 268 $^{\text{rad}}/_{\text{s}}$ to 107 $^{\text{rad}}/_{\text{s}}$. Based on the table the conclusion is drawn, that with increasing size and weight of the helicopter the oscillation frequency $\tilde{\alpha}$ decreases. In other words, the helicopter's ability to follow the oscillations increases. Therefore, below a certain frequency limit, the oscillations are propagated on the helicopter motion.

The oscillation frequencies of the CB5000 and the custom helicopter are low enough for the helicopters to follow. This has two consequences: First, the oscillations become visible, even during manual fight. Second, a controller based on Eqs. 3.32-3.33 does not work or shows poor flight performance. However, experiments with both helicopters have shown that this is not necessarily the case.

The reason is the following. It has been assumed, that the main-rotor of a small size helicopter is rigidly mounted to the fuselage, except the rotation around $\mathbf{f}_3$. However, for a small size helicopter the main-rotor is neither mounted completely rigid, nor are the main-rotor blades themselves completely rigid. Elastic dampers, usually rubber O-rings, are integrated into the rotor head of small size helicopters. They allow a certain flapping motion of the rotor, while they damp the overall flapping motion of the blades. Flapping hinges, which are typically used by full size helicopters, are normally not utilized by small size helicopters. As a result, the flexibility of the rotor-head and the blades reduces the influence of the flapping oscillations on the fuselage.

An estimation of oscillation frequencies for a flapping main-rotor, requires an extension of the presented model and a detailed analysis of the new model. However, to keep the focus of this thesis on the load transportation the model derivation and analysis have been omitted. Instead, an estimation of the minimum and maximum oscillation frequencies is presented.

The values in the table above are estimated for a completely rigid rotor head and completely rigid rotor blades. Therefore, theses values define the lowest expected oscillation frequencies for the presented helicopter types. For a freely flapping main-rotor, without any friction or additional damping, $m_F = 0$ and $I^F = 0$ are assumed. In this case the influence of the fuselage is completely neglected and Eq. 3.31 simplifies to $\hat{\alpha} = 2\,\omega_{MR}$. Therefore, $\hat{\alpha}$ defines the highest expected oscillation frequencies. The rightmost column of the table above contains the oscillation frequencies for the different helicopters. Its clearly visible that these frequencies are much too high for the helicopters to follow.

For a real system, depending on the selected dampers in the rotor head and elasticity of the rotor blades, the oscillation frequency is expected to be somewhere between the two extremes: completely rigid rotor head and blades, see $\tilde{\alpha}$ in the leftmost column, and completely free flapping, see $\hat{\alpha}$ in the rightmost column.

The answer to the question, whether the rotation dynamics of a helicopter can be simplified and represented by the algebraic Eqs. 3.32-3.33, therefore depends on the answer to the question, whether or not a rotor head damping can be found, that sufficiently suppresses the oscillations of the main-rotor. The higher the influence of the fuselage, the more it becomes difficult to find a suitable damping of the rotor head. The author knows from conducted flight experiments that, depending on the rotor head damping, oscillations of the whole helicopter do or do not occur during manual and autonomous

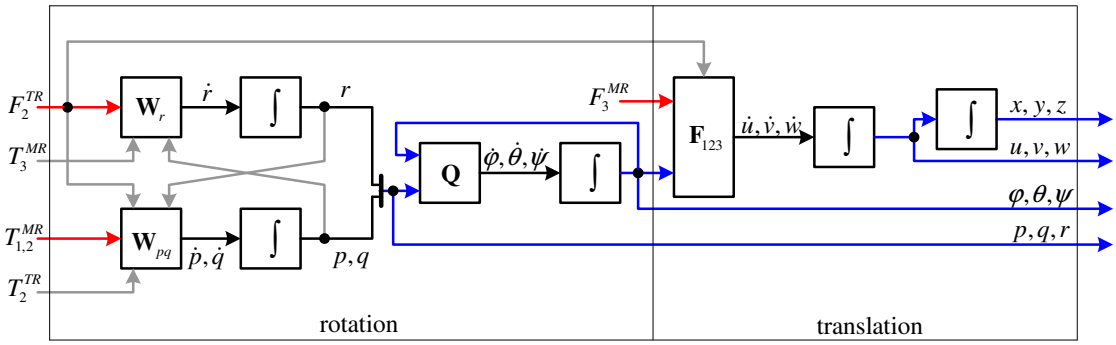

Figure 3.5: Rigid body model of a small size helicopter

flight. And that, with correct rotor head damping, a controller based on Eqs. 3.32-3.33 can provide good flight performance.

Fig. 3.5 summarizes the mechanical model, developed in this section. Forces and torques, which are considered as control inputs, are depicted by red arrows. Gray arrows indicate forces, torques or cross couplings that are considered disturbances for the particular blocks. The blue arrows represent the state variables. Control inputs enter the blocks from the left, results leave the blocks to the right and disturbances enter the blocks from the top or bottom.

The left side of Fig. 3.5 describes the rotation kinematics and dynamics of the model. The rotation dynamics of the helicopter are represented by the blocks $\mathbf{W}_{pq}$ and $\mathbf{W}_r$. The block $\mathbf{W}_{pq}$ is composed of Eqs. 3.21-3.22 and characterizes the change of the angular rates q and p, caused by $T_{1,2}^{MR}$. The block $\mathbf{W}_r$ is based on Eq. 3.23 and describes the change of the angular rates r, caused by F_2^{TR}. The outputs of $\mathbf{W}_{pq}$ and $\mathbf{W}_r$ are integrated into the angular rates p, q, r and fed into the block $\mathbf{Q}$. The block $\mathbf{Q}$ includes the rotation kinematics characterized by Eqs. 3.14-3.16. The output of the block is the derivative of the Euler-angles, which are integrated into the Euler-angles (ψ, θ, φ).

The right side of Fig. 3.5 describes the translation kinematics and dynamics of the model. The block $\mathbf{F}_{123}$ represents the translation dynamics of the helicopter, which is described by Eqs. 3.18-3.20. The block calculates the acceleration of the helicopter's CoM based on the current orientation of the helicopter, and therefore the orientation of the main-rotor lifting force vector $\mathbf{F}^{MR}$, and the current magnitude of the lifting force F_3^{MR}. The coordinates of the acceleration ($\dot{u}$, $\dot{v}$, $\dot{w}$) are the outputs of the block. The first integration results in the velocity coordinates (u, v, w) and the second integration results in the position coordinates (x, y, z) of the helicopter's CoM.

This concludes the derivation of the helicopter model. Single-, dual- and multi-lift configuration models are based on this model. These models are derived and validated in Ch. 5, and flight experiments are described in Ch. 7.

3.2 Bell-Hiller-Bar, Main- and Tail-Rotor

In order to understand the behavior of the Bell-Hiller-Bar and its coupling to the main-rotor, it is important to understand how forces and torques are generated by a helicopter rotor. The linkage of the tail-rotor is simpler than the linkage of the helicopter main-rotor. The angle of attack is coupled for both tail-rotor blades and it is only possible to change both angles simultaneously. This motion of the rotor blades is called a "collective" motion. Depending on the angle of attack and the rotational speed of the blades, the rotor generates a force perpendicular[6] to the rotor plane and a drag torque around the rotation axis.

Beside a "collective" motion, the main-rotor allows a "cyclic" motion as well, where the angle of attack of one blade increases and of the opposing blade decreases. The cyclic pitch angle α, which has direct influence on the angle of attack of the blades $\alpha_{\mathrm{mr1}}^{BL}$ is composed of the longitudinal pitch angle $\alpha_{\mathrm{f1}}^{SP}$, sometimes called roll angle, and the lateral pitch angle $\alpha_{\mathrm{f2}}^{SP}$, sometimes just called pitch angle of the swash-plate. The swash-plate, drawn blue-orange in Fig. 3.6, "mixes" the current pitch angle α from the lateral and longitudinal pitch angles $\alpha_{\mathrm{f1,2}}^{SP}$, the blade rotation angle $\gamma_{\mathrm{f3}}^{MR}$ and the collective pitch.

Assuming that the angle of attack of the blades is a non-linear function of the current pitch angle $\alpha_{\mathrm{mr1}}^{BL} = \xi(\alpha)$, it is possible to rewrite the equation into

$$\alpha_{\mathrm{mr1}}^{BL} = \xi(\cos(\gamma_{\mathrm{f3}}^{MR})\,\alpha_{\mathrm{f1}}^{SP} + \sin(\gamma_{\mathrm{f3}}^{MR})\,\alpha_{\mathrm{f2}}^{SP}) \tag{3.34}$$

Therefore, the actual attacking angle of the blades depends on the current position of the rotor blades, described by $\gamma_{\mathrm{f3}}^{MR}$, relative to the helicopter fuselage and the lateral and longitudinal angles $\alpha_{\mathrm{f1,2}}^{SP}$.

The disc of the spinning main-rotor is considered to be logically parted into four quarters of equal size, where opposing quarters belong to the same, lateral or longitudinal, cyclic angles. Assuming a certain, e.g. lateral, cyclic angle, the main-rotor blades have increased or decreased angle of attack within corresponding rotor disc quarters. The force generated by the rotor blades increases in one quarter, while it decreases in the opposing quarter. Therefore, both forces together generate torque, for example around the longitudinal axis, while the average lifting force is constant. This describes the general generation of torques and forces of the main-rotor.

However, small size helicopters often are augmented by a Bell-Hiller-Bar, which has direct influence on the attacking angle of the blades. Therefore, the coupling and functioning of the Bell-Hiller-Bar needs to be examined.

A schematic of the Bell-Hiller-Bar linkage, connecting swashplate and main-rotor blades, is shown in Fig. 3.6. The figure is simplified to provide a clear view of all important parts. The main-rotor, the Bell-Hiller-Bar and the orange part of the swash plate are moving with the constant angular velocity ω^{MR} relative to the fuselage frame $\mathbf{F}$. The angles $\alpha_{\mathrm{f1,2}}^{SP}$ and $\gamma_{\mathrm{f3}}^{BHB}$ are given relative to the fuselage frame $\mathbf{F}$ and the remaining angles are given relative to the main-rotor frame $\mathbf{MR}$. The figure shows a time instant, where both frames coincide. The orientation of the swash plate is given by angles $\alpha_{1,2}^{SP}$, which are

[6] This is an approximation, which is valid most of the time.

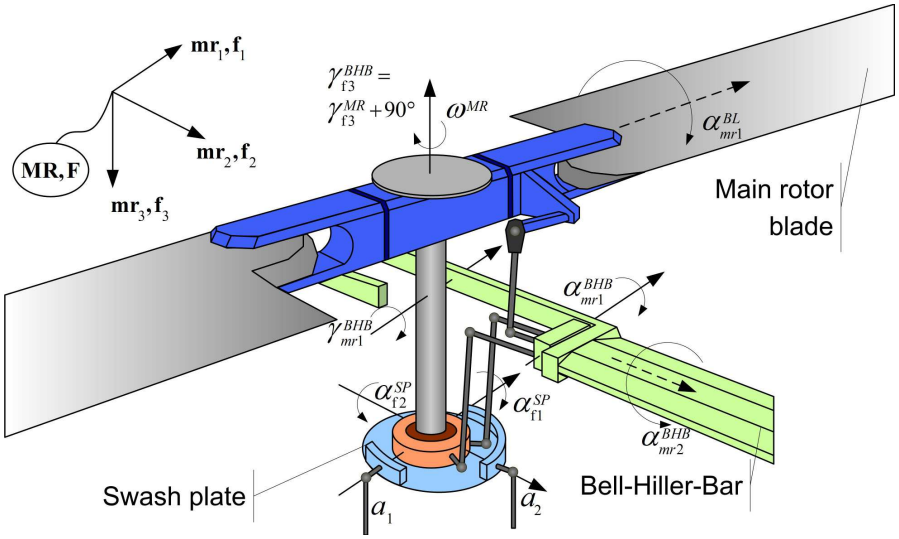

Figure 3.6: General schematic of the Bell-Hiller-Bar

adjusted by the actuators $a_{1,2}$. For simplicity only the linkage of the actuators is drawn. The orientation of the Bell-Hiller-Bar relative to the fuselage is given by the angles $\gamma_{\mathrm{f3}}^{BHB}$ and $\gamma_{\mathrm{mr1}}^{BHB}$. Both angles and their derivatives describe the state of the Bell-Hiller-Bar, and it should be noted that $\dot{\gamma}_{\mathrm{f3}}^{BHB} = \left|\omega^{MR}\right| = \text{constant}$.

The main-rotor and Bell-Hiller-Bar are considered to be in the state depicted in Fig. 3.6. The current angles $\gamma_{\mathrm{f3}}^{MR}$, $\gamma_{\mathrm{f3}}^{BHB}$ of main-rotor and Bell-Hiller-Bar are assumed to be fixed during the further examination and are neglected for the following considerations.

Fig. 3.7 is a sectional drawing of Fig. 3.6, where a cut through the $\mathbf{f}_{2,3}$-plane is shown. The left side shows a stylized view of the different components: The rotor-blade, Bell-Hiller-Bar and main-rotor shaft are drawn in gray, whereas the linkage is drawn without fill. The joint of two linkage segments is drawn in dark-gray, and the joint between linkage segment and another component is drawn in black. This avoids confusions, since three linkage joints are drawn above the Bell-Hiller-Bar, but only the rightmost of them is connected to the Bell-Hiller-Bar itself. The schematic on the right side of the figure is a further abstraction of the schematic presented on the left. Based on this figure, the kinematics of swash plate, Bell-Hiller-Bar, main-rotor-blade and linkage are calculated, where p_i denotes the i'th linkage joint, l_i describes the length of the i'th lever and the k'th connection point is given by h_k.

$$\alpha_{\mathrm{mr1}}^{BL} = \zeta(\alpha_{\mathrm{f1}}^{SP}, \gamma_{\mathrm{mr1}}^{BHB}) \tag{3.35}$$

$$\alpha_{\mathrm{mr1}}^{BL} \simeq \arccos\left(\frac{l_1 l_6 \cos\left(\alpha_{\mathrm{f1}}^{SP}\right) + l_5(l_4 + l_5 + l_6)\cos\left(\gamma_{\mathrm{mr1}}^{BHB}\right)}{(l_5 + l_6)\, l_8}\right) \tag{3.36}$$

Eq. 3.35 describes the relation between the angle of the swash plate $\alpha_{\mathrm{f1}}^{SP}$, the angle of the Bell-Hiller-Bar $\gamma_{\mathrm{mr1}}^{BHB}$ and the attacking angle of the blade $\alpha_{\mathrm{mr1}}^{BL}$, where ζ is a non-linear function. The linkage angle $\alpha_{\mathrm{mr1}}^{BHB}$ is directly determined by $\alpha_{\mathrm{f1}}^{SP}$ and $\gamma_{\mathrm{mr1}}^{BHB}$. The explicit

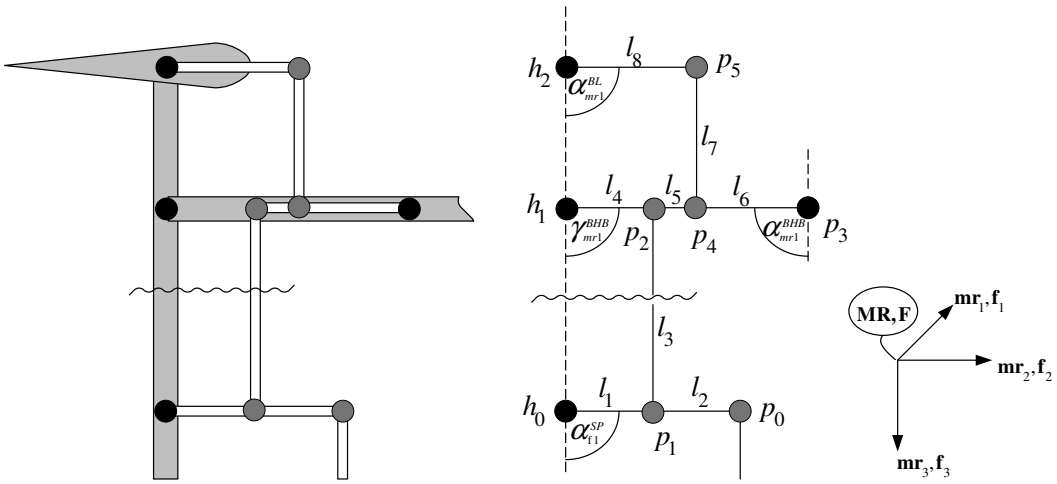

Figure 3.7: Two dimensional schematic of the Bell-Hiller-Bar and linkage

derivation of the function ζ based on the schematic presented in Fig. 3.7 is simple and requires only basic trigonometric knowledge. The function is only presented in an implicit form, because of its size. However, the complete function is presented in the additional equations document, which is accompanying this thesis on CD, see [Ber13, page 3ff.]. The Eq. 3.36 provides an approximation, which assumes that the vectors $v_1 = p_2 - p_1$ and $v_2 = p_5 - p_4$ are always parallel to basis vector $\mathbf{f}_3$. Based on this assumption a motion of p_1 parallel to $\mathbf{f}_3$ causes an equal motion of p_5 parallel to $\mathbf{f}_3$. For standard configurations, like the CB5000 helicopter, and small angles $\left|\alpha_{\mathrm{f1}}^{SP}\right| \leq 5°$, $\left|\gamma_{\mathrm{mr1}}^{BHB}\right| \leq 5°$ Eq. 3.36 represents a good approximation of the function ζ.

In summary, beside the swash plate angle $\alpha_{\mathrm{f1}}^{SP}$, the Bell-Hiller-Bar angle $\gamma_{\mathrm{mr1}}^{BHB}$ needs to be known for the calculation of the attacking angle of the main-rotor blades. Since the angle $\gamma_{\mathrm{mr1}}^{BHB}$ of the Bell-Hiller-Bar is not directly actuated, the angle depends only on the free[7] motion of the Bell-Hiller-Bar.

For this reason a motion estimation of the Bell-Hiller-Bar is necessary. Small blades[8], so called Bell-Hiller-Blades, are attached at the ends of the Bell-Hiller-Bar. Therefore, the motion of the Bell-Hiller-Bar is determined by the gyroscopic effect created by the spinning mass of the Bell-Hiller-Bar and the aerodynamic influence of the Bell-Hiller-Blades. The aerodynamic behavior of the Bell-Hiller-Blades depends on three properties: First, the air inflow, which depends on the angular velocity of the rotor blades, the helicopter's velocity and external influences like wind. Second, the blade attack angles, which depend on the orientation of the swash plate and the orientation of the stabilizer. And third, the aerodynamic properties of the Bell-Hiller-Blades like the blade profile. An obvious approach is the development of a Bell-Hiller-Bar model, which considers the spinning mass as well as the aerodynamic influence introduced through the Bell-Hiller-

[7] The force required to change the blade angle $\alpha_{\mathrm{mr1}}^{BL}$, including the friction in the linkage joints, is considered negligible small.

[8] Not drawn in Figure 3.6.

Blades, see e.g. [KT98, CS03a]. However, this approach has one major drawback. The underlying body model needs to consider one additional rigid body, the Bell-Hiller-Bar, which increases the model complexity significantly. This complicates model analysis and controller development. Therefore, a different approach is presented. The main-rotor is modeled as a solid spinning disc, compare Sec. 3.1, and only the general influence of the Bell-Hiller-Bar is considered.

Similar to B. Mettler [MKT00] the author considers the Bell-Hiller-Bar to function as a lagged rate feed-back. This feedback serves two main purposes: First, the compensation of short aerodynamic disturbances, e.g. caused by wind gusts, and second, the generation of angular speeds, which are approximately proportional to the applied cyclic angles. The latter can be deduced directly from manual flight experiments with and without Bell-Hiller-Bar. The discussion of the rigid body dynamics in Sec. 3.1.3 reveals, that the proposed model already satisfies this proportionality, see Eqs. 3.32-3.33. The explanation is simple. Since no non-linear aerodynamic effects are included in the rigid-body model, no feed-back controller is necessary to compensate these effects.

This implies, that the generation of torques and forces of the main-rotor can be approximated by simple algebraic relations, ignoring the actual motion of the Bell-Hiller-Bar altogether. This seems to be a very big simplification, but several experiments have shown that this simplification is feasible for the considered class of small size helicopters. However, the aerodynamic generation of torques and forces requires time. This is approximated by a linear first order delay.

3.3 Remaining Components

3.3.1 Actuators

The actuators used for small size helicopters are servomechanisms, also called servos, composed of a small motor, a feedback sensor, a gearbox and an integrated control electronic. The actuators are designed to provide a rotational motion of a sprocket, to which a lever is attached. Actuators for pure translational motion exist, but they are very rare and usually not used for helicopters. Therefore, they are not considered in this work. The input to the actuators s_x is a pulse-width coded signal of the desired angle. The integrated controller moves the sprocket to the desired angle, using the maximum speed permitted by motor and gearbox. Currently there are two types of actuators available - analog and digital. The controller of the analog actuators is considered to be equivalent to a P-controller, whereas the controller of the digital actuators is equivalent to a PID-controller. Additionally, some digital actuators allow the input signals to change at a higher rate than 50 Hz, which is the standard rate for servos.

The main properties of the actuators are duty stroke, the maximum acceleration, velocity and torque, the dead time and the controller type. The actuators used for small size helicopters are typically below industrial grade quality and normally only the duty stroke and the maximum rotation speed are known from specifications. To reduce the influence of the load on the actuator the actuator motors provide much more torque than necessary. As a result, the difference between digital and analog controllers

becomes negligible small and the relation between input signal s_x and output angle p_x is considered to be linear. For small size helicopters the linkage is usually attached to the actuator by means of a lever. To reduce the non-linearity between rotation of the lever and translation of the linkage, just a small range of the actuator's duty stroke is used. This reduces the importance of the dynamic behavior of the actuator, which is mainly determined by dead-time and maximum acceleration.

The static behavior of the actuators is modeled as linear relation between the input signal s_x and output angle p_x. The dynamic behavior of the actuators is approximated by a delay element.

3.3.2 Main-Engine

There are three types of engines available: Combustion engines, electric engines and jet engines. For combustion and jet engines main- and tail-rotor are driven by a single engine and the power is distributed between the rotors using a gearbox. Compared to combustion or jet engines, electric engines are of small size, very efficient and allow the utilization of one engine per rotor, and sometimes the tail-rotor is driven even without a gearbox.

Independent of the engine type the main properties are the maximum angular speed and torque and the engine dynamics.

It is deductible from the mechanical model of the helicopter (previously presented) and verified by manual flight experience, that constant angular speeds of main- ω^{MR} and tail-rotor ω^{TR} are required to achieve good flight performance. Therefore, the engines need to generate a constant angular speed, even during fast maneuvers and strong disturbances. In practice, for combustion and jet engines this is achieved by very simple means, like a feed-forward- or a PID-controller. For example, a simple PI-controller with feed-forward extension has been used for the UAVs described in Sec. 2.1. Most commercial controllers for electrical engines include a "governor-mode", where the angular speed is kept constant independent of load changes and no additional external controller is required. It has been verified in flight tests, that the solutions for combustion and electrical engines work very well.

Therefore, controller and engine are considered to be an entity. The controller almost fully compensates the dynamics of the engine. As a result, the angular speed is assumed to be constant for main- and tail-rotor.

3.3.3 Sensors

The system state estimation is a prerequisite for the control of small size helicopters. In turn, for a good state estimation the sensors are of crucial importance. Each sensor has unique characteristics in terms of data rate, bandwidth, resolution, drift, sensitivity, signal delay and dead-time.

Price, availability and mass usually limit the assortment. Therefore, often sensors are selected, which not fulfill all requirements. However, within certain limits sensor characteristics are improvable. For example through careful placement, additional calibration

or signal processing, e.g. filtering. However, signal delay and dead-time are very difficult to improve and are normally even worsened by signal processing.

For this work the assumption is made that only signal delay and signal dead-time need to be considered during the modeling and controller design. In other words, for the considered class of small-size helicopters, it is either possible to buy suitable sensors or to improve the sensor data, using the measures described above. For both cases, modeling and control, the signal delay and signal dead-time are approximated by a single first-order delay.

4 Control of Small Size Helicopters

This chapter describes the control of a single small size helicopter. A small size helicopter has four control inputs: The collective pitch of the main-rotor, the longitudinal and lateral cyclic pitch of the main-rotor, and the collective pitch of the tail-rotor. On the contrary the helicopter has six DoF and is therefore underactuated. This implies, that only four DoF are directly controllable and the remaining two are implicitly given by the system's kinematics and dynamics. The yaw angle ψ (heading) and the position (x, y, z) of the helicopter are directly controlled, whereas roll and pitch angles (φ, θ) are implicitly determined by the desired heading and position.

The non-linear controller of the helicopter is composed of three sub-controllers: A heading controller, a translation controller and an underlying controller of pitch and roll angles. As a result, the control of the orientation is composed of two independent controllers: the roll-pitch controller and the yaw controller.

The yaw controller will be called *heading controller* and the roll-pitch controller will be called *orientation controller* for the remainder of this work.

4.1 Abstract Control Inputs

The control inputs of a small size helicopter are the collective and cyclic pitches of the main-rotor and the collective pitch of the tail-rotor. A direct utilization of these signals for the controller design is inconvenient, since the basis for the controller design is the rigid body model. The model utilizes forces and torques as inputs rather than collective and cyclic pitches. The control inputs of the rigid body model are two forces F_3^{MR}, F_2^{TR} and two torques $T_{1,2}^{MR}$, compare Sec. 3.1 and Fig. 3.5.

It is necessary to approximate the collective and cyclic pitches of the main-rotor and the collective pitch of the tail rotor based on forces and torques utilized by the rigid body model. For Vertical Take-Off and Landing Vehicles (= VTOLs) this can be done using simple algebraic equations, like described in [KBMH07]. The following equations are valid for a CB5000 helicopter:

$$S_{roll}^{MR} = T_1^{MR}\, k_{cyc} + \Delta_{cyc} \tag{4.1}$$

$$S_{pitch}^{MR} = T_2^{MR}\, k_{cyc} + \Delta_{cyc} \tag{4.2}$$

$$S_{col}^{MR} = F_3^{MR}\, k_{col} + \Delta_{col} \tag{4.3}$$

$$S_{col}^{TR} = F_2^{TR}\, k_{tail} + \Delta_{tail} \tag{4.4}$$

The coefficients k_{xyz} and the offsets Δ_{xyz} have been estimated in flight experiments. The signal S_{col}^{TR} controls one actuator (servo), that directly changes collective pitch of

the tail-rotor. The signals S_{xyz}^{MR} control three actuators, which move the swash-plate of the main-rotor. The motion of the swash plate changes the blade angles of Bell-Hiller-Bar and main-rotor. The signals S_{roll}^{MR} and S_{pitch}^{MR} influence the longitudinal and lateral cyclic angles of the main-rotor, and the signals S_{col}^{MR} influences the collective angle of main-rotor. Although the generation process of actual cyclic angles is complex for the main-rotor, compare Sec. 3.2, the presented approximation has been proven valid through many flight experiments. All controllers presented in this thesis utilize the forces F_3^{MR}, F_2^{TR} and the torques $T_{1,2}^{MR}$ as control signals. For simulation purposes, the controllers are directly applicable to the rigid body model. In order to apply the controllers to the real helicopters, the signals are transformed, using Eqs. 4.1-4.4, into the control signals of the actuators.

4.2 Heading Controller

The rotation dynamic of a small size helicopter has been described and analyzed in Ch. 3. In particular, the following equation has been derived from Eq. 3.23:

$$\dot{r} = K\, F_2^{TR} + Z\left(T_3^{MR},\, p,\, q\right) \tag{4.5}$$

Considering the angular speed r, Eq. 4.5 behaves like a simple integrator with respect to the input force F_2^{TR}, where Z is a non-linear disturbance function. A simple hardware PI-controller, which utilizes only the measurement of a single gyroscope (angular speed r), already shows very good performance for this system. The other rates p and q are neither known nor considered by the controller. This verifies the assumption that the angular speed r is controllable independently for the remaining rates p and q.

It is simple to implement this controller using the IMU's reading of the angular speed r. However, for safety reasons the CB5000 helicopters are equipped with hardware r-rate controllers as well, which are used as a fallback during manual flight. Since a hardware controller is on board anyway, it is used as underlying controller for the heading controller presented here.

Eq. 3.16 describes the dependency between the derivative of the yaw angle $\dot{\psi}$ and the rates q and r for a given orientation. The yaw controller is designed for non acrobatic flight, where most of the time the angles θ and φ are zero or quite small. In that case the equation can be simplified to become:

$$\dot{\psi} \approx (q\sin(0) + r\cos(0))/\cos(0) = r \tag{4.6}$$

Considering the angle ψ, Eq. 4.6 behaves like an integrator with respect to the angular speed r. Therefore, a simple PI-controller is sufficient to control the heading. For small angles θ, φ the error, caused by the simplification, creates only small disturbances, which are easily corrected by the heading controller. The coefficients for the feedback loop are calculated using pole placement for a single integrator.

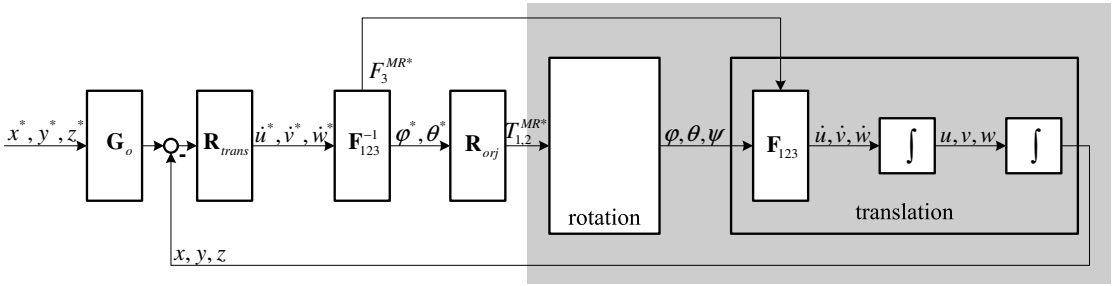

Figure 4.1: Scheme of the translation controller

4.3 Translation Controller

Fig. 4.1 depicts the scheme of the translation controller. Every block within the gray box belongs to the model of the helicopter and the remaining blocks belong to the controller. The desired position (x^*, y^*, z^*) enters the controller from the left. A pre-filter $\mathbf{G}_0$ is used to avoid an overshooting of the controller. The current position (x, y, z) of the helicopter is subtracted from the filtered desired position and fed into $\mathbf{R}_{trans}$. The block $\mathbf{R}_{trans}$ is composed of three independent PID-controllers, one for each coordinate, and its output is interpreted to be the desired acceleration ($\dot{u}^*$, $\dot{v}^*$, $\dot{w}^*$). The block $\mathbf{F}_{123}^{-1}$ is the inversion of the helicopter's translation dynamic $\mathbf{F}_{123}$, described by Eqs. 3.18-3.20. The desired angles (φ^*, θ^*) and the desired lifting force F_3^{MR*} are therefore calculated from the desired acceleration. The equations of $\mathbf{F}_{123}^{-1}$ are obtained solving Eqs. 3.18-3.20 for the angles φ, θ and the lifting force F_3^{MR}, neglecting F_2^{TR}:

$$\varphi^* = \arcsin\left(m\,\frac{-\dot{u}^*\sin(\psi)+\dot{v}^*\cos(\psi)}{F_3^{MR*}}\right) \tag{4.7}$$

$$\theta^* = \arcsin\left(m\,\frac{\dot{u}^*\cos(\psi)+\dot{v}^*\sin(\psi)}{F_3^{MR*}\cos(\varphi)}\right) \tag{4.8}$$

$$F_3^{MR*} = -\sqrt{(m\,\dot{u}^*)^2+(m\,\dot{v}^*)^2+(m\,g+m\,\dot{w}^*)^2} \tag{4.9}$$

The block of the orientation controller $\mathbf{R}_{orj}$ uses the desired angles to calculate desired torques $T_{1,2}^*$, required to achieve the desired orientation. In Sec. 4.4 the orientation controller is described in full detail.

A more detailed discussion of the translation controller is omitted here, since the structure of the controller is simple. Instead the main-rotor force generation is discussed using Eqs. 4.7-4.9.

Main-Rotor Force Generation Eqs. 4.7-4.9 provide an insight into the generation of arbitrary forces using the main-rotor. Like explained in Sec. 3 the force $\mathbf{F}^{MR}$ is approximately perpendicular to the main-rotor disc. Only the magnitude of the force $\mathbf{F}^{MR}$ is directly changeable through the collective pitch. Therefore, two steps are necessary to generate an arbitrary desired force $\mathbf{F}^{MR*} = m\,\dot{u}^*\,\mathbf{n_1} + m\,\dot{v}^*\,\mathbf{n_2} + (m\,g + m\,\dot{w}^*)\,\mathbf{n_3}$ using

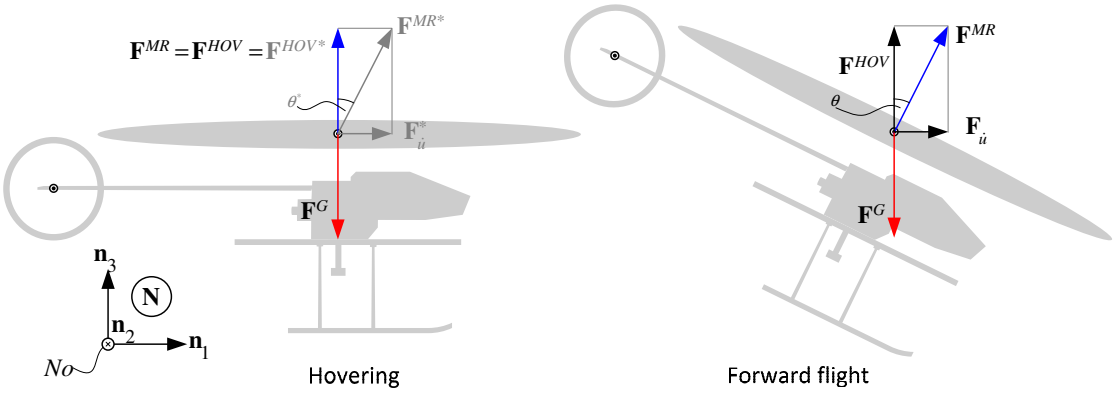

Figure 4.2: Force generation during forward flight

the main-rotor force $\mathbf{F}^{MR}$: First, a change of the main-rotor orientation and second, a magnitude adjustment of the force vector $\mathbf{F}^{MR}$.

Orientation change Eqs. 4.7-4.8 describe the calculation of the desired angles φ^* and θ^* based on the magnitude of the desired lifting force F_3^{MR*}, taking into account the desired acceleration and the current yaw-angle ψ of the helicopter.

Force adjustment Eq. 4.9 allows the calculation of the force magnitude $F_3^{MR*} = -|\mathbf{F}^{MR*}|$ from the desired acceleration $(\dot{u}^*, \dot{v}^*, \dot{w}^*)$ of the helicopter. The term mg in Eq. 4.9 describes the gravitational force.

It should be noticed, that the scalar F_3^{MR} has been defined in Sec. 3.1.3 to be $\mathbf{F}^{MR} = F_3^{MR}\,\mathbf{f}_3$. The desired force F_3^{MR*} needs to be non zero to avoid a singularity in Eqs. 4.7-4.8. This constrains the minimum vertical acceleration to nearly $-g\,\mathrm{m/s^2}$, where F_3^{MR*} is close to zero. However, for non acrobatic flight this represents only a small limitation. There is another singularity in Eq. 4.8 at $\varphi^* = \pm\pi/2$. Therefore, the desired angles have been limited to $\pm\pi/4$, which is more than sufficient for non acrobatic flight.

Fig. 4.2 shows the transition of a single helicopter from hovering to forward flight. This figure is used for the interpretation of Eqs. 4.7-4.9. The desired force $\mathbf{F}_3^{MR*}$ and the desired pitch angle θ^* are depicted on the left side of the figure. It is visible, that the desired main-rotor force vector $\mathbf{F}_3^{MR*}$ is the vector sum of desired force $\mathbf{F}_{\dot{u}}^*$, required for the horizontal acceleration, and $\mathbf{F}^{HOV*}$. Therefore, the desired magnitude of the main-rotor force is given by:

$$-\left|\mathbf{F}_3^{MR*}\right| = -\left|\mathbf{F}_{\dot{u}}^* + \mathbf{F}^{HOV}\right| = -\sqrt{(m\,\dot{u}^*)^2 + (m\,g)^2} = F_3^{MR*} \tag{4.10}$$

The equation is equivalent to Eq. 4.9, since the remaining desired accelerations $\dot{v}^*$, $\dot{w}^*$ are zero.

Alternative Calculation of the Desired Main-Rotor Force The considerations above represent a valid, but static interpretation of the Eqs. 4.7-4.9. The transitions from

F_3^{MR} to F_3^{MR*} and from the current angles φ, θ to the desired angles φ^*, θ^* have been neglected. These transitions are dynamic processes of different speeds. The generation of the force F_3^{MR} is a faster process than the generation of the torques $T_{1,2}^{MR}$. The reason is, that the collective angle is immediately propagated to the blade angles, whereas the propagation of a cyclic angle depends, among others, on the dynamics of the Bell-Hiller-Bar, see Sec. 3.2 for details. The rigid body kinematics and dynamics of the helicopter additionally delay the generation of angles φ, θ from the torques $T_{1,2}^{MR}$.

Based on these considerations the calculation of F_3^{MR*} from Eq. 4.9 is problematic, because F_3^{MR*} is calculated to fit the desired angles φ^*, θ^* and not the current angles φ, θ. A simple example illustrates this problem: A change of F_3^{MR} is considered to be instantaneous and the helicopter is considered to be hovering, with roll and pitch angles $\varphi = \theta = 0$. The desired accelerations are assumed to be $\dot{u}^*, \dot{v}^* \neq 0$ and $\dot{w} = 0$. Therefore, the helicopter shall accelerate only within the horizontal plane spanned by $\mathbf{n}_1$, $\mathbf{n}_2$. Using Eqs. 4.7-4.9 the angles φ^*, $\theta^* \neq 0$ and $F_3^{MR*} < F_3^{MR}$ are calculated[1].

A positive vertical acceleration $\dot{w} = -(F_3^{MR*} - F_3^{MR})/m$ is generated, since F_3^{MR} instantaneously changes to F_3^{MR*}, while the angles still remain zero. This causes an artificial disturbance, which needs to be compensated by the altitude controller. To overcome this problem Eq. 3.20 is solved for F_3^{MR}:

$$F_3^{MR*} = (\dot{w}^* + g)\, m/(\cos(\varphi)\cos(\theta)) \tag{4.11}$$

The desired lifting force is directly calculated from the desired vertical acceleration $\dot{w}^*$, considering the current roll and pitch angles. This implies, that the altitude controller is preferred compared to the controller for the horizontal motion in the $\mathbf{n}_{1,2}$-plane.

Based on Eq. 4.9 and Eq. 4.11 two translation controllers have been implemented and tested in real-flight experiments. Both designs have proven to be fully functional and perform well. However, flight experiments have shown, that a controller based on Eq. 4.11 outperforms a controller based on Eq. 4.9. As a result, the controller based on Eq. 4.11 has been utilized for all experiments presented in this thesis.

4.4 Orientation Controller

A scheme of the orientation controller is shown in Fig. 4.3. Like the translation controller scheme, every block within the gray box belongs to the model of the helicopter and the other blocks belong to the controller. The desired pitch and roll angles (θ^*, φ^*) are the inputs of the system. Together with the actual pitch and roll angles (θ, φ) they form a simple P-controller, with a feedback gain K_q. The resulting errors (e_1, e_2) are fed into the block $\mathbf{Q}^{-1}$, the inversion of the block $\mathbf{Q}$. The block $\mathbf{Q}$ contains the rotation kinematics of the helicopter, see Eqs. 3.14-3.16. These equations describe the calculation of the Euler-angles derivatives ($\dot{\varphi}$, $\dot{\theta}$, $\dot{\psi}$), from the angular speeds (p, q, r), for a given orientation. The equations of the inverse rotation kinematics are either calculated directly from Eq. 3.12 and Eq. 3.13 or through inversion of Eqs. 3.14-3.16. Independent from the

[1] It should be remembered, that $F_3^{MR*} < F_3^{MR} < 0$.

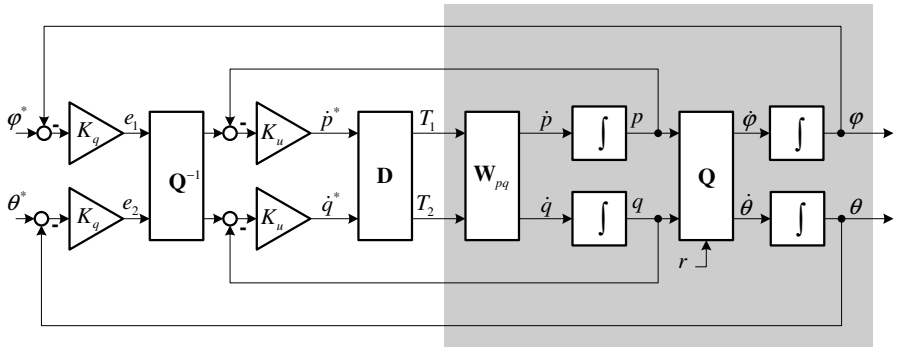

Figure 4.3: Scheme of the orientation controller

calculation method, the equations of the block $\mathbf{Q}^{-1}$ are given by:

$$\begin{aligned} p &= \dot{\varphi} - \dot{\psi}\sin(\theta) \\ q &= \dot{\theta}\cos(\varphi) + \dot{\psi}\cos(\theta)\sin(\varphi) \\ r &= -\dot{\theta}\sin(\varphi) + \dot{\psi}\cos(\theta)\cos(\varphi) \end{aligned} \tag{4.12}$$

The equation for r is only included for completeness. The angular speed r is controlled by the heading controller and therefore the calculation of r is not needed. To understand the purpose of the block $\mathbf{Q}^{-1}$, the blocks $\mathbf{Q}^{-1}$ and $\mathbf{Q}$ are considered to be directly connected for now. Since $\mathbf{Q}^{-1}$ is the inverse of $\mathbf{Q}$, both blocks together represent a identity transformation of the signals. In other words, both blocks together are replaceable through direct connections. Therefore, the system simplifies to a pair of integrators, for which a feedback loop with two P-controllers is sufficient.

Considering this result, the inner loop is examined. The inputs (e_1, e_2) of the block $\mathbf{Q}^{-1}$ are interpreted as desired Euler-angles derivatives ($\dot{\varphi}^*$, $\dot{\theta}^*$) and therefore the output is interpreted to be the desired rotation rates (p^*, q^*). Together with actual angular speeds (p, q) they form a P-controller, with a feedback gain K_u. The outputs of the controller can be interpreted as the desired derivatives of the rates ($\dot{p}^*$, $\dot{q}^*$), which are fed into the decoupling block $\mathbf{D}$. The purpose of the block $\mathbf{D}$ is to calculate the desired torques $T^*_{1,2}$ in such a way, that the block $\mathbf{W}_{p,q}$ will generate the desired derivatives of the rates. The block $\mathbf{W}_{p,q}$ represents the rotation dynamics of the helicopter, given by Eqs. 3.21-3.22. The design of $\mathbf{D}$ depends on the helicopter and is discussed later. For the analysis of the feedback loop, $\mathbf{D}$ is considered to be a perfect inversion of $\mathbf{W}_{p,q}$, like $\mathbf{Q}^{-1}$ is to $\mathbf{Q}$. In that case, both blocks together represent a identity transformation of the signals and only the two integrators remain in the feedback loop. Therefore, the orientation controller design simplifies to two PD-controllers for two double integrators.

4.4.1 Decoupling of the Rotation Dynamics

The presented controller is based on the assumption that an inversion $\mathbf{D}$ is found for $\mathbf{W}_{p,q}$, which satisfies $\mathbf{D}(\mathbf{W}_{p,q}(x, y)) = (x, y)$ with $x, y \in \mathbb{R}$. Like discussed in Sec. 3,

depending on the influence of the fuselage on the rotational dynamics of a helicopter, the Eqs. 3.21-3.22 can be simplified and analytically solved or not. It was shown, that for a sufficient small fuselage, the rotation dynamics of the helicopters simplify to the algebraic relations described by Eq. 3.32 and Eq. 3.33. Therefore $\mathbf{W}_{p,q}$ is composed of two algebraic equations and $\mathbf{D}$ is determined by solving these equations for the torques $T_{1,2}^{MR}$:

$$\begin{aligned} T_1^{MR} &= -q\,(I_{33}^{MR}\omega_{MR}) \\ T_2^{MR} &= p\,(I_{33}^{MR}\omega_{MR}) \end{aligned} \tag{4.13}$$

Since Eqs. 3.32-3.33 relate torques and rates algebraically, Fig. 4.3 is not correct for this case: The block $\mathbf{W}_{p,q}$ is not based on differential equations anymore, but on algebraic equations. Therefore, the integrators after the block are redundant and the whole K_u feedback loop becomes useless and needs to be removed. The complexity of the orientation model reduces from double integrators to single integrators and the complete orientation controller reduces to the K_q feedback loops.

For a helicopter with a large fuselage the block $\mathbf{W}_{p,q}$ is based on the Eqs. 3.21-3.22. The decoupling block $\mathbf{D}$ is calculated using methods from linear control theory. The Laplace transformation is applied to the differential equations and the following equations are derived for the system plant:

$$\begin{aligned} p(s)\,s &= k_1 T_1^{MR}(s) + k_2 q(s) \\ q(s)\,s &= k_3 T_2^{MR}(s) + k_4 p(s) \end{aligned} \tag{4.14}$$

The calculation of Eqs. 4.14 neglects the force F_2^{TR}, the torque T_3^{MR} and the angular speed r. These simplifications are feasible, like discussed during the design of the heading controller in Sec. 4.2. The constants k_x (with $x \in \{1,2,3,4\}$) are calculated from Eqs. 3.24, with $k_1 = m/K_{p3}$, $k_2 = K_{p1}/K_{p3}$, $k_2 = -m/K_{q3}$ and $k_4 = K_{q1}/K_{q3}$. Eqs. 4.14 are rewritten into V-Form $\mathbf{X} = \mathbf{F}\,(\mathbf{Y} + \mathbf{V}\,\mathbf{X})$:

$$\begin{aligned} \mathbf{X} &= (p(s),\, q(s))^T \\ \mathbf{Y} &= \left(T_1^{MR}(s),\, T_2^{MR}(s)\right)^T \\ \mathbf{F} &= \begin{bmatrix} k_1/s & 0 \\ 0 & k_3/s \end{bmatrix} \\ \mathbf{V} &= \begin{bmatrix} 0 & k_2/k_1 \\ k_4/k_3 & 0 \end{bmatrix} \end{aligned} \tag{4.15}$$

Using Eqs. 4.15 the plant is recalculated into canonical P-form ($\mathbf{X} = \mathbf{G}\,\mathbf{Y}$):

$$\mathbf{G} = (\mathbf{I} - \mathbf{F}\mathbf{V})^{-1}\mathbf{F} \tag{4.16}$$

$$\mathbf{G} = \frac{1}{s^2 - k_2 k_4} \begin{bmatrix} k_1 s & k_2 k_3 \\ k_1 k_4 & k_3 s \end{bmatrix} \tag{4.17}$$

Based on the system plant in canonical form, the decoupling plant $\mathbf{D}$ is determined. The decoupling is preformed by application of the decoupling block $\mathbf{D}$ and the decoupled

system input $\tilde{\mathbf{Y}}$ to the system plant ($\mathbf{Y} = \mathbf{D}\,\tilde{\mathbf{Y}}$). The decoupled system ($\mathbf{X} = \mathbf{G}\,\mathbf{D}\,\tilde{\mathbf{Y}}$) should behave like two independent integrators with respect to $\tilde{\mathbf{Y}}$. The desired plant ($\mathbf{G}_{des} = \mathbf{G}\,\mathbf{D}$) is therefore defined as:

$$\mathbf{G}_{des} = \begin{bmatrix} 1/s & 0 \\ 0 & 1/s \end{bmatrix} \tag{4.18}$$

Using this definition, the decoupling plant is calculated:

$$\mathbf{D} = \mathbf{G}^{-1}\mathbf{G}_{des} = \begin{bmatrix} \frac{1}{k_1} & -\frac{k_2}{k_1 s} \\ -\frac{k_4}{k_3 s} & \frac{1}{k_3} \end{bmatrix} \tag{4.19}$$

The system is described by $\mathbf{X} = \mathbf{G}_{des}\,\tilde{\mathbf{Y}}$ after the decoupling. The equation is solved for the new system input ($\tilde{\mathbf{Y}} = \mathbf{G}_{des}^{-1}\,\mathbf{X}$), and $\tilde{\mathbf{Y}} = (s\,p(s),\, s\,q(s))^T$ is calculated. The final decoupling equations are derived from $\mathbf{Y} = \mathbf{D}\tilde{\mathbf{Y}}$ and transferred back into the time domain:

$$\begin{aligned} T_1^{MR} &= \dot{p}/k_1 - k_2/k_1\, q \\ T_2^{MR} &= \dot{q}/k_3 - k_4/k_3\, p \end{aligned} \tag{4.20}$$

A comparison of Eqs. 4.20 and Eqs. 3.21-3.22 shows, that for a simple $\mathbf{G}_{des}$, like Eq. 4.18, the equations could have been directly calculated from Eqs. 3.21-3.22. However, the described approach has two advantages over the direct calculation: First, the desired system plant $\mathbf{G}_{des}$ has been specified and the behavior of the decoupled plant is assured to be equivalent to desired system plant: The resulting system behaves similar to two independent integrators. Second, it provides a simple method to validate, that the function of decoupling block $\mathbf{D}$ is not influenced by a non modeled time delay of the plant. This is shown in the frequency-domain. The transfer function G_{td} is considered to be a non modeled time delay. In that case the system plant is written to be:

$$\mathbf{X} = \mathbf{G}\,G_{td}\,\mathbf{Y} = \mathbf{G}\,G_{td}\,\mathbf{D}\,\tilde{\mathbf{Y}} = \mathbf{G}\,\mathbf{D}\,G_{td}\,\tilde{\mathbf{Y}} = \mathbf{G}_{des}\,G_{td}\,\tilde{\mathbf{Y}} \tag{4.21}$$

Eq. 4.21 shows that the decoupling works, even in presence of G_{td}. The transformation of the equation is valid, since G_{td} represents only a single function and not a matrix of functions. Therefore, the multiplication with G_{td} is commutative. For the algebraic decoupling of a small fuselage, described by Eqs. 4.13, the presented result is valid as well. The reason is, that the decoupling is purely algebraical and stays valid even in presence of G_{td}. This conclusion has been verified[2] in the frequency domain, using an approach analog to Eq. 4.21.

Eq. 4.21 implies that G_{td} is similar for all matrix components, which is a simplification. A helicopter normally is not rotation symmetric around the axis $\mathbf{f}_3$ and therefore different torques are needed to achieve similar lateral or longitudinal rotation rates. However, the decoupling block $\mathbf{D}$ is already accounting for this, since $\mathbf{D}$ is based on the rigid body

[2]Since the validation is straight forward, it is not described here.

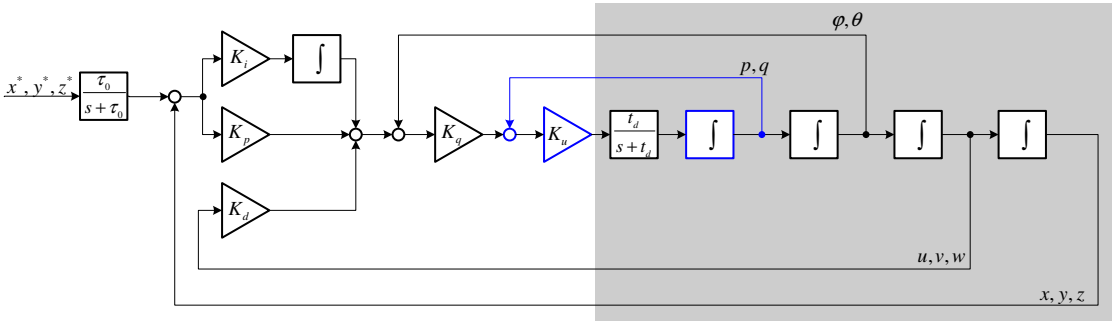

Figure 4.4: Linear model used for pole placement

model. Therefore, the different time delays are only caused by the time required to generate torques of different magnitudes. For normal flight conditions these differences are considered negligible small. Therefore, the simplification is a good approximation for small size helicopters.

In summary two decoupling blocks have been presented: First, the decoupling for a helicopter with small fuselage, based on direct inversion of the algebraic Eqs. 4.13. Second, the decoupling for a helicopter with big fuselage, based on a decoupling method from linear control theory, has been applied to the Eqs. 3.21-3.22. Additionally it has been shown, that although a non modeled time delay G_{td} influences the system behavior, it has no influence on the functioning of the decoupling blocks, independent of the fuselage size.

4.5 Calculation of Controller Coefficients

This section covers the calculation of the coefficients for the translation- and orientation-controller without heading. And the calculation of the coefficients for altitude- and heading-controller.

The control coefficients for translation- and orientation-controller, without heading, are calculated simultaneously. Sec. 4.5.1 and Sec. 4.5.2 cover the same control approach, but depending on the influence of fuselage different calculations are presented, see Sec. 3.1.3 for a discussion of the fuselage's influence on the rotation dynamics. In Sec. 4.3 an alternate translation control approach, which favors the altitude is presented. Consequently, the altitude control coefficients need to be calculated independent from the coefficients for the horizontal translation. This calculation is presented in the in Sec. 4.5.3. Finally, Sec. 4.5.4 describes the coefficient estimation for the heading controller.

4.5.1 Translation and Orientation Controller Coefficients for a Helicopter with a Big Fuselage

Fig. 4.4 shows the controller and the linearized model of a helicopter with a big fuselage. Every block within the gray box belongs to the model and every block outside belongs

to the controller. The schematic is based on Fig. 4.1 and Fig. 4.3, where the non-linearity of translation dynamics $\mathbf{F}_{1,2,3}$, rotation kinematics $\mathbf{Q}$ and rotation dynamics $\mathbf{W}_{pq}$ are canceled through $\mathbf{F}_{1,2,3}^{-1}$, $\mathbf{Q}^{-1}$ and $\mathbf{D}$. The blocks have been removed from the figure, since perfect inversion is assumed for $\mathbf{F}_{1,2,3}$, $\mathbf{Q}$ and $\mathbf{W}_{pq}$. Therefore, the dynamic behavior of the helicopter simplifies to a series of four integrators: Two for the rotation (inner loop) and two for the translation (outer loop). Additionally, a first order delay $G_{td} = t_d/(s+t_d)$ is included as approximation for non modeled time delay. The pre-filter $G_{\tau 0} = \tau_0/(s+\tau_0)$ is not required for the calculation of the controller coefficients and is included in the schematic only for completeness.

The control coefficients for a helicopter with a big fuselage are calculated, using the pole placement method from linear control theory. The transfer function of the helicopter is estimated from Fig. 4.4 excluding $G_{\tau 0}$:

$$G = \frac{k_q k_w k_x t_d s + k_i k_q k_w t_d}{s^6 + t_d s^5 + k_w t_d s^4 + k_q k_w t_d s^3 + k_q k_v k_w t_d s^2 + k_q k_w k_x t_d s + k_i k_w k_q t_d} \tag{4.22}$$

Eq. 4.22 describes a system of sixth order and therefore six desired poles are specified with $\lambda_{1,2,3,4,5,6}$. Solving the equation[3] $\prod_{i=1}^{6}(s-\lambda_i) = \mathrm{den}(G)$ for the control coefficients K_i, K_v, K_x, K_q, K_w, provides the following solution:

$$\begin{aligned}
k_i &= k_{iN}/-k_{qN} \\
k_x &= \sum_{i=1}^{6} k_{iN}/(k_{qN}\,\lambda_i) \\
k_v &= \sum_{i=1}^{6}\sum_{j=i+1}^{6} k_{iN}/(-k_{qN}\,\lambda_i\lambda_j) \\
k_q &= k_{qN}/\left(\sum_{i=1}^{6}\sum_{j=i+1}^{6} \lambda_i\lambda_j\right) \\
k_w &= \left(\sum_{i=1}^{6}\sum_{j=i+1}^{6} \lambda_i\lambda_j\right)/t_d
\end{aligned} \tag{4.23}$$

With :

$$\begin{aligned}
k_{iN} &= \lambda_1\lambda_2\lambda_3\lambda_4\lambda_5\lambda_6 \\
k_{qN} &= \sum_{i=1}^{6}\sum_{j=i+1}^{6}\sum_{k=j+1}^{6} k_{iN}/(\lambda_i\lambda_j\lambda_k)
\end{aligned} \tag{4.24}$$

Additional, λ_1 is given by:

$$\lambda_1 = -t_d - \lambda_2 - \lambda_3 - \lambda_4 - \lambda_5 - \lambda_6 \tag{4.25}$$

[3]The function $\mathrm{den}(x)$ provides the denominator of x.

Eqs. 4.24 define k_{iN}, k_{qN}, which describe the numerators of k_i and k_q respectively. To achieve a compact representation Eqs. 4.23 have been artificially rewritten into this nested notation.

One pole is not directly placeable, but implicitly given by the placement of the other poles, since the order of the system (six) is higher than the number of control coefficients (five). The pole λ_1 is selected as the dependent pole, but any other pole could have been selected instead. Eq. 4.25 describes the dependency of λ_1 from $\lambda_{2,3,4,5,6}$ and t_d. The equation is used to calculate a optimal pole placement, in terms of the fastest achievable system behavior, for a given time delay. Close investigation of Eq. 4.25 shows that a optimal pole placement is only achieved for equally placed poles, since the system behavior is always limited by the slowest, largest pole. Therefore, the optimal pole $\lambda_o = \lambda_{1,..,6} = -\frac{t_d}{6}$ is found replacing $\lambda_{1,...,6} = \lambda_o$ in Eq. 4.25 and solving for λ_o. This is the optimal pole placement for a given delay t_d. Placing any of the poles $\lambda_{1,...,6}$ below λ_o automatically implies that at least one of the remaining poles is placed above λ_o, which is dominating the system behavior negatively.

4.5.2 Translation and Orientation Controller Coefficients for a Helicopter with a Small Fuselage

Fig. 4.4 is usable as well for a helicopter with a small fuselage. The rotation dynamics simplify to algebraic equations, Eqs. 3.32-3.33, and the particular integrators and the feedback loop are neglected, which are the blocks with a blue frame. Therefore, the dynamic behavior of the helicopter reduces to a series of three integrators: One for the rotation (inner loop) and two for the translation (outer loop). The first order delay $G_{td} = t_d/(s + t_d)$ is included as approximation of a non-modeled time delay or dead-time. The pre-filter $G_{\tau 0} = \tau_0/(s+\tau_0)$ is not included for the calculation of the controller coefficients. The control coefficients are calculated, using the pole placement method. The transfer function of the helicopter is estimated from Fig. 4.4:

$$G = \frac{k_q k_x t_d s + k_q k_i t_d}{s^5 + t_d s^4 + k_q t_d s^3 + k_q k_v t_d s^2 + k_q k_x t_d s + k_q k_i t_d} \tag{4.26}$$

Eq. 4.26 describes a system of fifth order and therefore five desired poles are specified with $\lambda_{1,2,3,4,5}$. Solving the equation $\prod_{i=1}^{5}(s - \lambda_i) = \mathrm{den}(G)$ for the control coefficients K_i, K_v, K_x, K_q, provides the following solution:

$$\begin{aligned}
k_i &= -\frac{-\lambda_1\lambda_2\lambda_3\lambda_4\lambda_5}{\lambda_4\lambda_5 + \lambda_3(\lambda_4+\lambda_5) + \lambda_2(\lambda_3+\lambda_4+\lambda_5) + \lambda_1(\lambda_2+\lambda_3+\lambda_4+\lambda_5)} \\
k_x &= \frac{\lambda_2\lambda_3\lambda_4\lambda_5 + \lambda_1(\lambda_3\lambda_4\lambda_4 + \lambda_2(\lambda_4\lambda_5 + \lambda_3(\lambda_4\lambda_5)))}{\lambda_4\lambda_5 + \lambda_3(\lambda_4+\lambda_5) + \lambda_2(\lambda_3+\lambda_4+\lambda_5) + \lambda_1(\lambda_2+\lambda_3+\lambda_4+\lambda_5)} \\
k_v &= -\frac{\lambda_3\lambda_4\lambda_5 + \lambda_2(\lambda_4\lambda_5 + \lambda_3(\lambda_4+\lambda_5))}{\lambda_4\lambda_5 + \lambda_3(\lambda_4+\lambda_5) + \lambda_2(\lambda_3+\lambda_4+\lambda_5) + \lambda_1(\lambda_2+\lambda_3+\lambda_4+\lambda_5)} \\
&\quad + \frac{\lambda_1(\lambda_4\lambda_5 + \lambda_3(\lambda_4+\lambda_5) + \lambda_2(\lambda_3+\lambda_4+\lambda_5))}{\lambda_4\lambda_5 + \lambda_3(\lambda_4+\lambda_5) + \lambda_2(\lambda_3+\lambda_4+\lambda_5) + \lambda_1(\lambda_2+\lambda_3+\lambda_4+\lambda_5)} \\
k_q &= \frac{\lambda_4\lambda_5 + \lambda_3(\lambda_4+\lambda_5) + \lambda_2(\lambda_3+\lambda_4+\lambda_5) + \lambda_1(\lambda_2+\lambda_3+\lambda_4+\lambda_5)}{t_d}
\end{aligned} \tag{4.27}$$

Where, λ_1 is given by:

$$\lambda_1 = -t_d - \lambda_2 - \lambda_3 - \lambda_4 - \lambda_5 \tag{4.28}$$

The order of the system (five) is higher than the number of control coefficients (four) and one pole is not directly placeable. Again, an optimal pole placement, in terms of response time, is calculated. The optimal pole $\lambda_o = -\frac{t_d}{5}$ is found replacing $\lambda_{1,\ldots,5} = \lambda_o$ in Eq. 4.28 and solving for λ_o.

4.5.3 Altitude Controller Coefficients

The control coefficient calculation for an altitude controller based on Eq. 4.11 is presented here, see Sec. 4.3.

Eq. 4.11 considers only the desired vertical acceleration $\dot{w}^*$ for the calculation of F_3^{MR} and therefore the desired vertical acceleration $\dot{w}^*$ is always realized[4], independent from the current orientation of the helicopter. As a result, the dynamic behavior of the helicopter, for vertical translation, becomes equivalent to the behavior of a double integrator.

Additionally, the aerodynamic generation of the force F_3^{MR} is a fast process compared to the generation of the angles φ and θ, which are needed for a horizontal translation, compare Sec. 4.3. Therefore, the time delay for the generation of F_3^{MR} is considered negligible small and is not included in the calculation of the control coefficients.

$$G = \frac{k_x s + k_i}{s^3 + k_v s^2 + k_x s + k_i} \tag{4.29}$$

The transfer function is given by Eq. 4.29, which describes a simple double integrator with a PID-feedback loop. Since the order of the system (three) equals the number of control coefficients (three) all poles are directly placeable, by solving the equation $\prod_{i=1}^{3}(s - \lambda_i) = \mathrm{den}(G)$ for the control coefficients K_i, K_v, K_x:

$$\begin{aligned} k_i &= -\lambda_1\lambda_2\lambda_3 \\ k_x &= \lambda_2\lambda_3 + \lambda_1(\lambda_2 + \lambda_3) \\ k_v &= -\lambda_1 - \lambda_2 - \lambda_3 \end{aligned}$$

In practice all three poles have been placed equally, which provided good flight performance.

4.5.4 Heading Controller Coefficients

The PI heading controller has only two coefficients, the proportional and the integral gain. The reasons for the simplicity of the controller are the fast and simple dynamics of the yaw-axis, as well as the utilization of an underlying hardware controller, see Sec. 4.2 for details. In practice the gain of the hardware controller is tuned in flight, using a slider

[4] Within the angular limits selected for the UAVs, and assuming that required main-rotor force can be generated.

or a rotary knob on the radio controller. After the hardware controller has been set, the heading controller coefficients are estimated. The manual selection of control coefficients is sufficient for this controller. Several flight experiments have shown, that this method is easy to conduct and provides very good results.

5 Modeling of Slung Load Systems

This chapter covers the modeling of slung load systems. Non-linear single-, dual- and multi-lift models, utilized for simulation, are presented and discussed in Sec. 5.1. The controller designs, presented in Ch. 6, are based on simplified models, which are described in Sec. 5.2. In Sec. 5.1.2 rope oscillations are analyzed, and a model of the Load Transportation Device, flexible rope and load is derived and validated. The results of this section are utilized in Sec. 6.6 for the design of a load motion observer.

5.1 Elaborated Models for Simulation

The non-linear slung load models, using one or multiple helicopters, are based on the *helicopter model* presented in Ch. 3. The single-lift slung load transportation model is derived in Sec. 5.1.1, using a set of independent, generalized coordinates. The dual- and multi-lift models are derived in Sec. 5.1.3, using a set of generalized coordinates and a set of constraints. In both cases the Kane method is used for the modeling and the software Autolev is used to generate the equations.

5.1.1 Model for Single-Lift Configurations

In this section the model for non-linear single-lift slung load configurations is presented. The *helicopter model* described in Ch. 3 is used as basis for the modeling. To avoid confusion, the non-linear model, of single-lift slung load configurations, is referenced as *single-lift model*. The *single-lift model* is based on two assumptions:

- The rope, connecting load and helicopter fuselage, is rigid and massless.
- The load can be simplified as a mass point.

The simplification of the rope is discussed in Sec. 5.1.2. The reduction of the load to a single mass point is justifiable for small size helicopters, since a typical load for a small size helicopter is small in surface and volume. Additionally, the contribution of the load rotation to the overall motion of the system is small, and the actual orientation of the load is not required for typical slung load transportation tasks. The air drag of the load is low, because of the load's small surface and the low towing speeds $\leq 50\,\mathrm{km/h}$. Therefore, the influence of the aerodynamics on the load is negligible as well.

The *single-lift model* developed in this section is described by eight independent generalized coordinates: Six generalized coordinates from the *helicopter model* and two generalized coordinates, which describe the position of the load. The unattached load mass

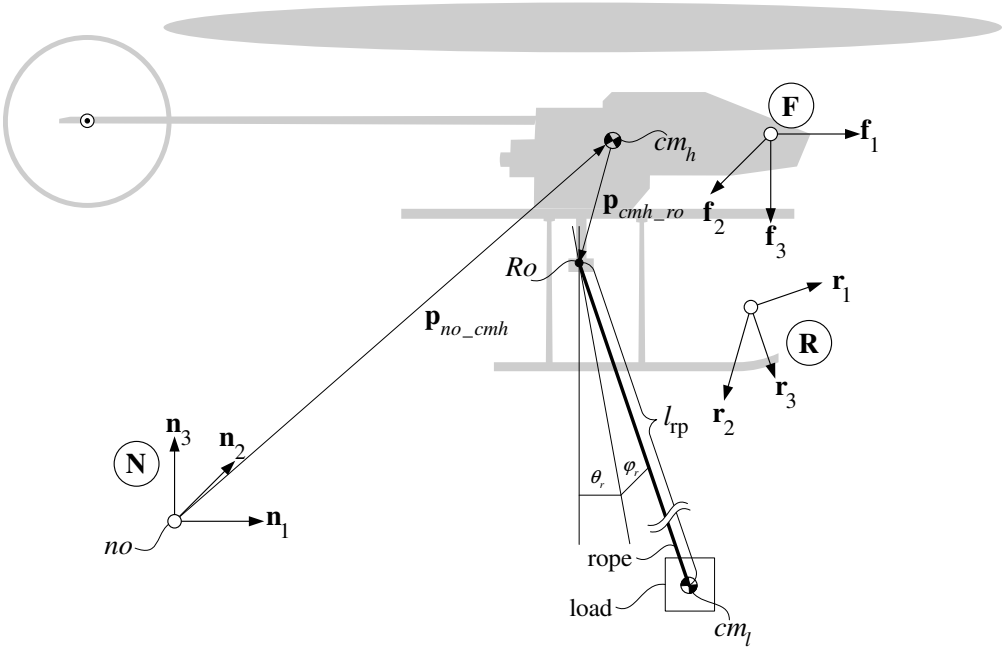

Figure 5.1: Single-lift configuration

point has three DoF and needs to be described by three independent coordinates. However, a rigidly modeled rope is connecting helicopter fuselage and load. This restricts the load to a spherical motion around the load mounting point *Ro*, see Fig. 5.1, with an radius equal to the rope length. The position of the load is therefore completely described by two independent generalized coordinates, the two angles θ_r, φ_r, and by the constant rope length l_{rp}.

The *single lift model* is composed of a rigid body for the fuselage F, a rigid body for the main-rotor *MR* and a mass point for the load. The kinematics of the helicopter are directly taken from the *helicopter model*. The position and velocity of the helicopter's CoM are given by

$$\mathbf{p}_{no\_cmh} = x\,\mathbf{n}_1 + y\,\mathbf{n}_2 + z\,\mathbf{n}_3 \tag{5.1}$$

$$\frac{d^{\mathbf{N}}\mathbf{p}_{no\_cmh}}{dt} = \dot{x}\,\mathbf{n}_1 + \dot{y}\,\mathbf{n}_2 + \dot{z}\,\mathbf{n}_3 = u\,\mathbf{n}_1 + v\,\mathbf{n}_2 + w\,\mathbf{n}_3 \tag{5.2}$$

The orientation of the fuselage frame, **F** relative to the inertial frame **N**, is described by the Euler angles 321 (ψ, θ, φ). The angular velocity of the fuselage frame is described, relative to the inertial frame **N**, by the angular speeds (p, q, r):

$$\omega_{\mathbf{F}-\mathbf{N}} = p\,\mathbf{f}_1 + q\,\mathbf{f}_2 + r\,\mathbf{f}_3 \tag{5.3}$$

Like discussed above, the position of the load is determined by the orientation of the rope and the rope length l_{rp}, where the orientation of the rope is completely described

by two angles. Within this thesis two different kinematic definitions of those angles are used, and one model variant is created for each kinematic definition. Both model variants introduce a new frame $\mathbf{R}$, see Fig. 5.1, whose basis vector $\mathbf{r}_3$ describes the orientation of the rope. Independent from the chosen definition the position of the load is described by

$$\mathbf{p}_{no\_cml} = \mathbf{p}_{no\_cmh} + \mathbf{p}_{cmh\_ro} + l_{rp}\,\mathbf{r}_3 \tag{5.4}$$

The vector $\mathbf{p}_{cmh\_ro}$ connects the helicopter's CoM and the rope connection point Ro, see Fig. 5.1. The position of the rope connection point Ro is defined relative to the reference point O:

$$\mathbf{dORo} = dORo_1\,\mathbf{f}_1 + dORo_2\,\mathbf{f}_2 + dORo_3\,\mathbf{f}_3 \tag{5.5}$$

The vector $\mathbf{p}_{cmh\_ro}$ is therefore described by

$$\mathbf{p}_{cmh\_ro} = \mathbf{dORo} - \mathbf{dOcm} \tag{5.6}$$

The definitions of the reference point O and the vector $\mathbf{dOcm}$ are given in Sec. 3.1.

The first model variant defines the orientation of the frame $\mathbf{R}$ relative to the helicopter fuselage frame $\mathbf{F}$, using the two angles θ_r^F and φ_r^F. The rotation around the lateral axis of the fuselage $\mathbf{f}_2$ is denoted by θ_r^F and the rotation around the changed longitudinal axis $\mathbf{f}_1'$ is described by φ_r^F. The rotation matrix $\mathbf{C_{R-F}}$ of the frame $\mathbf{R}$, relative to the helicopter fuselage frame $\mathbf{F}$, is therefore described by

$$\mathbf{C_{R-F}} = \mathrm{R}_{\mathbf{f2}}(\theta_r^F)\,\mathrm{R}_{\mathbf{f'1}}(\varphi_r^F) \tag{5.7}$$

$$= [\mathbf{r}_1\,\mathbf{r}_2\,\mathbf{r}_3] \tag{5.8}$$

Where $\mathbf{r}_{1,2,3}$ are the basis vectors of the frame $\mathbf{R}$. The angular speeds $p_r^F = \dot{\varphi}_r^F$, $q_r^F = \dot{\theta}_r^F$ of the frame $\mathbf{R}$ are used to calculate the angular velocity vector $\omega_{\mathbf{R-F}}$:

$$\omega_{\mathbf{R-F}} = \left(\left(\frac{d^{\mathbf{F}}\mathbf{r}_2}{dt}\cdot\mathbf{r}_3\right)\mathbf{r}_1 + \left(\frac{d^{\mathbf{F}}\mathbf{r}_3}{dt}\cdot\mathbf{r}_1\right)\mathbf{r}_2 + \left(\frac{d^{\mathbf{F}}\mathbf{r}_1}{dt}\cdot\mathbf{r}_2\right)\mathbf{r}_3\right) \tag{5.9}$$

$$= -p_r^F\,\mathbf{r}_1 - \cos(\varphi_r^F)\,q_r^F\,\mathbf{r}_2 + \sin(\varphi_r^F)\,q_r^F\,\mathbf{r}_3 \tag{5.10}$$

Two advantages justify the development of this model variant. The first advantage is, that the angles θ_r^F and φ_r^F provide a one-to-one correspondence to the angles physically measured by the LTD. Therefore, a direct comparison between simulated and measured angles is possible.

The rope force vector $\mathbf{F}^R = F^R\,\mathbf{r}_3$ is needed for the orientation controller proposed in Sec. 6.2. The measured magnitude of the force within the rope is denoted by F^R and the orientation of the force vector is described by $\mathbf{r}_3$. It should be noted that the orientations of the rope and force are equal, see Fig. 5.1. The orientation controller requires the vector $\mathbf{F}^R$ to be expressed in coordinates of the fuselage frame $\mathbf{F}$. Since $\mathbf{R}$ is defined relative to $\mathbf{F}$ for this model variant, the coordinates of $\mathbf{F}^R$ in $\mathbf{F}$ are directly calculable from θ_r^F and φ_r^F, without considering the orientation of $\mathbf{F}$. The simplification of this calculation is the second advantage of this model.

The second model variant defines the orientation of the frame $\mathbf{R}$ relative to the Newtonian frame $\mathbf{N}$, using the two angles θ_r^N and φ_r^N. The orientation of $\mathbf{R}$ relative to $\mathbf{N}$ is expressed by

$$\begin{aligned} \mathbf{C}_{\mathbf{R-N}} &= \mathrm{R}_{\mathbf{n3}}(\pi)\,\mathrm{R}_{\mathbf{n'2}}(\pi+\theta_r^N)\,\mathrm{R}_{\mathbf{n''1}}(\varphi_r^N) && (5.11)\\ &= [\mathbf{r}_1\,\mathbf{r}_2\,\mathbf{r}_3] && (5.12)\end{aligned}$$

The two constant rotations about π radian cause the frame $\mathbf{R}$ to coincide with the frame $\mathbf{F}$ for φ_r^N, $\theta_r^N = 0$ and φ, θ, $\psi = 0$.

The angular speeds $p_r^N = \dot{\varphi}_r^N$, $q_r^N = \dot{\theta}_r^N$ of the frame $\mathbf{R}$ are used to calculate the angular velocity vector $\omega_{\mathbf{R-N}}$:

$$\begin{aligned} \omega_{\mathbf{R-N}} &= \left(\left(\frac{d^{\mathbf{N}}\mathbf{r}_2}{dt}\cdot\mathbf{r}_3\right)\mathbf{r}_1 + \left(\frac{d^{\mathbf{N}}\mathbf{r}_3}{dt}\cdot\mathbf{r}_1\right)\mathbf{r}_2 + \left(\frac{d^{\mathbf{N}}\mathbf{r}_1}{dt}\cdot\mathbf{r}_2\right)\mathbf{r}_3\right) && (5.13)\\ &= p_r^N\,\mathbf{r}_1 + \cos(\varphi_r^N)\,q_r^N\,\mathbf{r}_2 - \sin(\varphi_r^N)\,q_r^N\,\mathbf{r}_3 && (5.14)\end{aligned}$$

This second model variant has one mayor advantage. The kinematic definition is equal to the one used for the simplified models presented in Sec. 5.2.2. For these simplified models the fuselage reduces to a single mass point. These models consider neither the fuselage orientation, nor the fuselage frame $\mathbf{F}$. Therefore, the kinematic definition of the first model variant is not applicable to the simplified models.

The following concludes the discussion of the two model variants: Although the kinematic definitions of both model variants are different, they describe the same physical system and are considered to be equivalent. The angles $(\theta_r^F,\, \varphi_r^F)$ are convertible to $(\theta_r^N,\, \varphi_r^N)$ and vice versa using simple trigonometric calculations. Both definitions of load angles are used in this work. The angles $(\theta_r^F,\, \varphi_r^F)$ are used within the orientation controller described in Sec. 6.2 and the angles $(\theta_r^N,\, \varphi_r^N)$ are used within the simplified models presented in in Sec. 5.2.2 and the translation controller derived in Sec. 6.3.

The second model variant is described in the remainder of this section, since the generated dynamic equations are simpler and easier to analyze. The angles and the angular speeds $(\theta_r^N,\, \varphi_r^N,\, p_r^N,\, q_r^N)$ and $(\theta_r,\, \varphi_r,\, p_r,\, q_r)$ are now used synonymously. Therefore, the state vector for the *single-lift model* is defined to be

$$\mathbf{X} = [x, y, z, \varphi, \theta, \psi, \varphi_r, \theta_r, u, v, w, p, q, r, p_r, q_r]^t \tag{5.15}$$

And the kinematic equations of the *single-lift model* are listed below:

$$\begin{aligned} \dot{x} &= u\\ \dot{y} &= v\\ \dot{z} &= w\\ \dot{\varphi} &= p + \tan(\theta)(q\sin(\varphi) + r\cos(\varphi))\\ \dot{\theta} &= q\cos(\varphi) - r\sin(\varphi)\\ \dot{\psi} &= (q\sin(\varphi) + r\cos(\varphi))\sec(\theta)\\ \dot{\varphi}_r &= p_r\\ \dot{\theta}_r &= q_r \end{aligned} \tag{5.16}$$

Similar to the *helicopter model*, the dynamic equations of the *single-lift model* are derived using the Kane method. Unfortunately, different to the *helicopter model,* the dynamic equations are very large and their presentation is not possible here. The result of the Kane method is not a set of explicit dynamic equations, but a set of equations, which contain the derivatives of the generalized speeds in linear form. These equations need to be solved for the derivatives of the generalized speeds to obtain the explicit form. The implicit equations of both variants are presented in the additional equations document, which is accompanying this thesis on CD, see [Ber13, page 9ff.] and [Ber13, page 16ff.] respectively.

For the *helicopter model* the Kane method provides six equations, which create two independent groups of three equations. One group includes only the translation dynamics and one group includes only the rotation dynamics of the helicopter. Both groups are solved independently for the explicit equations of the rotation and translation dynamics. This causes the dynamic equations to be very compact.

In anticipation of the analysis in Sec. 6.1 it is stated, that the attachment of a slung load, in a point different from the helicopter's CoM, creates a mutual coupling between the rotation and translation dynamics. Therefore, the equations generated for the *single-lift model*, are highly coupled. It is possible to derive an explicit solution from these equations, but the coupling causes the resulting dynamic equations to be very large.

However, to provide at least some insights in the dynamics of the *single-lift model*, the equations are generated under the assumption that the CoMs of the fuselage and the main-rotor are aligned. Therefore, the vectors **dOMRo** and **dOFo** are both zero vectors, compare Sec. 3.1 for a detailed explanation of these vectors. To improve clearness the drag torques T_3^{MR} and T_2^{TR} are neglected, preserving only the control inputs: The main-rotor force F_3^{MR}, the tail-rotor force F_2^{MR} and the main-rotor torques $T_{1,2}^{MR}$.

The following equations are generated by Kane method for the simplified *single-lift model*:

$$
\begin{aligned}
0 &= F_3^{MR}\,(s_\theta c_\varphi c_\psi - s_\varphi s_\psi) + F_2^{TR}\,(s_\psi c_\varphi + s_\varphi s_\theta c_\psi) - \dot{u}\,(m_F + m_{MR}) \\
&\quad -m_L\,\zeta_1(\dot{u},\,\dot{p},\,\dot{q},\,\dot{r},\,\dot{p}_r,\,\dot{q}_r) && (5.17)\\
0 &= F_3^{MR}\,(s_\theta s_\psi c_\varphi + s_\varphi c_\psi) - F_2^{TR}\,(c_\varphi c_\psi - s_\varphi s_\theta s_\psi) - \dot{v}\,(m_F + m_{MR}) \\
&\quad -m_L\,\zeta_2(\dot{v},\,\dot{p},\,\dot{q},\,\dot{r},\,\dot{p}_r,\,\dot{q}_r) && (5.18)\\
0 &= F_3^{MR}\,(c_\varphi c_\theta) - F_2^{TR}\,(s_\varphi c_\theta) - g\,(m_F + m_{MR}) - \dot{w}\,(m_F + m_{MR}) \\
&\quad -m_L\,\zeta_3(\dot{w},\,\dot{p},\,\dot{q},\,\dot{r},\,\dot{p}_r,\,\dot{q}_r) && (5.19)\\
0 &= T_1^{MR} - (I_{11}^F + I_{11}^{MR})\,\dot{p} - q\,r\,(I_{11}^{MR} - I_{22}^F + I_{33}^F) - q\,(I_{33}^{MR}\,\omega_{MR}) \\
&\quad -m_L\,\zeta_4(\dot{u},\,\dot{v},\,\dot{w},\,\dot{p},\,\dot{q},\,\dot{r}\,\dot{p}_r,\,\dot{q}_r) && (5.20)\\
0 &= T_2^{MR} - (I_{22}^F + I_{11}^{MR})\,\dot{q} + p\,r\,(I_{11}^{MR} - I_{11}^F + I_{33}^F) + p\,(I_{33}^{MR}\,\omega_{MR}) \\
&\quad -m_L\,\zeta_5(\dot{u},\,\dot{v},\,\dot{w},\,\dot{p},\,\dot{q},\,\dot{r}\,\dot{p}_r,\,\dot{q}_r) && (5.21)\\
0 &= F_2^{TR}\,dOT_1 + p\,q\,(I_{11}^F - I_{22}^F) - \dot{r}\,(I_{33}^F + I_{33}^{MR}) \\
&\quad -m_L\,\zeta_6(\dot{u},\,\dot{v},\,\dot{w},\,\dot{p},\,\dot{q},\,\dot{r}\,\dot{p}_r,\,\dot{q}_r) && (5.22)\\
0 &= -m_L\,\zeta_7(\dot{u},\,\dot{v},\,\dot{w},\,\dot{p},\,\dot{q},\,\dot{r},\,\dot{p}_r,\,\dot{q}_r) && (5.23)\\
0 &= -m_L\,\zeta_8(\dot{u},\,\dot{v},\,\dot{w},\,\dot{p},\,\dot{q},\,\dot{r},\,\dot{p}_r,\,\dot{q}_r) && (5.24)
\end{aligned}
$$

The functions $\zeta_{1\ldots8}$ are linear in their arguments and incorporate the model constants and the system state coordinates, without x, y, z. Three important insights are won from the equations:

First, the number of equations reduces to six, if the mass of the load m_L is assumed to be zero, since Eqs. 5.23-5.24 become zero. Solving Eqs. 5.17-5.19 for $(\dot{u},\,\dot{v},\,\dot{w})$ and Eqs. 5.20-5.22 for $(\dot{p},\,\dot{q},\,\dot{r})$, the resulting equations constitute the explicit dynamic equations of the *helicopter model*. This is an expected outcome, since the *single-lift model* should behave equal to the *helicopter model*, if no load is attached ($m_L = 0$).

Second, assuming $dORo_{1,2} = 0$ and $\mathbf{dOMRo} = \mathbf{dOFo} = \mathbf{0}$, the function ζ_6 becomes zero and Eqs. 5.17-5.21 and Eqs. 5.23-5.24 become independent of $\dot{r}$. Therefore, the load attachment has no direct influence on the generation of the angular speed r. Solving for $\dot{r}$, Eq. 5.22 becomes equivalent to Eq. 3.23 of the *helicopter model*. This causes the generation of the angular speed r to be equal for *helicopter model* and *single-lift model*. In Sec. 4.2 this equation serves, together with the kinematic equation of the yaw angle, which is equal for both models as well, as justification for the decoupling of the heading $(r,\,\psi)$ and orientation control $(p,\,q,\,\theta,\,\varphi)$. The equation shows, that the generation of r depends mainly on F_2^{TR} for small angular speeds p, q. Additionally, the kinematic equations show, that the generation of yaw angle depends mainly on the angular speed r for small pitch and roll angles. Therefore, the decoupling of heading (yaw-angle) and orientation (pitch-roll-angles) is as well feasible for the *single-lift model*. This is even valid under the less constraining assumption $dOMRo_{1,2} = dOFo_{1,2} = dORo_{1,2} = 0$. In this configuration the CoM of main-rotor and fuselage and the rope mounting point are all located within the rotation axis of the main-rotor. It should be mentioned, that this is a very common configuration. To improve the flight performance, pilots of small size

helicopters manually adjust the fuselage's CoM cm_F and locate it within the rotation axis of the main-rotor. The helicopters, used for all slung load experiments described in this thesis, satisfy this configuration.

Third, all equations are highly coupled through the functions $\zeta_{1...8}$. To derive explicit dynamic equations in a reduced form, the slung load rope is assumed to be attached in the helicopter's CoM with $\mathbf{dORo} = \mathbf{0}$. This limits the influence of the load to the translation dynamics of the model and causes $\zeta_{4,5,6}$ to become zero. Additionally, the functions $\zeta_{1,2,3}$ and $\zeta_{7,8}$ become independent from $(\dot{p},\, \dot{q},\, \dot{r})$, which is beneficial for the calculation of explicit equations. In general, Eqs. 5.17-5.24 are not modified by the simplification, except their functions $\zeta_{1...8}$. Based on these insights the simplified Eqs. 5.20-5.22 are solved for $(\dot{p},\, \dot{q},\, \dot{r})$, and the simplified Eqs. 5.17-5.19,5.23,5.24 are solved for $(\dot{u},\, \dot{v},\, \dot{w},\, \dot{p}_r,\, \dot{q}_r)$. This results into the following explicit equations:

$$\begin{aligned}
\dot{u} &= \Big(F_3^{MR}\,(s_\theta c_\varphi c_\psi - s_\varphi s_\psi) + l_{rp}\,m_l(s_{\varphi r} s_{\theta r}\dot{p}_r - c_{\varphi r} c_{\theta r}\dot{q}_r \\
&\quad +2\,p_r\,q_r\,s_{\varphi r} c_{\theta r} + (p_r^2 + q_r^2)\,s_{\varphi r} c_{\theta r})\Big)/m && (5.25)\\
\dot{v} &= \Big(F_3^{MR}\,(s_\theta s_\psi c_\varphi + s_\varphi c_\psi) + l_{rp}\,m_l(p_r^2\,s_{\varphi r} - c_{\varphi r}\dot{p}_r)\Big)/m && (5.26)\\
\dot{w} &= \Big(F_3^{MR}\,c_\varphi c_\theta - g\,(m_F + m_{MR}) + l_{rp}\,m_l(-s_{\varphi r} c_{\theta r}\dot{p}_r - c_{\varphi r} s_{\theta r}\dot{q}_r \\
&\quad +2\,p_r\,q_r\,s_{\varphi r} s_{\theta r} - (p_r^2 + q_r^2)\,c_{\varphi r} c_{\theta r})\Big)/m && (5.27)\\
\dot{p} &= \Big(T_1^{MR} - \omega\,q\,I_{33}^{MR} + q\,r\,(I_{22}^F - I_{33}^F - I_{11}^{MR})\Big)/(I_{11}^F + I_{11}^{MR}) && (5.28)\\
\dot{q} &= \Big(T_2^{MR} + \omega\,p\,I_{33}^{MR} + p\,r\,(-I_{11}^F + I_{33}^F + I_{11}^{MR})\Big)/(I_{22}^F + I_{11}^{MR}) && (5.29)\\
\dot{r} &= \Big(F_2^{TR}\,dOT_1 + p\,q\,(I_{11}^F - I_{22}^F)\Big)/(I_{33}^F + I_{33}^{MR}) && (5.30)\\
\dot{p}_r &= -F_3^{MR}\Big(-c_\psi c_{\varphi r} s_\varphi - c_\varphi c_{\varphi r} s_\theta s_\psi + c_\varphi c_\theta c_{\theta r} s_{\varphi r} \\
&\quad +c_\varphi c_\psi s_\theta\, s_{\varphi r} s_{\theta r} - s_\varphi s_\psi\, s_{\varphi r} s_{\theta r}\Big)/l_{rp}(m_F + m_{MR}) + q_r^2 c_{\varphi r} s_{\varphi r} && (5.31)\\
\dot{q}_r &= F_3^{MR}\Big(c_{\theta r} s_\varphi s_\psi/c_{\varphi r} + c_\varphi/c_{\theta r}(-c_\psi c_{\theta r} s_\theta + c_\theta s_{\theta r})\Big) \\
&\quad /l_{rp}(m_F + m_{MR}) + 2\,p_r\,q_r\,s_{\varphi r}/c_{\varphi r} && (5.32)
\end{aligned}$$

Where m denotes the mass of the complete system, with $m = m_{MR}+m_F+m_L$. Eqs. 5.25-5.27 depend on $\dot{p}_r$ and $\dot{q}_r$. However, after the substitution of $\dot{p}_r$ and $\dot{q}_r$ by Eqs. 5.31-5.32 an independent solution is derived. To obtain a compact set of equations this last step has been omitted.

Eq. 5.30 describes the generation of the angular speed r, where the tail-rotor force F_2^{TR} is considered the exclusive control input, see Sec. 4.2. Therefore, the influence of F_2^{TR} on the translation of the helicopter or the load motion is considered to be a disturbance. The magnitude of the disturbance corresponds to approximately 10 % of the main-rotor force, but several flight experiments have shown, that a controller based compensation of this disturbance is feasible. Therefore, the force F_2^{TR} has been neglected in Eqs. 5.25-5.27 and Eqs. 5.31-5.32 to reduce complexity.

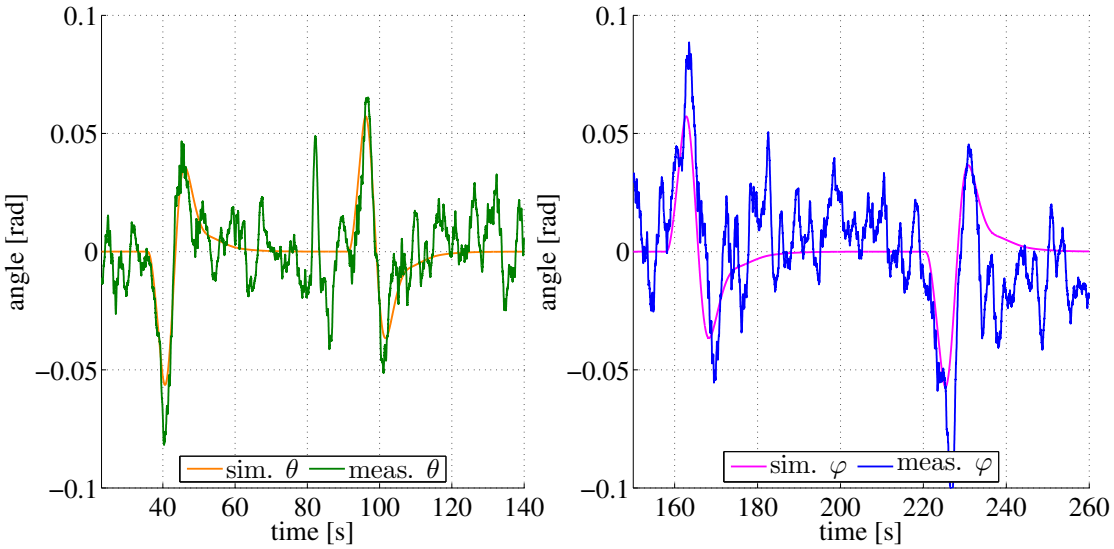

Figure 5.2: Orientation comparison: Non-linear model and real flight data (28.11.2007)

Eqs. 5.28-5.30 describe the generation of the angular speeds (p, q, r). The equations are independent from the translation of the helicopter or the motion load, since the rope is attached in the helicopter's CoM. Therefore, the equations are equivalent[1] to the rotation dynamics of the *helicopter model*, described by Eqs. 3.21-3.23.

The translation of the helicopter, described by Eqs. 5.25-5.27, and the motion of the load, described by Eqs. 5.31-5.32, are directly coupled to the main-rotor force F_3^{MR}. Like discussed in Sec. 4.3, the main-rotor force F_3^{MR} is used to generate the desired acceleration of the helicopter. This implies, that a translation controller for the *single-lift model* should incorporate the translation of the helicopter, as well as the motion of the load. This is utilized in Sec. 6.3, during the design of the translation controller for the single-lift configuration.

Model Validation The *single-lift model*, without simplifications, is validated against flight data. Without controller the *single-lift model* and the physical system are unstable. Therefore, the systems are evaluated with orientation and translation controller, and equal controllers and controller coefficients are used for both systems:

The generic orientation controller, derived in Sec. 6.2, and the translation controller for the single-lift configuration, derived in Sec. 6.3, are used for this validation. The parameters of the *single-lift model* have been chosen to match the real system as close as possible. The parameters of the helicopter are described in Sec. 2 and the coupled system is presented in the second experiment of Sec. 7.1. The flight data of the experiment is used as reference for the validation. To produce comparable simulation results, the desired trajectory of the experiment has been applied to the simulation.

[1] Eqs. 3.21-3.23 are more complex, but under the assumption $\mathbf{dOMRo} = \mathbf{dOFo} = \mathbf{0}$ they are equal.

The helicopter executed two steps of ±20 m along the two horizontal axis of a Newtonian reference frame **N**. The basis vectors of **N** are aligned as follows: $\mathbf{n}_1$ is pointing from South to North, $\mathbf{n}_2$ is pointing from East to West, $\mathbf{n}_3$ points upwards. The helicopter executed the first step about +20 m along $\mathbf{n}_1$ and back, and the second step about −20 m along $\mathbf{n}_2$ and back. The heading of the helicopter was fixed during the whole experiment and the helicopter's nose pointed north. For this heading the yaw angle ψ is equal to zero radian.

Like already discussed in Sec. 4.3, the force F_3^{MR}, which is approximately perpendicular to the main-rotor disc, is used to accelerate the helicopter. Assuming a yaw angle of zero radian and using the small angle approximation $\cos(\alpha) = 1$, for small angles α, Eqs. 5.25-5.26 simplify to:

$$\dot{u} = \Big(F_3^{MR}\, s_\theta + l_{rp}\, m_l(\dots)\Big)/m \tag{5.33}$$

$$\dot{v} = \Big(F_3^{MR}\, s_\varphi + l_{rp}\, m_l(\dots)\Big)/m \tag{5.34}$$

The terms multiplied by rope length and load mass (l_{rp}, m_l) describe the influence of the load on the helicopter's acceleration along $\mathbf{n}_{1,2}$. These terms are considered to be disturbances, which are compensated by the translation controller. A translation along $\mathbf{n}_1$ is therefore caused mainly by the force F_3^{MR} and the pitch angle θ and a translation along $\mathbf{n}_2$ is caused mainly by the force F_3^{MR} and the roll angle φ of the helicopter. For that reason Fig. 5.2 is split into two graphs. The left graph shows only the "pitch motion" during the first step and the right graph shows only the "roll motion" during the second step. This focuses on the angles important for the respective translational motion of the helicopter. This improves the clearness of the graphs, since the measured pitch and roll angles exhibit strong disturbances, caused by external influences, like wind, and measurement noise, e.g. caused by engine vibrations.

In Fig. 5.2 the measured pitch and roll angles are compared to the pitch and roll angles of the simulation. The static offsets of the measured angles have been removed to simplify a comparison to the simulated angles. The measured pitch angles exhibit less disturbances compared to the measured roll angles. An explanation is the higher inertia of the fuselage around the lateral axis. The average disturbances of both angles, ±0.02 rad pitch and ±0.03 rad roll, are still considered to be small. The disturbances are not present in the simulation, since they are caused by external influences like wind, which are unknown and unpredictable. However, during the execution of the flight steps, in the intervals [35 s, 65 s] and [90 s, 120 s], the correspondence between the pitch angles is clearly visible. Even during stronger disturbances of the measured angles, especially in the intervals [155 s, 185 s] and [220 s, 250 s], the correspondence between simulated and measured angles is clear to see. Therefore, simulated and measured angles show good correspondence generally.

The heading of the helicopter, described by the yaw angle ψ, has not been plotted for two reasons: First, the load attachment has almost no influence on heading of the helicopter, see discussion above and Eqs. 5.16, Eq. 5.30. Second, during the experiment neither a change in the desired heading, nor a major deviation of the measured heading, has occurred.

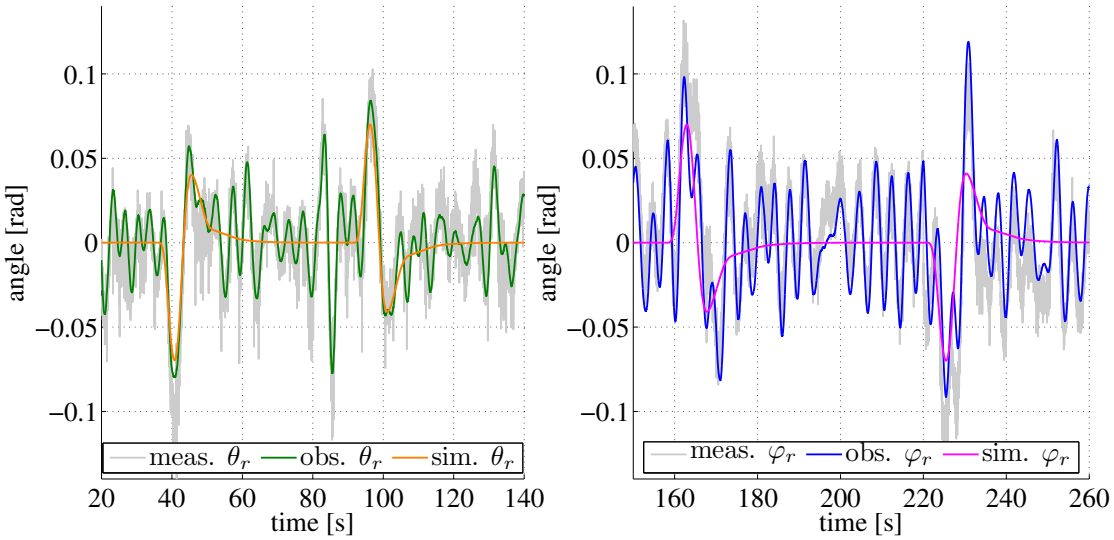

Figure 5.3: Load motion comparison - Non-linear model and real flight data (28.11.2007)

Fig. 5.3 shows a different result of the same experiment, where the measured and simulated load angles are compared. Unfortunately, the measured angles are very noisy and therefore an observer is used to estimate almost noise free angles. The observer is described in Sec. 6.6. The noise is caused by an oscillation of LTD and rope. The frequency of the noise is much higher than oscillation frequency of the load position, see Sec. 5.1.2 for a detailed explanation. This indicates, that the observed angles rather reflect true motion of the load than the measured angles. This has also been confirmed visually during the experiments, where the load moved slow and steady. Since no reference measurement of the load position is available, the observed angles are used to estimate the disturbance of the load motion. The average disturbance of both angles is considered to be small, about ± 0.04 rad for the pitch and ± 0.05 rad for the roll angle. A disturbance of ± 0.05 rad is equivalent to a disturbance of the load position of approximately ± 0.25 m, considering a rope length of 5 m.

A translation of the helicopter along $\mathbf{n}_1$ creates a load displacement along the same axis, which changes only the load pitch angle θ_r. The same is valid for a translation along $\mathbf{n}_2$ and the load roll angle φ_r. To improve clearness Fig. 5.3 is split into two graphs, similar to Fig. 5.2. The static offsets of the measured angles have been removed to simplify a comparison between observed and simulated angles. Like explained above, the disturbances and the noise are caused by external influences. During the execution of the flight steps, in the intervals [35 s, 65 s], [90 s, 120 s], [155 s, 185 s] and [220 s, 250 s], the correspondence between measured, observed and simulated angles is clearly visible.

To conclude this section the important results are summarized. The rotation dynamic of the *single-lift model* is highly coupled to the translation dynamic of helicopter and load, unless the rope of the slung load is directly attached in the helicopter's CoM. In this case the rotation dynamics of *single-lift model* and *helicopter model* are equivalent. This is an

expected, but important outcome, which completely coincides with the considerations of Sec. 6.1. The translation of the helicopter and the motion of the load are highly coupled, independent from the placement of the rope attachment point. Therefore, a translation controller needs to incorporate the translation of helicopter and load. Assuming the configuration $dOMRo_{1,2} = dOFo_{1,2} = dORo_{1,2} = 0$ and small pitch and roll angles (θ, φ), the attachment of a slung load has almost no influence on the generation of the angular speed r and the yaw angle ψ. This justifies a separate control of the heading ψ and remaining orientation angles (θ, φ). The helicopters for all presented slung load experiments satisfy this configuration, which is very common. The developed model has been validated using flight data. The author considers the correspondence between physical system and model to be good.

5.1.2 Modeling of the Rope

In this section the internal rope motion and the influence of the LTD on the measurement itself are investigated. The section is composed of two parts:

First, the motion of a slung load with one DoF is analyzed, under the condition that the ropes are approximated to be rigid and massless. The expected oscillation frequencies of idealized and roll-pendulum are derived and compared. The results of this first section are required for the validation of the model derived in the second section and in Sec. 6.6 for the design of the rope motion observer.

Second, a rope model is developed and validated in laboratory experiments. The model is designed to reflect the internal motion of the rope, as well as the motion of LTD and load. It is required for three purposes: First, to confirm that random oscillations, which were witnessed during several flight experiments, are caused by internal rope oscillations. Second, to predict the system behavior for different system parameters. This allows to estimate the rope oscillation sensitivity of a particular configuration. Additionally, it allows to search for configurations, which are robust against rope oscillations. Third, to investigate the usability of the model for the design of a rope motion observer. Additionally, this answers the question, whether or not it is possible to reconstruct the whole state of LTD, rope and load, using only the measured angles of the LTD.

Rigid Rope Models All presented slung load models are based on two assumptions. The ropes used for the load transportation are approximated to be massless and rigid, and the LTD, used for the measurement of the rope orientation, has no influence on the rope motion. Based on these assumptions the rope motion is approximated using the *roll-pendulum model* presented in Sec. 5.2.2. This motion analysis considers only one dimensional pendulum motion and only Eq. 5.94 is therefore taken from the dynamic equations of *roll-pendulum model*. The model is linearized using a small angle approximation with $\sin(\theta) = \theta$, $\sin(\theta)^2 = 0$ and $\cos(\theta) = 1$. To simplify the result q is eliminated from the equation, using the kinematic definition $\dot{\theta} = q$, see Eqs. 5.87:

$$\ddot{\theta} \;=\; \frac{-g\,(m_h + m_l)}{l\,m_h}\,\theta \tag{5.35}$$

A closed form solution of Eq. 5.35 is calculated:

$$\theta = C_1 \cos\left(\sqrt{\frac{g\,(m_h + m_l)}{l\,m_h}}\,t\right) + C_2 \sin\left(\sqrt{\frac{g\,(m_h + m_l)}{l\,m_h}}\,t\right) \tag{5.36}$$

Eq. 5.35 describes a harmonic oscillation, whose natural frequency is given by:

$$\omega_{rpd} = \sqrt{\frac{g\,(m_h + m_l)}{l\,m_h}} = \sqrt{\frac{g}{l}\left(\frac{m_l}{m_h} + 1\right)} \tag{5.37}$$

The natural frequency of the roll-pendulum therefore depends on the gravitational constant g, the rope length l and m_l/m_h, the load mass to helicopter mass ratio. Using typical parameters ($g \simeq 9.81\,\mathrm{m/s^2}$, $l = 5\,\mathrm{m}$, $m_l = 1.1\,\mathrm{kg}$, $m_l = 13\,\mathrm{kg}$) of a single-lift configuration presented in the experimental validation, see Sec. 7.1, the natural frequency of the roll-pendulum is $\omega_{rpd} = 1.46\,\mathrm{rad/s} = 0.46\,\mathrm{Hz}$. For this configuration the load mass is approximately 12 times smaller than the helicopter mass and therefore the ratio m_l/m_h is quite close to zero. Based on this outcome an estimate of the natural frequency for $m_l/m_h = 0$ seems feasible and therefore the limit for an infinite helicopter mass is calculated:

$$\lim_{m_h \to \infty} \omega_{rpd} = \lim_{m_h \to \infty} \sqrt{\frac{g}{l}\left(\frac{m_l}{m_h} + 1\right)} = \sqrt{\frac{g}{l}} = \omega_{pend} \tag{5.38}$$

Eq. 5.38 shows, that the natural frequency of the roll-pendulum becomes equals to the natural frequency of an idealized pendulum, for an infinite helicopter mass. The natural frequency of an idealized pendulum depends only on the earth acceleration g and the length of the pendulum l. Similar parameters, to those used for the natural frequency calculation of the roll-pendulum, are used to determine the natural frequency of the idealized pendulum. The resulting frequency is $\omega_{pend} = 1.40\,\mathrm{rad/s} = 0.445\,\mathrm{Hz}$. The result is almost equal to the natural frequency of the roll-pendulum, since the load mass to helicopter mass ratio m_l/m_h is close to zero. However, for higher load masses the difference between both frequencies increases.

The idealized pendulum approximation of the system composed of helicopter, rope and load is only valid, if the mounting point of the pendulum is not able to move. Since the rope is attached to the helicopter fuselage, an oscillation of the load imposes torques and forces on the helicopter, see the discussion in Sec. 6.1. In anticipation of Sec. 6.2 it is stated, that the influence of the pendulum on the helicopter orientation is compensated by the orientation controller, utilizing a feed-forward torque compensator. The influence of the load reduces to a force, which is attacking in the CoM of the helicopter. This force accelerates the helicopter and needs to be compensated by the translation controller. In anticipation of the results presented in Sec. 7.1 it is stated, that the translation controllers are able to compensate this force. As a result, the idealized pendulum approximation is assumed to be valid for the system composed of helicopter, rope and load. This insight is used for the design of the load motion observer in Sec. 6.6.

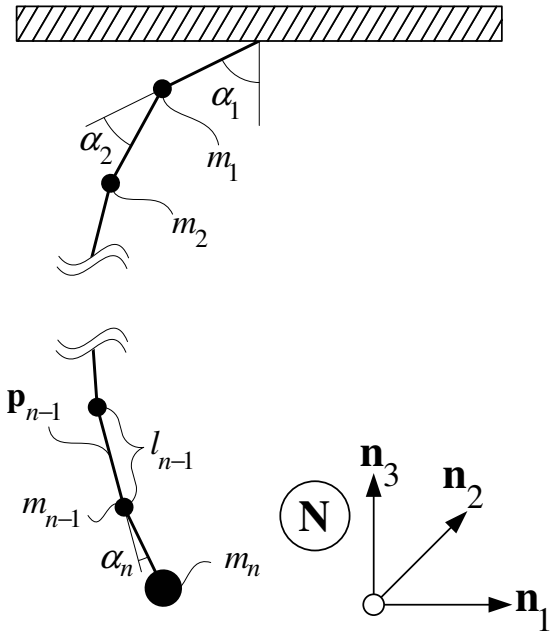

Figure 5.4: Simple flexible rope model

Flexible Rope Model For the following subsection the assumptions, that the ropes are rigid and massless and the measurement is not influenced by the LTD, are annulled. Before the development of the model, the internal motion of the rope needs to be investigated. Most of the time the rope is taut between the helicopter fuselage and the load, similar to the string of a music instrument. An external disturbance can therefore stimulate an internal oscillation of the rope. The load position and velocity are estimated from the angles measured by the LTD and therefore the oscillation leads to deviations of the load's position estimation. This is a serious problem for the controller. A good prediction of the load motion is of vital importance for the translation controllers of single- and dual-lift configurations. For low oscillation frequencies the controller, presented in Sec. 6.3, reacts on these position and velocity deviations. This reaction can stimulate further rope oscillations and the whole system can become unstable.

Multiple flight experiments have confirmed, that rope oscillations can occur randomly during flight. Possible causes are wind gusts, vibrations and the motion of the helicopter itself. The oscillations usually exhibit small amplitudes and cause only small angular deviations. During the Utrera 2009 experiment shown in Sec. 7.1, the jerk of the load's lift-off created rope oscillations with an amplitude of 0.01 rad. A position deviation of ± 5 cm is calculated, considering the rope length of 5 m. This seems negligible small, but a speed deviation of $\pm 0.6\,\mathrm{m/s}$ is calculated based on the measured oscillation frequency of approximately[2] 3 Hz. The frequency is low enough and the speed deviation is high enough for the controller to react on the disturbance.

[2]The sampling rate of 10 Hz allowed only a coarse estimation.

A problem similar to the internal rope oscillation is caused by the LTD. Like discussed in Sec. 2, the LTD is a mechanical device to estimate the orientation of the rope relative to the helicopter fuselage and to measure the force in the rope. Until now it has been assumed, that the measurement is not influenced by the LTD. However, the mechanic construction of the LTD itself constitutes a pendulum. The oscillation of the LTD and the internal oscillation of the rope are coupled strongly. An analysis of the LTD oscillation is presented in this section, during the discussion of experimental results. In anticipation of the analysis the following is stated. For the considered load mass between 1.5 kg and 4.5 kg, the influence of the LTD is strong and needs to be included in the model.

The results are compared to another model, which is based on the theory of sound. The eigenfrequencies of oscillating strings, e.g. a harp string, are calculated from tension F_t, mass μ and length of the string l:

$$\mathrm{f}_{\mathrm{string}}(n) = n \left(\sqrt{F_t/\mu}\right) / (2\, l_{rp}) \tag{5.39}$$

For $n = 1$ the fundamental eigenfrequency and for $n \geq 2$ the n'th harmonic of the fundamental eigenfrequency are calculated. Two assumptions are made usually in the theory of sound: The string has no inner rigidity and the mounting of the string is fixed. Both assumptions are not fulfilled completely, since the rope exhibits a certain resistance and neither helicopter nor load are absolutely fixed. However, the results show, that this model is usable for a first estimation of the expected rope oscillation frequencies.

In Fig. 5.4 the flexible rope model is depicted. To preserve clearness, not all symbols are shown in the drawing. The model consists of n mass points, which are connected through rigid massless links $\mathbf{p}_i$ of length l_i. The link of the top-most mass point is connected to a fixed base. All links and mass points are considered to constitute mini-pendulums. For example, the mass point m_{n-1} and the link $\mathbf{p}_{n-1}$ constitute a mini-pendulum, which is connected to the mass point m_{n-2}. The model is derived in two dimensional space. The pendulum motions in the$\mathbf{n_{1,3}}$ and the $\mathbf{n_{2,3}}$ plane are therefore treated independently. This is a simplification, but for small angles it is a very good approximation. The two dimensional approximation is justifiable, since internal rope oscillations usually exhibit only small amplitudes. Therefore, the mass points of the model are only allowed to move in the $\mathbf{n_{1,3}}$ plane. The angle α_i describes the orientation of $\mathbf{p}_i$ relative to $\mathbf{p}_{i-1}$. The angle α_1, of the first pendulum, is taken relative to $\mathbf{n_3}$. Therefore, for $\alpha_i = 0$, with $i \in \{1, \ldots, n\}$, all pendulums are parallel to $\mathbf{n_3}$ and the modeled rope hangs straight downwards. The angular rates $\dot{\alpha}_i$ are defined to be $\dot{\alpha}_i = d\,\alpha_i/dt$. The system state vector is given by:

$$\mathbf{X} = [\alpha_1, \ldots, \alpha_n,\, \dot{\alpha}_1, \ldots, \dot{\alpha}_n]^t \tag{5.40}$$

All mass points are subjected to the gravitational force $\mathbf{F}^G = m_i\, g\, \mathbf{n_3}$ and every mass point can be excited by a force $\mathbf{F}_i = \mathbf{n_1}\, F_i$. For every mini pendulum a simple friction approximation is realized using the forces $\mathbf{F}_i^{fr} = -\mathbf{v}_i\, k_i$, where $\mathbf{v}_i$ is the velocity vector, in the Newtonian frame $\mathbf{N}$, of the mass point m_i and k_i is the friction coefficient. The dynamic equations are derived using the Kane method, and the Autolev tool is used to generate the equations.

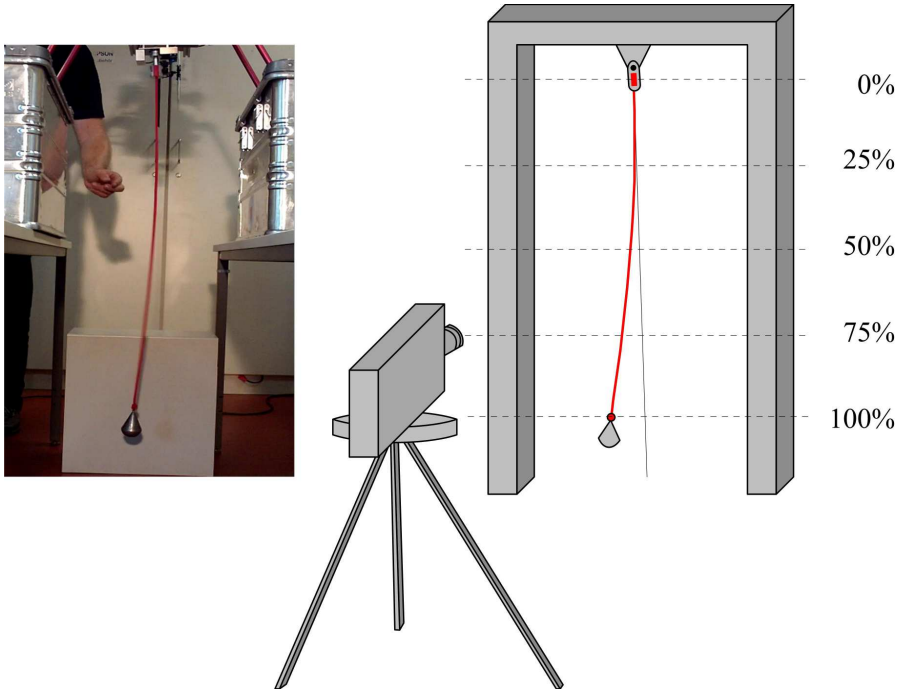

Figure 5.5: Experimental setup used for the validation of the rope model

Using $n = 1$ and $n = 2$, the dynamic equations of a simple (double) pendulum are derived. However, the generated equations become larger quickly, for $n > 2$. For that reason, the equations for $n \in \{1, 2, 5\}$ are not presented here, but in the additional equations document [Ber13, page 113ff.].

The validation of the model in laboratory experiments is presented next. In Fig. 5.5 the experimental setup, used for the validation of the rope model, is depicted. A pendulum composed of LTD, rope and load is stimulated by plucking the rope at approximately 50 % of the rope length. A video camera (60 FPS) is used to record the resulting oscillations. A rope of 0.9 m length and load weights of 1.5 kg, 3.0 kg and 4.5 kg are used for the experiments. The rope length of 0.9 m might seem strange, but in this case LTD, rope and load together constitute a pendulum of approximately 1.0 m length. The left part of Fig. 5.5 shows a still picture extracted from one of the videos. Only the bowing of the rope is directly visible in the image. It is necessary to extract the higher oscillation frequencies from the blurring of the rope, caused by the fast rope motion. This has been achieved by careful image processing, which allows an estimation of the rope motion with sub-pixel accuracy. The video processing is described here, since the exact extraction of the rope motion from the video is of big importance for the further analysis of the data.

The videos are preprocessed and converted from RGB into HSV color space, since this simplifies the color tracing process. Fig. 5.6 show the different steps of the video processing. A zero image is shown on the left side of the figure. This image is created from approximately 60 seconds of video material and therefore it is almost noise free.

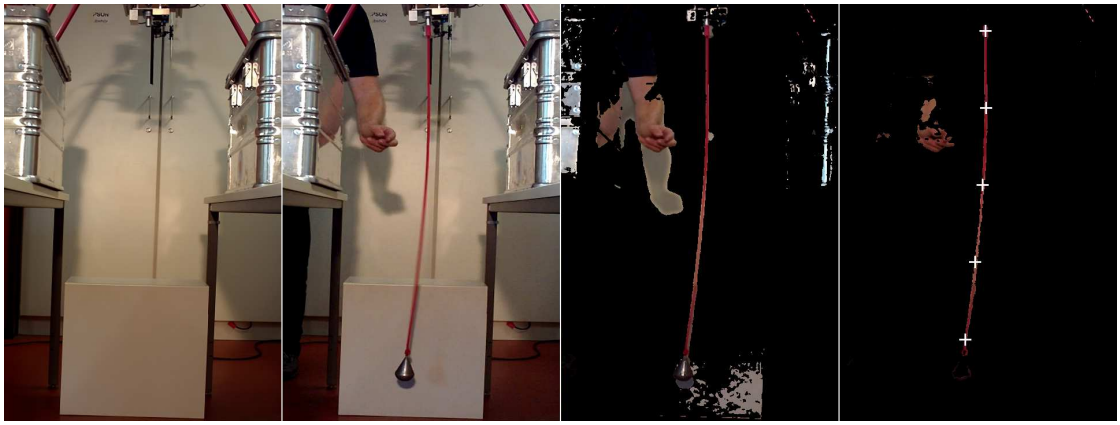

Figure 5.6: Video processing (left to right) - Zero image, experiment image, difference image, processed result

The image does not show LTD, rope or the load, and is used to separate foreground objects from the static background of the recorded videos. The second image from left shows a still image from an experiment and the third image shows the same scene, where the background is removed using the zero image. This image still exhibits a lot of background data, mainly caused by the arm, its reflection and shadow, since neither of them is present in the zero image. Finally, all colors different from the rope color are removed, like shown in the fourth image from left. This removes almost all background objects. However, a part of the arm is still visible, since its color matches a part of the rope. A simple heuristic is used to differentiate between the rope and remaining background objects, like the hand. The pendulum is almost vertically centered in the image at rest. Therefore, the rope color is searched close to the vertical center of the image. Then, the estimated rope position is used as the initial search position of the next video frame. This heuristic generates an almost outlier free estimation of the rope motion at the selected points. Only a short time after the rope stimulation, while the hand is still close to the rope, false rope positions are randomly estimated. These outliers have been removed in a post-processing step. It is possible to use a simple[3] plausibility check to remove these outliers. Linear interpolation is used to fill the gaps, caused by the removal of the outliers.

The rope motion is estimated at five different positions of the rope, using five image rows. These estimations are indicated by white crosses, see the rightmost image of Fig. 5.6. The rope positions are calculated as an average of all pixel positions, which were classified to belong to the rope. To achieve sub-pixel accuracy the rope positions of the two adjacent image rows are additionally calculated and the final position is estimates as the mean value of these three positions. The internal oscillations of the rope subside fast

[3]The outliers exhibit a very large amplitude, much larger than the amplitude of valid data.

and therefore the rope is stimulated several times to gather enough data. The resulting data sets are concatenated and transformed into the frequency domain, using the FFT (= Fast-Fourier-Transformation).

To make the comparison of experiment and simulation possible, the model is parametrized similar to the experimental setup. The model consists of 20 mass points: The top mass point models the LTD, where a mass of 0.25 kg and a pendulum length of 2.5 cm are used. The bottom mass point models the load, where either 1.5 kg, 3.0 kg or 4.5 kg are used. The corresponding pendulum lever is assumed to be part of the rope and therefore is modeled together with the rope. The rope is split into 18 parts, each modeled by a mass point with $1/18$ of the entire rope mass of 0.0110 kg. These mass points are connected by 19 massless links of 0.9/19 m length, where 17 links are required for the interconnections and two for the connections to LTD and load.

The simulated rope is stimulated by a short, weak impulse (10 ms, 2 N) using the force $\mathbf{F}_{10}$. This force attacks in the middle of the simulated rope, which is similar to the stimulation of the real rope in the experiments. Fig. 5.7 shows, from top to bottom, experimental (left) and simulation (right) data for 1.5 kg, 3.0 kg and 4.5 kg. The experimental and simulation data has been transferred into the frequency domain to simplify the analysis. The color of the lines denote the position of the points where the data is recorded/simulated. As seen in Fig. 5.7, experiments and simulation match closely and three frequency peaks are identified in each sub-figure.

First, the frequency of the load pendulum, which can be approximated for a stationary mounting point or high helicopter/payload ratios to be $\mathrm{f}_{pend} = 1/\left(2\pi\sqrt{l_{rp}/g}\right) = 1/\left(2\pi\sqrt{0.9/9.81}\right) \cong 0.52\,\mathrm{Hz}$. Experimental and simulated results match closely the calculated frequency with deviations of ± 0.02 Hz. It should be noted, that the first peak itself is not visible in the figure. The scaling of the figure has been selected in favor of the other two frequency peaks, since this analysis focuses on the internal rope motion and influence of the LTD. The pendulum oscillation would have overpowered the other frequency peaks and a logarithmic scaling would have emphasized the noise too much.

Second, the rope fundamental eigenfrequency, which is approximated using Eq. 5.39 from the theory of sound. Fundamental eigenfrequencies of 20 Hz, 29 Hz and 35 Hz are calculated for 1.5 kg, 3.0 kg and 4.5 kg respectively. It is important to notice, that the vision data has been recorded using a 60 FPS camera, which leads to a sampling frequency fs of 60 Hz. Therefore, the rope fundamental eigenfrequency is not accurate for the 4.5 kg experimental data figure. The undersampling of the vision data leads to a folding of the FFT-data at $\mathrm{fs}/2 = 30\,\mathrm{Hz}$. Therefore, the shown frequency peak at $\mathrm{fa} = 28\,\mathrm{Hz}$ is just an alias of the real frequency peak at $\mathrm{fs} - \mathrm{fa} = 32\,\mathrm{Hz}$. Considering this, the experimental and simulated results show very good correspondence. Additionally, the results are close to the calculated frequencies, based on the theory of sound.

And third, the peaks in the middle of the figure, which are a result of the LTD which oscillates without an attached rope with a frequency of 3.2 Hz. Through the rope coupling the frequency shifts up, towards the fundamental eigenfrequency of the rope. To verify that the middle peaks are caused by the LTD the simulation has been repeated, and during the second run the LTD has not been considered. The rope is composed of

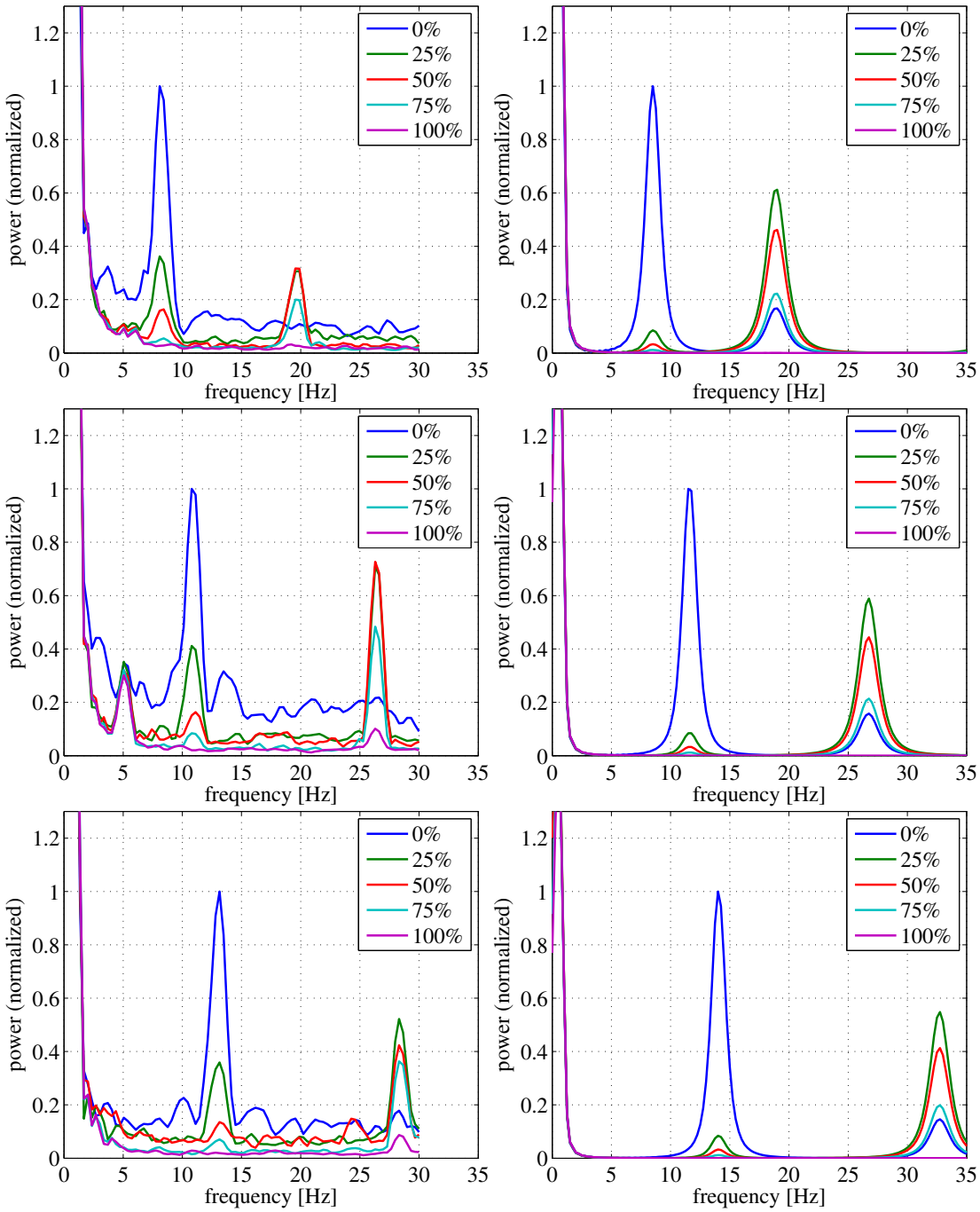

Figure 5.7: Rope model - Comparison between experimental data and simulation results
Positions - 0 % = LTD (top), 25−75 % = rope, 100 % = load (bottom)

19 parts, each modeled by a mass point of 1/19 the entire rope mass. These mass points are connected by 20 massless links of equal length. The simulation of this model exhibits only the frequency peaks of the load pendulum and the fundamental eigenfrequency of the rope. This proves that the middle peak is caused by the LTD. The LTD therefore contributes a significant part of the simulated and measured oscillations. For a payload of 1.5 kg the oscillation frequency of the LTD (8 Hz) is low enough, less than 10 Hz, for the helicopter to respond, whereas the frequency of the internal rope oscillation (19 Hz) is almost two times bigger. Therefore, for payloads less than 1.5 kg the LTD causes problematic, low frequency oscillations.

A short summary concludes the validation of the model. The simulation and experimental results match closely and therefore the model is considered to be a good approximation of the real system. The theory of sound provides Eq. 5.39, which is a good first approximation of the rope oscillations. However, with increasing frequency the accuracy of Eq. 5.39 decreases, while the results of the simulation stay close to the experimental results. Additionally, the model provides a good estimation of the LTD's influence on the rope oscillations.

After its successful validation, the model is used to predict the oscillation frequencies of LTD and rope, dependent from the utilized rope length. In Fig. 5.8 the simulated oscillation frequencies for a rope length of one, three, five, seven, nine and eleven meters are depicted. The simulation parameters are similar to the parameters used for the validation, and a load mass of 4.5 kg is used. Eq. 5.39 is used to calculate the fundamental eigenfrequency of the rope, as well as the first and second overtone. The prediction of higher overtones has been omitted, since the accuracy of this calculation decreases with higher frequencies. The calculated values are indicated by the asterisks in Fig. 5.8. The top-left sub-figure shows only one of the three calculated values, since the fundamental eigenfrequency of the rope is very high (28 Hz calculated, 27 Hz simulated). Therefore, the first and second overtone are outside the depicted frequency range. The oscillation frequency of the LTD is indicated by a vertical line. To provide better scaling of the figures, all frequencies below 1.5 Hz have been removed. It is important to notice, that this concerns only the load oscillations, which are not important for this analysis. Four important insights are won from Fig. 5.8: First, the fundamental rope frequency is approximately reciprocal proportional to the rope length. Second, the LTD oscillation frequency is almost independent from the rope length. Some deviations are visible, but the overall frequency is constant. Third, the LTD oscillation is amplified, if the fundamental rope frequency or an overtone is close to the LTD frequency. This is clearly visible, if the right-middle sub-figure is compared to left-middle sub-figure. The fundamental rope frequency and second overtone shown in the left-middle sub-figure exhibit approximately five times the power of the LTD frequency peak. The LTD frequencies shown in the right-middle sub-figure are amplified by the second overtone of the fundamental rope frequency and are more than two times stronger than the fundamental rope oscillation. Fourth, not all overtones of the rope's fundamental frequency are necessarily generated by the stimulation of the rope, which explains why the first overtone frequency is almost not present in the figure. In the upper-left sub-figure and in the middle-left

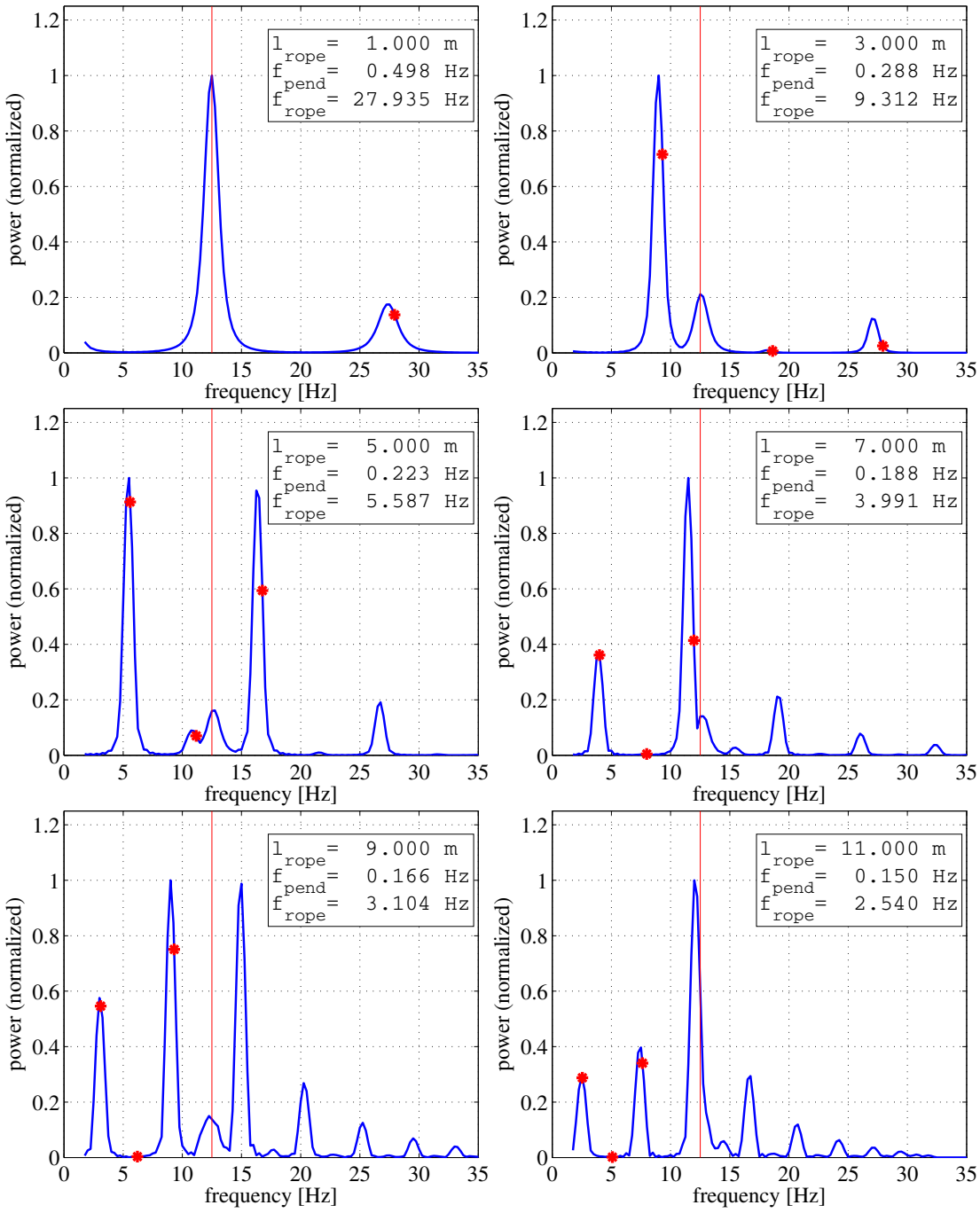

Figure 5.8: Rope model - Oscillation prediction for different rope lengths

sub-figure, close to LTD oscillation frequency, small frequency peaks are visible close to predicted first overtone.

The following conclusions are drawn, based on these results and the results obtained during the validation of the flexible rope model. With increasing load mass the rope's eigenfrequencies becomes higher and with increasing rope length the rope's eigenfrequencies becomes lower. The proportionality $f_{string} \propto \sqrt{m_l}/l_{rp}$ is derived from Eq. 5.39, with $F_t = m_l\, g$. At least for frequencies below 10 Hz this is a good approximation. This result has been verified by measurement and simulation. For short rope lengths below 3 m and high load masses above 4.5 kg the fundamental eigenfrequency of the rope is higher than the bandwidth of the closed loop system (10 Hz) and the helicopter does not respond to these oscillations. However, the rope length has stronger influence on the rope's eigenfrequency than the load mass. Considering rope lengths of 5 m/10 m the eigenfrequency becomes 5.87 Hz/2.97 Hz, even for a high load mass of 4.5 kg. The helicopter controller will react to those oscillations, which causes instabilities of the system. These oscillations have been witnessed during flight experiments.

To overcome this problem three solutions are proposed: First, the restriction to heavy payloads above 4.5 kg and short rope lengths below 3 m. The parameters guarantee a sufficient separation of the rope's eigenfrequencies and the oscillation frequency of the LTD. Second, the application of a low-pass filter. The frequency of the pendulum oscillation is very low (0.5 Hz, 0.157 Hz for a rope length of 1 m or10 m respectively). It is therefore possible to suppress the higher frequencies of rope and LTD using a low-pass filter. Third, the use of an observer to reconstruct the motion of the load.

The first approach imposes strong limitations and reduces the flexibility of the system. Therefore, this solution is not further investigated. The second and third approach are presented in detail in Sec. 6.6.

The following summary of the most important results concludes this section. The calculation of roll-pendulum and idealized pendulum eigenfrequencies have been presented. A flexible rope model has been derived to analyze the motion of the LTD and rope. This model is validated in laboratory experiments, and in parallel Eq. 5.39 from the theory of sound has been introduced. The equation allows a good approximation of the rope eigenfrequencies, for frequencies below 10 Hz. The influence of the LTD is not considered in this equation, but it is included in the presented flexible rope model. An important result of the laboratory experiments is, that with increasing load mass the oscillation frequency of the LTD shifts upwards. Therefore, for low payloads the LTD oscillation frequency is low enough for the helicopter to react. Furthermore, it has been concluded, that the oscillation frequency of the internal rope motion decreases with increasing load mass, whereas the LTD oscillation frequency depends only on the mass of the attached load. The influence of the rope length on the eigenfrequency of the rope is stronger (reciprocal proportional) than the influence of the load mass, which is proportional to the square root of the load mass. Using these results it is possible to find parameters for rope length and load mass, which allow the direct usage of the measured angles, since the oscillation frequencies of LTD and rope are too high for the helicopter to respond. However, this reduces the flexibility of system significantly and therefore the usage of a filter or of an observer is proposed.

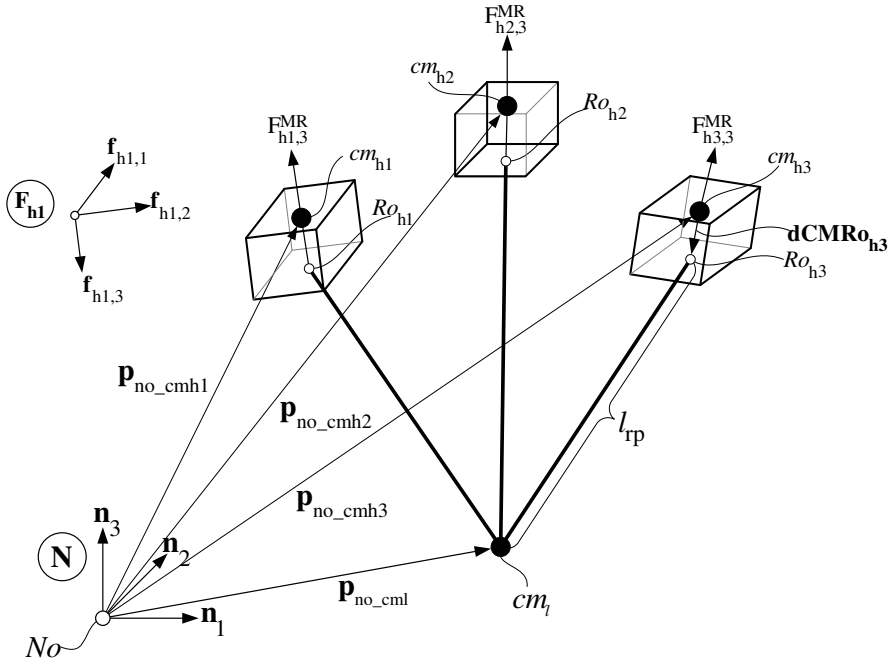

Figure 5.9: Multi-lift configuration

5.1.3 Model for Dual- and Multi-Lift Configurations

In this section the slung load model of two or more helicopters is derived, which is based on the *helicopter model* described in Ch. 3. The model is applicable for dual- and multi-lift slung load configurations. Depending on the actual configuration, the non-linear model is referenced as *dual-lift model* or *multi-lift model* respectively. The uncoupled model of a single helicopter is referenced as *helicopter model,* similar to the previous section.

For simplicity the helicopters are numbered consecutively and coordinates and speeds are extended by lower case helicopter numbers hx, with $x \in \mathbb{N}$. The *single-lift model* has been derived in the Sec. 5.1.1, using a minimal set of generalized coordinates and speeds. However, a different approach has proven to be very efficient for the derivation of *dual-lift* and *multi-lift model*.

The states of the individual helicopters are described similar to the *helicopter model*, but position and velocity of the load are described by three Cartesian coordinates and their derivatives. Therefore, the state vector of the *dual-lift model* consists of 30 variables, 24 variables for the two helicopters and six for the load, and the state vector of the *multi-lift model*, considering three helicopters, consists of 42 variables. Helicopters and load are connected through ropes. The ropes are considered to be always under stress and are therefore modeled to be rigid and massless. Therefore, each helicopter restricts the motion of the load and reduces the load's independent generalized speeds by one. For example, the *single-lift model* of Sec. 5.1.1 is composed of only one helicopter connected to one load. The load has two independent generalized speeds and is restricted to a

spherical motion around the rope attachment point *Ro*. The two helicopters of the *dual-lift model* restrict the load to a circular motion around a virtual line, which connects the rope attachment points Ro_{h1}, Ro_{h2} of the first and second helicopter. Therefore, the load of the *dual-lift model* has only one independent generalized speed left. And finally, the motion of the load is completely governed by the three helicopters of the *multi-lift model*.

In summary: The *single-lift model* has eight independent generalized speeds and, since it has been modeled using a minimal set of coordinates/speeds, the state vector includes 16 variables, see Sec. 5.1.1 for details. The *dual-lift model* has 13 independent generalized speeds, and the state vector includes 30 variables. The *multi-lift model* has 18 independent generalized speeds, and the state vector includes 42 variables. This implies that some state variables of *dual-lift model* and *multi-lift model* depend on other variables of the respective state vector.

The Kane method has been used to derive the dynamic equations. This method allows the utilization of dependent and independent generalized speeds for the definition of the kinematic equations. However, for the generation of dynamic equations a set of independent generalized speeds is required. Therefore, additional constraint equations need to be introduced to derive independent generalized speeds. The derivation of the constraint equations is discussed after the definition of kinematic equations for *dual-lift* and *multi-lift model*.

In Fig. 5.9 an overview of the *multi-lift model* is presented. The general structure of the *dual-lift model* is similar, but one of the helicopters needs to be removed; for example the second helicopter shown in the figure. The helicopters are drawn as cuboids to improve the clearness of the figure. However, different from their appearance the helicopters are fully modeled, similar to the *single-lift model* in Sec. 5.1.1 or the *helicopter model* in Ch. 3. To keep the figure simple, only the fuselage frame $\mathbf{F_{h1}}$ of the first helicopter is shown, and the frames $\mathbf{F_{h2}}$, $\mathbf{F_{h3}}$ of the second and third helicopter are omitted. The vector **dCMRo**, which connects the helicopter's CoM with the rope mounting point of the respective helicopter, is only drawn for the third helicopter, for the same reason. Each helicopter is described using six coordinates and speeds, similar to the *helicopter model*. Position and velocity of the CoM of the i'th helicopter are described by the vector $\mathbf{p}_{no\_cmhi}$ and its derivative, where the coordinates of the vector are defined relative to an inertial frame **N**:

$$\mathbf{p}_{no\_cmhi} = x_{hi}\,\mathbf{n}_1 + y_{hi}\,\mathbf{n}_2 + z_{hi}\,\mathbf{n}_3 \tag{5.41}$$

$$\mathbf{v}_{no\_cmhi} = \frac{d^{\mathbf{N}}\mathbf{p}_{no\_cmhi}}{dt} = u_{hi}\,\mathbf{n}_1 + v_{hi}\,\mathbf{n}_2 + w_{hi}\,\mathbf{n}_3 \tag{5.42}$$

The orientation of the i'th helicopter's fuselage frame $\mathbf{F_{hi}}$, relative to the inertial frame **N**, is given by the Euler-angles 3-2-1 (ψ_{hi}, θ_{hi}, φ_{hi}). The angular velocity of the fuselage frame $\mathbf{F_{hi}}$, relative to the inertial frame **N**, is described using the angular speeds (p_i, q_i, r_i):

$$\omega_{\mathbf{hi},\mathbf{F-N}} = p_{hi}\,\mathbf{f_{hi,1}} + q_{hi}\,\mathbf{f_{hi,2}} + r_{hi}\,\mathbf{f_{hi,3}} \tag{5.43}$$

Position and velocity of the load are given by the vector $\mathbf{p}_{no\_cml}$ and its derivative. The

coordinates (x_l, y_l, z_l) and (u_l, v_l, w_l) are defined in the **N** frame:

$$\mathbf{p}_{no\_cml} = x_l\,\mathbf{n}_1 + y_l\,\mathbf{n}_2 + z_l\,\mathbf{n}_3 \tag{5.44}$$

$$\mathbf{v}_{no\_cml} = \frac{d^{\mathbf{N}}\mathbf{p}_{no\_cml}}{dt} = u_l\,\mathbf{n}_1 + v_l\,\mathbf{n}_2 + w_l\,\mathbf{n}_3 \tag{5.45}$$

The kinematic equations of *dual-* and *multi-lift model* are summarized below. Only the equations of the first helicopter are presented exemplarily:

$$\begin{aligned}
\dot{x}_{h1} &= u_{h1} \\
\dot{y}_{h1} &= v_{h1} \\
\dot{z}_{h1} &= w_{h1} \\
\dot{\varphi}_{h1} &= p_{h1} + \tan(\theta_{h1})(q_{h1}\sin(\varphi_{h1}) + r_{h1}\cos(\varphi_{h1})) \\
\dot{\theta}_{h1} &= q_{h1}\cos(\varphi_{h1}) - r_{h1}\sin(\varphi_{h1}) \\
\dot{\psi}_{h1} &= (q_{h1}\sin(\varphi_{h1}) + r_{h1}\cos(\varphi_{h1}))\sec(\theta_{h1}) \\
&\vdots \\
\dot{x}_l &= u_l \\
\dot{y}_l &= v_l \\
\dot{z}_l &= w_l
\end{aligned} \tag{5.46}$$

For three or more helicopters, the state vector **x** of the *multi-lift model* is defined using the auxiliary vectors **q** and $\dot{\mathbf{q}}$:

$$\mathbf{q} = [x_1,\, y_1,\, z_1,\, \varphi_1,\, \theta_1,\, \psi_1, \cdots,\, x_3,\, y_3,\, z_3,\, \varphi_3,\, \theta_3,\, \psi_n,\, x_l,\, y_l,\, z_l]^t \tag{5.47}$$

$$\dot{\mathbf{q}} = [u_1,\, v_1,\, w_1,\, p_1,\, q_1,\, r_1, \cdots,\, u_3,\, v_3,\, w_3,\, p_3,\, q_3,\, r_3,\, u_l,\, v_l,\, w_l]^t \tag{5.48}$$

$$\mathbf{x} = [\mathbf{q};\, \dot{\mathbf{q}}] \tag{5.49}$$

For the *dual-lift model* the generalized coordinates and speeds of the third helicopter need to be removed from Eq. 5.47 and Eq. 5.48.

An extension of the model for four and more helicopters is possible. However, for more than three helicopters, the motion of the individual helicopters becomes constrained by the coupled system. The reason is, that each helicopter adds one constraint to the motion of the coupled system, because of the rigidly modeled rope. For up to three helicopters only the motion of the load is constrained. Beyond three helicopters, each additional helicopter constraints the motion of the coupled helicopters.

The presented model, considering three coupled helicopters, covers all important aspects of a multi-lift configuration and therefore models with more than three helicopters are not presented in this thesis.

The Kane method allows the specification of motion restrictions using speed constraints. Constraint equations may include constants, configuration variables and generalized speeds. These equations need to be linear with respect to the generalized speeds.

The specification of eligible constraint equations is an important part of the model development. Therefore, the derivation of the constraint equations, for the *dual-* and

multi-lift model, is discussed in the next paragraphs. For a first consideration the simplification $\mathbf{dCMRo_{hi}} = 0$ is applied. This places the rope attachment point in the CoM of the helicopters. The following additional constraint equation is introduced for every helicopter hx considered in the model:

$$l_{rp} = \left|\mathbf{p}_{rohi\_cml}\right| = \left|\mathbf{p}_{no\_cmhi} - \mathbf{p}_{no\_cml}\right| \tag{5.50}$$

$$l_{rp}^2 = (x_{hi} - x_l)^2 + (y_{hi} - y_l)^2 + (z_{hi} - z_l)^2 \tag{5.51}$$

The distance between the CoM of i'th helicopter cm_{hi} and the CoM of the load cm_l is equal to the constant rope length. Eq. 5.51 is equivalent to the square of the vectorial Eq. 5.50, which has been expressed in coordinates of the **N**-Frame. To utilize the equation in the Kane formalism, the constraint has to be expressed in linear terms of independent speeds. Therefore, Eq. 5.51 is differentiated with respect to time:

$$(x_{hi} - x_l)(u_{hi} - u_l) + (y_{hi} - y_l)(v_{hi} - v_l) + (z_{hi} - z_l)(w_{hi} - w_l) = 0 \tag{5.52}$$

It should be noticed, that the rope length l_{rp} is no longer part of the constraint equation, but it is still included implicitly through the initial configuration of the system.

This concludes the derivation of the simplified constraint equation. However, the equation is only valid, if the rope is directly attached to the CoM of the helicopter. For $\mathbf{dCMRo_{hi}} \neq \mathbf{0}$ the Eq. 5.51 changes to:

$$l_{rp}^2 = \mathbf{p}_{rohi\_cml}^2 = \left(\mathbf{p}_{no\_cmhi} + \mathbf{dCMRo_{hi}} - \mathbf{p}_{no\_cml}\right)^2 \tag{5.53}$$

$$l_{rp}^2 = \left(\begin{bmatrix} x_{hi} \\ y_{hi} \\ z_{hi} \end{bmatrix} + C_{N\_Fi} \begin{bmatrix} dCMRo_{hi,1} \\ dCMRo_{hi,2} \\ dCMRo_{hi,3} \end{bmatrix} - \begin{bmatrix} x_l \\ y_l \\ z_l \end{bmatrix} \right)^2 \tag{5.54}$$

The vector $\mathbf{dCMRo_{hi}} = (dCMRo_{hi,1},\, dCMRo_{hi,2},\, dCMRo_{hi,3})^T$ connects the CoM of the helicopter and the rope attachment point Ro_{hi}. The vector is expressed in coordinates of the helicopter fuselage frame $\mathbf{F_{hi}}$. The placement of fuselage, main-rotor, tail-rotor and rope mounting point is defined by the distance vectors (**dOFo**, **dOMRo**, **dOTRo**, **dORo**) relative to a reference point O, compare the *helicopter model* described in Sec. 3.1.3. Therefore, the vector $\mathbf{dCMRo_{hi}}$ depends on the other distance vectors and the mass distribution of the different components. Tail-rotor and the rope mounting point are modeled to be massless. Therefore, the coordinates $dCMRo_{hi,c}$ $c \in \{1, 2, 3\}$ of the vector $\mathbf{dCMRo_{hi}}$ are described by:

$$dCMRo_{hi,c} = dORo_{hi,c} - \left(dOFo_{hi,c}\, m_{hi,F} + dOMRo_{hi,c}\, m_{hi,MR}\right) / \left(m_{hi,F} + m_{hi,MR}\right) \tag{5.55}$$

The coordinates are specified relative to the fuselage frame $\mathbf{F_{hi}}$. The coordinates of vector $\mathbf{dCMRo_{hi}}$ need to be recalculated relative to **N**, since the coordinates of the vectors $\mathbf{p}_{no\_cmhi}$ and $\mathbf{p}_{no\_cml}$ are defined relative to the Newtonian frame **N**. This is achieved through a multiplication with the rotation matrix C_{N_Fi}, which describes the orientation of the fuselage frame $\mathbf{F_{hi}}$ relative to **N**. The new constraint equation depends not only on

the position of helicopter and load, but also on the orientation of the helicopter fuselage. Finally, the speed constraint equations are created through differentiation of Eq. 5.54 with respect to time:

$$\begin{aligned} 0 \quad = \quad & \left(\begin{bmatrix} x_{hi} \\ y_{hi} \\ z_{hi} \end{bmatrix} + C_{N\_Fi} \begin{bmatrix} dCMRo_{hi,1} \\ dCMRo_{hi,2} \\ dCMRo_{hi,3} \end{bmatrix} - \begin{bmatrix} x_l \\ y_l \\ z_l \end{bmatrix} \right) \\ & \cdot \left(\begin{bmatrix} u_{hi} \\ v_{hi} \\ w_{hi} \end{bmatrix} + \dot{C}_{N\_Fi} \begin{bmatrix} dCMRo_{hi,1} \\ dCMRo_{hi,2} \\ dCMRo_{hi,3} \end{bmatrix} - \begin{bmatrix} u_l \\ v_l \\ w_l \end{bmatrix} \right) \end{aligned} \tag{5.56}$$

The Kane method requires the constraint equation Eq. 5.52 to be linear in terms of independent speeds. The upper part of the dot product does not include any speeds and the derivative of the rotation matrix $\dot{C}_{N\_F}$ can be substituted by multiplication of C_{N_F} with the cross product matrix of the angular speeds of the helicopter fuselage:

$$\dot{C}_{N\_Fi} = C_{N\_Fi} \begin{bmatrix} 0 & -r_{hi} & q_{hi} \\ r_{hi} & 0 & -p_{hi} \\ -q_{hi} & p_{hi} & 0 \end{bmatrix} = C_{N\_Fi} \begin{bmatrix} p_{hi} \\ q_{hi} \\ r_{hi} \end{bmatrix}_{\times} \tag{5.57}$$

The Eq. 5.57 follows directly from differentiation of C_{N_F} with respect to time and substitution of $\dot{\varphi}$, $\dot{\theta}$, $\dot{\psi}$, using the kinematic Eqs. 3.14-3.16. Eq. 5.56 is linear in terms of generalized speeds and therefore represents a valid constraint equation.

After the derivation of the constraint equations, the generation of the models, using the Kane method, is briefly described. Every helicopter, participating in the slung load transportation, adds one constraint, expressed by Eq. 5.54, to the coupled system. The *dual-lift model* has 13 independent generalized speeds, but the state vector includes 30 variables with 15 generalized speeds. Therefore, two speeds are not independent and need to be calculated from the remaining state vector, using the two constraint equations. The speeds u_l and v_l have been selected for the *dual-lift model* and the constraint equations are solved for these variables. However, the concrete choice of dependent speeds is irrelevant, as long as the constraint equations are solvable for the selected variables. For example u_{h1} and v_{h2} are a valid selection as well, but u_{h1} and v_{h1} are not. For the latter selection the two constraint equations are not solvable, since both variables are only included in the first constraint equation and none of them is included in the second constraint equation. The *multi-lift model* has 18 independent generalized speeds, and the state vector includes 42 variables with 21 generalized speeds. Therefore, three speeds are dependent and need to be calculated from the remaining state vector. For the *multi-lift model* the speeds u_l, v_l and w_l have been selected and the constraint equations were solved for these variables.

Like discussed in Sec. 5.1.1, the Kane formalism generates dynamic equations in implicit form. These implicit equations need to be solved for linear and angular accelerations to derive the dynamic equations in explicit form. The more the implicit equations are coupled through the accelerations, the larger becomes the explicit result. The dynamic equations of the *single-lift model* are only presentable in simplified form, using several assumptions to reduce the complexity of the model, compare Sec. 5.1.1. The *dual-* and

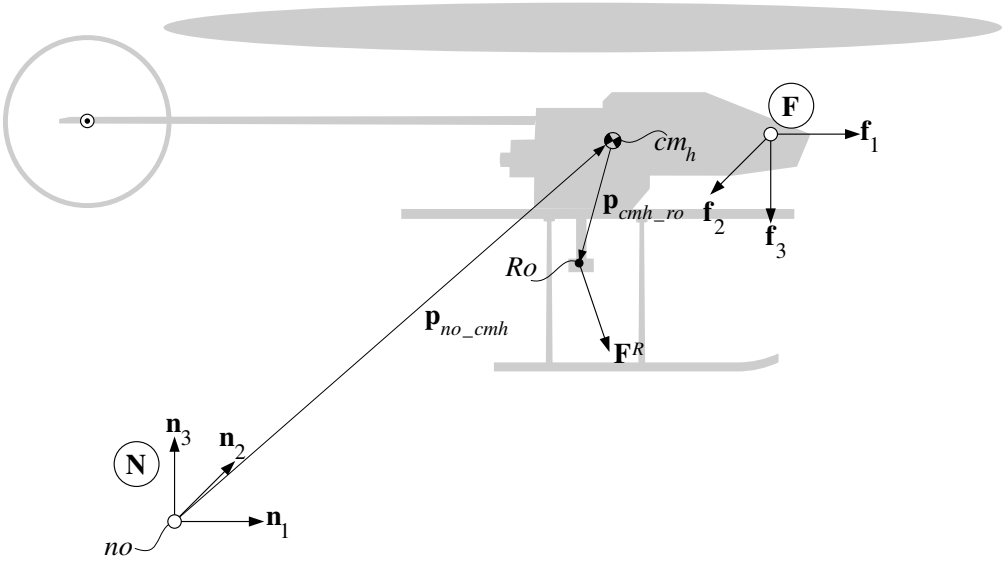

Figure 5.10: Influence of load/system coupling on the helicopter model

multi-lift models describe highly coupled systems, where the motion of each helicopter has influence of the motion of the load and the remaining helicopters. Therefore, the dynamic equations of the models are too complex to be presented here. Nevertheless, the non-simplified implicit dynamic equations for *dual-* and *multi-lift* models are presented in the additional equations document, which is accompanying this thesis on CD, see [Ber13, page 24ff.] and [Ber13, page 52ff.] respectively.

In the following, a different approach has been chosen to discuss partial aspects of the coupled slung load system.

Partial Slung Load Model The dynamic equations of a simplified model are derived. This model allows an examination of the influences, caused by the slung load attachment, for all configurations presented in this thesis. This is achieved through the generic application of influences, caused by the slung load attachment, to the uncoupled *helicopter model*.

All slung load configurations, presented in this thesis, share one important property. The connection between helicopters and coupled system is established in a single point *Ro*. This concentrates the influence of the coupled system into single force vector $\mathbf{F}^R$, applied in *Ro*. Therefore, the new model is an extension of the *helicopter model*, using the force $\mathbf{F}^R$. The resulting model is called *partial slung load model* for the remainder of this thesis, since the influence of the coupled system is only considered partially. Fig. 5.10 depicts the *partial slung load model*.

Since $\mathbf{F}^R$ is not restricted, neither in magnitude nor in direction, the *partial slung load model* covers more system configurations, than the single-, dual- and multi-lift configurations described in this thesis. However, the *partial slung load model* incorporates neither

the dynamics of the coupled system nor the influence of the helicopter on the coupled system. Therefore, it is neither possible nor intended to replace the other models by the *partial slung load model*. Nevertheless, the influence of the coupled system on the helicopter is completely considered and therefore the *partial slung load model* is usable for an analysis of this influence.

The kinematic equations of the *partial slung load model* are identical to the kinematic equations of the uncoupled *helicopter model* described in Ch. 3. The vector $\mathbf{F}^R = F_1^R\,\mathbf{n_1} + F_2^R\,\mathbf{n_2} + F_3^R\,\mathbf{n_3}$ is defined in coordinates of the Newtonian reference frame $\mathbf{N}$. The dynamic equations are derived using the Kane formalism, and the force vector $\mathbf{F}^R$ is incorporated. The resulting dynamic equations are almost similar to the *helicopter model*:

$$\dot{u} = \left(F_3^{MR}\left(s_\theta c_\varphi c_\psi - s_\varphi s_\psi\right) + F_2^{TR}\left(s_\varphi s_\theta c_\psi + s_\psi c_\varphi\right) + F_1^R\right)/m \tag{5.58}$$

$$\dot{v} = \left(F_3^{MR}\left(s_\theta s_\psi c_\varphi + s_\varphi c_\psi\right) + F_2^{TR}\left(s_\varphi s_\theta s_\psi - c_\varphi c_\psi\right) + F_2^R\right)/m \tag{5.59}$$

$$\dot{w} = -g - \left(F_3^{MR}\left(c_\varphi c_\theta\right) + F_2^{TR}\left(s_\varphi c_\theta\right) - F_3^R\right)/m \tag{5.60}$$

$$\begin{aligned}\dot{p} = {} & \left(T_1^{MR}\,m - F_2^{TR}\,K_{TR} + q\,K_{p1} + q\,r\,K_{p2}\right)/K_{p3} \\ & + F_1^R\left(s_\varphi s_\theta c_\psi + s_\psi c_\varphi\right)K_{p4} + F_2^R\left(s_\varphi s_\theta s_\psi + c_\varphi c_\psi\right)K_{p4} \\ & - F_3^R\left(s_\varphi c_\psi\right)K_{p4}\end{aligned} \tag{5.61}$$

$$\begin{aligned}\dot{q} = {} & \left(-(T_2^{MR} + T_2^{TR})\,m + p\,K_{q1} + p\,r\,K_{q2}\right)/K_{q3} \\ & - F_1^R\,c_\theta c_\psi\,K_{q4} + F_2^R\,c_\theta s_\psi\,K_{q4} + F_3^R\,s_\theta\,K_{q4}\end{aligned} \tag{5.62}$$

$$\dot{r} = \left(T_3^{MR} + F_2^{TR} dOTRo_1 + p\,q\,(I_{11}^F - I_{22}^F)\right)/(I_{33}^F + I_{33}^{MR}) \tag{5.63}$$

Where m denotes the mass of the helicopter and is defined as $m = m_F + m_{MR}$. The coefficients K_{px} and K_{qx}, with $x \in \{1,2,3\}$, are defined in Ch. 3. These coefficients depend only on constant parameters of the helicopter, including the constant angular speed of the main-rotor ω_{MR}. The coefficients K_{p4} and K_{q4} are defined as follows:

$$K_{p4} = (dOFo_3\,m_F + dOMRo_3\,m_{MR} - dORo_3\,m)/K_{p3} \tag{5.64}$$

$$K_{q4} = (dOFo_3\,m_F + dOMRo_3\,m_{MR} - dORo_3\,m)/K_{q3} \tag{5.65}$$

The equations are derived under the assumption $dOMRo_{1,2} = dOFo_{1,2} = dORo_{1,2} = 0$. This assumption has already been used for the derivation of the *single-lift model*. It places the CoM of fuselage and main-rotor and the rope mounting point *Ro* into the rotation axis of the main-rotor. The effects resulting from this placement, as well as the validity of the assumption for many real systems, have already been discussed in Sec. 5.1.1.

Eqs. 5.58-5.63 reveal a simple, but noteworthy property of the model. The equations simplify to the dynamic equations of the *helicopter model*, assuming a vector $\mathbf{F}^R = 0$, see Eqs. 3.18-3.20 and Eqs. 3.21-3.23 for a direct comparison.

In particular, the main-rotor force $\mathbf{F}^{MR}$ is still the only force available for the generation of arbitrary forces, acting on the helicopter's CoM. The orientation of the force is defined by the main-rotor plane, and the orientation of the main-rotor plane is reflected through the yaw-pitch-roll angles, see Eqs. 5.58-5.60. The force $\mathbf{F}^R$ and the tail-rotor force $\mathbf{F}^{TR}$

are present in these equations as well. The tail-rotor force $\mathbf{F}^{TR}$ is used for the control of the heading and the force $\mathbf{F}^{R}$ is determined by the dynamics of the coupled system.

Another important insight is won from Eq. 5.63. The vector $\mathbf{F}^{R}$ does not appear in this equation, whereas the remaining dynamic equations contain at least one component of $\mathbf{F}^{R}$. Therefore, the coupled system has no direct influence on the generation of the angular speed r. This justifies the decoupling of heading and remaining "orientation", for every slung load configuration[4], since Eq. 5.63 of the *partial slung load model* is similar to Eq. 5.30 of the *single-lift model* and Eq. 3.23 of the *helicopter model*. Together with the kinematic equation of the yaw angle, which is equal for all three models as well, this equation is utilized in Sec. 4.2 to justify the decoupling heading control (r, ψ) and "orientation" control (p, q, θ, φ). The idea is, that for small[5] angular speeds p, q, the generation of r depends almost only on the tail rotor force $\mathbf{F}^{TR}$. A separate controller is utilizable for the regulation of the angular speed r and yaw angle ψ, since for small pitch and roll angles the generation of the yaw angle ψ depends almost only on the angular speed r. A complete discussion of this topic is presented in Sec. 4.2.

A different important result is based on Eqs. 5.58-5.63. The influence of $\mathbf{F}^{R}$ needs to be compensated by the orientation as well as the translation controller, since $\mathbf{F}^{R}$ is present in all equations, but Eq. 5.63. This insight is utilized during the design of orientation and translation controllers presented in Ch. 6.

This concludes the short analysis of the *partial slung load model*. The remainder of this section is devoted to the validation of the *multi-lift model*.

Model Validation The *multi-lift model* without simplifications has been validated against flight data. Model and real system, together with orientation and translation controller, are evaluated, similar to the validation of the *single-lift model* in Sec. 5.1.1. Equal controller coefficients are used for both systems. The generic orientation controller, derived in Sec. 6.2, and the translation controller for multi-lift configurations, derived in Sec. 6.4, are used for the validation. The parameters of the *multi-lift model* have been chosen to match the real system as close as possible. The parameters of the helicopters are described in Sec. 2 and the coupled system is presented in second experiment of Sec. 7.2. The flight data of the experiment has been used as reference for the validation. To produce comparable simulation results the desired trajectories of the experiment are applied to the simulation. The helicopters executed two steps along both horizontal axis of the Newtonian reference frame $\mathbf{N}$. The basis vectors of $\mathbf{N}$ have been aligned as follows: $\mathbf{n}_1$ is pointing from South to North, $\mathbf{n}_2$ is pointing from East to West and $\mathbf{n}_3$ points upwards. The helicopters executed first a step about $-29.5\,\mathrm{m}$ along $\mathbf{n}_2$ and back, and second a step $30\,\mathrm{m}$ along $\mathbf{n}_1$ and back. The heading of the helicopters has been fixed during the whole experiment, with $\psi = 0$.

[4] Which satisfies the assumption $dOMRo_{1,2} = dOFo_{1,2} = dORo_{1,2} = 0$, see Sec. 4.2.
[5] A valid assumption for the considered operational range of the helicopter.

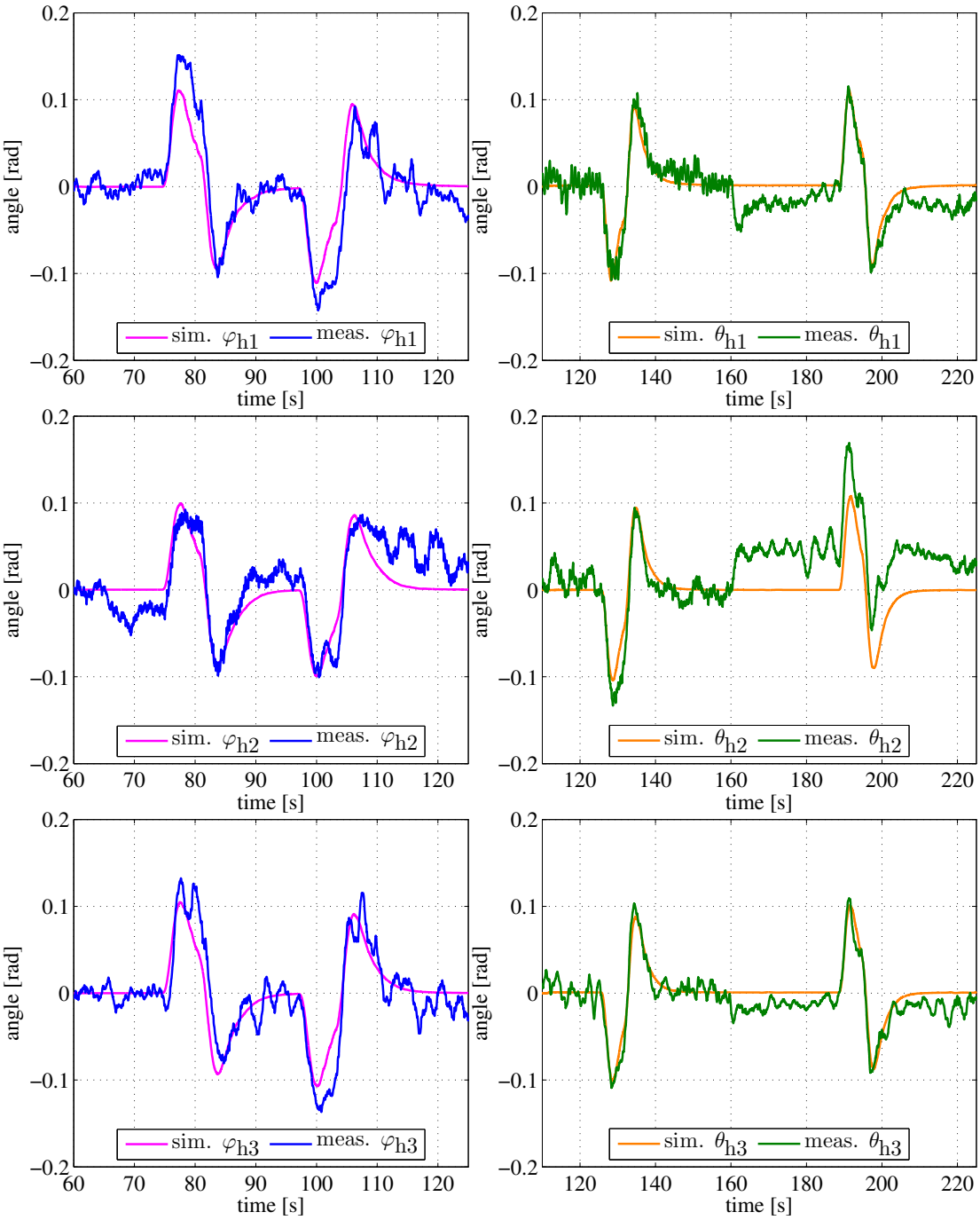

Figure 5.11: Orientation comparison - Non-linear model and real flight data (19.5.2008)

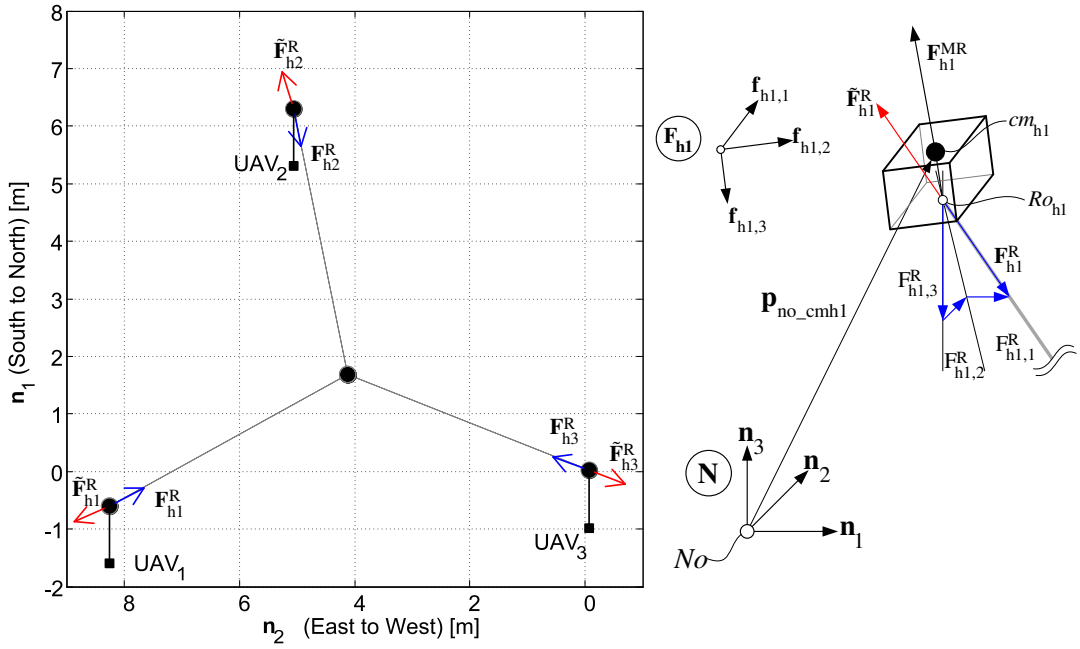

Figure 5.12: Left - Top view of the helicopter configuration, after load lift-off (19.5.2008) Right - Rope force $\mathbf{F}^R_{h1}$ and the compensation force $\tilde{\mathbf{F}}^R_{h1}$

Assuming $\psi = 0$ and using the small angle approximation $\cos(\alpha) = 1$ for small angles α, Eqs. 5.58-5.59 simplify to:

$$\dot{u} = \left(F_3^{MR}\, s_\theta + F_2^{TR}\, s_\varphi s_\theta + F_1^R\right)/m \tag{5.66}$$

$$\dot{v} = \left(F_3^{MR}\, s_\varphi - F_2^{TR}\, c_\varphi + F_2^R\right)/m \tag{5.67}$$

Where $F^R_{1,2}$ describe the influence of the coupled system and F_2^{TR} describes the influence of the tail-rotor on the helicopter's acceleration along $\mathbf{n}_{1,2}$. Both terms are considered to be disturbances, which are compensated by the translation controller. Therefore, a translation along $\mathbf{n}_1$ depends mainly on F_3^{MR} and the pitch angle θ of the helicopter, and a translation along $\mathbf{n}_2$ depends mainly on F_3^{MR} and the roll angle φ of the helicopter. For that reason, it is possible to split Fig. 5.11 into left and right sub-figures. The left graph shows only the "roll motion" during the first step and the right graph shows only the "pitch motion" during the second step.

The pitch and roll angles of the helicopters are compared to the pitch and roll angles of their simulated counterparts. Three helicopters have been used for the multi-lift experiments. Fig. 5.11 shows, from top to bottom, the angles of the first, second and third helicopter respectively. The static offsets of the measured angle have been removed to simplify the comparison with the simulated angles.

Measured and simulated angles show good correspondence. Especially during the execution of the flight steps, in the intervals [75 s, 90 s], [97 s, 112 s], [122 s, 142 s] and

[185 s, 205 s], the correspondence between measured and simulated angles is clearly visible. The roll angles exhibit more disturbances than the pitch angles. This effect is caused by the smaller inertia of the helicopter fuselage around the roll axis $\mathbf{f_1}$, which makes the roll angle less resilient against disturbances.

The measured pitch angles of all three helicopters show a common distinctive feature: After approximately 180 seconds the static offsets of the measured pitch angles change. The offset change is caused by the load deployment, which has been performed after 180 seconds. Until this time, the helicopters compensated the rope forces $\mathbf{F}_{hi}^{R}$ in order to transport the load and keep the flight formation.

In the following, the recorded change of pitch angles, during the load deployment, is validated. For that reason it is necessary to discuss the forces acting on the helicopter configuration before and after the load deployment.

On the left side of Fig. 5.12 the top view of a helicopter configuration is shown. The figure depicts a time instant of the multi-lift experiment during which the helicopters are hovering. The CoMs of the helicopters are drawn as black dots, whereas the tails are indicated by small black squares, which are connected to the CoMs through black lines. For the whole experiment the helicopters preserved this configuration well, see Sec. 7.2 for details.

On the right side of Fig. 5.12 the force $\mathbf{F}_{hi}^{R}$ and its components $\mathbf{F}_{hi}^{R} = F_{hi,1}^{R}\,\mathbf{n_1} + F_{hi,2}^{R}\,\mathbf{n_2} + F_{hi,3}^{R}\,\mathbf{n_3}$ are depicted. The vector component $F_{hi,3}^{R}$ describes the part of the force $\mathbf{F}_{hi}^{R}$, which needs to be compensated by the helicopter main-rotor force $\mathbf{F}_{hi}^{MR}$ in order to carry the load. Unless the rope is parallel to the vector $\mathbf{n_3}$, where rope and load hang straight downwards, at least one of the other two vector components is present. To preserve the flight formation it is necessary for dual- and multi-lift configurations to compensate these force components as well, using the main-rotor forces $\mathbf{F}_{hi}^{MR}$. Two dimensional projections of the rope forces $\mathbf{F}_{hi}^{R}$ and the corresponding compensation forces $\tilde{\mathbf{F}}_{hi}^{R}$ are depicted on the left side of Fig. 5.12. The force $\tilde{\mathbf{F}}_{hi}^{R}$ is the part of the main-rotor force $\mathbf{F}_{hi}^{MR}$, which is required to compensate the rope force, with $\tilde{\mathbf{F}}_{hi}^{R} = -\mathbf{F}_{hi}^{R}$. To simplify the discussion, the coordinates of $\tilde{\mathbf{F}}_{hi}^{R}$ are defined relative to the $\mathbf{N}$ frame:

$$\tilde{\mathbf{F}}_{hi}^{R} = \tilde{F}_{hi,1}^{R}\,\mathbf{n_1} + \tilde{F}_{hi,2}^{R}\,\mathbf{n_2} + \tilde{F}_{hi,3}^{R}\,\mathbf{n_3} \tag{5.68}$$

The vector $\tilde{\mathbf{F}}_{hi}^{R}$ should not be confused with the main-rotor force vector $\mathbf{F}_{hi}^{MR} = F_{hi,3}^{MR}\,\mathbf{f_3}$, which is required to generate $\tilde{\mathbf{F}}_{hi}^{R}$ and whose coordinates are defined relative to the fuselage frame $\mathbf{F}_{hi}$.

The orientation of $\tilde{\mathbf{F}}_{hi}^{R}$ is estimated from the orientation of the helicopters, since main-rotor lifting force $\mathbf{F}_{hi}^{MR}$ and compensation force $\tilde{\mathbf{F}}_{hi}^{R}$ are directly coupled to the orientation of the respective helicopter, see Sec. 3.1 for more details. The static compensation forces, depicted on the left side of Fig. 5.12, are calculated as follows:

$$\tilde{\mathbf{F}}_{hi}^{R} = \mathbf{F}_{hi}^{MR}(85\,\mathrm{s}) - \mathbf{F}_{hi}^{MR}(75\,\mathrm{s}) \tag{5.69}$$

After approximately 80 seconds the load has been lifted from the ground. The rope forces $\mathbf{F}_{hi}^{R}$ are calculated from the rope angles relative to the helicopter fuselage, which

are directly measured by the magnetic encoders of the LTD. The rope forces, depicted in left side of Fig. 5.12, have been measured after the first 85 seconds of the experiment. Assuming hovering conditions, where the load is lifted and at rest, the vectors $\tilde{\mathbf{F}}_{hi}^{R}$ and $\mathbf{F}_{hi}^{R}$ should be parallel, with $\tilde{\mathbf{F}}_{hi}^{R} = -\mathbf{F}_{hi}^{R}$. The left side of Fig. 5.12 depicts the system in hovering. The vectors are almost parallel. The deviations are caused by measurement errors, since the calculation of $\tilde{\mathbf{F}}_{hi}^{R}$ and $\mathbf{F}_{hi}^{R}$ depends on the estimated helicopter orientation and the measured encoder angles, which exhibit a lot noise[6]. However, the compliance of theoretical assumptions and measured vectors is clearly visible in the figure.

Using the static rope and compensation forces, it is possible to verify the change of pitch angle offsets, which occurs after the load deployment. In Fig. 5.11 the load deployment is visible in the interval [160 s, 165 s], where the pitch angles are depicted. Like mentioned above, the relative configuration of the helicopters has been preserved during the whole flight. Therefore, the configuration depicted in Fig. 5.12 is valid before, during and after the load deployment. Only the absolute coordinates of the helicopters are different, since the lift-off and deployment positions of the load differ as well. For the depicted heading ($\psi = 0$) the acceleration $\dot{u}_i$ along $\mathbf{n_1}$ is controlled through the main-rotor force $F_{hi,3}^{MR}$ and the pitch angle θ_i. This follows directly from Eq. 5.66, the kinematic Eqs. 5.46 and the definition of the position vector Eqs. 5.41-5.42. The component $\tilde{F}_{hi,1}^{R}$ of compensation force $\tilde{\mathbf{F}}_{hi}^{R}$ is determined by the pitch angle θ_i and $F_{hi,3}^{MR}$, using Newton's second law. With a similar approach it is possible to show, that only the component $\tilde{F}_{hi,2}^{R}$ of compensation force $\tilde{\mathbf{F}}_{hi}^{R}$ is determined by the roll angle φ_i and $F_{hi,3}^{MR}$. Therefore, only $\tilde{F}_{hi,1}^{R}$ needs to be considered for the examination of the pitch angle offset.

Based on the orientation of the vectors $\tilde{\mathbf{F}}_{hi}^{R}$, shown in the left side of Fig. 5.12, the following is estimated:

$$\tilde{F}_{h1,1}^{R} < 0 \text{ and } \tilde{F}_{h2,1}^{R} > 0 \text{ and } \tilde{F}_{h3,1}^{R} < 0 \tag{5.70}$$

During hovering $F_{hi,3}^{MR}$ is negative, since the vector component is defined to be $\mathbf{F}_{hi}^{MR} = F_{hi,3}^{MR}\,\mathbf{f_3}$, with $\mathbf{f}_3 = -\mathbf{n}_3$ for $\varphi_i, \theta_i = 0$. Therefore, it is possible to conclude from Eq. 5.66 that the angle θ_2 becomes smaller and the angles θ_1, θ_3 become larger, after the lift-off of the load, to generate the necessary compensation forces. On the contrary, after the load deployment the angle θ_2 becomes larger and the angles θ_1, θ_3 become smaller. This estimation complies with the static angle offsets after the load deployment, shown in Fig. 5.11.

A new variable $\delta\theta_i$ is introduced, which denotes the pitch angle offset of the i'th helicopter after the load lift-off. Assuming the depicted helicopter configuration, similar helicopter take-off weights and a consistent load distribution, the following equation is valid during hovering:

$$\delta\theta_2 = -(\delta\theta_1 + \delta\theta_3) \tag{5.71}$$

The equation follows directly from $\tilde{F}_{h2,1}^{R} = -(\tilde{F}_{h1,1}^{R} + \tilde{F}_{h3,1}^{R})$ and Eq. 5.66. A violation of the equation would destroy the formation of the helicopters. The angle offsets shown in Fig. 5.11 confirm this result.

[6] E.g. caused by the two-stroke engines.

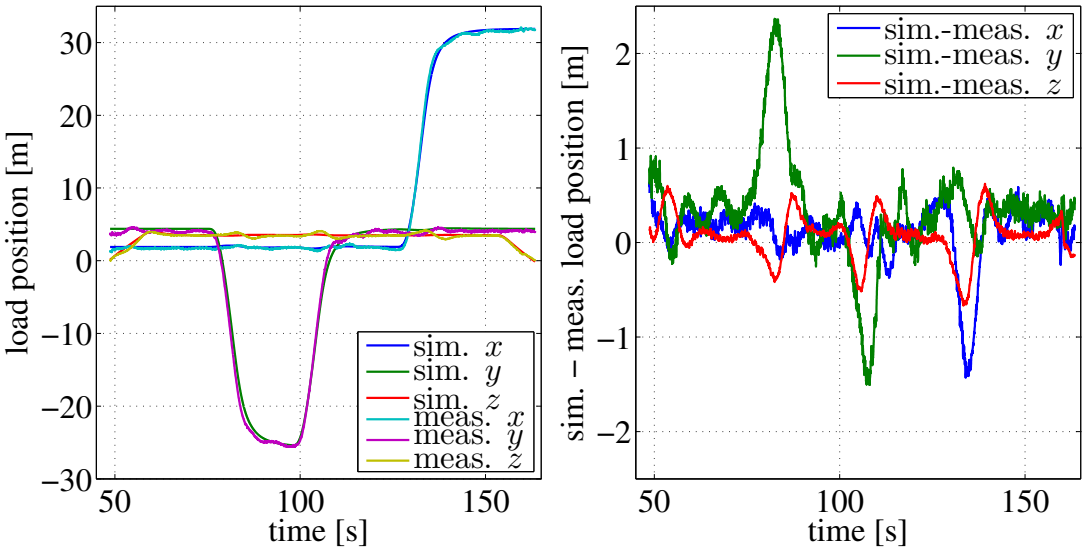

Figure 5.13: Load motion comparison of simulation and real flight data (19.5.2008)

To finish the discussion of Fig. 5.11 the most important results are summarized: Simulated and measured roll and pitch angles of all three helicopters show a good correspondence. After approximately 180 seconds the static offsets of the measured pitch angles change. This effect is caused by the deployment of the load, which is not considered by the simulation. The measured angle offsets comply with the estimation of the angle offsets. The presented theoretic estimation is based on the measured rope forces $\mathbf{F}_{hi}^{R}$ and the compensation forces $\tilde{\mathbf{F}}_{hi}^{R}$ and considers the configuration depicted on the left side of Fig. 5.12.

Finally, the real load position is compared to the simulated load position. The validation approach differs from the validation of the *single-lift model* presented in Sec. 5.1.1, where measured, observed and simulated rope angles are compared. For the *multi-lift model* a comparison of the rope angles is not as interesting as for the *single-lift model*, since the motion of the load is completely governed by the helicopters[7] and therefore no major oscillations are expected.

The load position of the real system is estimated from the measured rope angles. This estimation is described in Sec. 7.2. The left side of Fig. 5.13 shows the measured and simulated load positions, and a very good correspondence is visible. During phases of strong acceleration, e.g. between 80 and 90 seconds, the trajectory of the simulated load advances the trajectory of the real load. The right side of Fig. 5.13 emphasizes these deviations, showing the difference of the simulated and measured load position coordinates.

The ability to perform complex maneuvers close to hovering conditions, like the load

[7] This is only valid for the *multi-lift model*. The ropes of the real system are elastic and therefore the load is able to oscillate, but the rope tension damps these oscillations well.

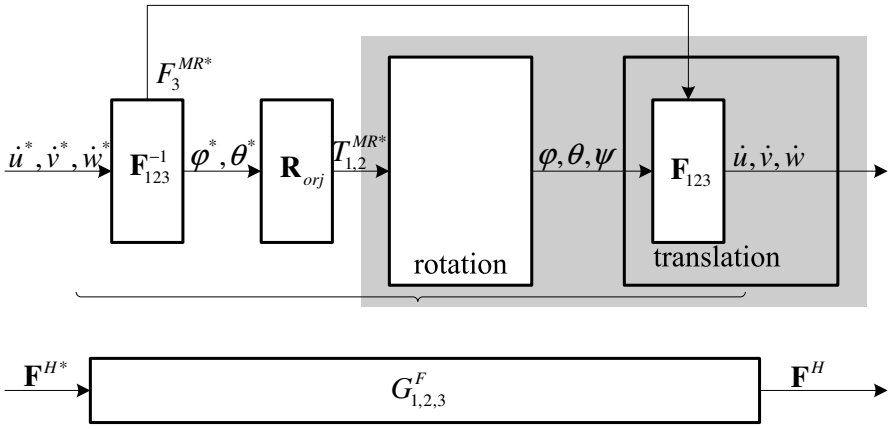

Figure 5.14: The force generator model

deployment, is an important feature of multi-lift system. Therefore, the hovering performance is considered an important property. The measured and simulated load positions show only deviations of $\pm 0.5\,\mathrm{m}$ during hovering, which is a very good result.

During fast flight maneuvers, deviations of up to $\pm 2\,\mathrm{m}$ are caused by the flexibility of the real ropes. Strong accelerations of the helicopters or strong wind results in rope bowing, which affects the measured angles and therefore the estimated load position. This complies with the results presented in Sec. 7.2, where wind gusts caused the ropes to bow about 9.5° and lead to deviations of approximately 2 m for the estimated load position.

5.2 Simplified Models for the Translation Controller Design

The models described so far are used for simulation and analysis of the different slung load configurations. After linearisation, these models are as well applicable for the controller design, using methods from linear control theory. A key element of the controller design discussed in Ch. 6 needs to be anticipated, to understand why additional simplified models have been used for the design of the translation controllers. The idea is to have a orientation controller that compensates the coupling between slung load and helicopter. The utilization of this orientation controller simplifies the design of the translation controllers and allows them to be based on simpler linear models, which do not exhibit this coupling. These are the models described in this section.

5.2.1 Linear Force Generator Model

The linear model presented in this section describes the functioning of the helicopter main-rotor as a force generator. Like discussed in Sec. 4.3, the helicopter main-rotor can only generate a force $\mathbf{F}^{MR}$ approximately perpendicular to the rotor disc. In order to generate an arbitrary force, the magnitude of $\mathbf{F}^{MR}$ has to be adapted and the main-rotor

orientation needs to be changed, using the main-rotor torques $T_{1,2}^{MR}$. Therefore, orientation controller and main-rotor together constitute a system, whose dynamic describes the generation process of arbitrary forces. The upper section of Fig. 5.14 shows a part of the translation controller and a part of the helicopter model, which are taken from the full schematic shown in Fig. 4.1. The desired accelerations $\dot{u}^*, \dot{v}^*, \dot{w}^*$ are the input signals of the inverse translation dynamics $\mathbf{F}_{123}^{-1}$ and the actual accelerations $\dot{u}, \dot{v}, \dot{w}$ are the output signals of the translation dynamics $\mathbf{F}_{123}$. Therefore, an acceleration generator is shown in the schematic.

The orientation controller $\mathbf{R}_{orj}$ and the model of the rotation dynamics are located in between the blocks $\mathbf{F}_{123}^{-1}$ and $\mathbf{F}_{123}$. The idea is to generate a linear model, similar to the lower part of Fig. 5.14, which describes the force generator functionality of model and controller shown above. This linear force generator model is applied to the translational models. This way the dynamic behavior of the helicopter is imprinted to simple translational models.

The remainder of this section is devoted to the derivation of the force generator model and its validation. The model is derived under the assumption, that the rotation dynamics of a helicopter are not influenced by the coupled system. Therefore, the model is independent from the number of coupled helicopters and applicable for all slung load configurations. The assumption is equivalent to the constraint, that the rope is attached directly in the CoM of the helicopter. This causes the vector $\mathbf{p}_{cm\_ro}$, connecting the rope mounting point *Ro* and the CoM *cm*, and the torque $\mathbf{T}^R = \mathbf{p}_{cm\_ro} \times \mathbf{F}^R$ to become zero.

The linear model is created in two stages: First, the linear model covering the rotation dynamics and the orientation controller is derived. An additional conversion into input and output forces $F_{1,2,3}^H$ is required, since the input and output to this model are the orientation angles φ, θ. This is done in the second stage. The block of the inverse translation dynamics $\mathbf{F}_{123}^{-1}$ is used for the calculation of desired main-rotor force F_3^{MR*} and desired angles φ^*, θ^* from the desired input forces $F_{1,2,3}^{H*}$. The block of the translation dynamics $\mathbf{F}_{123}$ is used for the calculation of the output forces $F_{1,2,3}^H$ from the main-rotor force F_3^{MR} and the angles φ, θ.

The dynamic behavior of the force generator model is governed by the orientation controller and the rotation dynamics of the helicopter, since $\mathbf{F}_{123}^{-1}$ and $\mathbf{F}_{123}$ are only composed of algebraic equations and add no dynamic contribution to the model. At least for the uncoupled small size helicopters this is valid. The force generator model is based on the non-linear kinematics and the rotation dynamics of a single uncoupled helicopter, described in Sec. 3.1, and the orientation controller, presented in Sec. 4.4. In Fig. 4.3 an overview of the non-linear model and rotation controller is given. The model is derived using the same approach applied for the calculation of the controller coefficients in Sec. 4.4. The non-linear model simplifies to a double integrator, assuming that the inversion blocks of the controller ($\mathbf{Q}^{-1}$, $\mathbf{D}$) match the blocks of the rotational kinematics and dynamics of the model ($\mathbf{Q}$, $\mathbf{W}_{q,p}$) perfectly. The resulting linear model is shown in Fig. 5.15. The former controller (white) and the former model (gray box) constitute the new model of the controlled rotation dynamics. The first order delay is introduced

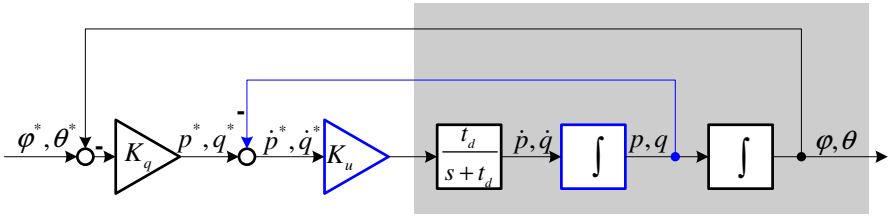

Figure 5.15: Linear model of rotation dynamics and orientation controller

to model the delay caused by the aerodynamics and the dynamics of the actuators, see Ch. 3. Simulation results have shown that the translation controllers for the single- and dual-lift configuration degrade in performance or even become unstable, if the time delay of the rotation dynamics is neglected in the force generator model. The transfer function of the model is directly read from Fig. 5.15:

$$G_{\varphi,\theta}^{SF} = \frac{K_q\, t_d}{s^2 + t_d\, s + K_q\, t_d} \tag{5.72}$$

$$G_{\varphi,\theta}^{BF} = \frac{K_q\, K_u\, t_d}{s^3 + t_d\, s^2 + K_u\, t_d\, s + K_q\, K_u\, t_d} \tag{5.73}$$

The resulting transfer function is either a third order delay $G_{\varphi,\theta}^{BF}$ (big fuselage) or second order delay $G_{\varphi,\theta}^{SF}$ (small fuselage), depending on the fuselage size of modeled helicopter. The influence of the fuselage size on the rigid body model is explained in detail in Sec. 3.1. The transfer function $G_{\varphi,\theta}^{SF}$ is read from Fig. 5.15, if the blocks with blue lines and the blue feedback loop are neglected.

Using the transfer functions of the angles, the final transfer function of the forces is derived. The desired accelerations are substituted by the desired forces, using $\dot{x}^* = F_x^*/m$, $x \in \{u, v, w\}$ in the non-linear block of the inverse translation dynamics $\mathbf{F}_{123}^{-1}$, compare Eqs. 4.7-4.8 and Eq. 4.11:

$$F_3^{MR*} = -F_3^{H*} \sec(\varphi) \sec(\theta) \tag{5.74}$$

$$\varphi^* = \arcsin\left(\left(-F_1^{H*} \sin(\psi) + F_2^{H*} \cos(\psi)\right) / F_3^{MR*} \right) \tag{5.75}$$

$$\theta^* = \arcsin\left(\left(F_1^{H*} \cos(\psi) + F_2^{H*} \sin(\psi)\right) \sec(\varphi) / F_3^{MR*} \right) \tag{5.76}$$

The desired main-rotor force F_3^{MR*} is calculated from the desired force F_3^{H*}, taking the current orientation of the main-rotor into account. This ensures that, independent from the current orientation[8] of $\mathbf{F}_3^{MR*}$, the desired force F_3^{H*} is generated by the main-rotor. In order to create the linear force generator model the equation is linearized. Assuming small angle approximations, with $\sec(\varphi) = \sec(\theta) = 1$, the equation simplifies to $F_3^{MR*} = -F_3^{H*}$.

[8] This is valid, because only non acrobatic flight is considered in this work and therefore $-\pi/4 > \varphi < \pi/4$ and $-\pi/4 > \theta < \pi/4$ are assumed.

Eqs. 5.75-5.76 describe the calculation of desired angles from desired forces. Based on the current helicopter heading ψ the forces $F_{1,2}^{H*}$ are distributed onto the desired angles(φ^*, θ^*). Since the heading is not part of the final force generator model an arbitrary value for ψ can be chosen. To simplify the equations $\psi = 0$ is selected. Using the small-angle approximation with $x = \arcsin(x)$ and $\sec(\varphi) = 1$, the equations simplify to $\varphi^* = F_2^{H*}/F_3^{MR*}$ and $\theta^* = F_1^{H*}/F_3^{MR*}$.

In the non-linear blocks of the translation dynamics $\mathbf{F}_{123}$, compare Eqs. 3.18-3.20, the accelerations are substituted by forces, utilizing $F_x^H = \dot{x}\, m$, $x \in \{u, v, w\}$. Here, the force F_2^{TR} has been neglected:

$$F_1^H = F_3^{MR}(\cos(\varphi)\sin(\theta)\cos(\psi) - \sin(\varphi)\sin(\psi)) \tag{5.77}$$
$$F_2^H = F_3^{MR}(\cos(\varphi)\sin(\theta)\sin(\psi) + \sin(\varphi)\cos(\psi)) \tag{5.78}$$
$$F_3^H = -F_3^{MR}\cos(\varphi)\cos(\theta) \tag{5.79}$$

Similar to the inverse translation dynamics, Eqs. 5.77-5.79 are simplified using small angle approximations. The heading is zero ($\psi = 0$) like above. The simplified equations become $F_1^H = F_3^{MR}\,\theta$, $F_2^H = F_3^{MR}\,\varphi$ and $F_3^H = -F_3^{MR}$.

Almost all equations of the force generator model are derived by now. However, to combine the linear equations of the translation dynamics, one equation is still missing. Eqs. 5.72-5.73 describe the dynamic generation of of angles from the desired angles and something similar is needed for the generation of main-rotor force from desired main-rotor force. The equation $F_3^{MR} = F_3^{MR*}\,G_{FMR3}$ is introduced, where G_{FMR3} is a transfer function, which describes the dynamics of the main-rotor force generation. In Eqs. 5.72-5.73 a first order delay is used, to model the time delay caused by the aerodynamics and the dynamics of the actuators. Two transfer function definitions are proposed. A first order delay $G_{FMR3} = t_{df}/(s + t_{df})$ with $t_{df} \gg t_d$ or a static gain with $G_{FMR3} = 1$. Since the generation of the main-rotor force is a much faster process than the rotation dynamics of the helicopter, the transfer function $G_{FMR3} = 1$ is proposed. The final force generator equations are derived using the linear equations of the translation dynamics and the transfer functions for angles and force:

$$F_1^H = F_3^{MR}\,G_{\varphi,\theta}\,F_1^{H*}\,G_{FMR3}/F_3^{MR} = G_{\varphi,\theta}\,G_{FMR3}\,F_1^{H*} \tag{5.80}$$
$$F_2^H = F_3^{MR}\,G_{\varphi,\theta}\,F_2^{H*}\,G_{FMR3}/F_3^{MR} = G_{\varphi,\theta}\,G_{FMR3}\,F_2^{H*} \tag{5.81}$$
$$F_3^H = G_{FMR3}\,F_3^{H*} \tag{5.82}$$

$G_{\varphi,\theta}$ is either $G_{\varphi,\theta}^{SF}$ or $G_{\varphi,\theta}^{BF}$, depending on the fuselage size of the modeled helicopter.

Model Validation Eqs. 5.80-5.82 are validated against the non-linear helicopter model. The force generator is used to produce forces acting on a single mass point, with a mass similar to the helicopter. Both, the non-linear helicopter model and the linear force generator model, use the same translation controller. The control loop is closed using the feedback of the non-linear model. The resulting control signals are applied to both models. Therefore, the motion of the mass point is governed by open loop control signals. The translation of the mass point is compared to the translation of the full model. The

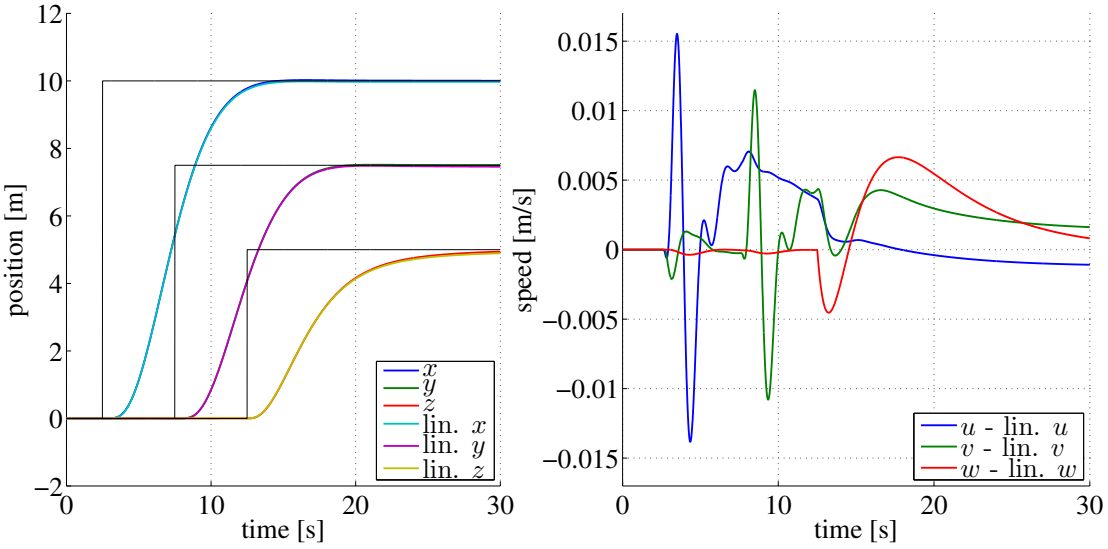

Figure 5.16: Comparison non-linear model and linear force generator model

non-linear model uses a dead-time of 120 ms for the generation of the torques, whereas the force generator uses the first order delay with$t_d = {}^1/_{0.12\,s}$.

The results of the comparison are shown in Fig. 5.16. The left part of the figure shows the response to three steps of 10 m, 7.5 m and 5 m, along different axis, for the non-linear model (x, y, z) and the linear model (x_{lin}, y_{lin}, z_{lin}). The motion of non-linear and linear model is almost similar, in fact most of the time it is difficult to distinguish the non-linear and linear trajectories. Therefore, the difference between both models is emphasized in the right part of the figure. The speed differences of both models are plotted, during the motion depicted on the left side. With a maximum difference of 1.6 $^{cm}/_{s}$ the motions of both models show close correspondence. Therefore, the force generator model is considered to be a very good approximation of the non-linear controller and the non-linear model.

5.2.2 Translational Model for Single- and Dual-Lift Configurations

This section describes the linear models used for the design of single- and dual-lift translation controllers. Unlike the force generator model, which is usable for all configurations, the translational models need to account for the load's DoF. The load has two remaining DoF for the single-lift configuration, which allows a spherical motion of the load, whereas the dual-lift configuration has only one DoF, which allows only a one dimensional circular motion. Nevertheless, the model, discussed in this section, is used for design of the single- and dual-lift translation controllers. The reason is, that the dual-lift translation controller is based on the application of two independent single-lift controllers. The model is therefore applicable for the dual-lift controller as well.

After the derivation of the translational model, it is compared to a roll-pendulum

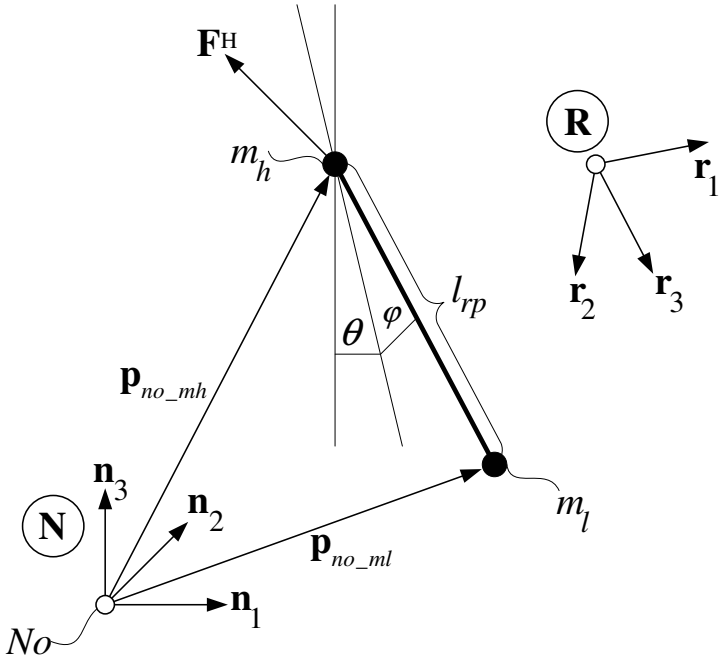

Figure 5.17: Pendulum composed of two mass points

model, in non-linear and linear form. The comparison serves verification purposes, since the roll-pendulum model is commonly known and often used as a textbook example, see e.g. [Kuy08]. To avoid confusion, the roll-pendulum model is referenced within this section as *roll-pendulum model*, whereas the derived model is plainly referred as *pendulum model*.

In Fig. 5.17 a pendulum consisting of two mass points is depicted. Both mass points are able to move in three dimensional space, relative to a Newtonian frame $\mathbf{N}$. They are connected by a rigid and massless rope of length l_{rp}. The mass point with the mass m_h is referenced as *helicopter mass point* and the mass point with the mass m_l is referenced as *load mass point*. The mass points are exposed to the gravity forces $\mathbf{F}^G_{\{l,h\}} = -m_{\{l,h\}}\, g\, \mathbf{n}_3$ and to a control force $\mathbf{F}^H = F^H_1\, \mathbf{n}_1 + F^H_2\, \mathbf{n}_2 + F^H_3\, \mathbf{n}_3$, which is acting on the *helicopter mass point*. For simplicity the gravity forces are not drawn in Fig. 5.17. The position of the *helicopter mass point* is described by the vector $\mathbf{p}_{no\_mh} = x\, \mathbf{n}_1 + y\, \mathbf{n}_2 + z\, \mathbf{n}_3$ and the position of the *load mass point* is given relative to the *helicopter mass point*, using the angles φ and θ:

$$\begin{aligned} \mathbf{p}_{no\_ml} &= \mathbf{p}_{no\_mh} + l_{rp}(\cos(\varphi)\sin(\theta)\, \mathbf{n}_1 + \sin(\varphi)\, \mathbf{n}_2 - \cos(\varphi)\cos(\theta)\, \mathbf{n}_3) \quad (5.83) \\ &= \mathbf{p}_{no\_mh} + l_{rp}\, \mathbf{r}_3 \quad (5.84) \end{aligned}$$

The angles φ and θ are taken relative to a reference frame $\mathbf{R}$. The static transition from $\mathbf{N}$ to the initial configuration of $\mathbf{R}$ is given by a rotation of π rad around $\mathbf{n}_1$. The angle θ describes a rotation around $\mathbf{r}_2$ and φ describes a rotation around the changed axis $\mathbf{r}'_1$.

The speeds u, v, w are defined through differentiation of $\mathbf{p}_{no\_mh}$ with respect to the frame $\mathbf{N}$:

$$\mathbf{v}_{no\_mh} = \frac{d^{\mathbf{N}}\mathbf{p_{no\_mh}}}{dt} = u\,\mathbf{n}_1 + v\,\mathbf{n}_2 + w\,\mathbf{n}_3 \tag{5.85}$$

The angular speeds p, q of the of the frame $\mathbf{R}$ relative to $\mathbf{N}$ are defined, using the angular velocity vector of $\mathbf{R}$ in $\mathbf{N}$:

$$\omega_{\mathbf{R-N}} = -p\,\mathbf{r}_1 - \cos(\varphi)\,q\,\mathbf{r}_2 + \sin(\varphi)\,q\,\mathbf{r}_3 \tag{5.86}$$

Therefore, the kinematic of the model is described by the following equations:

$$\begin{aligned} \dot{x} &= u \\ \dot{y} &= v \\ \dot{z} &= w \\ \dot{\varphi} &= p \\ \dot{\theta} &= q \end{aligned} \tag{5.87}$$

The Kane method is used to derive the dynamic equations of the model, and the software Autolev is used to get the equations in explicit form. To compact Eqs. 5.88-5.92, the sinus and cosine terms are written in abbreviated form: $s_x^y = \sin(x)^y$ and $c_x^y = \cos(x)^y$.

$$\begin{aligned} \dot{u} &= \Big(F_1^H\left(m_h + m_l - m_l\,c_\varphi^2 s_\theta^2\right) - F_2^H\,m_l\,c_\varphi s_\varphi s_\theta + F_3^H\,m_l\,c_\varphi^2 c_\theta s_\theta \\ &\quad + \Big(l_{rp}\,m_h\,m_l\,c_\varphi s_\theta(p^2 + q^2\,c_\varphi^2)\Big)\Big)/(m_h(m_h + m_l)) \end{aligned} \tag{5.88}$$

$$\begin{aligned} \dot{v} &= \Big(-F_1^H\,m_l\,c_\varphi s_\varphi s_\theta + F_2^H\left(m_h + m_l\,c_\varphi^2\right) + F_3^H\,m_l\,c_\varphi s_\varphi c_\theta \\ &\quad + \Big(l_{rp}\,m_h\,m_l\,s_\varphi(p^2 + q^2\,c_\varphi^2)\Big)\Big)/(m_h(m_h + m_l)) \end{aligned} \tag{5.89}$$

$$\begin{aligned} \dot{w} &= \Big(F_1^H\,m_l\,c_\varphi^2 c_\theta s_\theta + F_2^H\,m_l\,c_\varphi c_\theta s_\varphi + F_3^H\left(m_h + m_l - m_l\,c_\varphi^2 c_\theta^2\right) \\ &\quad + \Big(-g\,m_h(m_h + m_l) - l_{rp}\,m_h\,m_l\,c_\varphi c_\theta(p^2 + q^2\,c_\varphi^2)\Big)\Big)/(m_h(m_h + m_l)) \end{aligned} \tag{5.90}$$

$$\dot{p} = \frac{F_1^H\,s_\varphi s_\theta - F_2^H\,c_\varphi - F_3^H\,c_\theta s_\varphi - l_{rp}\,m_h\,q^2\,c_\varphi s_\varphi}{l_{rp}\,m_h} \tag{5.91}$$

$$\dot{q} = \frac{-F_1^H\,c_\theta - F_3^H\,s_\theta + 2\,l_{rp}\,m_h\,q\,p\,s_\varphi}{l_{rp}\,m_h\,c_\varphi} \tag{5.92}$$

All equations of the non-linear *pendulum model* are derived and a comparison to a *roll-pendulum model* becomes possible. The roll-pendulum described by Kuypers [Kuy08] is taken as reference. The reference model is two dimensional and therefore the motion of

the *pendulum model* is considered[9] only in the $\mathbf{n}_{1,3}$-plane. For that reason, $y = \varphi = v = p = 0$ is assumed and only Eq. 5.88, Eq. 5.90 and Eq. 5.92 are used. The kinematic equations of both models are equal[10]: $\dot{x} = u$ and $\dot{\theta} = q$. The upper roll-pendulum mass point, which corresponds to the *helicopter mass point* of the *pendulum model*, is moving on a track without friction and therefore the motion along $\mathbf{n}_3$ needs to be restricted as well for the *pendulum model*. To achieve this behavior, Eq. 5.90 is set to zero and solved for F_3^H. The resulting equation is inserted into Eq. 5.88 and Eq. 5.92 and the results are simplified into the following two equations:

$$\dot{u} = \frac{F_1^H + m_l \sin(\theta)\,(l_{rp}\,q^2 + g\,\cos(\theta))}{m_h + m_l \sin(\theta)^2} \tag{5.93}$$

$$\dot{q} = -\frac{g\,(m_h + m_L)\,\sin(\theta) + \cos(\theta)\,(F_1^H + l_{rp}\,m_l\,q^2\,\sin(\theta))}{l_{rp}\,(m_h + m_l \sin(\theta)^2)} \tag{5.94}$$

The structure[11] of Eqs. 5.93-5.94 is similar to the structure of the roll-pendulum equations. No force can be applied to the upper mass point of Kuypers' model, which is the only difference. The equations become equal, if F_1^H is set to zero.
The transfer functions of the *roll-pendulum model* are derived to compare *roll-pendulum model* and linearized pendulum model. The transfer functions of the position x and the angle θ are needed for the comparison, where the force F_1^H is used as control input. The dynamic Eqs. 5.93-5.94 are linearized at the equilibrium ($F_1^H = 0$, $\theta = 0$, $q = 0$). The kinematic equations $\dot{x} = u$ and $\dot{\theta} = q$ are already linear. The transfer functions are calculated from the resulting linear system:

$$G_x^{rpd} = \frac{l_{rp}\,s^2 + g}{l_{rp}\,m_h\,s^4 + g\,(m_h + m_l)\,s^2} \tag{5.95}$$

$$G_\theta^{rpd} = -\frac{1}{l_{rp}\,m_h\,s^2 + g\,(m_h + m_L)} \tag{5.96}$$

The kinematic equations of the *pendulum model* are already linear, see Eqs. 5.87, and therefore only the dynamic equations Eq. 5.93-5.94 need to be linearized. The linearisation is conducted using the equilibrium conditions φ, θ, p, $q = 0$, $F_{1,2}^H = 0$ and $F_3^H = g\,(m_h + m_L)$. The state- and the control-vector of the model are defined as $\mathbf{X} = (x,\, y,\, z,\, \varphi,\, \theta,\, u,\, v,\, w,\, p,\, q)^T$ and $\mathbf{U} = (F_1^H, F_2^H, F_3^H)$. Based on these definitions and conditions, the following linear state space model is derived.

[9] The $\mathbf{n}_{2,3}$-plane could have been used as well.
[10] Kuypers uses different variable names, $x, \dot{x}, \ddot{x}, \alpha, \dot{\alpha}, \ddot{\alpha}$ instead of $x, u, \dot{u}, \theta, q, \dot{q}$.
[11] The equations presented in [Kuy08] need to be transformed into a shape similar to Eqs. 5.93-5.94. This is achieved by solving the equations for the second order derivatives ($\ddot{x}$, $\ddot{\alpha}$).

$$\underbrace{\begin{bmatrix} & \mathbf{0}(5\times 5) & & \mathbf{I}(5\times 5) \\ 0 & 0 & 0 & 0 & \frac{g\,m_l}{m_h} & \\ 0 & 0 & 0 & \frac{g\,m_l}{m_h} & 0 & \\ 0 & 0 & 0 & 0 & 0 & \mathbf{0}(5\times 5) \\ 0 & 0 & 0 & -\frac{g\,(m_l+m_h)}{l_{rp}\,m_h} & 0 & \\ 0 & 0 & 0 & 0 & -\frac{g\,(m_l+m_h)}{l_{rp}\,m_h} & \end{bmatrix}}_{=\mathbf{A}} \underbrace{\begin{bmatrix} 0 & 0 & 0 \\ 0 & 0 & 0 \\ 0 & 0 & 0 \\ 0 & 0 & 0 \\ 0 & 0 & 0 \\ \frac{1}{m_h} & 0 & 0 \\ 0 & \frac{1}{m_h} & 0 \\ 0 & 0 & \frac{1}{m_h+m_l} \\ 0 & \frac{-1}{l_{rp}\,m_h} & 0 \\ \frac{-1}{l_{rp}\,m_h} & 0 & 0 \end{bmatrix}}_{=\mathbf{B}}$$

Where $\mathbf{0}(\mathrm{a}\times\mathrm{b})$ is a zero matrix of a rows and b columns and $\mathbf{I}(\mathrm{a}\times\mathrm{a})$ is a identity matrix of a rows and a columns. Through examination of $\mathbf{A}$ and $\mathbf{B}$ it becomes evident, that the linearisation decouples the motion along the different axis of the $\mathbf{N}$-frame completely. The state-vector $\mathbf{X}$ is decomposable into into $\mathbf{X}_x = (x,\, \theta,\, u,\, q)^t$, $\mathbf{X}_y = (y,\, \varphi,\, v,\, p)^t$ and $\mathbf{X}_z = (z,\, w)^t$, and the sub-model associated to $\mathbf{X}_x$ ($\mathbf{X}_y$, $\mathbf{X}_z$) describes the motion of the pendulum along $\mathbf{n}_1(\mathbf{n}_2,\, \mathbf{n}_3)$ respectively. Since, there is no coupling through the system matrix $\mathbf{A}$, the internal motion of each sub-model is independent from the other sub-models. The control-vector $\mathbf{U}$ is decomposable into $U_x = F_1^H$, $U_y = F_2^H$ and $U_z = F_3^H$, where each of the control vectors $U_{x,y,z}$ only influences the corresponding sub-model. Therefore, the state space model is composed of three completely independent sub-models.

For the comparison of the linear *pendulum model* with the linear *roll-pendulum model*, the transfer functions of linear pendulum model need to be calculated. The output matrix $\mathbf{C}$ and the feedthrough matrix $\mathbf{D}$ need to be specified for this calculation. Since the transfer functions of the upper mass point position and pendulum angle are known for the *roll-pendulum model*, only the transfer functions of first five elements of the pendulum state vector need to be calculated: The position x, y, z and angles φ, θ. Therefore, the output matrix $\mathbf{C}$ is defined to be $[\mathbf{I}(\mathbf{5}\times\mathbf{5})\,\mathbf{0}(\mathbf{5}\times\mathbf{5})]$. Since the system has no feedthrough, the matrix $\mathbf{D}$ is defined to be $[\mathbf{0}(\mathbf{5}\times\mathbf{3})]$.

$$\mathbf{G}^{pend} = \begin{bmatrix} G_x & 0 & 0 \\ 0 & G_y & 0 \\ 0 & 0 & G_z \\ 0 & G_\varphi & 0 \\ G_\theta & 0 & 0 \end{bmatrix} \tag{5.97}$$

The transfer functions of the pendulum model are shown in Eq. 5.97, with $G_x = G_y = G_x^{rpd}$, $G_\varphi = G_\theta = G_\theta^{rpd}$ and $G_z = \frac{1}{(m_h+m_l)\,s^2}$. The linear *pendulum model* is therefore composed of two independent linear *roll-pendulum models*, which describe the motion along $\mathbf{n}_{1,2}$, and a double integrator, which describes the motion along $\mathbf{n}_3$.

This is an important property of the linear model, which is utilized during the controller design in Sec. 6.3. The translation controllers for the different axes are designed

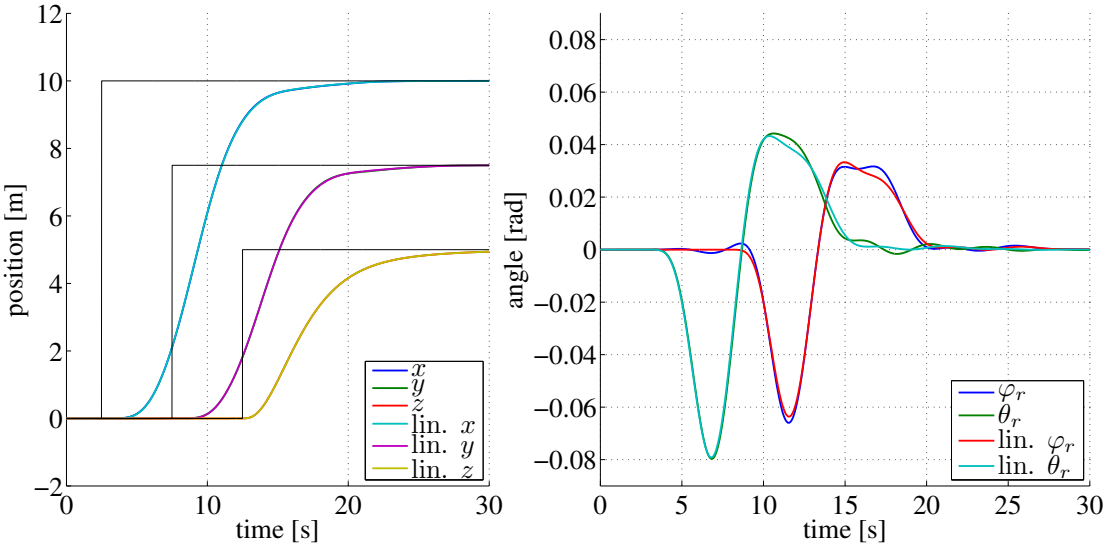

Figure 5.18: Comparison of non-linear and linear models of a single-lift configuration (position)

independently, because the motion in each axis is decoupled. The translation controllers, for the motion along $\mathbf{n}_{1,2}$, are based on the linear *roll-pendulum model* and the translation controller along $\mathbf{n}_3$ is based on a double integrator.

Model Validation The linear *pendulum model* and the linear *force generator model* are combined, to create a linear model of a single-lift load transportation configuration.

$$\mathbf{G}^{slc} = \begin{bmatrix} G_{\varphi,\theta}G_x & 0 & 0 \\ 0 & G_{\varphi,\theta}G_y & 0 \\ 0 & 0 & G_z \\ 0 & G_{\varphi,\theta}G_\varphi & 0 \\ G_{\varphi,\theta}G_\theta & 0 & 0 \end{bmatrix} \tag{5.98}$$

Eq. 5.98 describes the linear model, which is compared to the non-linear model of a single-lift configuration. The generic orientation controller, which is described in detail in Sec. 6.2, is used to stabilize the orientation of the non-linear model. The controller coefficients have been chosen similar to those used for the derivation of the *force generator model*. Two equal translation controllers are applied to the models, see Sec. 6.3. The controller loops are closed individually, using the feedback from the corresponding model. The non-linear model uses a dead-time of 120 ms for the generation of the torques, whereas the linear model uses the first order delay with $t_d = 1/0.12\,s$.

The results of the comparison are shown in Fig. 5.18. The left part of the figure shows the response to three steps of 10 m, 7.5 m and 5 m, along different axis, for the non-linear model (x, y, z) and the linear model (x_{lin}, y_{lin}, z_{lin}). The trajectories of non-linear and

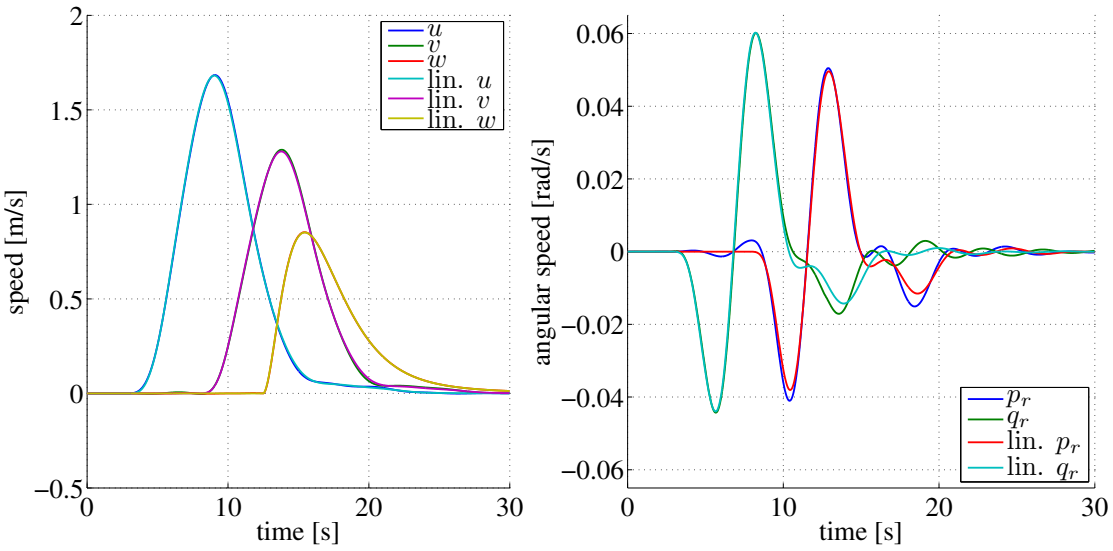

Figure 5.19: Comparison of non-linear and linear models of a single-lift configuration (speed)

linear model are almost equal and it is difficult to distinguish them. The right part of Fig. 5.18 shows the rope angles, during the motion depicted in the left part of the figure. The angles calculated by the linear and non-linear model are almost similar, but close to the maxima, at approx. 12 s and 17.5 s, deviations are visible. The maximum deviation is approximately 0.0041 rad. In Fig. 5.19 the speeds of the non-linear and linear model are compared. The translational motion of both models is almost indistinguishable, similar to Fig. 5.18. Only the angular speeds show some minor deviations about $\pm 0.003\,^{\mathrm{rad}}/_{\mathrm{s}}$.

The main reasons for the angular deviations are the non-linear coupling of rope angles, which has been lost in the linearisation process, and the use of different rope mounting points. The rope is mounted in the *helicopter mass point* of the linear model, whereas the rope of the non-linear model is attached to the helicopter fuselage, 0.3 m below the CoM of the helicopter. Like discussed in Sec. 6.1, the attachment of the rope in a point different from the CoM of the helicopter creates torques. The generic orientation controller compensates these torques, using feed forward techniques. However, the compensation is not perfect. The maximum deviation between linear and non-linear model reduces to 0.0015 rad, if the rope is attached in the CoM of the non-linear model and the steps along $\mathbf{n}_1$ and $\mathbf{n}_2$ are not executed simultaneously.

In summary, the translational and angular correspondence, between linear and non-linear model, is considered to be very good. The exposed similarity is more than sufficient for the main purpose of the model; the design of the single- and dual-lift translation controller.

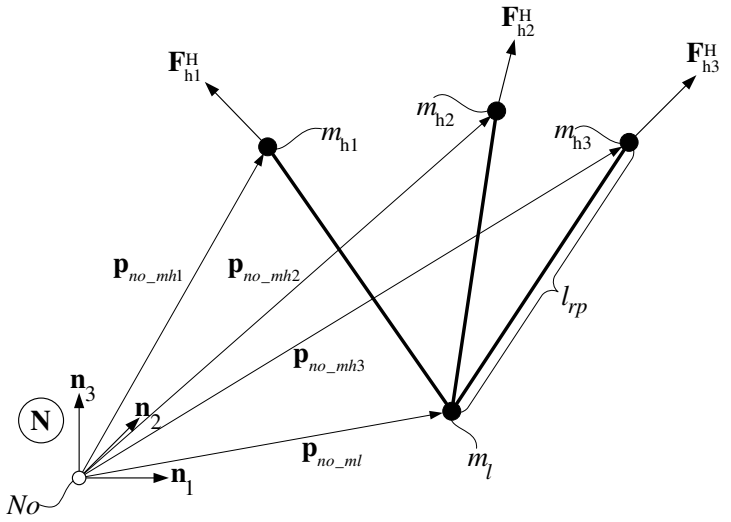

Figure 5.20: Simple translational model for the multi-lift configurations

5.2.3 Translational Model for Multi-Lift Configurations

This section describes a translational model for multi-lift configurations. The model is used for the design of one translation controller described in Sec. 6.4. Its main purpose is the calculation of the inverse translation dynamics, which is required by the controller. In Fig. 5.20 the multi-lift configuration, described by the model, is depicted. The helicopters as well as the load are simplified as mass points. The helicopter mass points are connected to the load mass point by ropes, which are assumed to be always under tension, and are modeled to be rigid and massless. The mass points are exposed to gravity forces $\mathbf{F}_i^G = -m_i\, g\, \mathbf{n}_3$ $(i \in \{1,2,3,l\})$, which are not drawn in Fig. 5.20. The control forces $\mathbf{F^H_{hi}} = F^H_{hi,1}\, \mathbf{n}_1 + F^H_{hi,2}\, \mathbf{n}_2 + F^H_{hi,3}\, \mathbf{n}_3$ are acting on the helicopter mass points. The position of the i'th helicopter mass point is described by the vector $\mathbf{p}_{no\_mhi}$ and the position of the load mass point is given by the vector $\mathbf{p}_{no\_ml}$. Both vectors are defined relative to the Newtonian reference frame $\mathbf{N}$ as follows:

$$\mathbf{p}_{no\_mhi} = x_{hi}\, \mathbf{n}_1 + y_{hi}\, \mathbf{n}_2 + z_{hi}\, \mathbf{n}_3 \tag{5.99}$$

$$\mathbf{p}_{no\_ml} = x_l\, \mathbf{n}_1 + y_l\, \mathbf{n}_2 + z_l\, \mathbf{n}_3 \tag{5.100}$$

The speeds of the mass points are defined through differentiation of $\mathbf{p}_{no\_mhi}$ and $\mathbf{p}_{no\_ml}$ with respect to the frame $\mathbf{N}$:

$$\mathbf{v}_{no\_mhi} = \frac{d^{\mathbf{N}}\mathbf{p}_{no\_mhi}}{dt} = u_{hi}\, \mathbf{n}_1 + v_{hi}\, \mathbf{n}_2 + w_{hi}\, \mathbf{n}_3 \tag{5.101}$$

$$\mathbf{v}_{no\_ml} = \frac{d^{\mathbf{N}}\mathbf{p}_{no\_ml}}{dt} = u_l\, \mathbf{n}_1 + v_l\, \mathbf{n}_2 + w_l\, \mathbf{n}_3 \tag{5.102}$$

The kinematic equations of the model are read directly from Eq. 5.101 and Eq. 5.102. The state vector of the model is defined as follows:

$$\mathbf{q} = [x_{h1},\, y_{h1},\, z_{h1},\, x_{h2},\, y_{h2},\, z_{h2},\, x_{h3},\, y_{h3},\, z_{h3},\, x_l,\, y_l,\, z_l]^t \tag{5.103}$$

$$\dot{\mathbf{q}} = [u_{h1},\, v_{h1},\, w_{h1},\, u_{h2},\, v_{h2},\, w_{h2},\, u_{h3},\, v_{h3},\, w_{h3},\, u_l,\, v_l,\, w_l]^t \tag{5.104}$$

$$\mathbf{x} = [\mathbf{q};\, \dot{\mathbf{q}}] \tag{5.105}$$

The state vector of the model consists of 24 variables, describing a system with potential 12 DoF. However, the mass points are connected by rigid and massless ropes. Therefore, each helicopter mass point restricts the motion and reduces the DoF of the load mass point by one. Since the kinematic equations do not account for these dependencies, they need to be considered in the system dynamics. This is achieved through the constraint of speeds or accelerations. In Sec. 5.1.3 the Kane method has been utilized to generate the dynamic equations, using velocity constrains. However, in this section the method described by Udwadia and Kalaba is used to generate the dynamic equations. The method of Udwadia and Kalaba is described in detail in [UK92, UK96b, UK96a]. This method has been chosen in attempt to generate a compact set of dynamic equations. Like discussed in Sec. 5.1.3, the Kane methods generates the equations in an implicit from. These equations need to be solved for the accelerations. Depending on the coupling of the implicit equations the explicit solution is compact (weak coupling) or very large (strong coupling). In contrast, the method described by Udwadia and Kalaba generates the dynamic equations directly in explicit form. The dynamic equations generated by the method of Udwadia and Kalaba are in fact more compact than the equations generated by the Kane method. The method of Udwadia and Kalaba has been applied, since a compact set of equations is beneficial for the derivation of the model's inverse dynamics.

The method of Udwadia and Kalaba uses several constraint equations to restrict the motion of the model. These constraints describe the fact, that the distance between helicopters and load is constant. They are similar to simplified constraints of *multi-lift model*, compare Eq. 5.50:

$$(\mathbf{p}_{no\_mhi} - \mathbf{p}_{no\_ml})^2 - l_{rp}^2 = 0 \tag{5.106}$$

The distance between the helicopter mass-point m_{hi} and the load mass-point m_l equals the rope length. This is a valid constraint, since the ropes are defined to be rigid and massless. However, to be usable for the method of Udwadia and Kalaba, the constraint needs to be expressed in terms of accelerations. Therefore, Eq. 5.106 is differentiated twice with respect to time and relative to the Newtonian frame $\mathbf{N}$:

$$\begin{aligned} \frac{d_2^{\mathbf{N}}(\mathbf{p}_{no\_mhi} - \mathbf{p}_{no\_ml})^2/2 - l_{rp}^2/2}{dt} &= (u_{hi} - u_l)^2 + (v_{hi} - v_l)^2 + (w_{hi} - w_l)^2 \\ &\quad +(x_{hi} - x_l)(\dot{u}_{hi} - \dot{u}_l) \\ &\quad +(y_{hi} - y_l)(\dot{v}_{hi} - \dot{v}_l) \\ &\quad +(z_{hi} - z_l)(\dot{w}_{hi} - \dot{w}_l) \end{aligned} \tag{5.107}$$

Based on Eq. 5.107 the constraint matrix $\mathbf{A}$ is derived:

$$\begin{bmatrix} dx_{h1} & dy_{h1} & dz_{h1} & 0 & 0 & 0 & 0 & 0 & 0 & -dx_{h1} & -dy_{h1} & -dz_{h1} \\ 0 & 0 & 0 & dx_{h2} & dy_{h2} & dz_{h2} & 0 & 0 & 0 & -dx_{h2} & -dy_{h2} & -dz_{h2} \\ 0 & 0 & 0 & 0 & 0 & 0 & dx_{h3} & dy_{h3} & dz_{h3} & -dx_{h3} & -dy_{h3} & -dz_{h3} \end{bmatrix} = \mathbf{A}$$

With $dx_{hi} = x_{hi} - x_l$, $dy_{hi} = y_{hi} - y_l$ and $dz_{hi} = z_{hi} - z_l$. Additional the constraint vector $\mathbf{b}$ is derived based on Eq. 5.107:

$$\mathbf{b} = \begin{bmatrix} -(\dot{x}_{h1} - \dot{x}_l) - (\dot{y}_{h1} - \dot{y}_l) - (\dot{z}_{h1} - \dot{z}_l) \\ -(\dot{x}_{h2} - \dot{x}_l) - (\dot{y}_{h2} - \dot{y}_l) - (\dot{z}_{h2} - \dot{z}_l) \\ -(\dot{x}_{h3} - \dot{x}_l) - (\dot{y}_{h3} - \dot{y}_l) - (\dot{z}_{h3} - \dot{z}_l) \end{bmatrix}$$

The matrix $\mathbf{M}$ describes the mass distribution of the system and is defined as follows:

$$\mathbf{M} = \begin{bmatrix} \mathbf{I(3x3)}\, m_{h1} & & & \\ & \mathbf{I(3x3)}\, m_{h2} & & \\ & & \mathbf{I(3x3)}\, m_{h3} & \\ & & & \mathbf{I(3x3)}\, m_l \end{bmatrix}$$

Finally, the vector $\mathbf{a}$ needs to be defined, which describes the unconstrained acceleration of the system. The unconstrained acceleration of a helicopter mass point m_{hi} is given by the auxiliary vector $\mathbf{a}_{hi}$. The mass point is subjected to the helicopter force $\mathbf{F^H_{hi}}$ and the gravitational force $\mathbf{F^G_i}$. The unconstrained acceleration of the load mass point m_l is described by the auxiliary vector $\mathbf{a}_l$, where only the gravitational force $\mathbf{F^G_l}$ is acting on the load mass point. Therefore, $\mathbf{a}$, $\mathbf{a}_{hi}$ and $\mathbf{a}_l$ are defined in coordinates of $\mathbf{N}$ as follows:

$$\mathbf{a}_{hi} = [F^H_{hi,1}/m_{hi},\, F^H_{hi,2}/m_{hi},\, F^H_{hi,3}/m_{hi} - g]^t \tag{5.108}$$

$$\mathbf{a}_l = [0,\, 0,\, -g]^t \tag{5.109}$$

$$\mathbf{a} = [\mathbf{a}_{h1};\, \mathbf{a}_{h2};\, \mathbf{a}_{h3};\, \mathbf{a}_l] \tag{5.110}$$

The acceleration of the constrained system is given by the following equation:

$$\ddot{\mathbf{q}} = \mathbf{a} + \mathbf{M}^{-1}\mathbf{A}^t(\mathbf{A}\mathbf{M}^{-1}\mathbf{A}^t)^*(\mathbf{b} - \mathbf{A}\mathbf{a}) \tag{5.111}$$

Where $(\ldots)^*$ denotes the Moore-Penrose-Inverse of the term within the brackets. Since $\mathbf{M}$ is a diagonal matrix of full rank, $\mathbf{M}^{-1}$ is calculated easily. However, the calculation of the Moore-Penrose-Inverse of $\mathbf{A}\mathbf{M}^{-1}\mathbf{A}^t$ results in a large matrix. It should be noted that for this specific case it is possible to calculate $(\mathbf{A}\mathbf{M}^{-1}\mathbf{A}^t)^{-1}$ instead of $(\mathbf{A}\mathbf{M}^{-1}\mathbf{A}^t)^*$, since $(\mathbf{A}\mathbf{M}^{-1}\mathbf{A}^t)$ is a square (3×3) matrix of full rank. Although the pseudo-inverse and the inverse are equal for every square matrix of full rank, the complexity of the result varies, depending on the matrix and the used software tool. Mathematica has been used for the symbolic calculations and the calculation of $(\mathbf{A}\mathbf{M}^{-1}\mathbf{A}^t)^*$ results into a very large matrix, which is equivalent to $(\mathbf{A}\mathbf{M}^{-1}\mathbf{A}^t)^{-1}$. However, the calculated result

of $(\mathbf{A}\mathbf{M}^{-1}\mathbf{A}^t)^{-1}$ is more compact and it has not been possible[12] to simplify the pseudo-inverse into a similar compact form. Therefore, it is important to calculate $(\mathbf{A}\mathbf{M}^{-1}\mathbf{A}^t)^{-1}$ instead of $(\mathbf{A}\mathbf{M}^{-1}\mathbf{A}^t)^*$. The explicit result of Eq. 5.111 is too complex to be presentable in this thesis. However, the complete Eq. 5.111 is presented in the additional equations document, which is accompanying this thesis on CD, see [Ber13, page 86ff.].

Model Inversion One of the translation controllers presented in Sec. 6.4 is based on the inverse translation dynamics of this model. For that reason, the inversion of Eq. 5.111 is shortly discussed. The constrained acceleration $\ddot{\mathbf{q}}$ is calculated from the unconstrained acceleration $\mathbf{a}$ with regard to the current system state, using Eq. 5.111. Therefore, the inversion of Eq. 5.111 allows the calculation of the necessary unconstrained acceleration $\mathbf{a}$ to achieve the desired constrained acceleration $\ddot{\mathbf{q}}$. In practice it is beneficial to calculate the force vector $\mathbf{x}$ instead of the acceleration vector $\mathbf{a}$, since the forces are considered to be the system inputs of the model. The vector $\mathbf{x}$ is defined as follows:

$$\mathbf{x}_i = [F^H_{hi,1}, F^H_{hi,2}, F^H_{hi,3}]^t \tag{5.112}$$

$$\mathbf{x} = [\mathbf{x}_{h1}; \mathbf{x}_{h2}; \mathbf{x}_{h3}] \tag{5.113}$$

The vector $\mathbf{x}$ is calculated to be:

$$0 = \mathbf{a} + \mathbf{M}^{-1}\mathbf{A}^t(\mathbf{A}\mathbf{M}^{-1}\mathbf{A}^t)^*(\mathbf{b} - \mathbf{A}\mathbf{a}) - \ddot{\mathbf{q}} \tag{5.114}$$

$$0 = \mathbf{C}\,\mathbf{x} - \mathbf{d} \tag{5.115}$$

The matrices and vectors of Eq. 5.114 are multiplied and expanded into a single vector with 12 elements, which represent twelve equations. The forces $F^H_{hi,j}$ occur only as linear terms in the equations and therefore it is possible to rewrite Eq. 5.114 into Eq. 5.115. The elements of the $\mathbf{C}$ matrix (12×9) represent the coefficients of the forces $F_{hi,j}$ and the elements of the $\mathbf{d}$ vector (12×1) represent the remainder, assuming $F^H_{hi,j} = 0$ for all forces. Finally, Eq. 5.115 is solved for the vector $\mathbf{x}$, to determine the equations of the inverse translation dynamics. Since the vector $\mathbf{x}$ has only 9 elements and the $\mathbf{C}$ matrix has twelve rows, the linear system of equations, represented by $\mathbf{C}\,\mathbf{x} - \mathbf{d}$, is over-determined. The system is solved using a least squares method to derive the solution, which requires the least amount of force for the motion generation. Eq. 5.115 is presented in the additional equations document, which is accompanying this thesis on CD, see [Ber13, page 92ff.]. This concludes the calculation of the inverse translation dynamics. The result is used in Sec. 6.4 for the design of a translation controller.

Model Validation The translational model of the multi-lift configuration is extended by the force generator model, to become comparable to the *multi-lift model*. The force generator model delays the generation of the forces $(F^H_{hi,1}, F^H_{hi,2})$ in the horizontal $\mathbf{n_{1,2}}$-plane. The generic orientation controller, see Sec. 6.2, with control coefficients similar to those utilized by the force generator model, is used to stabilize the orientation of the helicopters of the non-linear model. Two equal translation controllers are applied to the

[12] Because of limited resources and software limitations.

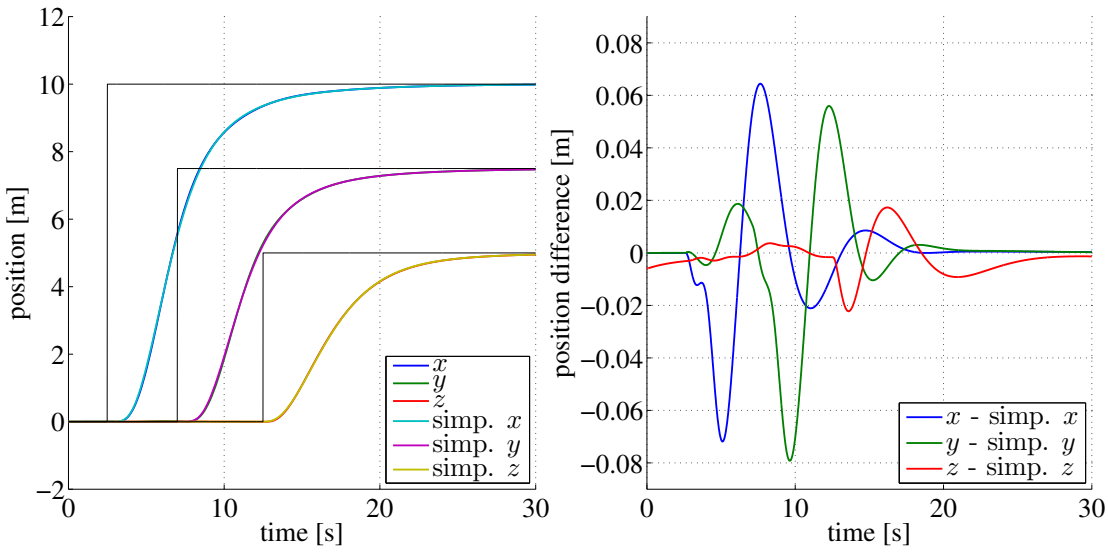

Figure 5.21: Comparison of simplified and complex *multi-lift model* (position)

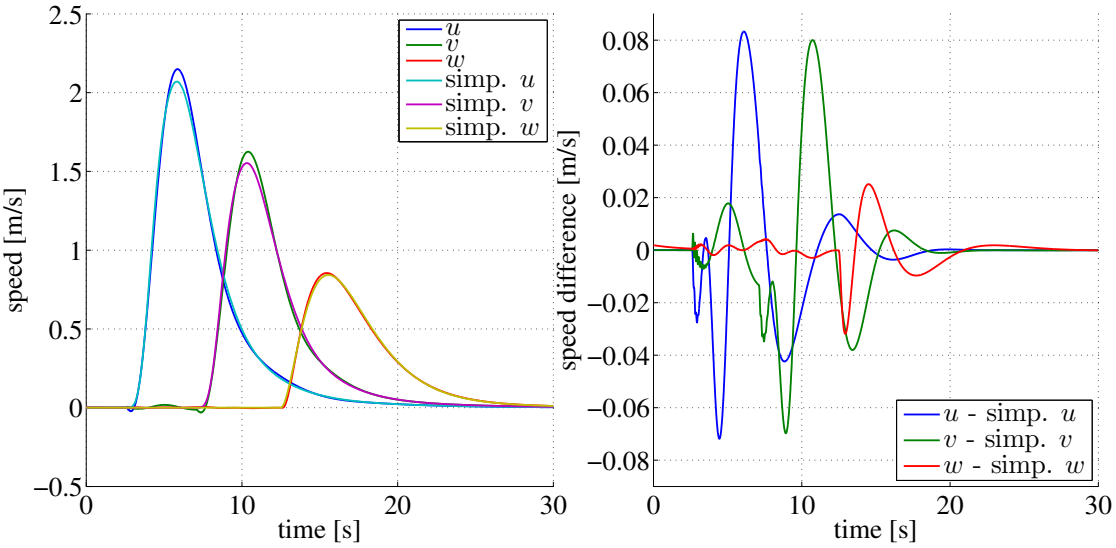

Figure 5.22: Comparison of simplified and complex *multi-lift model* (speed)

models, compare Sec. 6.4. The control loops are closed individually, using the feedback from the corresponding model. The non-linear model uses a dead-time of 120 ms for the generation of the torques, whereas the linear model uses a first order delay with $t_d = {}^{1}/_{0.12\,s}$.

The results of the comparison are shown in Fig. 5.21 and Fig. 5.22. The left part of Fig. 5.21 shows the position of the load for both models in direct comparison. Three steps of 10 m, 7.5 m and 5 m are presented, which were executed after 2.5 s, 5 s and 12.5 s respectively. The trajectories of both models show very good correspondence. The trajectories of both models are almost indistinguishable on the left side of the figure. To empathize the deviations, the difference between the trajectories is plotted in the right part of the figure. A maximum deviation of ±8 cm is depicted, which the author considers to be a very good result. The left part of Fig. 5.22 shows the velocity of the load for both models. The velocity difference is plotted on the right side of the figure. The author considers the depicted deviations of $\pm 8\,{}^{\mathrm{cm}}/_{\mathrm{s}}$ to be a very good result. Similar to the translational model for single- and dual- lift configurations, described in the previous section, the deviation is mainly caused by the different rope mounting points of the models.

In summary, the similarity of the motion between translational and *multi-lift model* is considered to be very good. The exposed similarity is more than sufficient for the main purpose of the model: The translation controller development for the multi-lift configuration.

6 Control of Slung Load Systems

This chapter is devoted to the design of the controllers for single-, dual- and multi-lift slung load configurations. In Sec. 6.1 an analysis of the problems, arising from the attachment of external slung loads to the helicopter fuselage, is presented. After this a discussion of the different control approaches follows. Similar to Ch. 4 the controllers are separated into orientation, see Sec. 6.2, and translation controllers, see Sec. 6.3-6.5. The presented orientation controller compensates the influence of the coupled system on the helicopter orientation. The compensation considers the disturbances caused by the coupling in a generic way and makes the controller independent from the actual slung load configuration. Therefore, only one orientation controller is necessary to cover all slung load configurations presented in this thesis. The design and implementation of this orientation controller has been one of the main challenges, during the creation of a flexible slung load system.

On the contrary, the presented translation controllers are designed specifically for each slung load configuration. The translation controller for single-lift configurations needs to consider two DoF of the load. The primary objective of the controller is to suppress and damp any oscillation of the load. The secondary objective is to move the load to the desired location. The translation controller for dual-lift configurations still needs to consider one DoF of the load and therefore the design objectives of the controller are similar to the single-lift controller. Additionally, the controller needs to keep the helicopters in their flight formation. Especially the separation distance between the helicopters needs to be preserved to avoid collision. The load of a multi-lift configuration has no DoF left and therefore its position is completely governed by the helicopters. For this translation controller the primary objective is to preserve the flight formation of the helicopters and the secondary objective is to move the load to the desired position.

A good estimation of the load position is important for the presented single- and dual-lift translation controllers, as well as for one variant of the multi-lift translation controller. Oscillations of LTD and rope disturb the positions estimation and cause system instabilities, see the discussion in Sec. 5.1.2. Therefore, the observation of the rope/load motion is presented in Sec. 6.6.

6.1 Problem Analysis

The model of a single uncoupled helicopter is the key element for the behavior description of a coupled slung load system. The basis for the modeling of the different slung load configurations and for this analysis is the model described in Sec. 3.1. The main properties of this non-linear model are shortly reviewed. The model is composed of two rigid bodies, the fuselage and the main-rotor disc, and it is augmented by a fist order delay

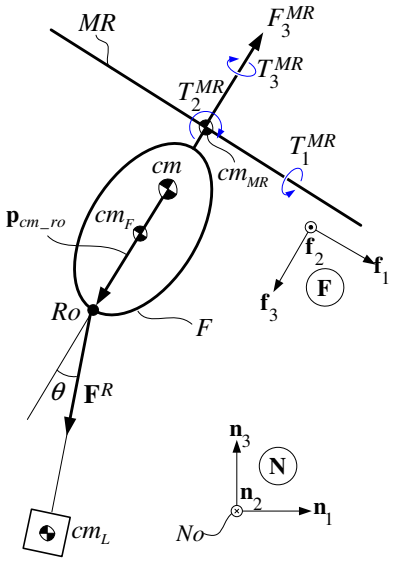

Figure 6.1: Force and torque caused by the attachment of slung loads

as an approximation of the delay caused by the aerodynamics and the dynamics of the actuators. Instead of physical system inputs e.g. actuator positions, abstract system inputs are used. The main-rotor lifting force F_3^{MR}, the main-rotor torques $T_{1,2}^{MR}$ and the tail rotor force F_2^{TR}. The physical system inputs are calculated from the abstract system inputs using algebraic relations, see Sec. 4.1.

The rotation and translation dynamics of the uncoupled helicopter model are linked, compare Eqs. 3.21-3.23 and Eqs. 3.18-3.20. The rotation dynamics influences the orientation of the helicopter and therefore the translation dynamics, but not vice versa. This is also visible in Fig. 3.5, where the arrows are pointing from the blocks of rotation dynamics $\mathbf{W}_{p,q,r}$ to the block of the translation dynamics $\mathbf{F}_{123}$, but not backwards. Therefore, the dynamic behavior of the uncoupled helicopter can be expressed by the following relation[1]:

$$\text{rotation} \Rightarrow \text{translation}$$

In Fig. 6.1 the attachment of the rope to the helicopter fuselage is shown. The vector $\mathbf{p}_{cm\_ro}$ connects the CoM *cm* of the helicopter and the rope attachment point *Ro*. A force $\mathbf{F}^R$ attacking in *Ro* generates a torque $\mathbf{T}^R = \mathbf{p}_{cm\_ro} \times \mathbf{F}^R$ acting on the helicopter, unless *Ro* is directly located in the CoM. In most practical cases it is physically impossible to place *Ro* directly into the CoM and therefore $\mathbf{p}_{cm\_ro} \neq 0$ is assumed. The torque $\mathbf{T}^R$ creates an additional coupling between the helicopter's translation and rotation dynamics. On one hand, the acceleration of the load is influenced by the motion of the point *Ro*, and the force $\mathbf{F}^R$ and torque $\mathbf{T}^R$ are determined by the acceleration of helicopter and load. On the other hand, a torque $\mathbf{T}^R$ leads to the rotation of the helicopter and therefore changes the translation of the helicopter, see the discussion above and Sec. 3.1.

[1]The symbol "⇒" should be read as "leads to".

Finally, this causes also an acceleration of the load. Therefore, the dynamic behavior of the coupled helicopter is expressed by the following relation:

$$\text{rotation} \Leftrightarrow \text{translation}$$

This coupling of rotational and translational motion is the main issue, which is created by the attachment of a slung load to the helicopter fuselage. Even a "simple" translation of the helicopter, e.g. horizontal with constant acceleration, leads to an oscillation of the angle θ. At least for the used small size helicopters and load weights, the torques caused by the load $\mathbf{T}^R$ and the control torques $T_{1,2}^{MR}$ are in the same order of magnitude. For full size helicopters this problem is known well. Since an attachment in the CoM is normally impossible, the rope is attached "underneath" the CoM without lateral or longitudinal offset. This reduces the torques caused by the slung load, at least during hovering. In Sec. 6.2 the generic orientation controller is presented, which is an effective solution to the problem.

6.2 Generic Orientation Controller

The reliable control of the orientation is a requirement for the successful control of small size helicopters. The relation between the orientation of a single uncoupled helicopter and the generation of forces for a translational motion has already been discussed in Sec. 4.3. An important insight has been won based on this discussion: The generation of arbitrary forces, using the main-rotor lifting force F_3^{MR}, requires the reorientation of the main-rotor plane, since the main-rotor lifting force F_3^{MR} is mostly perpendicular to the main-rotor plane, and a magnitude adaption of F_3^{MR}. The attachment of a slung load or the coupling of a slung load system normally creates torques, which act on the helicopter. This creates a strong coupling between the translation and rotation dynamics of the system, and prohibits a direct utilization of the orientation controller for an uncoupled helicopter.

Two orientation controllers, which overcome this problem, are presented in this section. Both orientation controllers are based on the non-linear orientation controller for uncoupled helicopters, presented in Sec. 4.4.

The first controller is depicted in Fig. 6.2. All blocks with gray background are part of the model and the remaining blocks are part of the controller. The controller is similar to the controller presented in Sec. 4.4. Only the block $\mathbf{D}$ is replaced by the block $\tilde{\mathbf{D}}$. The block $\mathbf{D}$ represents the decoupling equations for the rotation dynamics of a single uncoupled helicopter. This block has been directly derived, in Sec. 4.4, from the rotation dynamics of the model, which are partially[2] represented by the block $\mathbf{W}_{pq}$. In contrast to $\mathbf{D}$ the block $\tilde{\mathbf{D}}$ is based on the inverse dynamics of the complete coupled system. The block $\tilde{\mathbf{D}}$ allows the calculation of the torques, required to generate the desired angular speeds, if the complete system state $\mathbf{x}_{sys}$ is known. It should be noted, that the complete system state is composed of the state of the helicopter itself, additionally coupled helicopters and the load.

[2]To improve clearness, the generation of the angular speed r is not included in the drawing.

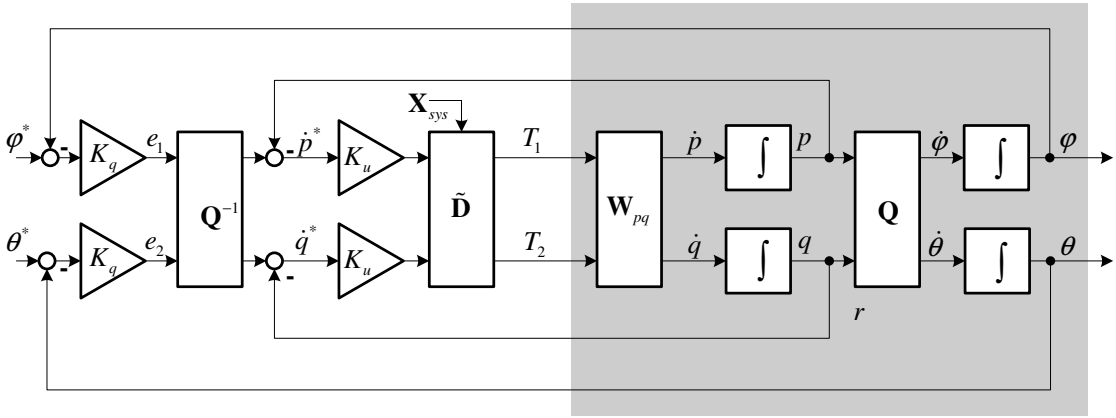

Figure 6.2: Orientation controller, using inverted system dynamics

The calculation of the inversion block $\tilde{\mathbf{D}}$ needs to be discussed for the *single-* and *multi-lift model*. The *single-lift model* has been presented in Sec. 5.1.1. The torques $T_{1,2}^{MR}$ are only present within two equations Eq. 5.20-5.21, which are directly solvable for $T_{1,2}^{MR}$. The reduced[3] system state $\mathbf{x}_{sys} = [\mathbf{q}; \dot{\mathbf{q}}]$, coordinates and speeds, and the derivatives $\ddot{\mathbf{q}} = [\dot{u}, \dot{v}, \dot{w}, \dot{p}, \dot{q}, \dot{r}, \dot{p}_r, \dot{q}_r]^t$ are required to calculate $T_{1,2}^{MR}$. In simulation the estimation of $\ddot{\mathbf{q}}$ is very easy, since $\ddot{\mathbf{q}}$ can be taken directly from the model, before the first integration step. However, it is difficult to estimate $\ddot{\mathbf{q}}$ from sensor data of a real helicopter. Most[4] sensors measure positions or speeds and therefore these measurements need to be numerically differentiated to estimate the accelerations. The presence of noise requires the filtering of the measurement before the numerical differentiation, which introduces additional delay into the estimation of $\ddot{\mathbf{q}}$. Therefore, the inversion is recalculated to avoid an utilization of the accelerations. Eqs. 5.17-5.24 are solved for $(\dot{u}, \dot{v}, \dot{w}, \dot{r}, \dot{p}_r, \dot{q}_r)$ and $T_{1,2}^{MR}$. The resulting equations for $T_{1,2}^{MR}$ depend only on the reduced system state and $(\dot{q}, \dot{p})$, but not on $(\dot{u}, \dot{v}, \dot{w}, \dot{r}, \dot{p}_r, \dot{q}_r)$. Looking at Fig. 6.2 it is noticeable, that $(\dot{q}^*, \dot{p}^*)$ are inputs of the inversion block $\tilde{\mathbf{D}}$ and $(\dot{q}, \dot{p})$ are outputs of the dynamics block $\mathbf{W}_{pq}$. Therefore, $(\dot{q}, \dot{p})$ are renamed to become $(\dot{q}^*, \dot{p}^*)$. Based on this interpretation the equations for $T_{1,2}^{MR}$ depend only on the inputs $(\dot{q}^*, \dot{p}^*)$ and the reduced system state $\mathbf{x}_{sys}$.

The calculation of the inversion block $\tilde{\mathbf{D}}$ for the *multi-lift model*, presented in Sec. 5.1.3, is in general similar to the calculation for the *single-lift model*. However, the author was not able to determine a algebraic solution for $\tilde{\mathbf{D}}$, since the dynamic equations of the *multi-lift model* are highly coupled. Instead, the dynamic equations have been linearized for every time-step and the resulting linear equations are solved using singular-value-decomposition.

Two possible weaknesses of the block $\tilde{\mathbf{D}}$ have been already identified during the design of the inversion based orientation controller. First, $\tilde{\mathbf{D}}$ needs to be specifically designed for every slung load configuration, since the block $\tilde{\mathbf{D}}$ is based on inversion of the dynamic

[3] Without position and velocity of the helicopter's CoM, given by x, y, z and u, v, w.
[4] Except accelerometers, but they require gravitational compensation and additional filtering.

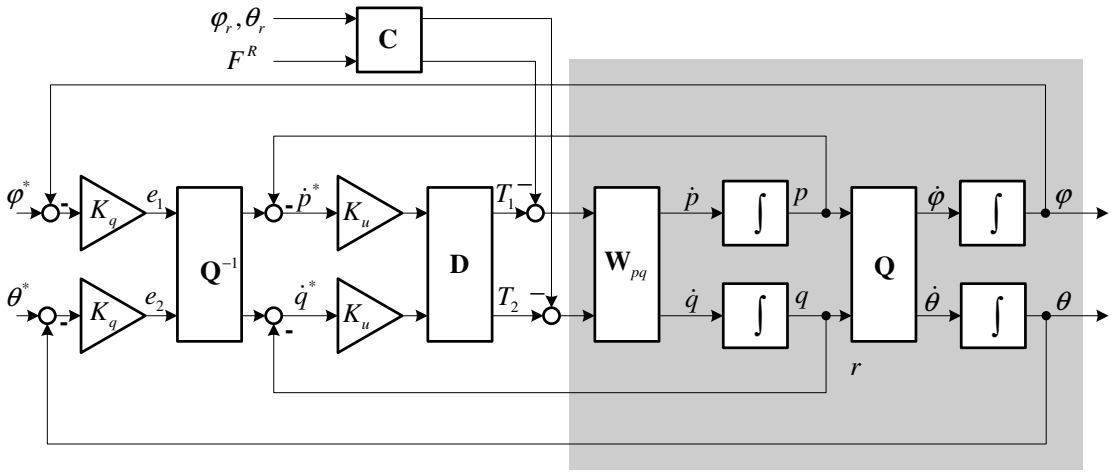

Figure 6.3: Orientation controller, using torque compensation based on measured rope force and rope angles

equations of the complete system. Second, non-linear inversions, like the block $\tilde{\mathbf{D}}$, are in general known to be sensitive against parameter variations. For the decoupling block $\mathbf{D}$ of the uncoupled helicopter this has been proven unproblematic, since the block depends only on few system parameters, which can be estimated with high accuracy. The block $\tilde{\mathbf{D}}$ is much more complex, since it is based on the dynamic equations of the whole system. Therefore, compared to the block $\mathbf{D}$ more parameters need to be known.

Since two drawbacks of the inversion based solution became already apparent during the controller design, a second solution has been developed in parallel. Fig. 6.3 shows the orientation controller of an uncoupled helicopter, presented in Sec. 4.4, which has been extended by a torque compensator block $\mathbf{C}$. Similar to Fig. 6.2, all blocks with gray background are part of the model and the remaining blocks are part of the controller. The key idea for the design of the extended orientation controller has already been presented in Sec. 5.1.3, during the discussion of the *multi-lift model*. Independent from the actual system configuration the helicopter(s) are connected to the slung load, or the coupled system, in a single point. This single point is the rope mounting point *Ro*, which is located somewhere on the helicopter fuselage and is connected to the helicopter's CoM by the vector $\mathbf{p}_{cmh\_ro}$. An attached slung load or a coupled system is only able to influence the helicopter through this point. This influence is expressible as a single force vector $\mathbf{F}^R$, which is attacking at the connection point *Ro*, see Fig. 5.10. The torque compensator block $\mathbf{C}$ uses the measured force vector for the calculation of the torque $\mathbf{T}^R = \mathbf{p}_{cmh\_ro} \times \mathbf{F}^R$ acting on the helicopter fuselage. The estimated torque $\mathbf{T}^R$ is subtracted from the torques calculated by the orientation controller. The influence of the coupled load or the coupled system is therefore compensated using feed-forward techniques.

The force vector is measured using the sensors of the LTD. The magnitude $F^R = \left|\mathbf{F}^R\right|$ of the force is directly estimated by the LTD's force sensor and the orientation of the

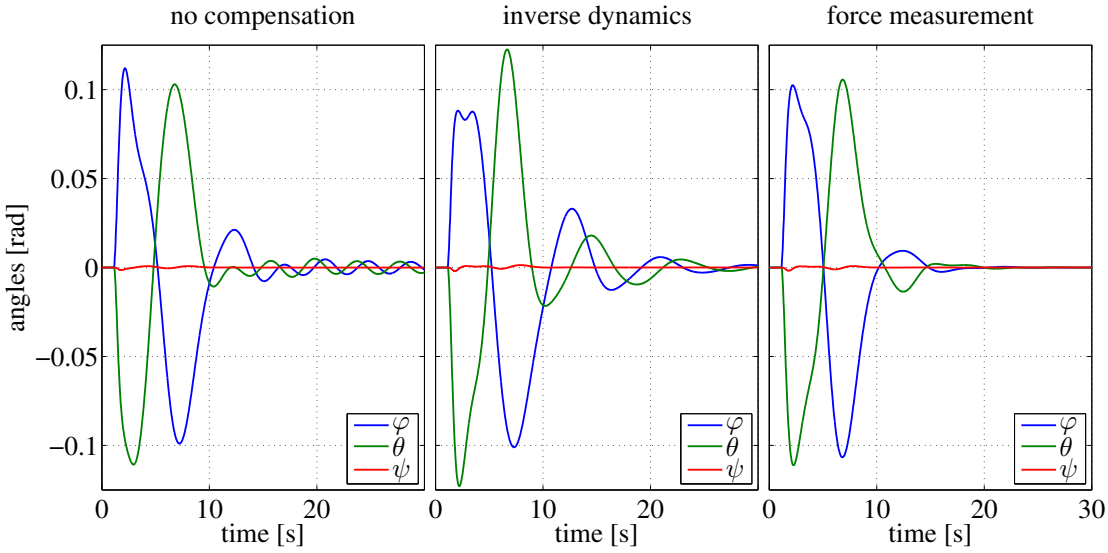

Figure 6.4: Comparison of different orientation controllers

force vector is estimated relative to helicopter, using the two angles φ_r^F, θ_r^F. The angles are measured by the magnetic encoders of the LTD. The orientation of the rope frame $\mathbf{R}$ relative to the fuselage frame $\mathbf{F}$ is expressed by $\mathbf{C_{R-F}} = \mathrm{R}_{\mathbf{f2}}(\theta_r^F)\,\mathrm{R}_{\mathbf{f'1}}(\varphi_r^F)$, see Sec. 5.1.1 for a detailed description of the different frames. The force vector is completely described by $\mathbf{F}^R = F^R\,\mathbf{r}_3$, and the orientation of the basis vector $\mathbf{r}_3$ is described relative to the helicopter's fuselage frame through $\mathbf{r}_3 = \mathbf{C_{R-F}}\,\mathbf{f}_3$.

In simulation the force vector is estimated using Newtons law:

$$\mathbf{F}^R \quad = \quad (\dot{u}\,\mathbf{n}_1 + \dot{v}\,\mathbf{n}_2 + \dot{w}\,\mathbf{n}_3)\,m_h - (F_3^{MR}\,\mathbf{f}_3 + F_2^{TR}\,\mathbf{f}_2 - g\,m_h\,\mathbf{n}_3) \tag{6.1}$$

Eq. 6.1 is explained as follows: The actual acceleration of the helicopter's CoM, described by $\dot{u}$, $\dot{v}$ and $\dot{w}$, is the result of all forces acting on the helicopter. The known forces, the main-rotor force F_3^{MR} and the tail-rotor force F_2^{TR} and the gravitational force, are subtracted from this total force. Therefore, the remaining force has to be caused by the coupled system.

In Fig. 6.4 the performance of the orientation controllers based on inversion and torque compensation is compared to the performance of the orientation controller for a single uncoupled helicopter. The *single-lift model,* presented in Sec. 5.1.1, is used for the comparison. Almost all model parameters have been chosen similar to the experiment conducted near Berlin in the year 2007, which is described in Sec. 7.1. Only the load mass has been increased to 2.5 kg, to accentuate the influence of the load motion on the helicopter orientation. The different orientation controllers are utilized by the translation controller presented in Sec. 6.3. An initial step of approximately 14.14 m from $(0, 0, 0)$ to $(10, -10, 0)$ is presented to the translation controller at the beginning of the simulation. After approximately 10 s the helicopter reaches the desired position and the pitch θ and roll φ angles should quickly converge towards zero. The yaw angle ψ is drawn for

completeness only, since the control of heading ψ and orientation(φ, θ) are separated, see Sec. 4.2. Small deviations of the yaw angle are visible for large pitch and roll angles, since the control separation is based on a simplification, which assumes small roll and pitch angles. However, these deviations are quickly compensated by the heading controller.

The left sub-figure shows the result of the orientation controller for a single uncoupled helicopter without additional compensation. After approximately 12 s periodic oscillations of pitch and roll angles become visible. The amplitude of the oscillations is slowly rising and therefore the system is unstable. An oscillation frequency of approximately 0.22 Hz indicates that these oscillations are caused by the load motion. A pendulum oscillation frequency of 0.22 Hz is calculated based on the rope length $l = 5$ m, see Eq. 5.38. This demonstrates, that the torques caused by the slung load attachment impair the functioning of the orientation controller up to a point where the controlled system becomes unstable.

The middle and right sub-figure show the simulation results for the orientation controllers based on inverse system dynamics and on torque compensation respectively. To estimate the parameter variation sensitivity of both controllers, the model parameters of controllers have been chosen different from the actual model parameters. The location of the rope mounting point *Ro* has been identified to have strong influence on both controllers and therefore a deviation of 5 cm has been used for the simulation. Comparing the middle and the right sub-figure it becomes evident, that the orientation controller based on the inverse system dynamics is more sensitive to parameter variation than the orientation controller based on torque compensation. Additionally, the orientation controller based on the inverse system dynamics depends on all parameters of the model, whereas the orientation controller based on the torque compensation depends only on the position of the helicopter's CoM and the vector $\mathbf{p}_{cmh\_ro}$ connecting the helicopter's CoM and the rope mounting point *Ro*. Therefore, only the model parameters of the helicopter are required. The measurement of $\mathbf{F}^R$ includes all remaining parameters of the coupled system implicitly.

In a direct comparison the torque compensation based controller has many benefits. The orientation controller is independent from the coupled system, since its complete influence on the helicopter is measured through $\mathbf{F}^R$. Therefore, only one generic orientation controller is required to cover all slung load configurations. The torques compensation requires less system parameters to be known and is more robust against parameter variation. The torque compensation requires only local measurements, whereas the model inversion requires knowledge of the whole system state. Dual- or multi-lift configurations require reliable real-time communication between the different helicopters, to estimate the complete system state. A communication failure of just one helicopter in a multi-lift configuration impairs the orientation controllers of all helicopters, since a part of the system state is missing. In general the same problem exists for the centralized translation controller presented in Sec. 6.4. However, the failure of an orientation controller usually causes the system to become unstable immediately, whereas the translation control is less sensitive. For example, assuming a good working orientation controller and hovering conditions, the control outputs of the translation controller, the desired orientation (φ^*, θ^*) and the desired lifting-force (F_3^{MR*}), can be held constant for several seconds,

without the system becoming unstable. The only drawback of the torque compensation is the requirement of an additional force sensor for every helicopter. The magnetic encoders, utilized for the estimation of the load position and velocity, are required by both orientation controllers, since the state of the load needs to be known for the controller based on inverse dynamics as well.

The benefits of the torque compensation controller clearly outweigh its drawbacks and therefore the torque compensation controller has been used for all flight experiments. The possibility of using one well known and extensively tested[5] orientation controller, which has been extended to provide the necessary torque compensation for all slung load configurations, significantly simplified the conduction of the flight experiments.

6.3 Translation Controller for Single-Lift Configurations

The manual piloted, single-lift, slung load transportation is the only slung load transportation method used commercially, see the overview in Sec. 1.1. Usually a pilot tries to avoid oscillations of the slung load through the limitation of acceleration and deceleration of the helicopter. In case of strong load oscillations, e.g. caused by a piloting error or external disturbances, the pilot tries to hover or translate with constant velocity, until the oscillation subsides on its own. Only very skilled and experienced pilots are able to damp the load oscillation actively. Chances are good, for an inexperienced pilot, to amplify the load oscillations, in an attempt to dampen them.

The single-lift translation controller, presented in this section, provides the active damping of the load oscillations. Strong load oscillations stress the structure of the helicopter and require a lot of energy to compensate. Therefore, the primary objective of the controller is to dampen the load oscillation. The movement of the load along a desired trajectory is the secondary objective of the controller.

The presented controller is inspired by a classical state feedback control approach for overhead cranes. The helicopter is considered to be equivalent to a overhead crane trolley. The main difference between helicopter and trolley is that a trolly allows the almost immediate application of control forces, whereas a helicopter needs to generate all required forces through the main-rotor lifting force and helicopter orientation, which delays the generation of arbitrary forces significantly. In Sec. 5.2.1 the force generator model has been introduced, which describes the force generation process of the helicopters. Based on the force generator model, a linear translational model for the single- and dual-lift configuration has been derived in Sec. 5.2.2. This model is used for the design of the controller and for the calculation of the feedback coefficients.

Before the controller design is presented, two properties of the model need to be recalled shortly: First, the linear model decouples the horizontal translation of the helicopter in $\mathbf{n}_{1,2}$-plane and the motion of the load, completely from the vertical translation along $\mathbf{n}_3$. Therefore, the altitude is controlled separately, using the PID translation controller of a single uncoupled helicopter, see Sec. 4.3. Second, the linear model decouples the motion of helicopter and load along $\mathbf{n}_1$ from the motion of helicopter and load along $\mathbf{n}_2$.

[5] In simulation and flight experiments.

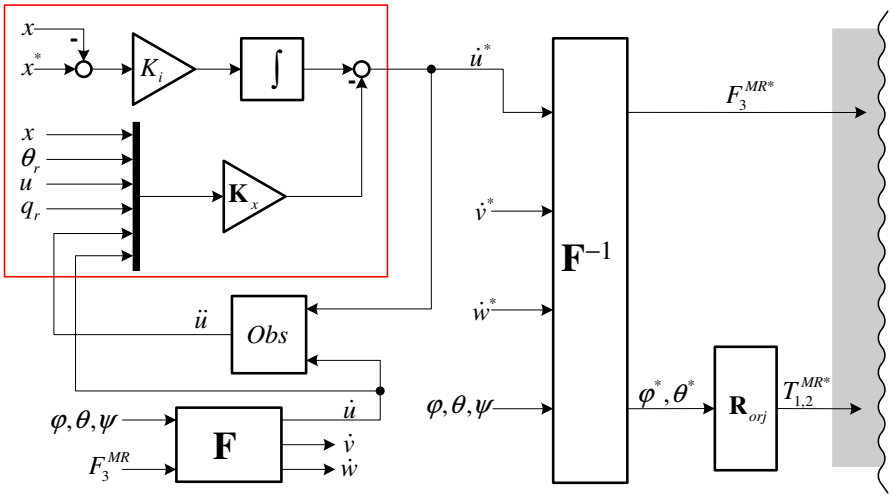

Figure 6.5: Translation controller for single-lift configurations

The angles φ_r, θ_r describe the load position according to Eq. 5.83. Since the model has been linearized during hovering, see Sec. 5.2.2 for details, the system state is split[6] into two independent sets: (x, θ_r, u, q_r) and (y, φ_r, v, p_r). This simplification is only valid close to hovering conditions for sufficient small angles (φ_r, θ_r). However, it is a good approximation for the flight conditions considered in this work.

The schematic of the translation controller is shown in Fig. 6.5. The translation controller is composed of three independent entities, and each entity is responsible for the translation along one axis $\mathbf{n}_{1,2,3}$ of the Newtonian reference frame. The altitude controller is not drawn to improve the clearness of the figure, since the vertical motion along $\mathbf{n}_3$ is controlled by a simple PID-controller. Translations along $\mathbf{n}_1$ and $\mathbf{n}_2$ are controlled independently, but similar for both axis. Therefore, only the controller for the translation along the axis $\mathbf{n}_1$ is depicted exemplarily.

A classical PI-state-feedback controller is used for the translation along the axis $\mathbf{n}_1$ and $\mathbf{n}_2$. A red frame highlights the controller in Fig. 6.5: The actual helicopter position x is subtracted from the desired position x^* to calculate the control deviation, which is amplified by the controller gain K_i and then integrated. This is the integrating part of the controller, which ensures that the control deviation converges towards zero, even in the presence of unknown disturbances like steady wind. The proportional part of the PI-controller has been omitted, since the avoidance and damping of load oscillations are the primary objectives of the controller. The movement of the load towards the desired position is only a secondary objective. The proportional term of the controller improves only the time, which is required by the helicopter to reach the desired position. However, this causes stronger acceleration of the helicopter, which causes load oscillations. It should be noted that the secondary control objective defines not the helicopter to reach the desired position, but the load to reach it. Therefore, not only the translation time

[6]The vertical motion of the helicopter along $\mathbf{n}_3(z, w)$ is ignored, since it is controlled separately.

needs to be considered, but also the time required to damp the load oscillations. It has been determined in simulation, that a pure integral controller outperforms the PI-controller for this particular system and therefore the proportional term has been omitted.

The remaining part of the PI-state-feedback controller is the feedback of the state itself. The scalar product of system state $(x,\, \theta_r,\, u,\, q_r,\, \dot{u},\, \ddot{u})^t$ and control vector $\mathbf{K}_x$ is subtracted from the output of the I-controller. The result is interpreted as the desired acceleration $\dot{u}^*$, which is fed together with desired accelerations $\dot{v}^*$, calculated by the second PI-state-feedback controller, and $\dot{w}^*$, calculated by the PID altitude controller, into the block of the inverse translation dynamics $\mathbf{F}^{-1}$ of a single uncoupled helicopter. The block $\mathbf{F}^{-1}$ does not compensate the force $\mathbf{F}^R$ caused by the load. The compensation is achieved indirectly through the two state feed-back controllers and is included in the desired accelerations $\dot{u}^*$ and $\dot{v}^*$. The PID-controller, which controls the helicopter's altitude through the desired acceleration $\dot{w}^*$, does not account for the force $\mathbf{F}^R$. However, the PID-controller is able to compensate any disturbances, caused by the force $\mathbf{F}^R$, quickly, since the generation of the acceleration $\dot{w}$ is preferred by the block $\mathbf{F}^{-1}$, see Eq. 4.11 in Sec. 4.3 for details. It should be remembered, that the orientation controller $\mathbf{R}_{orj}$ compensates the torques $\mathbf{T}^R = \mathbf{p}_{cm\_ro} \times \mathbf{F}^R$ caused by the force $\mathbf{F}^R$, see Sec. 6.2 for details.

The first four elements of the feed-back depicted in Fig. 6.5 describe the system state of the linearized roll pendulum presented in Sec. 5.2.2: The position/speed of the upper mass-point $(x,\, u)$ and the angle and angular speed of the connected lower mass-point $(\theta_r,\, q_r)$. Until now the last two elements of the state vector $(\dot{u},\, \ddot{u})$ have been ignored. These elements describe the acceleration $\dot{u}$ and the jerk $\ddot{u}$ of the upper roll-pendulum mass-point. Both quantities have been introduced into the system state through the extension of the roll-pendulum model with the force generator model. A helicopter is not able to generate arbitrary forces directly and therefore the generation of forces is considered to be a dynamic process, which is modeled by a second order delay, assuming a small helicopter fuselage, or a third order delay, assuming a big helicopter fuselage, see Sec. 5.2.1 for details. Through the application of Newton's second law the force generator model is interpreted to be an acceleration generator. Instead of the desired force $F^{H*}_{1,2,3}$ the desired acceleration $(\dot{u}^*,\, \dot{v}^*,\, \dot{w}^*)$ is the input of the model and instead of the actual force $F^{H}_{1,2,3}$ the actual acceleration $(\dot{u},\, \dot{v},\, \dot{w})$ is the output of the model, see Fig. 5.14. Consequently the internal states of the model are reinterpreted to be the actual jerk $(\ddot{u},\, \ddot{v},\, \ddot{w})$ and the actual acceleration $(\dot{u},\, \dot{v},\, \dot{w})$.

Estimation of Acceleration and Jerk For a real helicopter system the estimation of acceleration and jerk is difficult. Therefore, several acceleration estimations have been compared and a jerk observer has been constructed.

It is possible to use the IMU's accelerometers for a direct measurement of the acceleration, but the resulting signals are very noisy and require a gravity compensation. Even though it is possible to use the unfiltered acceleration in the controller, the noise degrades the controller performance. Filtering improves the signal quality, but adds delay to the signal, which is again degrading the controller performance. Another possibility

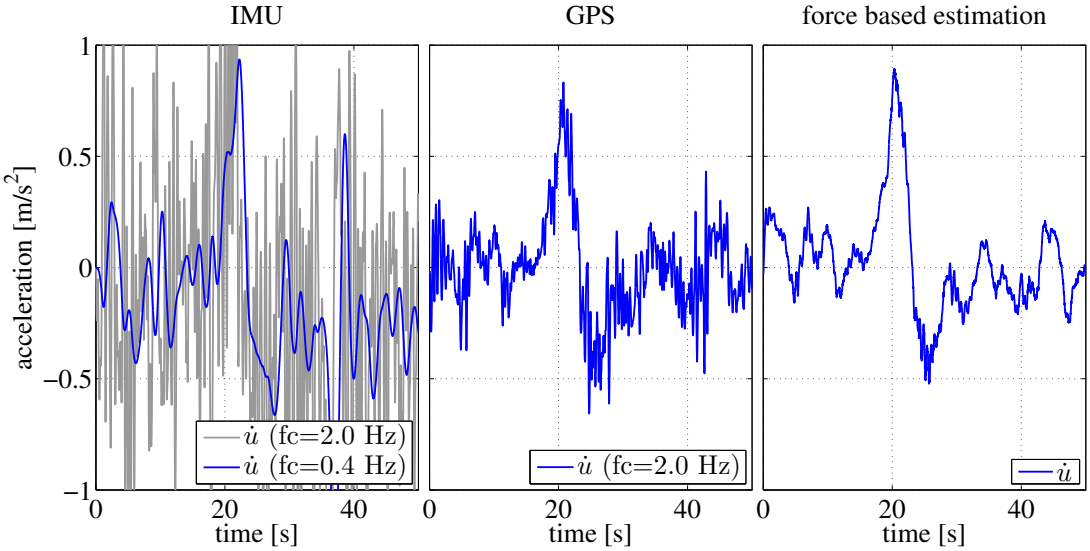

Figure 6.6: Comparison of different acceleration estimation methods

is the acceleration estimation based on the velocity measurement of the GPS. However, this method requires the filtering of the velocity before the numerical differentiation, too. Therefore, a third approach to estimate the current acceleration ($\dot{u}$, $\dot{v}$, $\dot{w}$) is introduced. The acceleration is calculated using the translation dynamics of a single uncoupled helicopter, represented by the block **F** in Fig. 6.5. The current helicopter orientation, given by the Euler-angles (φ, θ, ψ), and the current helicopter lifting-force F_3^{MR} are utilized for the calculation. For simplicity and clearness, this approach will be called *model based* approach from now on.

The *model based* approach provides only an approximation of the true acceleration for two reasons: First, no direct measurement of the current lifting-force F_3^{MR} is available and therefore the desired lifting-force F_3^{MR*} has been used instead. This substitution is based on the assumption that the lifting-force F_3^{MR} is equal to desired lifting-force F_3^{MR*}, except for the delay caused by the aerodynamics of the main-rotor and the dynamics of the actuators. Second, the translation dynamics of a single uncoupled helicopter does not consider the motion of the load.

The translation dynamics of the *single-lift model* could have been used instead, since it considers the influence of the load. This requires knowledge of the load motion, see the simplified Eqs. 5.25-5.27. Nevertheless, the translation dynamic of a single uncoupled helicopter has been used, since this estimation is applicable for every slung load configuration. This result is utilized in Sec. 6.5, where two independent single-lift controllers are applied to one dual-lift slung load configuration.

Because of the simplifications made above, the acceleration estimation depends only on the helicopter orientation, which can be estimated very well, and the lifting force, which is approximated by the desired lifting-force.

Despite the simplifications, the *model based* approach allows a good estimation of

the current helicopter acceleration. In Fig. 6.6 a comparison of all three acceleration estimation methods is depicted, and the estimated acceleration $\dot{u}$ along $\mathbf{n}_1$ is exemplarily plotted. The figure shows a short part of the single-lift experiment conducted in 2007, which is fully described in Sec. 7.1. The left, middle and right part of the figure show the results of the IMU, GPS and *model based* estimation, respectively. The accelerations estimated by IMU and GPS are filtered by a 4^{th} order Butterworth low pass filter, with a cut-off-frequency of fc = 2 Hz. The strong noise of the acceleration estimated by the IMU prohibits a structural comparison with the other estimations and therefore the original signal is additionally filtered using a cut-off-frequency of fc = 0.4 Hz. The general structure of the acceleration signals has been verified to be similar to the estimations of the other methods, using this strongly filtered signal. The acceleration estimated through IMU measurements exhibits either too much noise, using a 2 Hz filter, or too much delay, using a 0.4 Hz filter, to be utilized by the controller. The acceleration derived from the GPS velocity shows less noise. Nevertheless, a 2 Hz filter has to be applied to the velocity, before the calculation of the numerical derivative. The resulting acceleration signal is good enough to be used by the controller. However, the *model based* estimation delivers an almost noise free acceleration, which does not require any additional filtering. Compared to the *model based* estimation, the GPS and IMU acceleration signals are approximately delayed by 0.4 s or 2 s respectively. The *model based* estimation is therefore considered an accurate and precise method to obtain the acceleration of the helicopter.

The direct estimation of the jerk $\ddot{u}$ is difficult. Even the acceleration estimated by the *model based* method requires filtering before the calculation of the discrete derivative. The observer, represented by the Obs block in Fig. 6.5, has been constructed as solution to this problem. It is based on the force generator model described in Sec. 5.2.1. The model has two states $\dot{u}$ and $\ddot{u}$, where the acceleration $\dot{u}$ is already known. A reduced Luenberger observer is constructed to utilize this knowledge. Additionally the observer utilizes the desired acceleration $\dot{u}^*$, which is obtained from the output of the translation controller. The observer has been calculated using a standard textbook pole placement approach presented in [Föl08].

Coefficient Calculation of the Translation Controller The control coefficient vector $\mathbf{K}_x$ is calculated from the linear model presented in Sec. 5.2.2, using a linear quadratic optimization technique. To allow a simultaneous calculation of the integrator coefficient K_i, the model state is extended by $x_i = \int -x\,dt$, the integral of the negated helicopter position[7] over time. The complete system state vector is therefore given by $\mathbf{x} = (x,\, \theta_r,\, u,\, q_r,\, \dot{u},\, \ddot{u},\, x_i)^t$. The feedback coefficient vector $\mathbf{K}$, assuming a state feedback controller with $\mathbf{u} = -\mathbf{K}\mathbf{x}$, is calculated through minimization of the quadratic cost function $J(u) = \int_0^\infty (\mathbf{x}^t\mathbf{Q}\mathbf{x} + \mathbf{u}^t\mathbf{R}\mathbf{u})\,dt$. The weight matrix $\mathbf{Q}$ of the system state and the

[7] The position error is fed back in Fig. 6.5, but this makes no difference for the coefficient calculation.

weight matrix $\mathbf{R}$ of the control input vector $\mathbf{u}$ have been estimated empirically in real flight experiments:

$$\mathbf{Q} = \left| \begin{array}{ccccccc} 1/50 & 0 & 0 & 0 & 0 & 0 & 0 \\ 0 & 1 & 0 & 0 & 0 & 0 & 0 \\ 0 & 0 & 1/50 & 0 & 0 & 0 & 0 \\ 0 & 0 & 0 & 1 & 0 & 0 & 0 \\ 0 & 0 & 0 & 0 & 1/50 & 0 & 0 \\ 0 & 0 & 0 & 0 & 0 & 1/50 & 0 \\ 0 & 0 & 0 & 0 & 0 & 0 & 1/50 \end{array} \right|, \mathbf{R} = 0.1\,\mathbf{I}(7 \times 7)$$

It should be noted, that the matrix $\mathbf{Q}$ amplifies the load angle θ_r and its angular speed q_r about 50-times compared to the remaining state variables. Therefore, the controller reaction on the load motion is strengthened, like demanded at the beginning of this section.

An evaluation of the controller performance based on simulation has been omitted in the presence of results based on flight experiments. The author refers to Sec. 7.1, where the results of the real flight experiments are presented and the performance of the controller is discussed.

6.4 Translation Controller for Multi-Lift Configurations

Two different ideas have been evaluated for the multi-lift controller design: A distributed approach, where each helicopter utilizes its own translation controller and the controllers solely utilize the local system state to close the feedback loop. And a centralized approach, featuring one global controller for all helicopters, which utilizes the complete system state, all helicopters and load, for the feedback calculation.

In Fig. 6.7 the distributed control approach is depicted. The concept is simple, the nonlinear controller presented in Sec. 4.3 is used locally for each helicopter. Like discussed in Sec. 5.1.3, the constraints imposed by the rigidly modeled ropes cause the motion of the load to be completely governed by the motion of the helicopters. Assuming that each helicopter is able to follow the specified trajectories, the load follows its trajectory as well. The controllers are not adapted for the multi-lift load transportation and therefore the forces caused by the coupled system are considered to be disturbances, which need to be compensated by the controllers.

Unless explicitly mentioned the blocks of Fig. 6.7 are equal to the blocks presented in Sec. 4.3, in particular compare Fig. 4.1. Therefore, the details of the blocks are omitted here. The desired position coordinates x_i^*, $y_i^*$and z_i^* of the i'th helicopter are fed through the pre-filter $\mathbf{G}_{i,0}$. The position deviation is created, using the current position of the helicopter (x_i, y_i, z_i), and fed into the translation controller $\mathbf{R}_{i,trans}$, which generates the desired accelerations $\dot{u}_i^*$, $\dot{v}_i^*$ and $\dot{w}_i^*$.

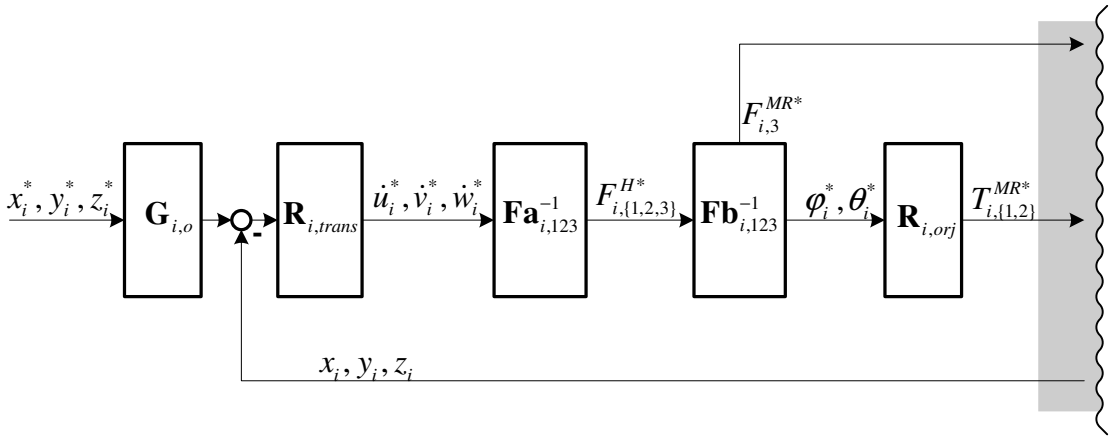

Figure 6.7: Distributed translation controller for multi-lift configurations

The block of the inverse translation dynamics $\mathbf{F}_{123}^{-1}$ of the uncoupled helicopter, see Eqs. 4.7-4.8, is split into the block $\mathbf{Fa}_{i,123}^{-1}$:

$$\begin{aligned} F_{i,1}^{H*} &= \dot{u}_i^* \, m \\ F_{i,2}^{H*} &= \dot{v}_i^* \, m \\ F_{i,3}^{H*} &= (\dot{w}_i^* + g) \, m \end{aligned} \tag{6.2}$$

And the block $\mathbf{Fb}_{i,123}^{-1}$:

$$\begin{aligned} \varphi_i^* &= \arcsin\left(\frac{-F_{i,1}^{H*}\sin(\psi_i) + F_{i,2}^{H*}\cos(\psi_i)}{F_{i,3}^{MR*}}\right) \\ \theta_i^* &= \arcsin\left(\frac{F_{i,1}^{H*}\cos(\psi_i) + F_{i,2}^{H*}\sin(\psi_i)}{F_{i,3}^{MR*}\cos(\varphi_i)}\right) \\ F_{i,3}^{MR*} &= F_{i,3}^{H}/(\cos(\varphi_i)\cos(\theta_i)) \end{aligned} \tag{6.3}$$

In the block $\mathbf{F}_{123}^{-1}$ the desired angles φ_i^*, θ_i^* and the desired main-rotor force $F_{i,3}^{MR*}$are directly calculated from the desired acceleration ($\dot{u}_i^*$, $\dot{v}_i^*$, $\dot{w}_i^*$) and the current orientation of the helicopter (φ_i, θ_i, ψ_i). The separation introduces an intermediate step into the calculation: First, from Eqs. 6.2 the intermediate forces $F_{i,\{1,2,3\}}^{H*}$ are calculated, where $F_{i,\{1,2,3\}}^{H*}$ represents the desired force the helicopter should generate. Second, based on the desired forces $F_{i,\{1,2,3\}}^{H*}$ and the current orientation of the helicopter, the desired angles φ_i^*, θ_i^* and the desired main-rotor force $F_{i,3}^{MR*}$ are calculated, using Eqs. 6.3. This artificial separation into two blocks has been introduced, since the centralized translation controller requires the block $\mathbf{Fb}_{i,123}^{-1}$. To improve the comparability of both controllers, the separation is already introduced here. It is noteworthy, that the block $\mathbf{Fa}_{i,123}^{-1}$ is the only part of the translation controller, which accounts for the influence of the load. The

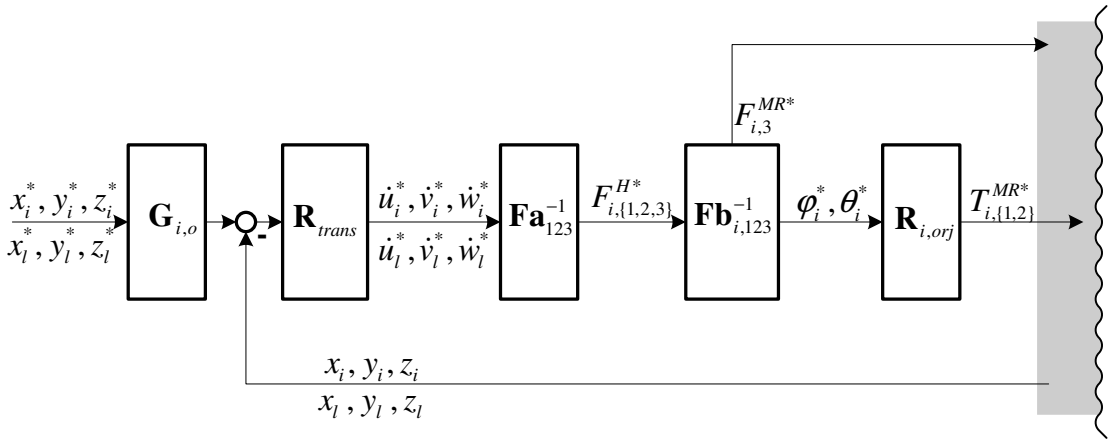

Figure 6.8: Global translation controller for multi-lift configurations

load mass is considered within the mass constant $m = m_h + m_l/3$, where additionally to the helicopter mass m_h one third of the load mass m_l is included. The block $\mathbf{R}_{i,orj}$ is only depicted for completeness and denotes the extended orientation controller described in Sec. 6.2.

For the correct functioning of the decentralized control scheme each helicopter needs to follow the specified trajectories with high accuracy. The individual translation controllers need to compensate external disturbances as well as the influence of the coupled system, since neither the dynamic influence of the load nor the coupling to the remaining helicopters are considered by the translation controllers. The advantages of the decentralized control scheme are its simplicity, the fact that it is based on a reliable and well tested translation controller and that each translation controller depends only on the local system state. Therefore, no additional communication is required to propagate the state of the other helicopters or to estimate the state of the load.

In Fig. 6.8 the centralized control approach is shown. The controller is based on the inversion of the simplified *multi-lift model* presented in Sec. 5.2.3. Different to the nonlinear *multi-lift model* described in Sec. 5.1.3, the helicopters are simplified to be mass points to which arbitrary forces $F_{i,\{1,2,3\}}^{H}$ are applicable. Based on theses forces the acceleration of helicopters ($\dot{u}_i$, $\dot{v}_i$, $\dot{w}_i$) and load ($\dot{u}_l$, $\dot{v}_l$, $\dot{w}_l$) is calculated. The inversion of the model allows the estimation of the forces $F_{i,\{1,2,3\}}^{H}$ required to achieve the desired acceleration of helicopters and load. A pre-filter is applied to the desired position coordinates x_i^*, y_i^* and z_i^* of the i'th helicopter and to the desired position coordinates of the load (x_l^*, y_l^*, z_l^*). The position deviation of helicopters and load is fed into the global translations controller $\mathbf{R}_{trans}$. Internally the position controller block $\mathbf{R}_{trans}$ is composed of 4×3 independent PID controllers. One controller for each coordinate, which makes three controllers for every helicopter and three controllers for the load. The resulting desired acceleration of helicopters ($\dot{u}_i^*$, $\dot{v}_i^*$, $\dot{w}_i^*$) and load ($\dot{u}_l^*$, $\dot{v}_l^*$, $\dot{w}_l^*$) is fed into the block $\mathbf{Fa}_{123}^{-1}$. The block is based on the inverted, simplified *multi-lift model* and is used to estimate the desired forces $F_{i,\{1,2,3\}}^{H*}$, which should be generated by the helicopters. It is noteworthy,

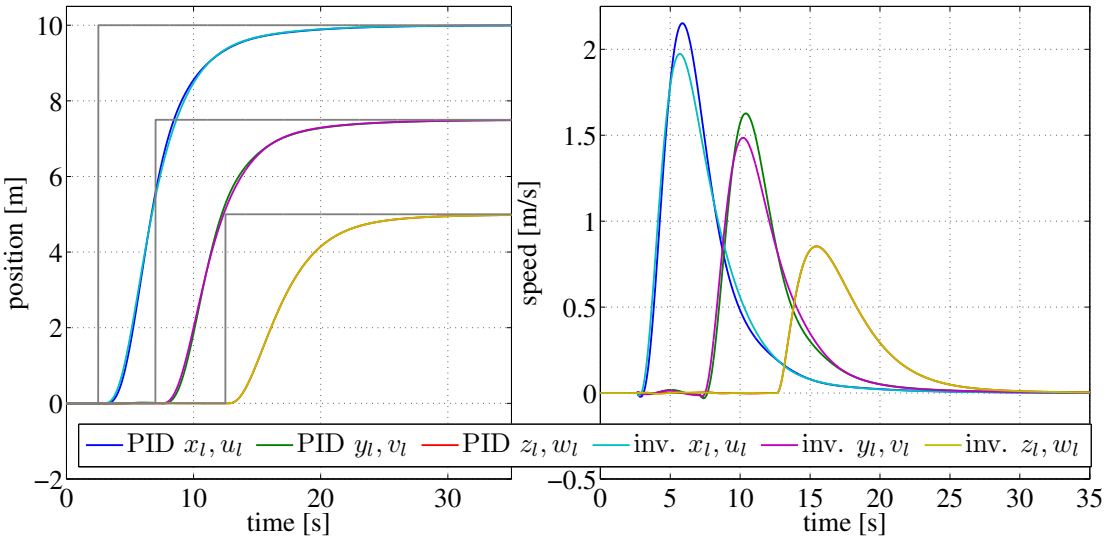

Figure 6.9: Controller based on inverse translation dynamics compared to independent PID controllers

that the inverse model provides 12 equations for the estimation of the nine elements of the force vectors $F^{H*}_{i,\{1,2,3\}}$. The system of equations is therefore over-determined. The reason is, that it is not possible to apply a force directly to the load. The motion of the load is only influenced indirectly through the helicopter forces $F^{H}_{i,\{1,2,3\}}$. Therefore, the desired acceleration ($\dot{u}^*_l$, $\dot{v}^*_l$, $\dot{w}^*_l$) of the load needs to be considered in the estimation of the forces $F^{H*}_{i,\{1,2,3\}}$ as well, which explains the three additional equations. The singular value decomposition is used to calculate the least squares solution of the equations and estimate the forces $F^{H*}_{i,\{1,2,3\}}$. The block $\mathbf{Fb}^{-1}_{i,123}$ is used to calculate the desired angles φ^*_i, θ^*_i and the desired main-rotor force $F^{MR*}_{i,3}$ of the i'th helicopter, based on the desired forces $F^{H*}_{i,\{1,2,3\}}$ and the current orientation of the helicopter. This block equals $\mathbf{Fb}^{-1}_{i,123}$ from the distributed control approach. The block $\mathbf{R}_{i,orj}$ of the extended orientation controller is only depicted for completeness.

A drawback of the centralized control approach is the requirement of real-time communication, which is necessary to propagate the system states of helicopters and load. For every control cycle the whole system state needs to be known and therefore a loss of communication can be critical. Without communication the controller needs to rely on the last known state, which can be quickly outdated by external disturbances like wind gusts. However, a major benefit of the centralized control approach is, that the translation dynamics of the helicopters and load as well as the coupling are considered through the inclusion of the inverse model. The centralized controller is therefore expected to outperform the decentralized controller in terms of disturbance compensation and general flight performance.

The flight performance of the two control approaches has been evaluated in simulation.

The controllers are applied to the complex *multi-lift model* presented in Sec. 5.1.3. The model parameters are chosen similar to the parameters of the real system, which have been used during the AWARE demonstration 2009, see Sec. 6.4 for details. The coefficients of the PID controllers, utilized by both control approaches, are calculated similar to controller coefficients for a single uncoupled helicopter, like described in Sec. 4.5. Equal coefficients have been used for both control approaches, to preserve the comparability of the simulation results. Fig. 6.9 shows the results of the simulation and allows a performance comparison of both control approaches. The left side of the figure depicts the position of the load during the execution of three position steps, where the desired position steps are plotted in gray. The right side of the figure shows the velocity of the load during the flight maneuvers. The different position trajectories are almost indistinguishable, only the speeds show some visible deviations. The distributed controller shows a higher maximum speed of the load and slightly stronger acceleration of the load than the centralized controller. The time responses of both control approaches are almost equal, with a slight advantage of the centralized controller, which indicates that the centralized controller is slightly more efficient than the distributed controller. However, the overall performance of both controllers is considered to be almost equal.

The centralized controller is based on model inversion, which is claimed in literature to be sensitive to variation of model parameters. The robustness of both control approaches against parameter variation has therefore been estimated. Both controllers have proven to be quite robust against parameter variation in simulation. For example, the trajectory deviation of the centralized controller increases only by 4 cm for the experiment depicted in Fig. 6.9, for 5 % deviation of rope length or load weight or position of the rope attachment point.

The distributed control approach has been chosen for the conduction of the flight experiments, since the flight performance of both control approaches is almost equal and the distributed controller does not require the propagation of the entire system state. The results of the flight experiments are presented in Sec. 7.2.

6.5 Translation Controller for Dual-Lift Configurations

The dual-lift configuration is considered to be an intermediate between single- and multi-lift configuration. Similar to the single-lift configuration the load still has the possibility to oscillate, but the oscillation is limited to one degree of freedom. Similar to the multi-lift configuration, the reduction of DoF is caused by the coupling of an additional helicopter. The proposed control approach is therefore an intermediate between the single-lift controller, presented in Sec. 6.3, and the multi-lift controller, presented in Sec. 6.4.

The single-lift controller is applied to stabilize the load, since the load has still one DoF and requires active stabilization. Two independent translation controllers are used, one for each helicopter, similar to the approach of the distributed multi-lift controller.

In Fig. 6.10 the schematic of the dual-lift controller is depicted. It is almost identical to the schematic of the multi-lift controller, except for the controller blocks $\mathbf{R}_{i,trans}^{xy}$ and $\mathbf{R}_{i,trans}^{z}$, which replace the controller $\mathbf{R}_{i,trans}$ used for the multi-lift configuration. The

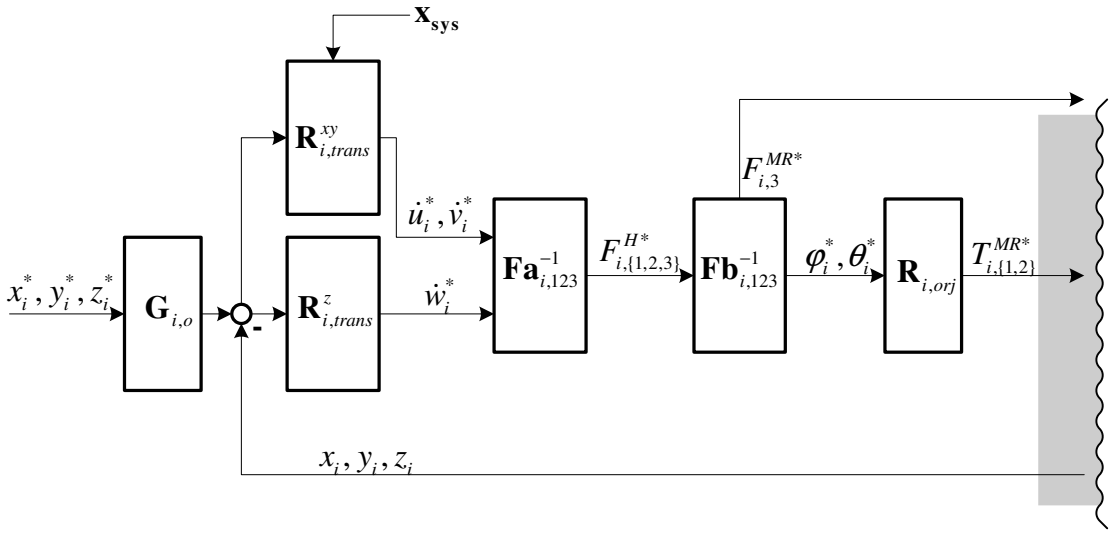

Figure 6.10: Distributed translation controller for dual-lift configurations

block $\mathbf{R}^{xy}_{i,trans}$ includes two state-feedback controllers, similar to the one presented in Sec. 6.3. These controllers stabilize the helicopters' horizontal motion within the $\mathbf{n}_{1,2}$-plane, and avoid and dampen load oscillations. The state-feedback controller requires knowledge of the complete system state $\mathbf{x_{sys}}$, including both helicopters and load, similar to single-lift controller. The altitude is stabilized using a PID controller, which is included in the block $\mathbf{R}^{z}_{i,trans}$.

The performance of the control approach has been evaluated in simulation. The controllers are applied to the complex multi-lift model presented in Sec. 5.1.3, which has been configured for two helicopters. The model parameters used for simulation match the parameters of the real system, used for the AWARE demonstration 2009, except for a reduced load mass of 3 kg and a smaller rope length of 10.77 m. The load mass has been reduced, since only two helicopters are involved in the load transportation. The calculation of controller coefficients is almost similar to the calculation of the controller coefficients for the single-lift configuration, see Sec. 6.3. However, only half of the load mass $m_l/2$ is considered for the calculation of the feed-back coefficients, since each helicopter should carry half of the load mass, averaged over time. The forces, required to keep the separation distance of both helicopters, are neglected for the calculation of the control coefficients. These forces are considered to be disturbances, which need to be compensated by the controller.

In Fig. 6.11 the simulation results are depicted. The left side shows the position of the load and the right side shows the corresponding speeds. Three steps of 10 m, along the basis vectors of the Newtonian reference frame, are depicted. The corresponding desired position steps are plotted gray on the left side of the figure. The position step responses look almost equal, but the plotted speeds accentuate the differences between them. The configuration of helicopters and load needs to be known for a correct interpretation of

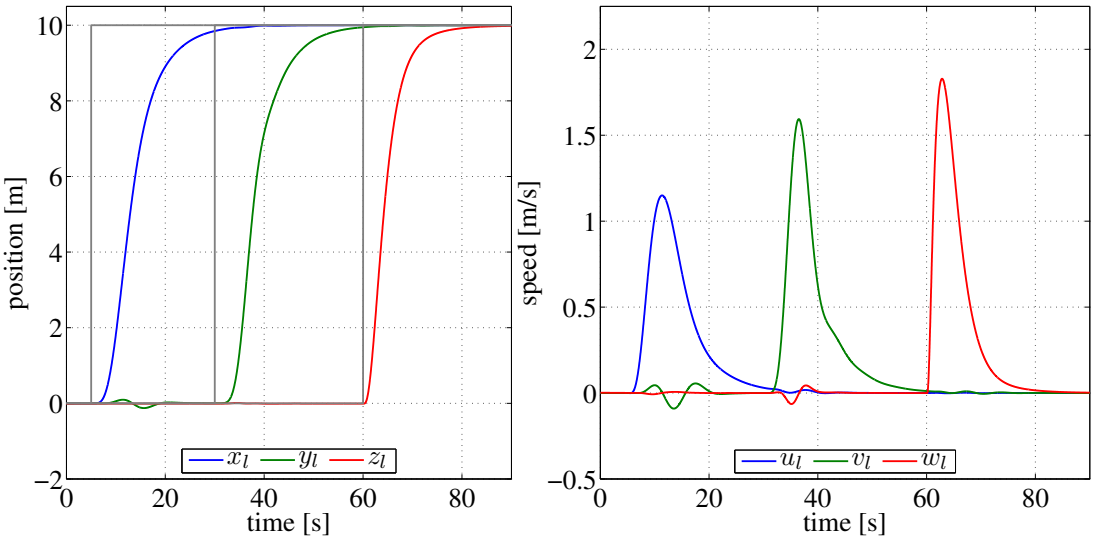

Figure 6.11: Simulation results, distributed translation controller for dual-lift configurations

the results. In the beginning the helicopters are at the positions $(-5, 0, 10)$, $(5, 0, 10)$ and the load is at the position $(0, 0, 0)$. Therefore, the formation is similar to a triangle within the $\mathbf{n}_{1,3}$-plane. The first desired position step is given along the basis vector $\mathbf{n}_1$.

The rigidly modeled ropes prohibit a oscillation of the load within the $\mathbf{n}_{1,3}$-plane, instead a small speed along $\mathbf{n}_2$ is visible after approximately 18 seconds. This speed is caused by a orientation deviation of the helicopters during the maneuver. The deviation is small, but sufficient to excite a small oscillation of the load. During the second position step along $\mathbf{n}_2$ the load is able to oscillate in the $\mathbf{n}_{2,3}$-plane. A strong acceleration with a maximum speed of $1.6\,\mathrm{m/s}$ is visible, but only a small oscillation is visible in the speed w_l of the altitude coordinate, between 38 and 40 seconds. The third position step is presented along $\mathbf{n}_3$ (altitude). The vertical step response of the PID controllers differs from the horizontal step responses of the state-feedback controllers. This has been expected, since control method and control coefficients differ.

The author considers the performance of the presented controller to be sufficiently good. Especially, if the simplicity of the control approach is taken into account. The dual-lift controller is presented in this work for two reasons: First, to demonstrate the successful utilization of the proposed orientation controller, like described in Sec. 6.2, for the control of a dual-lift configuration. Second, to complete the examination of the control approaches for different slung load configurations.

The author considers the first point to be very important. There are many possibilities to construct more elaborated translation controllers, but the presented dual-lift controller demonstrates how much the translation controller design can be simplified, utilizing the proposed orientation controller.

6.6 Observation of Load Motion

In Sec. 5.1.2 the need for an rope/load motion observer became apparent. This section describes the design, implementation and validation of this observer.

Two different ideas for the observer design are discussed in this section. The first approach reconstructs the whole state of LTD, rope and load from the measured angles, whereas in the second approach observes only the desired/expected behavior of the load. To avoid confusion the observer based on the first approach is called *complex load motion observer* and the observer based on the second approach is called *simplified load motion observer*.

The *complex load motion observer* is based on the LTD-rope-load model presented in Sec. 5.1.2. The model is composed of five mass-points, one for the LTD, one for the load and three for the rope, and is parametrized similar to the laboratory setup described in the same section. Actually, a model composed of twenty mass-points, which is completely equal to the model from Sec. 5.1.2, has first been used for the design of the observer. However, the results of the five and twenty mass-point models are almost equal. To simplify matters the five mass-point model has been used for the observer design. The state vector of the model is given by $\mathbf{x} = [\alpha_1, \ldots, \alpha_5, \dot{\alpha}_1, \ldots, \dot{\alpha}_5]^t$, and the angular rates $\dot{\alpha}_i$ are defined by $\dot{\alpha}_i = d\,\alpha_i/dt$. The model is linearized using the equilibrium conditions $\alpha_i = 0$ and $\dot{\alpha}_i = 0$ ($i \in \{1, \ldots, 5\}$). Under these conditions the LTD/rope/load pendulum is at rest and hangs straight downwards, along $\mathbf{n}_3$. The results of the linearisation are presented in state space form:

$$\begin{bmatrix} -\frac{1}{l_{ltd}} & \frac{(m_l+m_{rp})}{l_{ltd}m_{ltd}} & 0 & 0 & 0 \\ \frac{1}{l_{ltd}} & -\frac{l_{rp}(m_l+m_{rp})+4\,l_{ltd}(m_l+m_{ltd}+m_{rp})}{l_{ltd}l_{rp}m_{ltd}} & \frac{12\,m_l+8\,m_{rp}}{l_{rp}m_{rp}} & 0 & 0 \\ 0 & \frac{4\,(m_l+m_{ltd}+m_{rp})}{l_{rp}m_{ltd}} & -\frac{24\,m_l+20\,m_{rp}}{l_{rp}m_{rp}} & \frac{12\,m_l+4\,m_{rp}}{l_{rp}m_{rp}} & 0 \\ 0 & 0 & \frac{12\,m_l+12\,m_{rp}}{l_{rp}m_{rp}} & -\frac{24\,m_l+12\,m_{rp}}{l_{rp}m_{rp}} & \frac{12\,m_l}{l_{rp}m_{rp}} \\ 0 & 0 & 0 & \frac{12\,m_l+8\,m_{rp}}{l_{rp}m_{rp}} & -\frac{24\,m_l+4\,m_{rp}}{l_{rp}m_{rp}} \end{bmatrix} = \mathbf{A_{2,1}}$$

$$\begin{bmatrix} -\frac{k_{ltd}}{m_{ltd}} & 0 & 0 & 0 & 0 \\ -\frac{(4\,l_{ltd}+l_{rp})(3\,k_{rp}m_{ltd}-k_{ltd}m_{rp})}{l_{rp}m_{ltd}m_{rp}} & -\frac{3k_{rp}}{m_{rp}} & 0 & 0 & 0 \\ \frac{4\,l_{ltd}(3\,k_{rp}m_{ltd}-k_{ltd}m_{rp})}{l_{rp}m_{ltd}m_{rp}} & 0 & -\frac{3k_{rp}}{m_{rp}} & 0 & 0 \\ 0 & 0 & 0 & -\frac{3k_{rp}}{m_{rp}} & 0 \\ \frac{4\,k_{rp}(l_{ltd}+l_{rp})(3\,m_l-m_{rp})}{l_{rp}m_lm_{rp}} & k_{rp}(\frac{12}{m_{rp}}-\frac{4}{m_l}) & k_{rp}(\frac{9}{m_{rp}}-\frac{3}{m_l}) & k_{rp}(\frac{6}{m_{rp}}-\frac{2}{m_l}) & -\frac{k_{rp}}{m_l} \end{bmatrix} = \mathbf{A_{2,2}}$$

$$\mathbf{A} = \begin{bmatrix} \mathbf{0}(5 \times 5) & \mathbf{I}(5 \times 5) \\ g\,\mathbf{A_{2,1}} & \mathbf{A_{2,2}} \end{bmatrix}$$

The matrix $\mathbf{A}$ is too big to be displayed at once and therefore it is split into the submatrices $\mathbf{A_{2,1}}$ and $\mathbf{A_{2,2}}$. The matrices $\mathbf{0}$(a × b) and $\mathbf{I}$(a × a) are a zero matrix of a rows

and b columns and an identity matrix of a rows and a columns. The length of LTD lever and rope are denoted by l_{ltd} and l_{rp}. The mass of LTD, rope and load is given by m_{ltd}, m_{rp} and m_l. The constants k_{ltd} and k_{rp} describe the damping coefficients of the LTD and the rope. Finally, the symbol g denotes the gravitational constant. The input and output matrices $\mathbf{B}$ and $\mathbf{C}$ of the model are defined as follows:

$$\mathbf{B} = \begin{bmatrix} & & \mathbf{0(5\times 5)} & & \\ \frac{1}{l_{ltd}m_{ltd}} & 0 & 0 & 0 & 0 \\ -\frac{4\,l_{ltd}+l_{rp}}{l_{ltd}l_{rp}m_{ltd}} & \frac{12}{l_{rp}m_{rp}} & 0 & 0 & 0 \\ \frac{4}{l_{rp}m_{ltd}} & -\frac{24}{l_{rp}m_{rp}} & \frac{12}{l_{rp}m_{rp}} & 0 & 0 \\ 0 & \frac{12}{l_{rp}m_{rp}} & -\frac{24}{l_{rp}m_{rp}} & \frac{12}{l_{rp}m_{rp}} & 0 \\ 0 & 0 & \frac{12}{l_{rp}m_{rp}} & -\frac{24}{l_{rp}m_{rp}} & \frac{4}{l_{rp}m_l} \end{bmatrix}$$

$$\mathbf{C} = \begin{bmatrix} l_{ltd} & 0 & 0 & 0 & 0 & \\ l_{ltd}+\frac{l_{rp}}{4} & \frac{l_{rp}}{4} & 0 & 0 & 0 & \\ l_{ltd}+\frac{l_{rp}}{2} & \frac{l_{rp}}{2} & \frac{l_{rp}}{4} & 0 & 0 & \mathbf{0(5\times 5)} \\ l_{ltd}+\frac{3\,l_{rp}}{4} & \frac{3\,l_{rp}}{4} & \frac{l_{rp}}{2} & \frac{l_{rp}}{4} & 0 & \\ l_{ltd}+l_{rp} & l_{rp} & \frac{3\,l_{rp}}{4} & \frac{l_{rp}}{2} & \frac{l_{rp}}{4} & \end{bmatrix}$$

$$\mathbf{D} = \mathbf{0}$$

The input vector $\mathbf{u}$ (5×1) allows the stimulation of every mass point, which follows directly from the matrix $\mathbf{B}$. The stimulation immediately effects at least one additional mass point, with exception of the load mass point. Independent from the point of stimulation, the motion is propagated successively through all state variables, by the dynamic matrix $\mathbf{A}$. The reason is, that the motion of every mass point has direct influence on the neighbor mass points, to which it is connected. This is especially visible in the submatrix $\mathbf{A_{2,1}}$, where the alteration of an angle[8] α_i causes a change of the rates $\dot{\alpha}_{i-1}$, $\dot{\alpha}_i$ and $\dot{\alpha}_{i+1}$, which are integrated to become α_{i-1}, α_i and α_{i+1}.

These preliminary considerations are important for the observer design. Since the whole state of the model needs to be reconstructed only from the LTD measurements, every stimulation of rope or load needs to be propagated through the model and needs to be reflected in the motion of the LTD. The observability of the model is calculated and discussed later in this section.

The system has no feedthrough and therefore the matrix $\mathbf{D}$ is a zero matrix. The output matrix $\mathbf{C}$ calculates from the state vector the horizontal (along $\mathbf{n_1}$) position deviations of the mass points, see Fig. 5.4. This calculation makes the observed state of the model comparable to the results of the laboratory experiments. For the observer design the output matrix $\mathbf{C}$ is replaced by the following row vector: $\hat{\mathbf{C}} = [1,0,0,0,0,0,0,0,0,0]$. The reason is, that only the first element of the state vector, the angle α_1 of the LTD, is a measurable quantity. The derivative $\dot{\alpha}_1$ could have been included in $\hat{\mathbf{C}}$ as well, but $\dot{\alpha}_1$ is not directly measurable by the encoders. The measured angle needs to be filtered before

[8] With exception of α_1 and α_5, which only change the rates $\dot{\alpha}_1$, $\dot{\alpha}_2$ and $\dot{\alpha}_4$, $\dot{\alpha}_5$ respectively.

the calculation of the numerical derivative, since the signal of the magnetic encoder is very noisy. The filtering introduces additional delay to the signal and reduces the usability of the derived signal.

The results of an observer based on α_1 and $\dot{\alpha}_1$ have been compared to the results of an observer utilizing only α_1. Depending on the cut-off frequency of the filter, the results of the observer utilizing α_1 and $\dot{\alpha}_1$ are equal or worse than the results of the observer utilizing only α_1. For that reason the utilization of $\dot{\alpha}_1$ is not further investigated.

An observability Gramian is used to verify the observability of the model. The Gramian matrix $\mathbf{W_o}$ is calculated solving $\mathbf{A^t W_o + W_o A + \hat{C}^T \hat{C}} = 0$. This approach is only possible, if the system matrix is stable. This is the case for the selected model parameters, since the real parts of all eigenvalues of $\mathbf{A}$ are negative. The model is observable, if all eigenvalues of $\mathbf{W_o}$ are greater than zero. Again, this is the case for the selected model parameters, but the three smallest eigenvalues are very close to zero: $8 \cdot 10^{-12}$, $2 \cdot 10^{-10}$ and $3 \cdot 10^{-8}$. States with big eigenvalues are easier to observe than states with small eigenvalues, since there is a qualitative relationship between observability and the eigenvalues of the Gramian. Therefore, it is either difficult or impossible to observe the complete state of the real system, based only on the measured LTD angle. Nevertheless, the observer has been implemented and tested. The reason is, that the author was not sure whether or not it is necessary to observe all elements of the state with high accuracy for a good estimation of the load motion. The complete observer is described by the following equations:

$$\begin{aligned} \dot{\mathbf{x}}_{\mathbf{obs}} &= \mathbf{A}\,\mathbf{x}_{\mathbf{obs}} + \mathbf{B}\,\mathbf{u}_{\mathbf{obs}} + \mathbf{R}\,(\mathbf{y} - \hat{\mathbf{y}}_{\mathbf{obs}}) \\ \hat{\mathbf{y}}_{\mathbf{obs}} &= \hat{\mathbf{C}}\,\mathbf{x}_{\mathbf{obs}} + \mathbf{D}\,\mathbf{u}_{\mathbf{obs}} \\ \mathbf{y}_{\mathbf{obs}} &= \mathbf{C}\,\mathbf{x}_{\mathbf{obs}} + \mathbf{D}\,\mathbf{u}_{\mathbf{obs}} \end{aligned} \tag{6.4}$$

Where $\mathbf{y_{obs}}$ is used for the comparison to the laboratory experiments and $\hat{\mathbf{y}}_{\mathbf{obs}}$ is used to close the feedback loop of the observer. The vector $\mathbf{u_{obs}}$ is included only for completeness, similar to the matrix $\mathbf{D}$. The input vector $\mathbf{u_{obs}}$ is assumed to be zero, since the external disturbances of the LTD, rope and load are unknown. The coefficient vector $\mathbf{R}$ of the feedback loop is calculated as a linear-quadratic state-feedback regulator, using the matrices $\mathbf{A}^t$ and $\mathbf{C}^t$.

Before the presentation of the experimental results the *simplified load motion observer* is derived. The key idea of the second design approach is to create an observer based on the simplified model, which has been used for the controller design. This observer is considered to be a very specific filter, which rejects all influences not considered by the controller. The observer model is based on the model presented in Sec. 5.2.2, except for two alterations: First, the mass of the upper mass point is considered to be infinite and the acceleration of the upper mass point is given by a vector $\mathbf{a} = \dot{u}\,\mathbf{n_1} + \dot{v}\,\mathbf{n_2}$. Second, the motion of the upper mass point is restricted to the $\mathbf{n_{1,2}}$-plane, see Fig. 5.17 for the definition of the Newtonian frame $\mathbf{N}$.

The resulting model is a hybrid of idealized- and roll-pendulum. The motion of the lower mass point has no influence on the motion of the upper mass point, because of the infinite mass of the upper point. However, the upper mass point is able to move, since

its acceleration is given by the vector **a**. The reason for the creation of this hybrid model and the purpose of the vector **a** are explained after the comparison of both observer approaches. Position and velocity of the upper mass point have no direct influence on the motion of the lower mass point, different from the acceleration of the upper mass point. Therefore, position and velocity of the upper mass point are not part of the system state. The system state is completely described by the two angles (φ, θ) and the angular speeds (p, q), see Sec. 5.2.2 for the details. The kinematic and dynamic equations are given as follows:

$$\begin{aligned} \dot{\varphi} &= p \\ \dot{\theta} &= q \\ \dot{p} &= (\dot{u}\, s_\varphi s_\theta - \dot{v}\, c_\varphi - g\, s_\varphi c_\theta - l_{rp}\, q^2\, c_\varphi s_\varphi)/l_{rp} \\ \dot{q} &= (-\dot{u}\, c_{\theta\varphi} - g\, s_\theta + 2\, l_{rp}\, p\, q\, s_\varphi)/(l_{rp} c_\varphi) \end{aligned} \tag{6.5}$$

The model is linearized under equilibrium conditions, with ($\varphi = \theta = p = q$). Considering the system state vector $\mathbf{x} = [\varphi, \theta, p, q]$, the following state space model is derived:

$$\mathbf{A} = \begin{bmatrix} 0 & 0 & 1 & 0 \\ 0 & 0 & 0 & 1 \\ -g/(l_{ltd}+l_{rp}) & 0 & 0 & 0 \\ 0 & -g/(l_{ltd}+l_{rp}) & 0 & 0 \end{bmatrix} \quad \mathbf{B} = \begin{bmatrix} 0 & 0 \\ 0 & 0 \\ 0 & -1/(l_{ltd}+l_{rp}) \\ -1/(l_{ltd}+l_{rp}) & 0 \end{bmatrix}$$

$$\mathbf{C} = \begin{bmatrix} l_{ltd}+l_{rp} & 0 & 0 & 0 \\ 0 & l_{ltd}+l_{rp} & 0 & 0 \end{bmatrix} \quad \hat{\mathbf{C}} = \begin{bmatrix} 1 & 0 & 0 & 0 \\ 0 & 1 & 0 & 0 \end{bmatrix} \quad \mathbf{D} = 0$$

The system matrix **A** of the observer is not stable, unlike the system matrix of the *complex observer* model previously presented. Therefore, it is not possible to show the observability of the model using a Gramian matrix. However, it is possible to show the observability, using the observability matrix $\mathbf{Ob} = [\hat{\mathbf{C}}, \hat{\mathbf{C}}\mathbf{A}, \hat{\mathbf{C}}\mathbf{A}^\mathbf{2}, \hat{\mathbf{C}}\mathbf{A}^\mathbf{3}]^t$. The rank of the observability matrix is equal to the number of model states and therefore all states are observable. It should be noted that this method is numerically not very stable and the result may not be correct for complex models. In fact, the rank of observability matrix of the *complex observer* model is only eight. This is the reason why the observability of the complex observer has been calculated using a Gramian matrix.

Both observers are constructed similar to Eqs. 6.4. At this point, the design of the *simplified load observer* might appear confusing, since both observers differ not only in the modeling of LTD and rope. The load motion of the *complex observer* is restricted to the plane $\mathbf{n}_{1,3}$, whereas the load of the *simplified observer* moves in 3D-space, but is limited to a spherical motion around the mounting point with two DoF. The mounting point of the *complex observer* model is fixed, whereas the acceleration of mounting point of the *simplified observer* model can be specified. The model of the *complex observer*

allows to apply a force on each of the mass points of LTD, rope and load, whereas the *simplified observer* model does not.

The reason is, that the model of the complex observer has been taken without alteration from Sec. 5.1.2, but in anticipation of the comparison results the *simplified observer* model has already been adapted for its real world application. The purposes of these adaptions are discussed after the observer comparison. They have no influence on the comparison itself, since the motion is restricted to the plane $\mathbf{n}_{1,3}$ and the input vector $\mathbf{u}_{\mathbf{obs}}$ is assumed to be zero for both models.

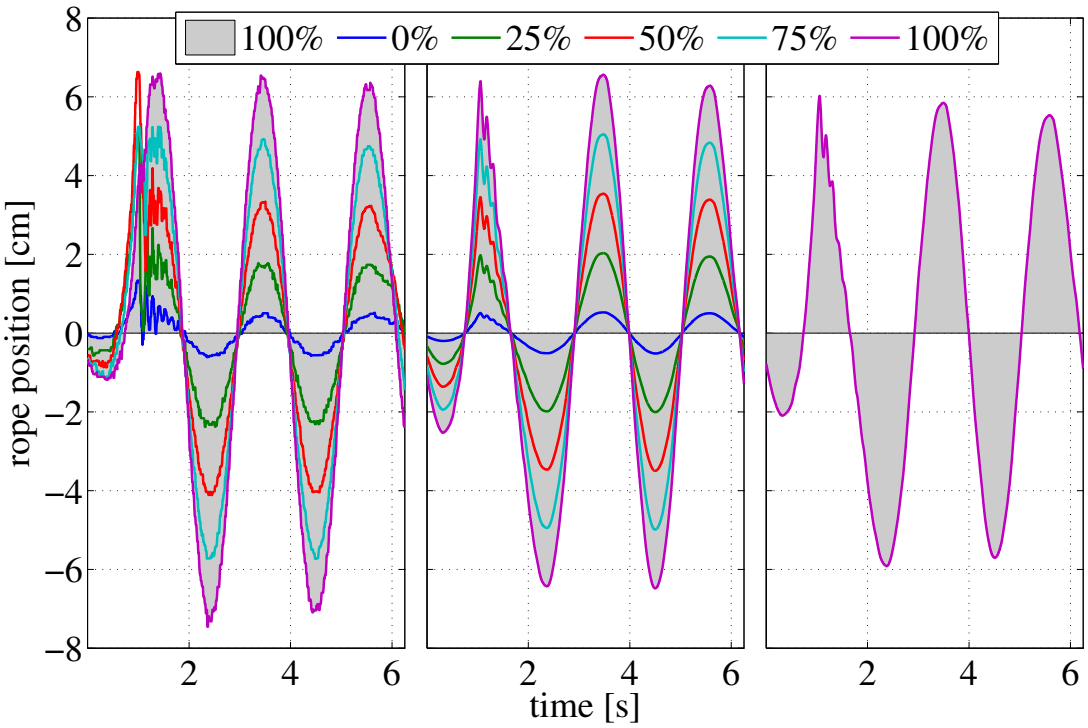

Figure 6.12: Comparison of the LTD-rope-load motion
Left to right - measurement, complex and simplified observer
Position - 0 % = LTD (top), 25−75 % = rope, 100 % = load (bottom)

Fig. 6.12 presents a comparison of laboratory measurements and system states, reconstructed by both observers. The different lines show the horizontal displacement of LTD, rope and load according to Fig. 5.5. The motion of the LTD is given by the blue line and the motion of the load[9] is depicted by a purple line and a gray area. The other three lines describe the motion of the load at 25 %, 50 % and 75 % of the rope length. After approximately one second the rope is picked shortly, at approximately 50 % of the rope length. In the left sub-figure, which represents the measurement, the picking motion is

[9] This describes the motion of the point, which is connecting rope and load, but for the considered small lead weight it is a sufficient approximation.

clearly visible. Additionally, it is well distinguishable from the oscillation of the load, which reaches a first maximum approximately 0.4 s after the rope stimulation. The oscillation frequency of the load is about 0.5 Hz, which is almost the oscillation frequency of an idealized pendulum of the same length. It is important to notice, that beside this slow oscillation, the rope picking and the resulting LTD-rope oscillations are almost not visible in the load motion itself. In an optimal case, the observers should reconstruct the motion of the load only from the measured LTD angle, where the high frequency oscillations of LTD and rope should not be visible in the reconstructed load motion.

The middle sub-figure shows the results of the *complex observer*. The rope stimulation and the resulting LTD and rope oscillations, are clearly visible in the observed load motion. Especially during the rope picking, the observed load motion exhibits a larger amplitude compared to the reference measurement. After the initial disturbance the phase of the observed oscillations converges quickly towards the measurement, whereas the amplitude of the observed oscillation stays smaller than the measured amplitude. This indicates that not all observed state elements converge, at least within the depicted time frame of approximately four seconds, towards the real system state. The observability Gramian indicates that some state elements are difficult to observe, which is confirmed by the experiment. The smaller amplitude of the observed oscillations indicates that the bowing of the rope is not correctly reproduced. An additional result is found, considering the load motion after the decay of the internal rope oscillation in the interval [2 s, 4 s]. The measured amplitude is about 7 cm and the observed amplitude is about 6 cm, which is still a better estimation than the direct calculation from the measured LTD angles (not shown, about 5 cm). The observer has therefore the ability to partially reconstruct the rope bowing. Compared to the direct calculation from the measured LTD angles this is considered a significant improvement.

The right sub-figure shows the results of the *simplified observer*. Since the model considers neither the influence of the LTD nor the flexibility of the rope, the observer is considered to be a specialized filter, which suppresses oscillations with frequencies different from the pendulum frequency of 0.52 Hz. The phase of the observed oscillations converges quickly towards the measurement after the initial disturbance, whereas the amplitude of the observed oscillation stays significantly smaller than the measurement. This is expected, since the rope bowing is not considered in the model. After the decay of the internal rope oscillation in the interval [2 s, 4 s], the amplitude of the observed load motion is similar to the amplitude calculated from the measured LTD angles (not shown, about 5 cm). This small load oscillation amplitude is considered to be a major drawback of this observer. However, during and shortly after the rope stimulation, in the interval [1 s, 2 s], the *simplified observer* efficiently filters high frequency oscillations of LTD and rope. The load motion estimation of the *simplified observer* exhibits less high frequency oscillations than the estimation of the *complex observer*, even if a scale factor of 1.15 is applied to match the amplitudes of the low frequency oscillations.

The *simplified load motion observer* has been selected for the conduction of flight experiments. Two reasons justify this decision: First, the *simplified observer* shows a better rejection of the high frequency oscillations, caused by LTD or rope. Second, the *simplified observer* requires only the knowledge of one parameter, the rope length, whereas the

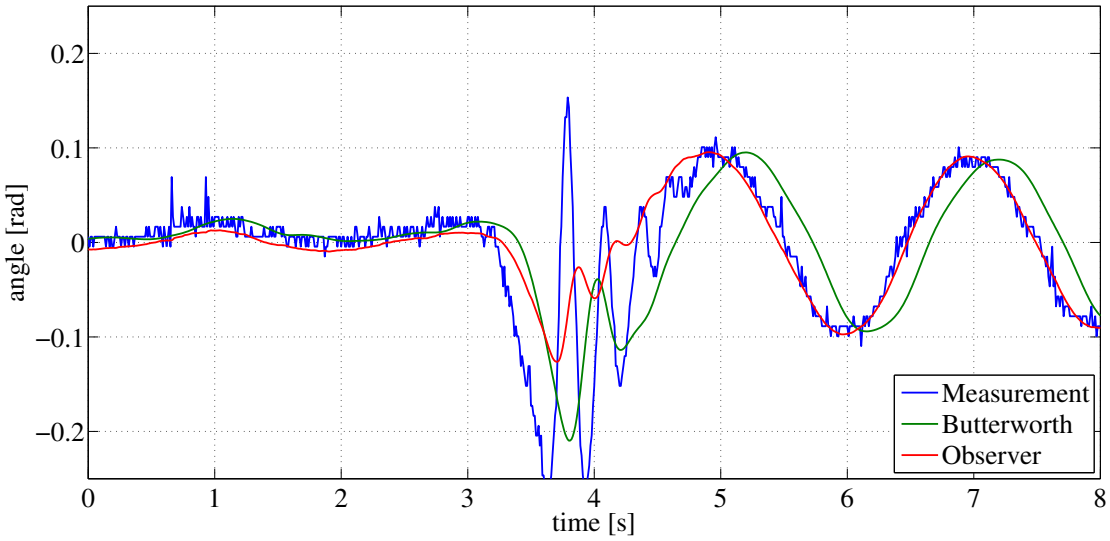

Figure 6.13: Comparison of measured, filtered and observed angles

complex observer depends on parameters of LTD (mass, lever length, damping coefficient) and rope (mass, length, damping coefficient).

The *simplified observer* resembles a specialized filter, therefore it is legitimate to compare it against a standard low-pass filter. In Fig. 6.13 the performance of the *simplified observer* is compared to a 4^{th} order Butterworth low-pass filter, with a cutoff frequency $\mathbf{f_c} = 2\,\text{Hz}$, using experimental data. During the disturbance between 3 s and 5 s, the filter shows more noise sensitivity than the observer. Furthermore the filter shows a significant time delay, while the observer does not. Therefore, the observer outperforms the filter in every aspect.

It should be noted that the depicted curves denote angles and not horizontal position deviations like shown in Fig. 6.12. The position deviations are useful to emphasize the oscillations at different positions. However, the model of the *simplified observer* has only four states, which directly describe the motion of the load, using two angles. Since the kinematics of model and real LTD are equal, it is feasible to compare the measured and observed angles, instead of the position deviations.

This concludes the validation of the observers in laboratory experiments. In summary the following is stated: Two observers, based on a complex and a simplified model have been reviewed. The *complex observer* estimates the load motion with a higher accuracy than the *simplified observer*, but the *simplified observer* shows a better rejection of high frequency oscillations. Compared to a Butterworth low-pass filter the *simplified observer* is less sensitive to disturbances and shows less delay.

Before the flight validation, two model adaptions of the *simplified observer* need to be reviewed. These adaptions have been mentioned earlier in this section, but were not discussed. The original model has been presented in Sec. 5.2.2. Different from the original, the model is considered to be a hybrid between an idealized pendulum and an

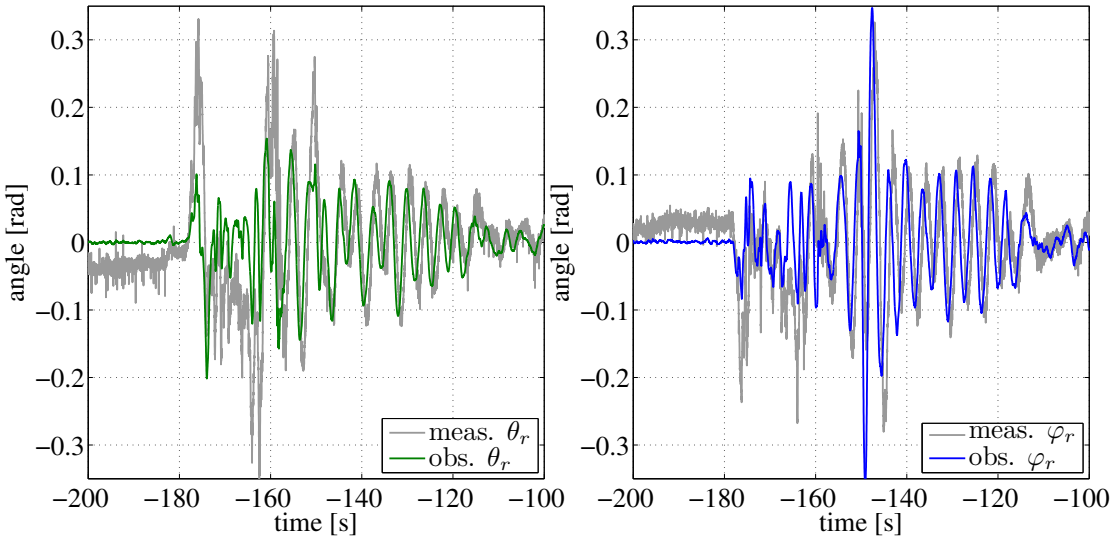

Figure 6.14: Berlin 07 - Measured and observed rope angles shortly before and after the manual-autonomous transition

roll pendulum, where the motion of the upper mass point is not influenced by the motion of the load. However, the acceleration of this point is specifiable, using the vector $\mathbf{a}$. The reason is, that in flight the observer works parallel to a translation controller. The motion of the helicopter and therefore the rope mounting point, which constitutes the upper mass point of the pendulum model, is mainly governed by the translation controller and not the dynamics of the load. The vector $\mathbf{a}$ is used to introduce the estimated acceleration of the rope mounting point into the observer. During hovering the magnitude of the vector $\mathbf{a}$ is very small and can be neglected, but during normal flight maneuvers it needs to be considered. For the laboratory experiments the rope mounting point has been fixed and therefore the acceleration vector has been negligible. The restriction of the upper mass point to move only within the $\mathbf{n_{1,2}}$-plane is the second adaptation. The reason is, that for small load angles a vertical acceleration of the upper mass point, along $\mathbf{n_3}$, has almost no influence on the oscillation of the lower mass point, compare Fig. 5.17 for an overview. Furthermore, the model has been linearized under equilibrium conditions, where the rope vector, connecting upper and lower mass point, is parallel to $\mathbf{n_3}$. A vertical acceleration of the upper mass point, causes no oscillation of the lower mass point in this particular configuration, although both mass points are accelerated along $\mathbf{n_3}$. Therefore, the influence of vertical acceleration on the pendulum oscillation has been lost during the linearisation process. To improve simplicity, the movement of the upper mass point has been restricted to the $\mathbf{n_{1,2}}$-plane, before the linearisation.

Fig. 5.3 has been presented during the validation of the non-linear *single-lift model*. The figure shows measured, observed and simulated rope angles, during forward and sideward flight maneuvers. Fig. 6.14 shows a new aspect of the same experiment. The figure presents measured and observed rope angles during the load lift-off, as well as during the

transition from manual control to autonomous flight. Both are typical maneuvers during which oscillations of LTD and rope occur. Until −180 seconds helicopter and load are still on the ground. Between −180 and −160 seconds the helicopter is in the air and manually piloted, while the load is still on the ground. At approximately −160 seconds the load is lifted from the ground and at −150 the transition from manual to autonomous flight occurs. It should be noted that two different translation controllers are used during the experiment. The translation controller of a single uncoupled helicopter, like presented in Sec. 4.3, has been used first. This controller does not consider the motion of the load. At approximately −120 seconds the single-lift translation controller has been activated. This controller actively stabilizes the motion of the load and has been presented in Sec. 6.3.

The depicted experiment is split into two important phases. During the first phase, until −160 seconds, the load is still on the ground and therefore the rope and the LTD are oscillating at high frequencies. The second phase begins with the load lift-off. Some high frequency disturbances are still present, but the slow pendulum motion is dominating the measured angles. The observer rejects most of the high frequency oscillations during the first phase. Only one short, but major, oscillation is measured and observed at −180 seconds, which has been caused by a strong acceleration during the manual piloted take-off. The observer converges towards the low frequency load motion, almost immediately after the beginning of the second phase. Based on these results the performance of the observer, in terms of disturbance rejection and angle estimation, is considered to be good. The proposed observer therefore represents a feasible solution to the problem of LTD and rope oscillations. In Sec. 7.1 a flight experiment is presented, where the observer has been used online. Additionally, this experiment demonstrates that under certain conditions, in this case strong wind gusts, the single-lift slung load transportation is not possible without utilization of the observer.

7 Experimental Validation

This chapter covers the experimental validation of the models and controllers, presented in this work.

7.1 Single-Lift Configuration

The experiments shown in Fig. 7.1 and Fig. 7.2 were conducted on the 28.11.2007 on a experimental site near Berlin. Both experiments cover the single-lift slung load transportation. The hardware setup of both experiments was identical. The technical parameters of the helicopter are described in Sec. 2 and therefore omitted here. A pear-shaped lead weight of 0.57 kg was used as load. Helicopter and load were coupled, using a mountaineering cord of 4.78 m length, which stretches to about 4.92 m length under load. LTD, mountaineering cord and load constitute a pendulum of approximately 5 m length. The weather conditions for both experiments were good. During both experiments almost no steady wind and no wind gusts were present and therefore the external disturbances were reduced to a minimum.

The experiment shown in Fig. 7.1 serves two purposes: First, to demonstrate the efficiency of the torque compensator and second, to validate the idealized pendulum approximation of helicopter and load. The non-linear translation controller for a single helicopter without slung load has been used, see Sec. 4.3 for details. To achieve stable flight, in presence of the slung load, the extended non-linear orientation controller, described in Sec. 6.2, has been utilized.

The left side of the figure shows the coordinates of the helicopter's CoM (x_h, y_h, z_h) relative to a Newtonian reference frame $\mathbf{N}$, where the coordinates x_h, y_h describe the position in the horizontal plane and z_h denotes the altitude. The right side of the figure shows the coordinates of the load (x_l, y_l, z_l) relative to the same reference frame $\mathbf{N}$. The transition from manual to autonomous flight is executed at 0 s and this moment fixes the origin of Newtonian reference frame $\mathbf{N}$ and defines the current position of the helicopter to be (0.5, 0, 0). For this reason $z_h = 0$ does not specify the ground level, but the altitude of the manual-autonomous transition. The gray line shows the desired position of helicopter and load. Steps of 9.5 m and -10 m were executed after 125 and 170 seconds.

Since the translation controller does not incorporate the load motion, the position of the helicopter should not change during the hovering period from 0 to 125 seconds. The hovering performance of the helicopter, shown in left side of Fig. 7.1, is considered to be good. After the manual-autonomous transition and a short settling time of approximately 15 seconds, the position deviation of the helicopter stayed below 40 cm. An experiment without slung load was conducted on the same day to estimate the ground truth for the

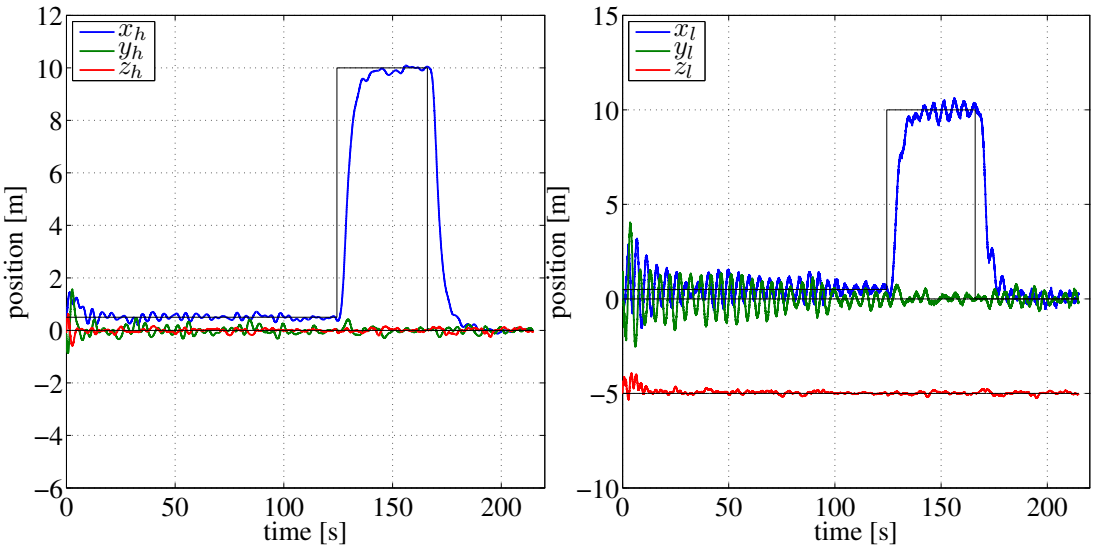

Figure 7.1: Berlin 2007 - Slung load transportation using one UAV (PID controller)

hovering performance. The non-linear controller, with equal controller coefficients and without torque compensator, has been utilized. A hovering deviation of about 34 cm has been recorded for this experiment. Therefore, the strong oscillation of the load, shown on the right side of the figure, had therefore almost no influence on the position of the helicopter. Based on this results the efficiency of the torque compensator is considered to be very good. This is an important result, since all translation controllers, presented in Ch. 6 of this work, require an orientation controller, which already considers the influence of the slung load or of the coupled system.

The examination of the load motion depicted in the right part of Fig. 7.1 exhibits two properties: First, the load oscillates with an almost constant frequency of 0.2212 Hz and an average amplitude of 1.5 m. Second, the oscillation seems to subside slowly. Considering a rope length of 5 m and a load / helicopter mass ratio of 0.044, the expected frequency of an idealized pendulum is 0.2229 Hz and the expected frequency of a roll pendulum is 0.2278 Hz.

There are two reasons why the oscillation of the load, shown on the right side of the figure, slowly subsides. The small and steady compensation movements during the hovering and the smooth and steady motion of the helicopter during flight cause only small excitations of the load. No significant external disturbances were present, because of the very good weather conditions during that day. Several experiments have shown, that load oscillations will be repeatedly excited in the presence of wind gusts. The following summarizes the results of the experiment: The motion of helicopter and slung load shown in Fig. 7.1 comply to the expected behavior. The position of the helicopter is well stabilized, but the oscillation of the load is almost not damped.

The experiment shown in Fig. 7.2 has been conducted directly after the experiment shown in Fig. 7.1. Instead of the non-linear PID-controller the state feedback controller

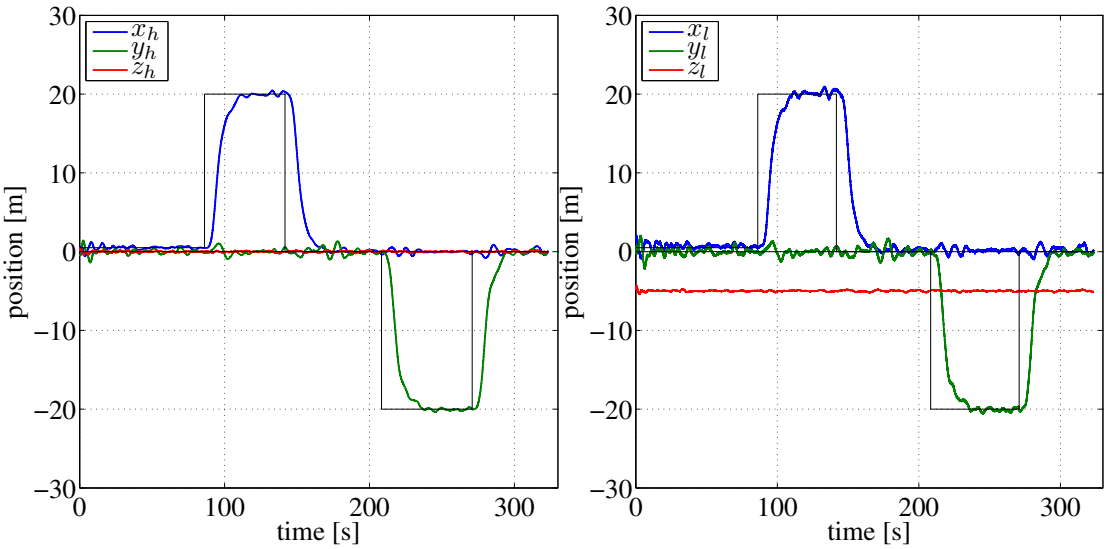

Figure 7.2: Berlin 2007 - Slung load transportation using one UAV (state feedback controller)

presented in Sec. 6.3 is used. This experiment is one of the first successfully conducted single-lift slung load transportations of the "Laboratory for autonomous flying robots"[1] of the TU Berlin. At this time the effect of random rope oscillation had not occurred. The load motion observer from Sec. 6.6 has therefore not been used during this experiment.

The left side of the figure shows the coordinates of the helicopter's CoM (x_h, y_h, z_h) and the right side of the figure shows the coordinates of the load (x_l, y_l, z_l) relative to a Newtonian reference frame **N**. The orientation of the reference frame **N** is similar to orientation of the reference frame of the previous experiment. The transition from manual to autonomous flight is executed at the time instant of 0 s. The origin of the reference frame is fixed relative to the position of the helicopter at this time instant, similar to the previous experiment. The gray line shows the desired position of helicopter and load. Two steps of approximately[2] ± 20 meters are executed along the horizontal axis of the reference frame. During the first 15 seconds strong oscillations of the load are visible. This is a temporary effect caused by the transition, which will be ignored for the further analysis. Helicopter and load show position deviations of ± 1.2 m during the execution of the position steps. The deviation is visible along the horizontal axis, which is not utilized for the considered position step. For example, a deviation of y_h, y_l is visible within the time range [90 s, 105 s]. The effect has been caused by the magnetic compass of the helicopter, which has not been calibrated correctly for the experiment. The compass heading deviated from the true geographic heading, because of a calibration error. A deviation of approximately 5° has been reconstructed from the log-files. A translation towards the

[1] This includes the author.
[2] The first step is only 19.5 m, from (0.5, 0, 0) to (20, 0, 0).

Figure 7.3: Utrera 2009 - Typical slung load motion: Hovering - Acceleration - Deceleration - Hovering

compass "north" therefore leads to a true north-west motion, that needs to be corrected by the GPS measurement. This implies, that the position deviation is not caused by the slung load. However, it is still possible to evaluate the performance of the slung load controller during the hovering periods. The investigation of time periods between the execution of position steps shows, that load oscillations caused by the preceding translation are quickly damped. This behavior is particularly visible within the time range [208 s, 240 s]. A load oscillation ($x_l \pm 1\,\mathrm{m}$) is caused by the position step from (0, 0, 0) to (0, −20, 0), within the time range [208 s, 240 s], but right after the helicopter reached the desired position the oscillation completely subsided. The results of the experiment are summarized as follows. The controller shows good hovering performance, with an deviation of the load position about ±0.8 m. Helicopter and load followed the presented position steps, but the calibration error leads to temporary position deviations of helicopter and load, as well as to temporary load oscillations. The controller performance is considered to be good, since this is one of the first successful slung load transportation experiments. Despite the compass problems the experiment has been chosen by the author, since it allows to estimate the progress made within two years of research, by comparing it to the results of the experiments conducted in Utrera 2009.

Within the scope of the AWARE project[3] several slung load experiments were conducted, but before these experiments are discussed, the motion of a typical single lift slung load transportation shall be described in detail. Fig. 7.3 shows helicopter and load during different stages of the load transportation. During hovering, before the beginning of the motion, the load is directly underneath the helicopter. The helicopter will quickly follow the load, if e.g. a wind gust displaces it. This suppresses upcoming oscillations. Then the helicopter returns slowly to its original position, without introduction of new oscillations. During the acceleration/deceleration phases the helicopter runs ahead/after the load. During flight with constant velocity the load is almost directly underneath

[3]Platform for Autonomous self-deploying and operation of Wireless sensor-actuator networks cooperating with AeRial objEcts

the helicopter. This depends on the aerodynamic resistance of the load, but for small speeds and a small sized load this is valid. At the destination position helicopter and load simultaneously come to rest, if no external disturbances occur. The author considers Fig. 7.3 to provide better impressions of the single-lift slug load transportation than the plain plots of position coordinates.

The flight data shown in Fig. 7.4 has been recorded on the 27.5.2009, during the AWARE experiments 2009 in Utrera. The figure shows one flight step of 5 meters and one of 15 meters. A jerry can connected to the LTD using a rope, has been transported by the helicopter over distances of 5 and 15 meters. The mountaineering cord of the experiment conducted 2007 has been reused. The rope length is 4.78 m without and 4.92 mwith load). The jerry can was partially filled with water, with a the total weight of can and water of 1.1 kg. During the experiment wind gusts of 30 $^{\mathrm{km}}/_{\mathrm{h}}$ have been measured, which caused the repeated displacement of the load. During the experiment the load motion observer has been utilized successfully.

The position of the load is required to stabilize the load, which is calculated using LTD angles. In flight, the rope is normally taut between helicopter fuselage and load. The rope begins to oscillate like a string of a music instrument, if it is animated by external influences like wind gusts . The purpose of the load motion observer is to estimate the position of the load, while rejecting oscillations of rope and LTD, compare Ch. 6. Two types of experiments have been conducted. The first, without the observer, to prove that rope oscillations occur during real flight experiments and the second, with the observer, to prove that the load motion observer is a solution to the problem. Fortunately the strong wind gusts caused rope oscillations right during the first experiment. The experiment needed to be aborted, due to the strong controller responses. Therefore, the first experiment is considered a successful "failure".

In the second experiment the load motion observer has been used to damp the rope oscillations, while preserving the motion of the load. The helicopter performed an autonomous take off and lifted the load off the ground after approximately 25 seconds. Two different translation controllers have been used during the experiment. A non-linear PID controller for the take off phase until the load's lift off and the state feedback controller, described in Sec. 6.3, for the load transportation. The transition between the controllers lead to small altitude loss during the switching, see z_h at approximately 25 s. The load has been lifted autonomously and the initial load oscillations were quickly dampened. Wind gusts of 30 $^{\mathrm{km}}/_{\mathrm{h}}$ lead to damped oscillations of the load during hovering, with a maximum amplitude of 0.5 meters. For real world applications this is a good value, considering the weather conditions.

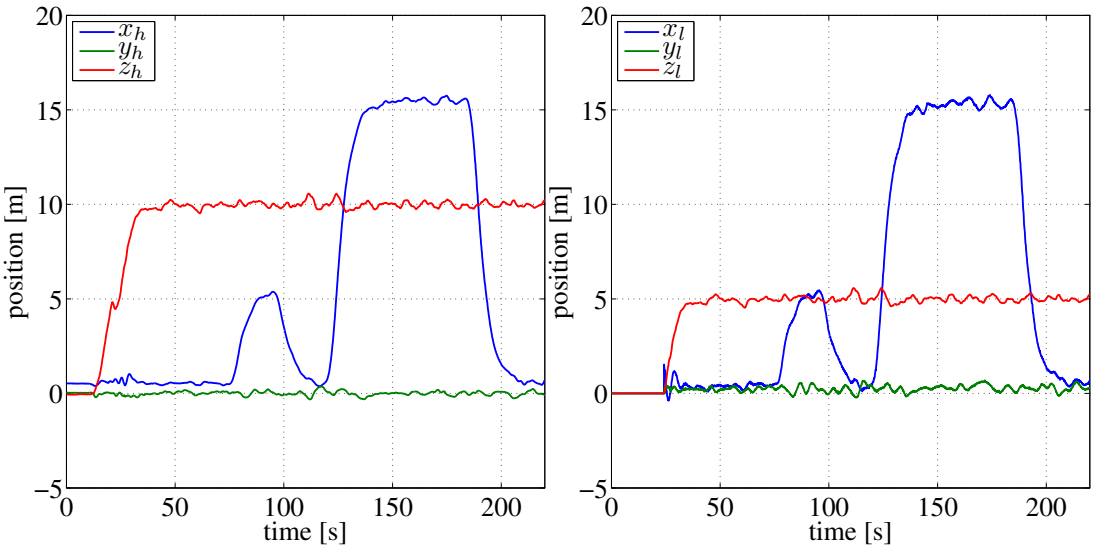

Figure 7.4: Utrera 2009 - Slung load transportation using one UAV

Furthermore, a clear progress is visible, if the experiment is compared to the experiment from the year 2007:

- The weight of the transported load almost doubled - 1.1 kg vs. 0.57 kg
- A jerry can has been transported, which provides a much larger surface for wind gusts to attack, compared to the piriform lead weight used 2007
- Strong wind gusts of 30 $^{\mathrm{km}}/_{\mathrm{h}}$ were present
- The position deviation improved from ± 0.8 m to ± 0.5 m during hovering

Therefore, the experiment is considered a success.

In summary, the experiments showed the necessity and demonstrated the functioning of the load motion observer. They validated the chosen control approach and indirectly the non-linear and linear models, which have been used to develop and simulate the controller.

This section concludes with a short reflection about absolute load positioning, using the LTD. Only an approximate estimation of the absolute load position is possible, because of the rope bowing caused by wind. For example, a rope bowing error of 5° causes a deviation of 0.44 m from the real position, considering a rope length of 5 m. For real world applications two solutions exist: First, the use of additional sensors to estimate the position of the load, for example a vision based estimation. Second, the manual placement of the load by the UAV operator. The operator changes the UAV position step by step, until the load is directly above the desired position. The manual placement is favorable whenever an exact GPS position of the placement location is unknown and

Figure 7.5: Utrera 2009 - Multi-lift configuration: Flight - During deployment - After deployment

can not be measured before the take off. In that case the helicopter operator uses his visual feedback of the deployment process to maneuver the load to the desired position.

7.2 Multi-Lift Configuration

A collage of three photographs, taken during the experiments in Utrera 2009, is presented in Fig. 7.5. The photographs show a multi-lift slung load configuration, composed of three helicopters and load, in flight, during and after the load deployment. The collage provides a visual impression of the multi-lift slung load transportation and additionally shows the rope bowing caused by wind. The ropes show almost no bowing in the left photograph, an indication that there was no major wind gust or strong steady wind at the time the picture has been taken. In contrast, strong wind has been present at the time the middle and the right photograph were taken. The middle photo shows the state shortly before the load deployment, where the load is still tautening the ropes. Nevertheless, the rope of the left helicopter is clearly bowing down and left. A deviation of 9.5° is estimated visually from the photo for the left helicopter, comparing the rope close to the LTD with a straight connection between LTD and load. The right photo has been taken shortly after the deployment of the load. The slackened ropes would normally bow downwards and towards the helicopters, like the rope of the left helicopter, but the strong wind is bowing the ropes of all helicopters to the left.

These bowing effects are the reason why the load position estimation method needs to be presented ahead of the experimental results. Like briefly discussed in Sec. 7.1, the rope bowing prevents an exact estimation of the load position from the measured LTD angles. For example, a measurement error of approximately 2 m is calculated, considering the 9.5° deviation of the left rope, shown the middle photograph of Fig. 7.5, and a rope length of 12 m. However, the true load positioning error is considered to be less than 2 m,

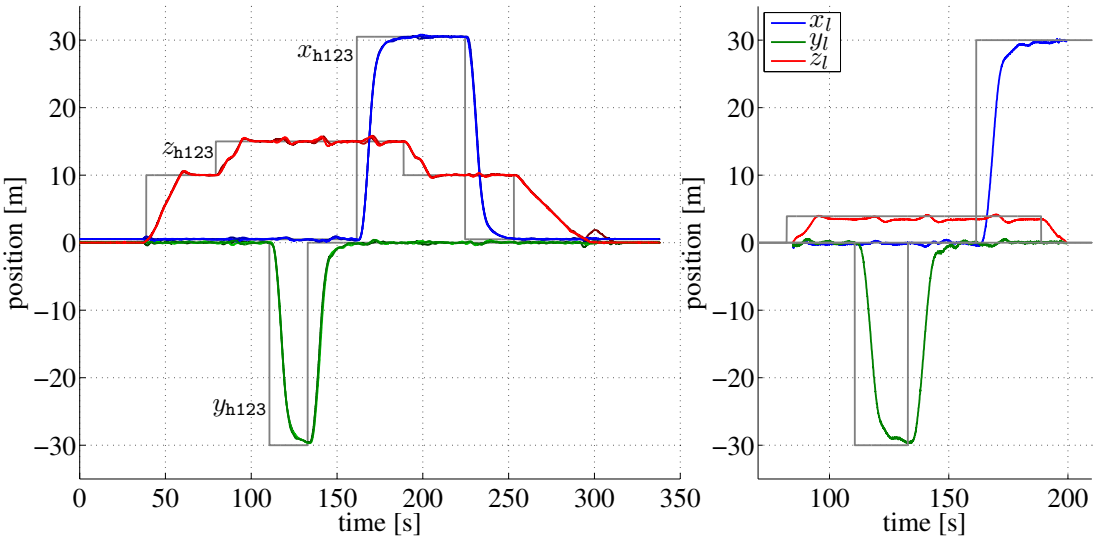

Figure 7.6: Berlin 2008 - Load transportation with three UAVs

since the load has been successfully deployed in a 2x2 meter wide area. A good position estimation based on the measured LTD angles is necessary, since all experiments have been conducted without additional load position reference measurements.

The idea behind the position estimation method is the following. Three helicopters are participating in the load transportation and therefore the rope bowing[4] causes three different load position estimations. These load positions are combined to improve the position estimation. Instead of a simple mean value calculation the positions are weighted by the estimated bowing of the rope, which is a measure for the accuracy of the LTD angles. The middle photograph in Fig. 7.5 shows, that the rope bowing is not similar for all ropes. The reason is, that the wind not only causes rope bowing, but additionally displaces the load. This causes a non equal load force distribution on the ropes and the ropes are therefore tightened differently. The actual force caused by the wind gusts is unknown, but it is nevertheless possible to approximate the influence of the rope bowing. The more force is applied to tighten a rope, the less is the influence of external disturbances on the rope bowing. The estimated load positions are therefore weighted by the ratio of the locally measured rope force and the sum of all measured rope forces. After that, the load position is estimated as sum of the weighted positions.

This method does not provide the exact load position, but it reduces the measurement error. In absence of a reference sensor this has only been validated visually. Nevertheless, this method has been used to calculate the load position estimation for Figs. 7.6-7.8. It is worth mentioning, that the rope-bowing has no influence on the functioning of the torque compensator, since the force is always acting along the rope. Therefore, the force orientation is always measured correctly by the LTD.

[4]For simplicity other influences like sensor noise, sensor resolution, calibration errors, etc. are neglected.

The experiment, whose results are depicted in Fig. 7.6, has been conducted at an experimental site near Berlin on the 19.5.2008. The UAVs have been arranged as an equilateral triangle with an edge length of 8 m. A load of approximately 5 kg, a jerry can filled with water, was connected to the LTDs, using mountaineering cords of 12 m length. The mountaineering cords stretch under stress to approximately 12.44 m length. The weather conditions have been good during the experiment, in particular almost no wind was present.

The left part of the figure shows the motion of the helicopters relative to their initial take off positions. The coordinate x_{hx} denotes the motion from south to north, y_{hx} describes motion from east to west and z_{hx} characterizes an upwards motion. The right part of the figure shows the motion of the load relative to its initial position. The coordinates (x_l, y_l, z_l) describe the motion along the same axis similar to (x_{hx}, y_{hx}, z_{hx}). The desired positions, like they were presented to the controller, are depicted by gray lines. The helicopters performed an autonomous take off after 40 s and an autonomous landing after approximately 295 s. The load was lifted from the ground after 85 s and was deployed after 200 s. To demonstrate the robustness of the proposed control approach the weight of the load has not been considered in the translation controller. Therefore, the load is only considered in the orientation controller, through the LTD force measurement. The neglected load weight leads to an altitude overshooting of approximately 0.6 m, after 61 and 96 seconds. Additionally, strong accelerations within the horizontal plane, like seen after 118 seconds, cause altitude deviations of about ± 0.6 m. After load deployment these deviations reduce to ± 0.35 m, compare Fig. 7.6 after 232 seconds, which is a good value for an outdoor helicopter.

In Fig. 7.7 a 2D overview of a different load transportation experiment with three UAVs is shown. The experiment has been conducted within the scope of the AWARE project 2009. During the whole flight, including take off and landing, the helicopters should maintain a triangle formation with a distance of 8 m between all helicopters. Ropes of 12 m length[5] were used to lift a load of approximately 5 kg. The load itself consisted of a WiFi webcam mounted on a suitcase. During the experiment the helicopters performed autonomous take off, deployment and landing. Wind gusts of 30 km/h were recorded during the experiment. The motion of the helicopters is plotted in blue, the motion of the load is plotted in red and the ropes are plotted in gray at time steps of one second. Only the motion from take off until load deployment is shown to improve the clearness of the deployment process. The flight direction is indicated by an arrow. It is recognizable that the motion of the load is clearly within extends of the deployment area, the top of a building, during the last phase of the deployment.

Fig. 7.8 allows a quantitative view of the flight, where the position of helicopters and load is plotted against time. The left part of the figure shows the position of the helicopters relative to their respective take off positions. All helicopters need to move along the same relative trajectory to preserve the triangular formation during the flight.

The helicopters followed the trajectory with a precision of 0.4 meters, but during the motion towards the building, between 185 and 200 seconds, a bigger deviation of two

[5] The ropes stretch to 12.44 m under stress.

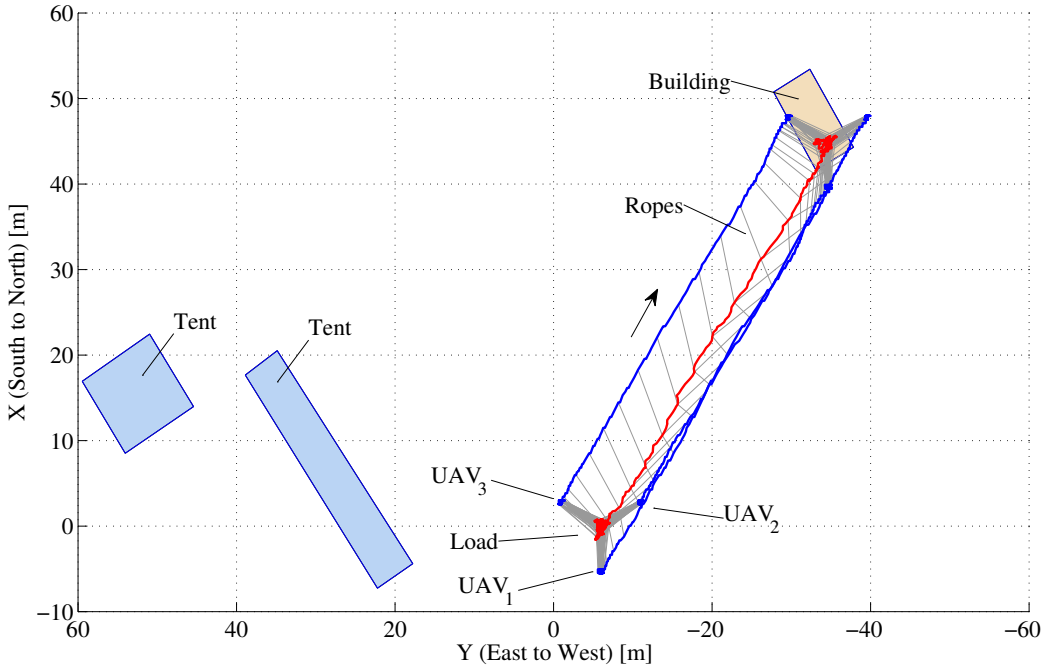

Figure 7.7: Utrera 2009 - Load transportation using three UAVs (2D-overview)

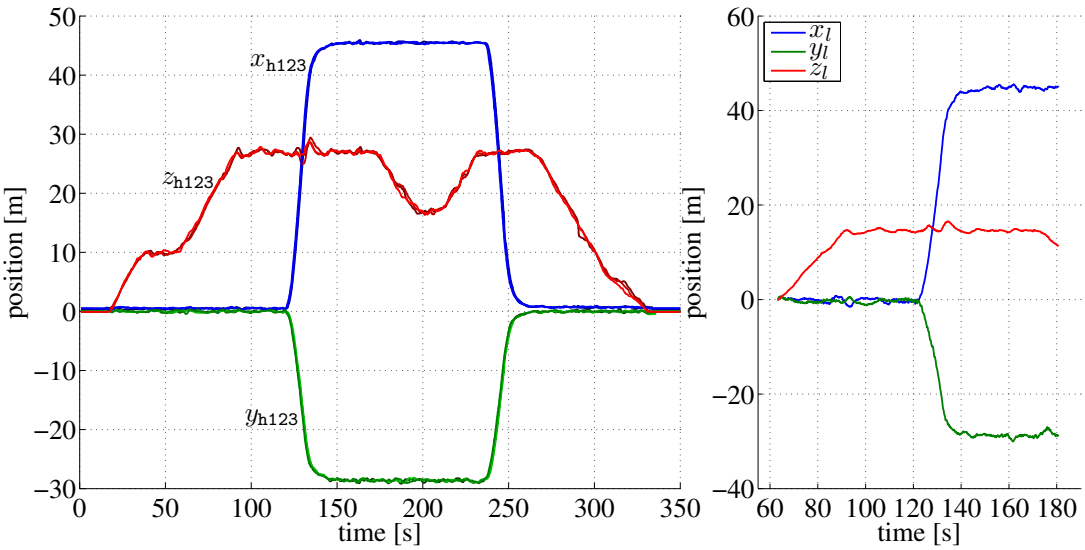

Figure 7.8: Utrera 2009 - Load transportation using three UAVs

meters in the z-axis of all helicopters is visible. The load mass has not been considered in the helicopter controller to demonstrate the robustness of the system. The altitude controller therefore requires some time to compensate for the extra weight, during periods of acceleration. It is clearly visible, that after the deployment, on the way back to the take off position (between 295 and 315 seconds) no bigger deviation in the z-axis is noticeable. The right part of Fig. 7.8 shows the motion of the load during the experiment. Similar to the single-lift load transportation, the position of the load is estimated from the angles measured by the LTD. But unlike the single-lift load transportation, the estimations of all three UAVs have been combined to provide a better approximation of the absolute load position. It should be noted that due to a possible bowing of the ropes, e.g. caused by steady wind, the measured position may deviate from the real load position, see the discussion at the beginning of this section. Improvements of this issue are discussed in Ch. 8. The load followed the desired trajectory, with a maximum deviation of one meter, during the whole flight. Considering the wind conditions during that day, the achieved accuracy was very good. The load has been successfully placed within a 2x2 meter deployment zone, on the top of the building.

8 Conclusions

The content of the thesis, as well as important results and achievements, are reviewed in this chapter. The presented conclusions are summarized and an outlook of further research is given.

8.1 Review

A general survey of external load transportation has been presented in Ch. 1, where several slung load configurations have been described. This allowed the classification of the proposed slung load transportation system. The work covered single-, dual- and multi-lift configurations based on small size helicopters. Each helicopter utilized one rope attachment point. No additional constructs, like spreader-bars, have been used for dual- or multi-lift configurations.

The utilized UAVs and required hardware components have been described briefly in Ch. 2. Additionally, the chapter included a short review of the ground station as well as the utilized software framework.

Ch. 3 and Ch. 4 presented the modeling and control of a single uncoupled helicopter. They constitute the basis, which has been required for the chapters covering the modeling and control of different slung load configurations. A non-linear model and a non-linear controller have been presented. The modeling approach and the controller design have been developed at the Technische Universität Berlin and were verified by many flight experiments. Both, model and controller, have been utilized for the development of the slung load transportation system.

Ch. 5 has been dedicated to the modeling of different slung load configurations. The derivation and validation of two non-linear models has been described, where both models together covered all considered single- dual- and multi-lift configurations. The models were verified using flight data and good correspondence between flight and simulation data has been demonstrated. These non-linear models have been useful for simulation, but their complexity hindered their application for analysis and controller design. Therefore, simplified models of single dual- and multi-lift configuration have been derived as well. The models were based on a linear *force generator model*, which encapsulates the non-linear generation process of arbitrary forces typical for helicopters. The utilization of this force generator allowed the creation of complex model behavior, using much simpler translational models. For example, the non-linear *multi-lift model* has been approximated using a simple translational model composed of four interconnected mass points (three helicopters and one load). The forces, which were applied to the helicopter mass points, have been generated using the *force generator model*. The simplified models have

been validated against the non-linear models, where the behavior correspondence of the models has been considered to be good.

The examination of internal rope and LTD oscillations completed the chapter. A model describing LTD, rope and load has been developed and verified. Simulation, laboratory and flight data showed good correspondence. The examination of simulation results revealed, that it is possible to avoid rope and LTD oscillations through the proper choice of rope length and load mass. However, this strategy limits the general applicability of the load transportation system. Instead the usage of an observer has been proposed.

Ch. 6 covered the control of slung load configurations and started with an analysis of the problems, which arise from the slung load attachment. The attachment of an external load to any point of the fuselage, except the CoM of the helicopter, creates torques acting on the helicopter. These torques change the orientation of the helicopter and, since the orientation is directly linked to the force generation of the main-rotor, change the translation of the helicopter. In return, this stimulates to motion of the load and create torques. The control of the helicopter orientation has therefore been identified to be the key to the control of complex slung load systems.

A generic, in terms of being independent from the actual slung load configuration, orientation controller has been presented. This controller is an extended version of the orientation controller for an uncoupled single helicopter. The influence of the slung load is compensated using the measured rope force vector, which summarizes the complete influence of the coupled system.

A PI-state-feedback controller has been proposed for the translation control of single-lift configurations. The feedback loop requires an estimation of the current jerk and acceleration of the helicopter. A model based acceleration estimation and a jerk observer have therefore been developed. The acceleration estimation is based on the orientation of the helicopter and the desired main-rotor lifting force, which are both easily ascertainable quantities. The results obtained by the estimation exhibited less noise than the accelerations calculated from IMU or GPS measurements.

A distributed non-linear controller has been proposed for multi-lift configurations. The controller is based on the translation controller for a single uncoupled helicopter. The transfer from a single uncoupled helicopter to a coupled multi-lift configuration became possible through the utilization of the generic orientation controller, which compensates most influences of the coupled system.

The controller for the dual-lift configuration has been considered to be an intermediate between the controllers for single- and multi-lift configurations. Consequently the proposed controller has been a combination of the PI-state-feedback for single- and the distributed controller for multi-lift configurations.

The controllers for single- and multi-lift configurations have been validated in flight experiments and the dual-lift configuration has been validated through simulation. The chapter ended with the presentation of a load motion observer, which estimates the load motion in presence of LTD and rope oscillations. The observer has been validated in laboratory and flight experiments, where the observer approximated the true motion of the load well.

For the development of the presented load transportation system many theoretical

methods exist. Most of these approaches work very well in simulation and real flight experiments are required to estimate their practicability. Therefore, the preparation and conduction of flight experiments has been a very important aspect of the thesis. The presented load transportation system has proven its functioning and reliability in many real flight experiments. Consequently, Ch. 7 has been dedicated to the evaluation of several flight experiments. The presented flight results for single- and multi-lift configurations demonstrated the capabilities of the proposed load transportation system and included an evaluation during adverse weather conditions. The experiments provided a final verification of the proposed modeling and control approach. The author considers the achieved results to be very good.

8.2 Conclusion

The development of an autonomous load transportation system based on several small size helicopters is described in this thesis. The load transportation system itself represents a novelty, and three aspects are in particular worth mentioning: The flexibility, the reliability and the validation of the system, using real flight experiments.

Most of the system's flexibility is based on its good scalability: It is possible to utilize one, two or more helicopters depending on the requirements of the transported load. The only hardware required additionally is one LTD for each autonomous helicopter. The scalability is caused by the fact, that for each helicopter the influence of the whole coupled system is estimated, using the LTD measurements and the helicopter state. Therefore, independent of the number of participating helicopters, the influence of the coupled system is determined similarly and it is always[1] possible to describe the influence of the coupled system using a single force vector. This insight is an important result of this work.

A direct consequence is the development of the generic orientation controller. The utilization of the generic orientation controller adds flexibility to the system. It reduces the requirements of the translation controllers and therefore simplifies their design. For example, depending on the requirements and the number of participating helicopters a specialized translation controller is required. The stabilization of the load is usually the most important requirement for a single-lift configuration, whereas the flight formation of the helicopters is crucial for a multi-lift configuration. The requirements above are considered for the single- and multi-lift configuration controllers presented in this thesis, but depending on the actual task other requirements might be of more importance. For example, an equally balanced load distribution is an important requirement for a multi-lift configuration, which is transporting a load close to the payload limitation of the system. The generic orientation controller provides a stabilized helicopter orientation, with a known dynamic behavior, independent from the coupled system. Therefore, only the requirements of the load transportation task need to be considered during the design of the translation controller, which simplifies the design and validation process.

[1] For the considered system class, with one rope mounting point per helicopter.

The reliability of the system is mainly caused by its fundamental design. Beside the equipment for the autonomous operation only the LTD is required. The LTD is a Cardan joint with angle and force sensors, which is a simple, inexpensive and robust device. Compared to other solutions, like the vision based estimation of the load position, the simplicity of the LTD provides higher reliability, especially during unsteady and adverse weather conditions. The LTD is not[2] affected by dust or rain, which is a major advantage over optical systems. The load position estimation of the LTD degrades in presence of internal oscillations of LTD or rope. However, a specially designed load motion observer and measurements of multiple helicopters improve the accuracy. The final version of the system allowed the placement of a load on a 2x2 meter wide deployment zone, during adverse weather conditions with wind gusts of 30 km/h, which the author considers to be a good result.

The validation of the load transportation system is one of the main achievements of this work. The author is aware of the fact, that other groups demonstrated the single-lift load transportation before the experiments in 2007. However, the presented system supports not only the single-lift load transportation, but also the dual- and multi-lift load transportation. On the 28.11.2007 the single-lift and on the 20.12.2007 the multi-lift load transportation have been successfully demonstrated in flight experiments. The latter has been, to the knowledge of the author, the world-wide first demonstration of a multi-lift load transportation.

Beside a plain demonstration of the system's functioning, the validation serves an additional important purpose. The real flight experiments are needed for the identification of design weaknesses and their correction. One example of such an improvement is the load motion observer, which had been designed after the first rope oscillations have been witnessed in flight experiments. The analysis of the LTD and rope motion as well as the design and validation of the load motion observer are important contributions of this thesis. The utilization of the load motion observer realizes a stable system and a reliable estimation of the load motion, based on the LTD's measurement and the helicopter's motion.

Another example is the estimation of jerk and acceleration from the current helicopter orientation and the desired lifting force of the main-rotor. The estimation algorithm has been designed, after the suboptimal performance of the single-lift controller had been witnessed during a flight experiment. The analysis of flight data revealed that the estimation based on GPS velocity data exhibited too much noise and that additional filtering would cause too much delay.

These are two major examples, which highlight the importance of the validation in real flight experiments. During three years of research many of these experiments have been conducted. As a result, the reliability and the overall performance of the system improved continuously, up to the state presented during the AWARE experiments 2009 and described in this thesis. The presented load transportation system is therefore a novelty in many aspects (flexibility, reliability and validation).

[2]Dust has no effect up to a certain point. The joints may block, if too much dirt gets into them.

8.3 Further Research

The presented work covers many aspects of the slung-load transportation, using small-size helicopters. However, it is natural, that at certain points of the work some research lines needed to be truncated, in order to meet the main goal of the work. Therefore, the author wants to point out some promising further research topics.

Validation of the dual-lift configuration. The flight validation of the dual-lift configuration is one aspect, which has been omitted because of time constraints. The good simulation performance of translation controller presented in Sec. 6.5 and its simple design support the feasibility of flight experiments.

Improved rope modeling. In the current state, rope collision and collapsing, as well as rope bowing, are not considered in simulation. The treatment of the rope in the non-linear models should therefore be improved. Especially the implementation of load balancing controllers, for dual- or multi-lift configurations, requires the models to support rope collision and collapsing.

Improved load position estimation. The position of the load is calculated, using the rope orientation close to the fuselage and the rope length. The rope bowing reduces the accuracy of the load position estimation. In Sec. 7.2 the author presents an algorithm, which improves the load position estimation for the multi-lift configuration and which works well. Nevertheless, this algorithm does not improve the estimation for single-lift configurations. Therefore, the author proposes an additional reference measurement of the load motion using an optical system. In this configuration the author considers the LTD to be the main- and the optical measurement to be an auxiliary-reference, which is utilized whenever available. This way the system preserves its reliability and will be functioning even without optical measurement.

Load balancing. Several experiments have shown, that the stress caused by the load is not evenly distributed on the different helicopters. In its current state the multi-lift configuration controller does not perform any kind of load balancing. The balancing serves two purposes: First, it reduces the stress for the individual helicopters to a minimum and therefore reduces the risk of failure. Second, it is necessary for the operation close to the payload limitation of the system, where one helicopter is simply not able to handle the additional load, which is caused by uneven balancing. The measured rope force vectors already include all necessary information required for the balancing.

Nomenclature

Abbreviations

CoM	Center of Mass, page 21
GPS	Global Positioning System, page 21
IMU	Intertial Measurement Unit, page 21
LTD	Load Transportation Device, page 22
UAV	Unmanned Aerial Vehicle, page 21

Block Symbols

$\mathbf{C}$	Torque compensation block, page 110
$\mathbf{D}$	Block describing the decoupling of rotation dynamics for a helicopter, page 47
$\tilde{\mathbf{D}}$	Decoupling block based on the inverse dynamics of the complete system, page 108
$\mathbf{F}_{123}^{-1}$	Block describing the inverse translation dynamic of a single-helicopter, page 44
$\mathbf{F}_{123}$	Block describing the translation dynamic of a single-helicopter, page 44
$\mathbf{Fa}_{i,123}^{-1}$	First part of the block $\mathbf{F}_{i,123}^{-1}$, page 119
$\mathbf{Fb}_{i,123}^{-1}$	Second part of the block $\mathbf{F}_{i,123}^{-1}$, page 119
$\mathbf{G}_0$	Block of pre-filter transfer functions, page 44
$\mathbf{G}_{i,0}$	Block of pre-filter transfer functions of the i'th helicopter, page 118
$\mathbf{Q}$	Bock describing the rotation kinematics of a helicopter, page 46
$\mathbf{Q}^{-1}$	Bock describing the inverse rotation kinematics of a helicopter, page 46
$\mathbf{R}_{orj}$	Orientation controller including torque compensation, page 115
$\mathbf{R}_{i,orj}$	Orientation controller including torque compensation of the i'th helicopter, page 121
$\mathbf{R}_{trans}$	Global PID translation controller block, page 120

$\mathbf{R}_{trans}$	PID translation controller block, page 44
$\mathbf{R}^{xy}_{i,trans}$	Translation controller block for horizontal motion, page 122
$\mathbf{R}^{z}_{i,trans}$	Translation controller block for vertical motion, page 122
$\mathbf{R}_{i,trans}$	PID translation controller block of the i'th helicopter, page 118
$\mathbf{W}_{p,q}$	Block describing the rotation dynamics for a helicopter (only for the rates p and q are considered), page 47
$\mathbf{W}_{p,q,r}$	Block describing the rotation dynamics for a helicopter, page 107

Mathematical Symbols

$(p^F_r,\, q^F_r)$	Rotational velocities, see $\omega_{\mathbf{R}-\mathbf{F}}$, page 57
$(p^N_r,\, q^N_r)$	Rotational velocities, see $\omega_{\mathbf{R}-\mathbf{N}}$
$(\psi,\, \theta,\, \varphi)$	Euler-angles 321, which describe the orientation of the fuselage frame **F** relative to inertial frame **N**, page 29
$(\psi^*,\, \theta^*,\, \varphi^*)$	Desired orientation of the helicopter, page 44
$(\dot{u}^*,\, \dot{v}^*,\, \dot{w}^*)$	Desired acceleration of the helicopter, page 44
$(x^*,\, y^*,\, z^*)$	Desired position of the helicopter, page 44
m_L	Mass of the load, page 61
α	Angular acceleration of a rigid body, page 27
α	Cyclic pitch angle of a rotor blade, page 36
$\alpha^{BL}_{\mathrm{mr1}}$	Attacking angle of the blades (main-rotor), page 36
$\alpha^{SP}_{1,2}$	Orientation angles of the swash plate, page 36
$\alpha^{SP}_{\mathrm{f1}}$	Lateral pitch angle, page 36
$\alpha^{SP}_{\mathrm{f2}}$	Longitudinal pitch angle, page 36
$\alpha_{\mathbf{F}-\mathbf{N}}$	Angular acceleration of frame **F** relative to frame **N**, page 27
$\alpha_{\mathbf{MR}-\mathbf{N}}$	Angular acceleration of frame **MR** relative to frame **N**, page 27
$\alpha_{\mathbf{TR}-\mathbf{N}}$	Angular acceleration of frame **TR** relative to frame **N**, page 27
$\hat{\alpha}$	Highest expected helicopter oscillation frequency, page 34
$\tilde{\alpha}$	Lowest expected helicopter oscillation frequency, page 33

cm	Center of mass of the helicopter, page 29
cm_F	Center of mass of the fuselage, page 27
cm_{hi}	Center of mass of the i'th helicopter, $cm_{h1} = cm_h = cm$, page 57
cm_l	Center of mass of the load, page 57
cm_{MR}	Center of mass of the main-rotor, page 27
cm_{TR}	Center of mass of the tail-rotor, page 27
$\mathbf{dCMRo_{hi}}$	Distance vector, connects the CoM of the i'th helicopter with the rope attachment point Ro_{hi}, page 79
$\delta\theta_i$	Pitch angle offset of the i'th helicopter, after load lift-off, page 87
dOcm	Distance vector between the control point O and the CoM of the helicopter, page 30
dOFo	Distance vector between the control point O and the fuselage frame origin Fo, page 30
dOMRo	Distance vector between the control point O and the main-rotor frame origin MRo, page 30
dORo	Distance vector between the control point O and the rope connection point Ro, page 57
dOTRo	Distance vector between the control point O and the tail-rotor frame origin TRo, page 30
F	Fuselage frame of the helicopter, page 36
F	The fuselage of a helicopter, page 26
$\mathbf{F}^{MR}$	Main-rotor force vector: $\mathbf{F}^{MR} = F_3^{MR}\mathbf{f}_3$, page 30
F_3^{MR*}	Desired lifting force of the main-rotor, page 44
$\mathbf{F}^R$	Rope force vector: $\mathbf{F}^R = F_1^R\,\mathbf{n_1} + F_2^R\,\mathbf{n_2} + F_3^R\,\mathbf{n_3}$, page 82
$\mathbf{F}_{hi}^R$	Rope force vector (i'th helicopter): $\mathbf{F}_{hi}^R = F_{hi,1}^R\,\mathbf{n_1} + F_{hi,2}^R\,\mathbf{n_2} + F_{hi,3}^R\,\mathbf{n_3}$, page 86
$\tilde{\mathbf{F}}_{hi}^R$	Rope force compensation vector (i'th helicopter): $\tilde{\mathbf{F}}_{hi}^R = \tilde{F}_{hi,1}^R\,\mathbf{n_1} + \tilde{F}_{hi,2}^R\,\mathbf{n_2} + \tilde{F}_{hi,3}^R\,\mathbf{n_3}$, page 86
$\mathbf{F}^{TR}$	Tail-rotor force vector: $\mathbf{F}^{TR} = F_2^{TR}\mathbf{f}_2$, page 30
$\mathbf{F_{hi}}$	Fuselage frame of the i'th helicopter, page 77

f_{rope}	Eigenfrequencies of a string, with $\mathrm{f_{rope}}(n) = n\left(\sqrt{F_t/\mu}\right)/(2\,l_{rp})$, page 68
$\mathbf{f}_1$	First basis vector of the fuselage frame $\mathbf{F}$, page 36
$\mathbf{f}_2$	Second basis vector of the fuselage frame $\mathbf{F}$, page 36
$\mathbf{f}_3$	Third basis vector of the fuselage frame $\mathbf{F}$, page 36
Fo	Origin of the fuselage, page 27
G	Gravitational acceleration $G = g$ in $\mathrm{m/s^2}$, page 45
g	Gravitational acceleration $g = G$ in $\mathrm{m/s^2}$, page 45
$G^{BF}_{\varphi,\theta}$	Transfer function of the controlled helicopter orientation for a big fuselage, page 91
$\mathbf{G}^{pend}$	Transfer functions of a roll pendulum, page 97
$G^{SF}_{\varphi,\theta}$	Transfer function of the controlled helicopter orientation for a small fuselage, page 91
$\mathbf{G}^{slc}$	Transfer functions describing a linearized single lift configuration, page 98
G_{FMR3}	Transfer function of main-rotor lifting force generation, page 92
$\gamma^{MR}_{\mathrm{f3}}$	Blade rotation angle, page 36
G_{td}	Time delay transfer function, page 49
$\mathbf{I}$	Moment of intertia of a body, page 27
$\mathbf{I}^F$	Moment of intertia of the fuselage, page 27
$\mathbf{I}^{MR}$	Moment of intertia of the main-rotor, page 27
$\mathbf{I}^{TR}$	Moment of intertia of the tail-rotor, page 27
Kx	Constant coefficient x, page 31
$\mathbf{L}$	Angular momentum, page 27
l_{rp}	Rope length, page 56
λ_i	Pole i of a linear time invariant system, page 52
m_F	Mass of the fuselage, page 27
m_{MR}	Mass of the main-rotor, page 27
m_{TR}	Mass of the tail-rotor, page 27

MR	Main-rotor frame of the helicopter, page 36
MR	The main-rotor of a helicopter, page 26
mr1	First basis vector of the main-rotor frame **MR**, page 36
mr2	Second basis vector of the main-rotor frame **MR**, page 36
mr3	Third basis vector of the main-rotor frame **MR**, page 36
MRo	Origin of the main-rotor, page 27
N	Newtonian reference frame. The origin No varies from experiment to experiment, page 26
$\mathbf{n}_2$	Second basis vector of the frame **N**. The vector points from East to West, page 26
$\mathbf{n}_3$	Third basis vector of the frame **N**. The vector points upwards, page 26
$\mathbf{n}_1$	First basis vector of the frame **N**. The vector points from South to North, page 26
ω	Angular velocity of a rigid body, page 27
ω^{MR}	Constant rotational velocity of the main-rotor, page 40
ω^{TR}	Constant rotational velocity of the tail-rotor, page 40
$\omega_{\mathbf{F-N}}$	Angular velocity of frame **F** relative to frame **N**. Defined as follows: $\omega_{\mathbf{F-N}} = p\,\mathbf{f}_1 + q\,\mathbf{f}_2 + r\,\mathbf{f}_3$, page 27
$\omega_{\mathbf{hi,F-N}}$	Angular velocity of frame $\mathbf{F_{hi}}$ (of the i'th helicopter) relative to **N** Defined as follows: $\omega_{\mathbf{hi,F-N}} = p_{hi}\,\mathbf{f_{hi,1}} + q_{hi}\,\mathbf{f_{hi,2}} + r_{hi}\,\mathbf{f_{hi,3}}$, page 77
$\omega_{\mathbf{MR-N}}$	Angular velocity of frame **MR** relative to frame **N**, page 27
ω_{pend}	Natural frequency of an idealized pendulum, with $\omega_{pend} = \sqrt{\frac{g}{l}}$, page 66
$\omega_{\mathbf{R-F}}$	Angular velocity of frame **R** relative to the frame **F** Defined as follows: $\omega_{\mathbf{R-F}} = -p_r^F\,\mathbf{r}_1 - \cos(\varphi_r^F)\,q_r^F\,\mathbf{r}_2 + \sin(\varphi_r^F)\,q_r^F\,\mathbf{r}_3$, page 57
$\omega_{\mathbf{R-N}}$	Angular velocity of frame **R** relative to the frame **N** Defined as follows: $\omega_{\mathbf{R-N}} = p_r^N\,\mathbf{r}_1 + \cos(\varphi_r^N)\,q_r^N\,\mathbf{r}_2 - \sin(\varphi_r^N)\,q_r^N\,\mathbf{r}_3$, page 58
$\omega_{\mathbf{R-N}}$	Angular velocity of frame **R** relative to frame **N** Defined as follows: $\omega_{\mathbf{R-N}} = -p\,\mathbf{r}_1 - \cos(\varphi)\,q\,\mathbf{r}_2 + \sin(\varphi)\,q\,\mathbf{r}_3$, page 95

ω_{rpd}	Natural frequency of a roll pendulum, with $\omega_{rpd} = \sqrt{\frac{g}{l}\left(\frac{m_l}{m_h}+1\right)}$, page 66
$\omega_{\mathbf{TR}-\mathbf{N}}$	Angular velocity of frame **TR** relative to frame **N**, page 27
p	Rotation rate, see $\omega_{\mathbf{F}-\mathbf{N}}$, page 29
$\mathbf{p}_{cm}$	Position vector of the helicopter's CoM, with $\mathbf{p}_{cm} = x\,\mathbf{n}_1 + y\,\mathbf{n}_2 + z\,\mathbf{n}_3$, page 29
p_{hi}	Rotation rate, see $\omega_{\mathbf{hi},\mathbf{F}-\mathbf{N}}$, page 77
$\mathbf{p}_{no\_cmhi}$	Position vector of the i'th helicopter's CoM, with $\mathbf{p}_{no\_cmhi} = x_{hi}\,\mathbf{n}_1 + y_{hi}\,\mathbf{n}_2 + z_{hi}\,\mathbf{n}_3$, page 77
$\mathbf{p}_{no\_cml}$	Position vector of the load's CoM, with $\mathbf{p}_{no\_cml} = x_l\,\mathbf{n}_1 + y_l\,\mathbf{n}_2 + z_l\,\mathbf{n}_3$, page 78
$\mathbf{p}_{no\_mh}$	Position vector of the *helicopter mass point*, with $\mathbf{p}_{no\_mh} = x\,\mathbf{n}_1 + y\,\mathbf{n}_2 + z\,\mathbf{n}_3$, page 94
$\mathbf{p}_{no\_mhi}$	Position vector of the i'th *helicopter mass point*, with $\mathbf{p}_{no\_mhi} = x_{hi}\,\mathbf{n}_1 + y_{hi}\,\mathbf{n}_2 + z_{hi}\,\mathbf{n}_3$, page 100
$\mathbf{p}_{no\_ml}$	Position vector of the *load mass point*, with $\mathbf{p}_{no\_ml} = \mathbf{p}_{no\_mh} + l_{rp}\,\mathbf{r}_3$, page 94
$\mathbf{p}_{no\_ml}$	Position vector of the *load mass point*, with $\mathbf{p}_{no\_ml} = x_l\,\mathbf{n}_1 + y_l\,\mathbf{n}_2 + z_l\,\mathbf{n}_3$, page 100
p_x	The actual angle of a servo actuator, page 40
φ	Roll angle, see (ψ, θ, φ), page 29
ψ	Yaw angle, see (ψ, θ, φ), page 29
q	Rotation rate, see $\omega_{\mathbf{F}-\mathbf{N}}$, page 29
q_{hi}	Rotation rate, see $\omega_{\mathbf{hi},\mathbf{F}-\mathbf{N}}$, page 77
$\mathbf{R}$	Rope frame **R**, whereat the basis vector $\mathbf{r}_3$ describes the orientation of the rope, page 57
r	Rotation rate, see $\omega_{\mathbf{F}-\mathbf{N}}$, page 29
r_{hi}	Rotation rate, see $\omega_{\mathbf{hi},\mathbf{F}-\mathbf{N}}$, page 77
R_{MR}	Radius of the main-rotor, page 27
R_{TR}	Radius of the tail-rotor, page 27

$\rho(r)$ Rotor density function, page 27

Ro Rope connection point Ro, sometimes called rope mounting point, page 57

s_x Pulse-width coded signal of the desired angle of a servo actuator, page 39

$\mathbf{T}$ Torque, page 27

$\mathbf{T}^{MR}$ Main-rotor torque vector: $\mathbf{T}^{MR} = T_1^{MR}\mathbf{f}_1 + T_2^{MR}\mathbf{f}_2 + T_3^{MR}\mathbf{f}_3$, page 30

$T_{1,2}^*$ Desired main-rotor torques, page 44

$\mathbf{T}^{TR}$ Tail-rotor torque vector: $\mathbf{T}^{TR} = T_2^{TR}\mathbf{f}_2$, page 30

θ Pitch angle, see (ψ, θ, φ), page 29

TR The tail-rotor of a helicopter, page 26

TRo Origin of the tail-rotor, page 27

u Velocity coordinate, see $\mathbf{v}_{cm}$, page 29

u_{hi} Velocity coordinate, see $\mathbf{v}_{no\_cmhi}$, page 77

u_l Velocity coordinate, see $\mathbf{v}_{no\_cml}$, page 78

v Velocity coordinate, see $\mathbf{v}_{cm}$, page 29

$\mathbf{v}_{cm}$ Velocity vector of the helicopter's CoM, with
$\mathbf{v}_{cm} = \frac{d^{\mathbf{N}}\mathbf{p}}{dt} = \dot{x}\,\mathbf{n}_1 + \dot{y}\,\mathbf{n}_2 + \dot{z}\,\mathbf{n}_3 = u\,\mathbf{n}_1 + v\,\mathbf{n}_2 + w\,\mathbf{n}_3$, page 29

v_{hi} Velocity coordinate, see $\mathbf{v}_{no\_cmhi}$, page 77

v_l Velocity coordinate, see $\mathbf{v}_{no\_cml}$, page 78

$\mathbf{v}_{no\_cmhi}$ Velocity vector of the i'th helicopter's CoM, with
$\mathbf{v}_{no\_cmhi} = \frac{d^{\mathbf{N}}\mathbf{p}_{no\_cmhi}}{dt} = u_{hi}\,\mathbf{n}_1 + v_{hi}\,\mathbf{n}_2 + w_{hi}\,\mathbf{n}_3$, page 77

$\mathbf{v}_{no\_cml}$ Velocity vector of the i'th helicopter's CoM, with
$\mathbf{v}_{no\_cml} = \frac{d^{\mathbf{N}}\mathbf{p}_{no\_cml}}{dt} = u_l\,\mathbf{n}_1 + v_l\,\mathbf{n}_2 + w_l\,\mathbf{n}_3$, page 78

$\mathbf{v}_{no\_mh}$ Velocity vector of the *helicopter mass point*, with
$\mathbf{v}_{no\_mh} = \frac{d^{\mathbf{N}}\mathbf{p}_{\mathbf{no\_mh}}}{dt} = u\mathbf{n}_1 + v\mathbf{n}_2 + w\mathbf{n}_3$, page 95

$\mathbf{v}_{no\_mhi}$ Velocity vector of the i'th *helicopter mass point*, with
$\mathbf{v}_{no\_mhi} = \frac{d^{\mathbf{N}}\mathbf{p}_{no\_mhi}}{dt} = u_{hi}\mathbf{n}_1 + v_{hi}\mathbf{n}_2 + w_{hi}\mathbf{n}_3$, page 101

$\mathbf{v}_{no\_ml}$ Velocity vector of the *load mass point*, with
$\mathbf{v}_{no\_ml} = \frac{d^{\mathbf{N}}\mathbf{p}_{no\_ml}}{dt} = u_l\mathbf{n}_1 + v_l\mathbf{n}_2 + w_l\mathbf{n}_3$, page 101

$V_s(r)$	Rotor disc volume slice, page 27
w	Velocity coordinate, see $\mathbf{v}_{cm}$, page 29
w_{hi}	Velocity coordinate, see $\mathbf{v}_{no\_cmhi}$, page 77
w_l	Velocity coordinate, see $\mathbf{v}_{no\_cml}$, page 78
x	Position coordinate, see $\mathbf{p}_{cm}$, page 29
x_{hi}	Position coordinate, see $\mathbf{p}_{no\_cmhi}$, page 77
x_l	Position coordinate, see $\mathbf{p}_{no\_cml}$, page 78
$\xi(\alpha)$	Non-linear function of the current pitch angle, page 36
y	Position coordinate, see $\mathbf{p}_{cm}$, page 29
y_{hi}	Position coordinate, see $\mathbf{p}_{no\_cmhi}$, page 77
y_l	Position coordinate, see $\mathbf{p}_{no\_cml}$, page 78
z	Position coordinate, see $\mathbf{p}_{cm}$, page 29
z_{hi}	Position coordinate, see $\mathbf{p}_{no\_cmhi}$, page 77
z_l	Position coordinate, see $\mathbf{p}_{no\_cml}$, page 78
ζ	Non-linear function of Bell-Hiller-Bar mixing, page 37

Bibliography

[Bai08] N. Bailey. *The Helicopter Pilot's Manual*. The Crowood Press Ltd., 2008.

[BBCH06] M. Bisgaard, J. Bendtsen, and A. L. Cour-Harbo. Modelling of generic slung load system. In *AIAA Modeling and Simulation Technologies Conference and Exhibit*, 2006.

[BBlCH07] M. Bisgaard, J. D. Bendtsen, and A. la Cour-Harbo. Model based vs. model free state estimation for helicopter slung load system. In *AIAA Guidance, Navigation and Control Conference and Exhibit*, 2007.

[Ber05] M. Bernard. Entwurf und implementierung einer steuerung für kooperierende autonome hubschrauber. Master's thesis, Technische Universität Berlin, 2005.

[Ber13] M. Bernard. A system of autonomously flying helicopters for load transportation, 2013. Additonal Equations <bernard_phd_thesis_additional_equations.pdf>.

[Bis07] M. Bisgaard. *Modeling, Estimation, and Control of Helicopter Slung Load System*. PhD thesis, Department of Electronic Systems Section for Automation and Control Aalborg University, 2007.

[BK09] M. Bernard and K. Kondak. Generic slung load transportation system using small size helicopters. In *IEEE International Conference on Robotics and Automation*, 2009.

[BK10] M. Bernard and K. Kondak. Load transportation system based on autonomous small size helicopters. In *Aeronautical Journal*, volume 114, pages 191–198, 2010.

[BKH06] M. Bernard, K. Kondak, and G. Hommel. *Embedded Systems - Modeling, Technology, and Applications*, chapter Framework for Development and Test of Embedded Flight Control Software for Autonomous Small Size Helicopters, pages 159–168. Springer, 2006.

[BKH08a] M. Bernard, K. Kondak, and G. Hommel. *Autonomous Systems - Self-Organization, Management, and Control*, chapter A Slung Load Transportation System Based on Small Size Helicopters, pages 49–61. Springer Netherlands, 2008.

[BKH08b] M. Bernard, K. Kondak, and G. Hommel. Load transportation system based on autonomous small size helicopters. In *23rd Bristol UAV Systems Conference*, 2008.

[BKM+07] M. Bernard, K. Kondak, N. Meyer, Y. Zhang, and G. Hommel. Elaborated modeling and control for an autonomous quad-rotor. In *Int. Unmanned Air Vehicle Systems Conf.*, pages 2375 – 2380, 2007.

[BlCHB07] M. Bisgaard, A. la Cour-Harbo, and J. Bendtsen. Full state estimation for helicopter slung load system. In *AIAA Guidance, Navigation and Control Conference and Exhibit*, 2007.

[BlCHJB07] M. Bisgaard, A. la Cour-Harbo, E. N. Johnson, and J. D. Bendtsen. Vision aided state estimator for helicopter slung load system. In *17th IFAC Symposiumon Automatic Control in Aerospace*, 2007.

[BOC07] M. Béjar, A. Ollero, and F. Cuesta. Modeling and control of autonomous helicopters. In C. Bonivento, L. Marconi, C. Rossi, and A. Isidori, editors, *Advances in Control Theory and Applications*, volume 353 of *Lecture Notes in Control and Information Sciences*, pages 1–29. Springer Berlin / Heidelberg, 2007.

[Bra76] A. R. S. Bramwell. *Helicopter Dynamics*. Edward Arnold, 1976.

[CB75] E. M. Cliff and D. B. Bailey. Dynamic stability of a translating vehicle with a simple sling load. *Journal of Aircraft*, 12:773–777, 1975.

[CK90] L. S. Cicolani and G. Kanning. Equations of motion of slung load systems with results for dual lift. Technical report, NASA Ames Reserach Center, 1990.

[CK92] L. S. Cicolani and G. Kanning. Equations of motion of slung-load systems, including multilift systems. Technical report, NASA Ames Reserach Center, 1992.

[CMS+01] L. S. Cicolani, A. H. McCoy, R. Sahai, P. H. Tyson, M. B. Tischler, A. Rosen, and G. E. Tucker. Flight test identification and simulation of a uh-60a helicopter and slung load. Technical report, NASA Center: Ames Research Center, 2001.

[CS03a] R. Cunha and C. Silvestre. Dynamic modeling and stability analysis of model-scale helicopters with bell-hiller stabilizing bar. In *AIAA Guidance, Navigation, and Control Conference*, 2003.

[CS03b] R. Cunha and C. Silvestre. Simmodheli: A dynamic simulator for model-scale helicopters. In *11th Mediterranean Conference on Control and Automation*, 2003.

[CSP03] R. Cunha, C. Silvestre, and A. Pascoal. A path following controller for model-scale helicopters. In *European Control Conference*, 2003.

[Dee06] C. Deeg. *Modeling, Simulation, and Implementation of an Autonomously Flying Robot*. PhD thesis, Technische Universität Berlin, 2006.

[DKL+07] H. Dharmayanda, T. Kang, Y. J. Lee, S. Sung, and S. Konkuk Univ. Motion stability of small scale helicopter using state feedback. In *International Conference on Control, Automation and Systems*, 2007.

[DM85] L. B. Della-Moretta. Aircraft towing and carrying linkage systems having high stability. Technical report, United States Patent, 1985.

[FG02] D. Fusato and G. Gulieri. Fligth dynamics of an articulated rotor helicopter with an external slung load. *Journal of the American Helicopter Society*, 39:577–586, 2002.

[Föl08] O. Föllinger. *Regelungstechnik*, chapter 13 Entwurf vollständiger Zustandsrückführungen, pages 501–513. Verlagsgruppe Hüthig Jehle Rehm GmbH, 2008.

[FMKK09] J. Fink, N. Michael, S. Kim, and V. Kumar. Planning and control for cooperative manipulation and transportation with aerial robots. In *Int. symposium of robotics research*, 2009.

[FPK77] L. Feaster, C. Poli, and R. Kirchhoff. Dynamics of a slung load. *Journal of Aircraft*, 14:115–121, 1977.

[FTBL00] C. R. Frost, M. B. Tischler, M. Bielefield, and T. LaMontagne. Design and test of flight control laws for the kaman burro unmanned aerial vehicle. In *AIAA Atmospheric Flight Mechanics Conference*, 2000.

[FvdW95] D. Faille and A. van der Weiden. Robust regulation of a flying crane. In *Proceedings of the 4th IEEE Conference on Control Applications*, 1995.

[GB76] N. K. Gupta and A. E. Bryson. Near-hover control of a helicopter with a hanging load. *Journal of Aircraft*, 13:217–222, 1976.

[Gla30] H. Glauert. The stability of a body towed by a light wire. Technical Report 1312, Great Britain Aeronautical research Committee, 1930.

[Gla34] H. Glauert. Heavy flexible cable for towing a heavy body below an aeroplane. Technical report, Great Britain Aeronautical research Committee, 1934.

[GMBO04] A. Gonzalez, R. Mahtani, M. Bejar, and A. Ollero. Control and stability analysis of an autonomous helicopter. In *Automation Congress*, 2004.

[GSCA07] B. Guerreiro, C. Silvestre, R. Cunha, and D. Antunes. Trajectory tracking h2 controller for autonomous helicopters: and aplication to industrial chimney inspection. In *17th IFAC Symposium on Automatic Control in Aerospace*, 2007.

[HCC87] J. H. C. Curtiss. Studies of the dyncamics of the twin-lift system. Technical report, Department of Mechanical and Aerospace Engineering Princeton University, 1987.

[HT88] R. A. Hess and P. M. Tran. Pilot/vehicle analysis of a twin-lift helicopter configuration in hover. *Journal of Guidance, Control, and Dynamics*, 11:465–472, 1988.

[Joh94] W. Johnson. *Helicopter Theory*. Dover, 1994.

[KBHK05] K. Kondak, M. Bernard, G. Hommel, and D. Kopanev. High performance position control of an autonomous small size helicopter. In *IASTED Int. Conf. on Robotics and Applications*, 2005.

[KBLH06] K. Kondak, M. Bernard, N. Losse, and G. Hommel. Elaborated modeling and control for autonomous small size helicopters. In *ISR/ROBOTIK 2006 Joint conference on robotics*, 2006.

[KBMH07] K. Kondak, M. Bernard, N. Meyer, and G. Hommel. Autonomously flying vtol-robots: Modeling and control. In *IEEE Int. Conf. on Robotics and Automation*, pages 2375 – 2380, 2007.

[KDH+04] K. Kondak, C. Deeg, G. Hommel, M. Musial, and V. Remuß. Mechanical model and control of an autonomous small size helicopter with a stiff main rotor. In *IEEE/RSJ Int. Conf. on Intelligent Robots and Systems*, 2004.

[KSS02] H. J. Kim, D. H. Shim, and S. Sastry. Flying robots: Modeling, control and decision making. In *IEEE International Conference on Robotics &Automation*, 2002.

[KT98] S. K. Kim and D. M. Tilbury. Mathematical modeling and experimental identication of a model helicopter. In *AIAA Guidance, Navigation, and Control Conference*, 1998.

[KT04] S. K. Kim and D. M. Tilbury. Mathematical modeling and experimental identification of an unmanned helicopter robot with flybar dynamics. *Journal of Robotic Systems*, 21:95–116, 2004.

[Kuy08] F. Kuypers. *Klassische Mechanik*, chapter 3.3, pages 50–51. WILEY-VCH, 2008.

[LCPM03] M. La Civita, G. Papageorgiou, and T. Messner, W.C AND; Kanade. Integrated modeling and robust control for full-envelope flight of robotic helicopters. In *ICRA '03. IEEE International Conference on Robotics and Automation*, 2003.

[LCPMK03] M. La Civita, G. Papageorgiou, W. C. Messner, and T. Kanade. Design and flight testing of a gain-scheduled h-inf loop shaping controller for wide-envelope flight of a robotic helicopter. In *American Control Conference*, 2003.

[LJR99] C.-I. Lim, R. P. M. Jr., and A. A. Rodrguez. An interactive modeling, simulation, animation and real-time control (mosart) twin lift helicopter system environment. In *Proceedings of the American Control Conference*, 1999.

[Mac73a] Maciolek. Multi-lift aircraft control system. Technical report, United States patent office, 1973.

[Mac73b] J. R. Maciolek. Direct lift, drag and heading improvement for multi-lift aircraft control system. Technical report, United States Patent, 1973.

[Met70] A. R. Mettam. Wind-tunnel investigations of instability in a cable-towed body system. Technical report, Aeronautical Research Councel Reports and Memoranda, 1970.

[MFK10] N. Michael, J. Fink, and V. Kumar. Cooperative manipulation and transportation with aerial robots. *Autonomous Robots*, 1:1–14, 2010.

[MKFK09a] N. Michael, S. Kim, J. Fink, and V. Kumar. Kinematics and statics of cooperative multi-robot aerial manipulation with cables. Technical report, University of Pennsylvania, Philadelphia, PA, 2009.

[MKFK09b] N. Michael, S. Kim, J. Fink, and V. Kumar. Kinematics and statics of cooperative multi-robot aerial manipulation with cables. In *ASME Int. Design Engineering Technical Conf. & Computers and Information in Engineering Conf.*, San Diego, CA, 2009.

[MKT00] B. Mettler, T. Kanade, and M. B. Tischler. System identification modeling of a model-scale helicopter. Technical report, Journal of the American Helicopter Society, 2000.

[MP73] E. C. Micale and C. Poli. Dynamics of slung bodies utilizing a rotating wheel for stability. *Journal of Aircraft*, 10:760–763, 1973.

[MP93] M. Mittal and J. V. R. Prasad. Three-dimensional modeling and control of a twin-lift helicopter system. *Journal of Guidance, Control, and Dynamics*, 16:86–95, 1993.

[MPS91a] P. K. A. Menon, J. V. R. Prasad, and D. P. Schrage. Nonlinear control of a twin-lift helicopter configuration. *Journal of Guidance, Control, and Dynamics*, 14:1287–1293, 1991.

[MPS91b] M. Mittal, J. Prasad, and P. Srage. Nonlinear adaptive control of a twin lift helicopter system. In *IEEE Control Systems*, 1991.

[MPS92] M. Mittal, J. V. R. Prasad, and D. P. Schrage. Comparison of stability and control characteristics of two twin-lift helicopter configurations. *Nonlinear Dynamics*, 3:199–223, 1992.

[PC73] C. Poll and D. Cromack. Dynamics of slung bodies using a single-point suspension system. *Journal of Aircraft*, 10:80–86, 1973.

[PDB+07] K. Peng, M. Dong, M. C. Ben, G. Cai, Y. L. Kai, and H. L. Tong. Design and implementation of a fully autonomous flight control system for a uav helicopter. In *26'th Chinese Control Conference*, 2007.

[Phi44] W. H. Phillips. Stability of a body stabilized by fins and suspended from an airplane. Technical report, NACA, 1944.

[Phi49] W. H. Phillips. Theoretical analysis of oscillations of a towed cable. Technical Note 1796, NACA Langley Aeronautical Laboratory Langley Air Force Base, Va., 1949.

[Pin70] W. J. G. Pinsker. A form of lateral instability of lifting free-flight models towed by a helicopter. Technical report, Aeronautical Research Councel Reports and Memoranda, 1970.

[RR92] H. K. Reynolds and A. A. Rodriguez. H-inf control of a twin lift helicopter system. In *Proceedings oft the 31th Conference on Decision and Control*, 1992.

[RRR89] R. Raz, A. Rosen, and T. Ronen. Active aerdynamic stablization of a helicopter/sling-load system. *Journal of Aircraft*, 26:822–828, 1989.

[Ser00] F. S. Service. *Rotorcraft Flying Handbook*. U.S. Department of Transportation Federal Aviation Administration, 2000.

[Sha63a] R. E. Shanks. Experimental invesitgation of the dynamic stability of a towed parawing glider air cargo delivery system. Technical report, NASA, 1963.

[Sha63b] R. E. Shanks. Experimental invesitgation of the dynamic stability of a towed parawing glider model. Technical report, NASA, 1963.

[Sha65] R. E. Shanks. Experimental invesitgation of the dynamic stability and controlability of a towed model of a half-cone reentry vehicle. Technical report, NASA, 1965.

[SSD07] K. L. Sorensen, W. Singhose, and S. Dickerson. A controller enabling precise positioning and sway reduction in bridge and gantry cranes. *Control Engineering Practice*, 15:825–837, 2007.

[SSK97] N. Singer, W. Singhose, and E. Kriikku. An input shaping controller enabling cranes to move without sway. In *American Nuclear Society 7th Topical Meeting on Robotics and Remote Systems*, 1997.

[Stu01] R. Stuckey. Mathematical modelling of helicopter slung-load systems. Technical report, Air Operations Division, DSTO Aeronatical And Maritime Research Laboratory, 2001.

[TTC04] C. R. Theodore, M. B. Tischler, and J. D. Colbourne. Rapid frequency-domain modeling methods for unmanned aerial vehicle flight control applications. *Journal of Aircraft*, 41:735–743, 2004.

[UK92] F. E. Udwadia and R. E. Kalaba. A new perspetive on constrained motion. In *Mathematical and Physical Sciences*, 1992.

[UK96a] F. E. Udwadia and R. E. Kalaba. *Analytical Dynamics*. Cambridge University Press, 1996.

[UK96b] F. E. Udwadia and R. E. Kalaba. Equations of motion for mechanical systems. *Journal of Aerospace Engineering*, 9:64–69, 1996.

[Wag06] W. Wagtendonk. *Principles of Helicopter Flight*. Aviation Supplies & Academics, Inc., 2006.